

Sensitivity and Background Estimates for Phase-II of the COMET Experiment

Benjamin Edward Krikler
of Imperial College London

A dissertation submitted to Imperial College London
for the degree of Doctor of Philosophy

Abstract

Declaration

This dissertation is the result of my own work, except where explicit reference is made to the work of others, and has not been submitted for another qualification to this or any other university. This dissertation does not exceed the word limit for the respective Degree Committee.

Benjamin Edward Krikler

Acknowledgements

Contents

1. The History and Theory of Charged Lepton Flavour Violation (CLFV)	2
1.1. The Muon and the Birth of the Standard Model	2
1.2. Neutrino Oscillations Break Lepton Flavour Conservation	6
1.3. In Search of Charged Lepton Flavour Violation (CLFV)	8
1.3.1. Motivations and Status	8
1.3.2. Muon CLFV Channels	10
2. Muon-to-Electron Conversion and the Muonic Atom	13
2.1. Muon Decay in Orbit	16
2.2. Muon Nuclear Capture	18
2.3. SINDRUM-II: Present Limits	19
3. The COMET Experiment	21
3.1. Overview of Signal and Backgrounds	22
3.2. General Experimental Techniques	24
3.2.1. Proton Beam Energy and Production Target	24
3.2.2. Particle Transport through Bent Solenoids	26
3.2.3. Stopping Target Material and Beam Pulsing	28
3.3. COMET Phase-I	31
3.4. COMET Phase-II	33
3.5. Schedule and Status	35
4. Offline Software and The COMET Simulation	39
4.1. Developing the COMET Offline Framework	39
4.2. Overview of ICEDUST	42
4.3. The COMET Simulation	44
4.3.1. Handling Geometry	46
4.3.2. Field Calculation	49
4.3.3. Production Target Simulations	52

4.3.4. Extending the Geant4 Physics Modelling	54
5. COMET Phase-II: Optimisation	60
5.1. Optimisation Strategy	60
5.2. Production Target Optimisation	62
5.2.1. Configuration	62
5.2.2. Length Scan	63
5.2.3. Radius scan	65
5.2.4. Final Result	68
5.3. Dipole Strengths of the Muon Beamline	69
5.3.1. Large-sample Production Target Simulation	69
5.3.2. The Optimised Dipole Field Strengths	70
5.4. Electron Spectrometer's Dipole	72
5.4.1. Method and Potential Short-comings	72
5.4.2. Results	73
5.5. Stopping Target Position	76
5.6. Collimators in the Muon Beamline	82
5.6.1. Collimator Placement	83
5.6.2. Collimator Height Optimisation	86
5.7. The Beam and Decay-in-Orbit Blockers	90
5.8. Summary of optimised parameters	93
5.9. Future optimisations	94
6. COMET Phase-II: Signal Sensitivity	96
6.1. Muon Stopping Rate	96
6.2. Acceptance of Stopping Target Electrons	98
6.2.1. Geometric Acceptance	99
6.2.2. Timing Window Efficiency	100
6.2.3. Momentum Cut Efficiency	101
6.2.4. Total Signal Acceptance	103
6.3. Single Signal Event Sensitivity (SES) and Run Time	104
7. COMET Phase-II: Backgrounds	107
7.1. Muon Decay in Orbit (DIO)	107
7.2. Radiative Muon Capture (RMC)	109
7.2.1. Calculation and Simulation of RMC	112
7.2.2. Aluminium-26 and Radiative Muon Capture (RMC)	113

7.3.	Radiative Pion Capture (RPC)	114
7.3.1.	Photons from Radiative Pion Capture (RPC)	116
7.3.2.	Pion Stopping Rate	116
7.3.3.	Simulating RPC	117
7.4.	Antiprotons in the Beam	119
7.4.1.	Antiproton Production Rate and Spectrum	120
7.4.2.	Simulating Antiprotons	124
7.4.3.	Results of simulation	126
7.4.4.	Reducing Antiproton Backgrounds Further	133
7.5.	Direct Beam-Related Backgrounds	133
7.6.	Cosmic Ray Background	137
7.7.	Summary of Background Rates	141
7.7.1.	Backgrounds Not Considered	142
7.7.2.	Principal Uncertainties	143
7.8.	Further Studies and Improvements	144
8.	Summary	145
A.	Drifts in a Bent Solenoid	150
A.1.	Uniform Solenoidal Field	150
A.2.	Field in a Bent Solenoid	150
A.3.	Drift Calculation	151
A.3.1.	Gradient Drift	151
B.	Kinematic End-point for Antiproton Production	153
B.1.	Derivation	154
C.	Revisiting the Stopping Target Region	157
C.1.	Understanding the Stopping Target Region	157
C.2.	Improving the Target Design	159
C.2.1.	Muon Stopping Rate	161
C.2.2.	Signal Acceptance	162
C.2.3.	Summary and Future Improvements	162
D.	Summary of the AlCap Experiment	163
	List of Simulation Configurations	165

List of Acronyms 166

Bibliography 168

Chapter 1.

The History and Theory of Charged Lepton Flavour Violation (**CLFV**)

“Who ordered that?”

— The author, upon presentation of ‘ika-no-ikizukuri’ (live squid sashimi) at a collaboration meeting in Fukuoka, Kyushu Island

1.1. The Muon and the Birth of the Standard Model

In 1897, the British physicist Thomson discovered the first sub-atomic particle: the electron. Over the next 30 years or so, the supposedly indivisible object of the atom was divided multiple times, giving way to the neutron, the proton, and the first anti-particle, the positron. Far from the simple, solid sphere previously assumed, the atom had become a dynamic object, with a cloud of negative electrons bound to a positive nucleus consisting of neutrons and protons.

That the electrons were bound to the nucleus was readily understood due to their opposite electric charges, but the nucleus itself posed two bigger problems. Firstly, some nuclei had been observed to emit ‘beta-rays’ and change a proton to a neutron in the process (beta-rays are now known to be electrons or positrons). Secondly, the nucleus consisting of only neutral and positive particles pose a problem since the positive charges should repel one another. In both cases, something new was needed to resolve these challenges.

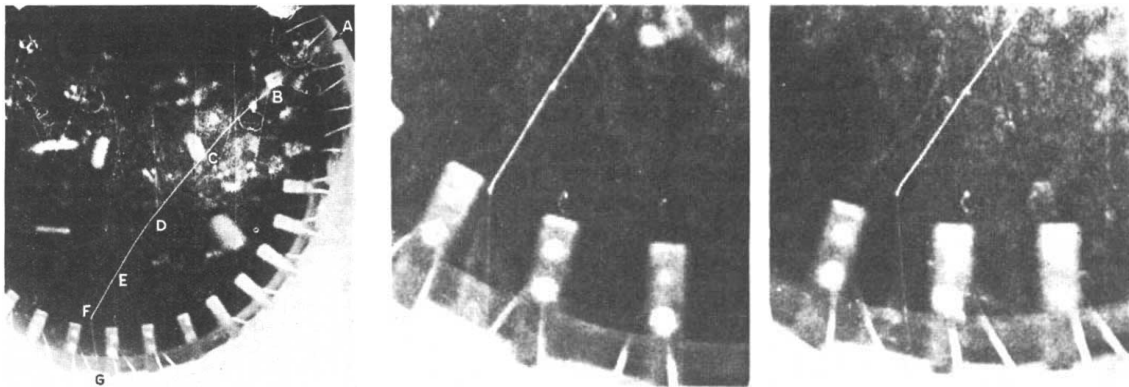


Figure 1.1.: One of the earliest cloud chamber photographs of a muon, taken in 1940 [85]. In the left-most image the muon enters the chamber at point A and travels to point F, where it eventually decays to an electron which can be seen faintly leaving the image at point G. The images to the right are a stereoscopic zoom in on point F, showing the relatively slow and more ionising muon and the faster, less ionising electron.

In 1935, Yukawa – a physicist from Japan, where this thesis will often return – proposed a solution to the second challenge. He suggested that, as for the electromagnetic force binding electrons to the nucleus via the exchange of some carrier particle (the photon), an exchanged particle could explain the very strong force that helped to glue protons to neutrons to form the nucleus. Unlike the photon, though, this particle would have to be massive and readily absorbed by the protons and neutrons. Yukawa was even able to predict the mass of this particle via the uncertainty principle, finding it to be around 100 MeV [89].

Then, in 1937, a particle with a mass very close to this prediction was observed in cosmic ray events by several physicists in Japan [74] and the US [73, 78]. But the initial hopes that this was indeed the Yukawa particle faded quickly as this particle easily penetrated through the matter of the detectors, whilst Yukawa’s particle should be rapidly absorbed. So unexpected was this new particle with its mass in between that of an electron and a proton and its relatively long lifetime, that Rabi was (also) forced to ask, “Who ordered that?”. It took some time, but eventually this particle became known as the muon.

The muon was interesting because it seemed to interact very weakly with matter, and because it seemed only to decay to an electron. For this to happen, something else has to be emitted in order to conserve momentum and energy, given that the electron is about 207 times lighter than the muon. There were two obvious possibilities for the ‘something else’: a photon, or a neutrino-antineutrino pair.

Whilst trying to solve the first issue of nuclear beta-decay, another new particle had been proposed, called the neutrino. When a proton inside a nucleus becomes a neutron (or vice versa), an electron (or positron) is emitted. The difference in the mass between the original and final nuclei had a fixed value, and yet electrons were observed with a range of energies all less than the value of this difference. The neutrino was proposed as a solution: a massless particle was carrying away the missing energy and had the additional property of interacting only very weakly making it nearly impossible to detect. By studying the spin of the parent and daughter nuclei it was also realised that the neutrino had spin of $\hbar/2$.

Muon decay was similar to this, in that the electron appeared with less energy than was available to it. On the other hand, it was clear from the spectrum of emitted electrons that not one, but two neutrinos were being emitted. Being spin half-particles, either the neutrino was its own anti-particle, or one would be a neutrino and the other an anti-neutrino. Either way, having two neutrinos emitted posed its own challenge since the two neutrinos would be able to annihilate with one another, and muon decay to a photon and electron would become comparably large. Searches for a muon decaying to a photon and electron were performed starting with the experiment of Hincks and Pontecorvo [58], shown in Fig. 1.2. Since these experiments came back empty handed it was concluded that something else, something new, had to be introduced to distinguish one neutrino from the other, such that they were unable to annihilate one another.

This something became known as ‘lepton flavour’. One neutrino carried away the ‘flavour’ of the muon, the other cancelled out the ‘flavour’ of the electron, so that if you started with a muon, you finished with either a muon or a muon-neutrino. Similarly, since muon decay starts with no electrons you must finish with no electron flavour, achieved by having an electron and electron-antineutrino simultaneously produced. Nowadays, this is known as Lepton Flavour Conservation and was cemented into theory when muon-neutrinos were identified in an experiment at Brookhaven in 1962. This experiment produced a beam of neutrinos by the decay of pions (the modern name for Yukawa’s particle) to a muon. If Lepton Flavour Conservation did not exist, if they could be made to interact in a detector , the neutrinos would produce either electrons or muons, and since only muons were observed, Lepton Flavour Conservation was confirmed. observed muons produced from the neutrinos originally emitted when a pion (the modern name for Yukawa’s particle) decays to a muon [39].

Thus, not only had the discovery of the muon been the discovery of a new charged particle, but it was also responsible for a new neutrion and a new law of conservation!

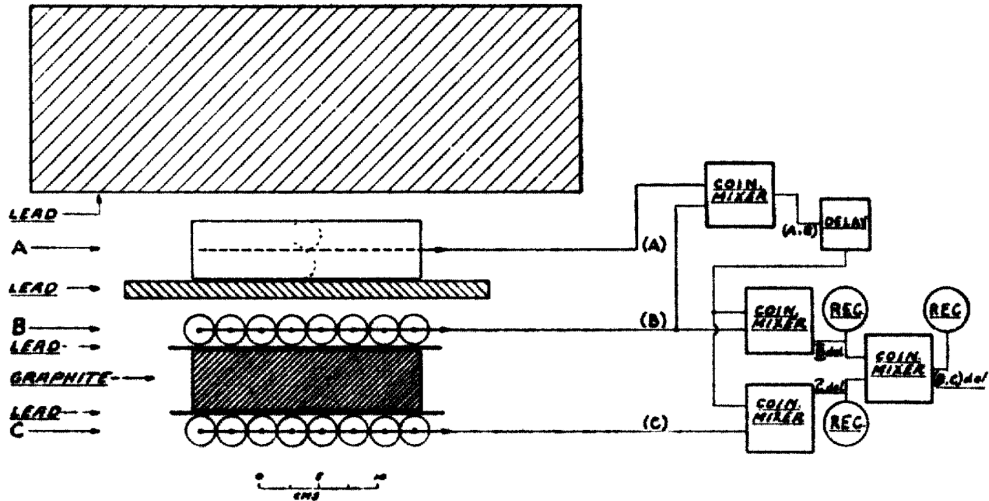


Figure 1.2.: The setup of the first experiment to look for photons produced during muon decay taken from [58]. Cosmic muons arrived from the top, slowing down in the big block of lead, triggering two Geiger-Muller counters (A and B) as they passed and eventually coming to stop in the graphite. From there, electrons and any potential photons would be detected in the counters above and below the graphite (B and C). No photons were seen in coincidence with an electron from muon decay, which lead theorists to hypothesise two distinct neutrino flavours.

Yet this conservation law is somewhat accidental. Noether's theorem tells us that for every system with a continuous symmetry, some quantity will remain conserved. This is the rule that gives us conservation of momentum, energy, and angular momentum (the conserved properties) in systems that are the same regardless of their place, time, or direction (the continuous symmetries). An extension of this theorem applies for local transformations of the system's 'gauge', which is any property that when changed has no impact on the physics outcome, such as the absolute value of the ground in an electric circuit. In particle physics, this extension gives rise to the various particle charges, such as the electromagnetic charge caused by the $U(1)$, or simple phase, of a particle's wavefunction and the even more abstract $SU(2)$ and $SU(3)$ hypercharges of the weak and strong (colour) forces. In the case of the conservation of lepton flavour however, no such symmetry exists. Instead, this conservation is embedded into the Standard Model (SM) of particle physics through the electroweak theory and lepton universality.

In addition to the leptons and their interactions via the electroweak forces, the SM describes the quark sector and their interactions via Quantum Chromodynamics (QCD). Quarks are the particles that make up the neutrons and protons (not only have we divided the atom, but also its constituents) and even the pion, Yukawa's predicted particle that was discovered in 1947. Built around the frameworks of local gauge invariance, quantum

field theory, and spontaneous symmetry breaking, the [SM](#) has been one of the most rigorously tested theories, and with only a few exceptions has held up incredibly well to measurements so far.

1.2. Neutrino Oscillations Break Lepton Flavour Conservation

Around the same time that the muon neutrino was discovered, work was already underway that would start to put holes in Lepton Flavour Conservation. In 1968, Raymond Davis Jr. and his group at Brookhaven measured the number of electron neutrinos coming from the sun and found there to be about one third of what was expected [40]. This puzzle remained until it was solved by experiments in Canada and Japan in the early 2000s: the neutrinos were being produced in the expected quantity, but as they travelled from where they were produced to the detectors on earth, they were changing their flavour! Nowadays, experiments in Japan and the US, such as the T2K [11] and Nova [21] experiments, produce beams of muon neutrinos only to detect them hundreds of kilometres away as electron neutrinos.

Explaining this requires that neutrinos have mass, although far less than any other of the particles in the [SM](#). Not only that, but the neutrino states with definite mass are not the same as the flavour states by which neutrinos interact with everything else. A particle's propagation depends on its energy and mass eigenstate and since these are mixes of flavour eigenstates, the overlap with a given flavour eigenstate will change as a neutrino propagates. In the case of neutrinos, this results in an oscillation, where the probability of detecting a neutrino in a given flavour state depends on how far it has travelled.

As it was for the discovery of the muon, the discovery of the non-zero value of the neutrino mass and the oscillation between neutrino flavour states has opened a whole host of new questions. How does the neutrino acquire its mass? Why is the mass scale so much smaller than any other known particle? As the only chargeless, massive fermion in the [SM](#), what is the nature of this mass: Is it produced via an interaction with the Higgs or via a Majorana mechanism, in turn making the neutrino into its own antiparticle? Is it a combination of these mechanisms?

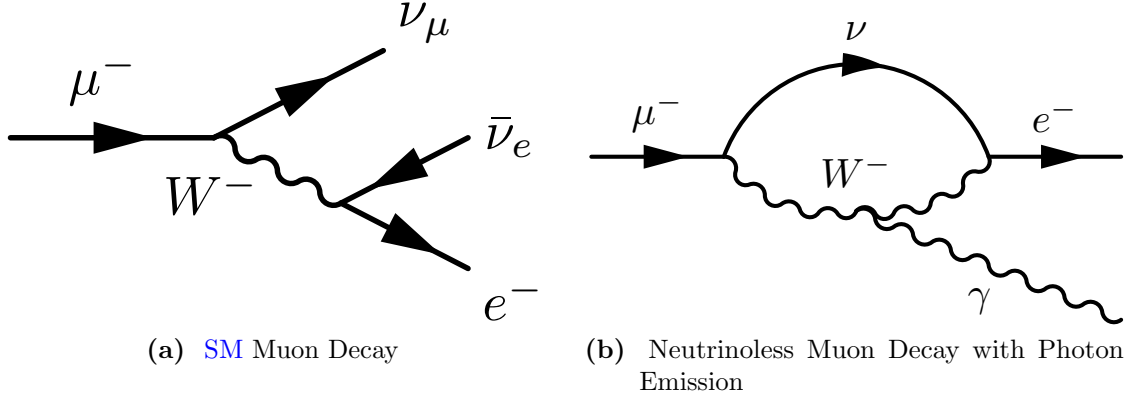


Figure 1.3.: Feynman diagram for the neutrinoless muon decay to a photon and electron mediated by a neutrino oscillation. Although allowed in the SM with neutrino oscillations, the actual rate from this diagram is well below present experiment sensitivities. A similar diagram was envisaged to show that the lack of observation of $\mu^\pm \rightarrow e^\pm \gamma$ implied distinct neutrino flavours.

Either way, it is clear that the neutrinos themselves do not conserve lepton flavour, and this immediately makes it possible that the charged leptons – the electron, the muon, and the tau – also break Lepton Flavour Conservation. How neutrinos can cause this is demonstrated in Fig. 1.3b, where the muon neutrino annihilates with the electron neutrino whilst energy and momentum are conserved by the emitted photon. We can nowadays calculate the rate for such a diagram and find it to be heavily suppressed:

$$\mathcal{BR}(\mu \rightarrow e\gamma) \propto \left| \sum_i U_{\mu i}^* U_{e i} \frac{m_{\nu_i}^2}{M_W^2} \right|^2 < 10^{-54}, \quad (1.1)$$

where $U_{\alpha i}$ is an element of the mass-mixing matrix transforming the α flavour state to the i -th mass state with mass M_{ν_i} (the Pontecorvo-Maki-Nakagawa-Sakata ([PMNS](#)) matrix), and M_W is the mass of the W -boson. This rate can be considered doubly suppressed: the summation over the different mass eigenstates produces a GIM suppression, whilst the mass imbalance between the neutrinos and the W -boson suppresses this further.

Emission of a photon is not the only additional muon decay process made possible by neutrino oscillations. A negative muon that has become bound to the nucleus of an atom (discussed further in [2](#)) will also be able to convert to an electron without emitting neutrinos via the diagrams shown in Fig. [1.4](#). In this case, however, the rate calculation is complicated by the quark and gluon contents of the nucleus, form factors of the quarks and gluons in the nucleons and nucleons in the nucleus, and the interference that can occur between each diagram.

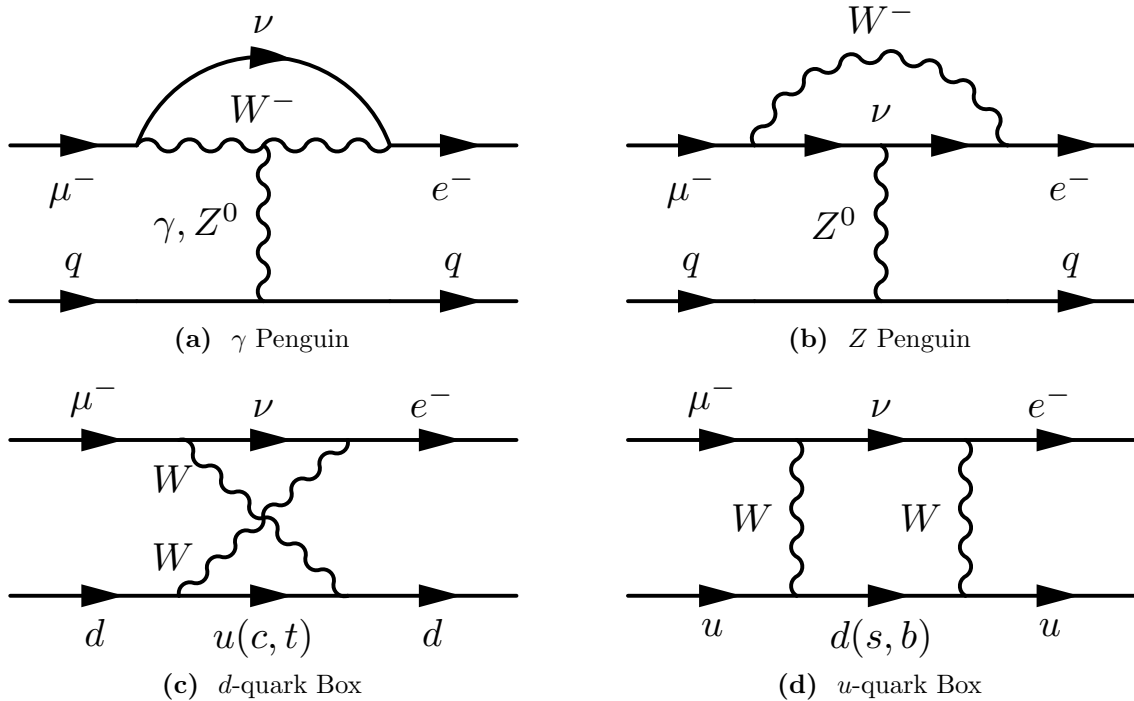


Figure 1.4.: Feynman diagram for the neutrinoless muon decay in the presence of an atomic nucleus – μ - e conversion – caused by neutrino oscillations. Compared to $\mu^\pm \rightarrow e^\pm \gamma$ there are now four possible diagrams, so that the rate depends on the nucleus and picks up interference terms.

1.3. In Search of Charged Lepton Flavour Violation (CLFV)

1.3.1. Motivations and Status

Searches for Lepton Flavour Violation (LFV) go back right to the discovery of the muon, but that is not to say that they ended there. Over the past eighty years or so, experiments have continued to push the limits on such processes down through around 13 orders of magnitude. As accelerator technology improved, rather than rely on cosmic sources, intense beams of muons can now be made and tau leptons generated at the large colliders. Table ?? shows the current limits on a (non-exhaustive) list of the possible CLFV observables.

Of the searches involving muon decays the three most searched for modes have been $\mu^\pm \rightarrow e^\pm \gamma$ ('mu to e gamma'), $\mu^- N \rightarrow e^- N$ (' μ - e conversion'), and $\mu^\pm \rightarrow e^+ e^- e^\pm$ ('mu three e'). From an experimental perspective these modes are attractive since the Lepton

Flavour Conserving-counterparts all have neutrinos in the final state, and since these neutrinos are massless they typically carry away around half the available energy. By removing the neutrinos from the final state, then, a clear separation between the signal and the Standard Model version appears. It is in these modes that the experimental limits have seen the greatest improvement with time, as shown in Fig. ??.

The [SM](#) nowadays faces many other difficulties beyond neutrino masses such as dark matter and energy, the stability of the vacuum, and the unification of gravity, the electroweak force, and [QCD](#). A vast number of extensions to the [SM](#) try to address these issues. The assumption that New Physics introduces no additional flavour changing is often referred to as Minimal Flavour Violation, and used to reduce the number of parameters contained in Beyond the Standard Model ([BSM](#)) theories, but just how valid is such an assumption? As an accidental symmetry in the [SM](#), whether or not these extensions produce [CLFV](#) is very difficult to constrain by some theoretical reasoning, and must instead be directly measured.

Beyond directly producing [CLFV](#), trying to answer the many questions raised by the small, non-zero neutrino masses is helped by searches for [CLFV](#). In many of the proposed models, such as in type-I and type-II see-saw mechanisms [CLFV](#) rates are significantly enhanced [43]. If heavy neutrinos exist they can remove both the GIM suppression and the mass imbalance that cause the rates from the [SM](#) with neutrino oscillation to be so small.

Lastly, there are a number of recent anomalies, in particular with muon measurements, that hint at [CLFV](#). The experimentally measured value of $g - 2$ of the muon has disagreed with the theoretical prediction by around 3σ for the one and a half decades, even widening as the theoretical prediction has been improved [27, 29]. At the same time, measurements of the proton radius using the hyperfine structure of muonic hydrogen has shown a 7σ discrepancy [16] with other methods. Both of these could be explained by interactions of the muon with some new physics, typically a new vector Boson [61, 69], and can be invoked to directly produce CLFV [57].

In addition, a number of collider-based measurements have turned up anomalies. The LHCb experiment, studying the branching fraction ratio, R_K , of $B^+ \rightarrow K^+ l^+ l^-$ with $l = \mu, e$, have found a deviation of about 2.6σ favouring the di-electron decay [8]. At the same time, the ratio for the decay $B^0 \rightarrow D^{*+} l^- \bar{\nu}$ where $l = \mu, \tau$, $R(D^*)$, has been found to disagree with the SM, at each of the LHCb [9], Belle [10] and Babar [68] experiments, with a combined discrepancy of around 3.9σ [67]. At CMS an excess in $h \rightarrow \tau\mu$ decays

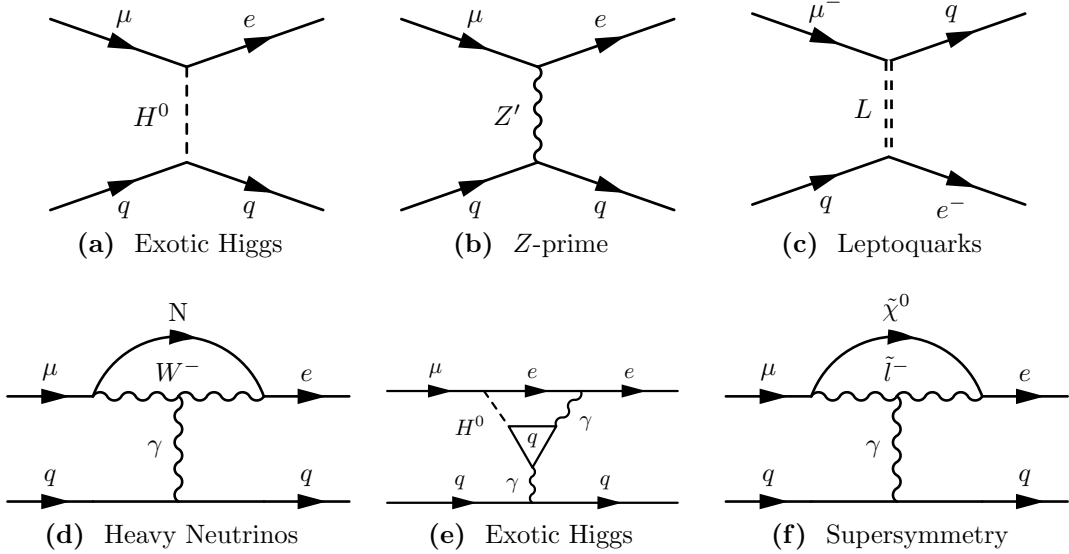


Figure 1.5.: Feynman diagrams that produce μ - e conversion through New Physics models. The upper three diagrams ((a) to (c)) all connect to the nucleus via some massive exchange particle, whereas the lower three diagrams ((d) to (f)) all connect via an exchanged photon. In addition to interactions with the quarks, since μ - e conversion interacts with the whole nucleus, there are also models where the interaction involves external gluon lines.

during Run-1 of the LHC [62] was observed with a significance of 2.4σ , although analysis of Run-II has not seen this [34]. Although many of these discrepancies directly only require lepton non-universality, this can be shown to imply CLFV in many cases [53].

Lastly, for cosmological purposes CLFV can play an important role in the Baryon Asymmetry of the Universe that we observe. Many models generate this asymmetry in the early universe via leptonic CP-violation. However, it has been shown that if CLFV processes occur at the present limits, the Baryon Asymmetry generated by these means can be washed out [42].

1.3.2. Muon CLFV Channels

Fig. 1.5 shows a variety of Feynman diagrams for μ - e conversion involving new particles and couplings predicted by many BSM theories. The large variety of models to which μ - e conversion would be sensitive makes this a particularly attractive search channel for New Physics [14].

It can also be seen how complementary the different muon CLFV channels will be. In the case of leptoquarks for example, shown in Fig. 1.5c, clearly one would expect at some level μ - e conversion to take place, but to generate a signal in a $\mu^\pm \rightarrow e^+e^-e^\pm$ experiment would be harder. Similarly, the relative sensitivities between $\mu^+ \rightarrow e^+\gamma$ searches and μ - e conversion searches can be used to pin down what the New Physics is in the case of a positive observation, or heavily constrain multiple different models in the case of a null measurement. This is apparent from the fact that New Physics can be classed as photonic (such as the lower three diagrams in Fig. 1.5) or like a four-Fermi contact interaction (as in the upper three diagrams in Fig. 1.5). The new physics which kicks in at some new mass scale is integrated away to leave an effective, low-energy field theory.

By constructing a toy Lagrangian consisting of two new interaction terms, one being photonic and the other a contact term, it is possible to study the relative sensitivities of μ - e conversion and μ^-e^- gamma searches. The interaction terms in such a Lagrangian would look like:

$$L = \frac{1}{\kappa + 1} \frac{m_\mu}{\Lambda^2} (\bar{\mu}_R \sigma^{\mu\nu} e_L F_{\mu\nu}) + \frac{\kappa}{\kappa + 1} \frac{1}{\Lambda^2} (\bar{\mu}_L \gamma^\mu e_L) (\bar{q}_L \gamma_\mu q_L) \quad (1.2)$$

where κ is a dimensionless parameter that determines to what degree the new physics appears photonic ($\kappa \rightarrow 0$) or four-Fermi-like ($\kappa \rightarrow \infty$).

If the underlying new physics is photonic in nature, then one can expect a direct search for μ^-e^- gamma to be more sensitive: coupling the photon to the nucleus of an atom will pick up an extra factor of α , bringing the rate down by about two orders of magnitude. On the other hand, if the new physics favours interacting directly with the nucleus, as a four-Fermi contact term, then μ - e conversion would be more sensitive. In this case, producing an out-going photon would still be possible, but would require the quark lines to reconnect, suppressing this by a factor α and various loop factors. All of this is pulled together in Fig. 1.6, where the relative sensitivities of the most recent $\mu^+ \rightarrow e^+\gamma$ search and several μ - e conversion experiments is shown. From this it can also be seen that the sorts of mass scales that can be probed are several orders of magnitude greater than can be reached in direct searches, such as at the LHC or B-factories.

Experiments that search for CLFV with intense muon beams, therefore, make for highly sensitive tests of New Physics, which together can push the answers to some of the fundamental challenges facing the Standard Model of particle physics. Although there are models for which μ - e conversion has the most sensitivity, others favour $\mu^+ \rightarrow e^+\gamma$

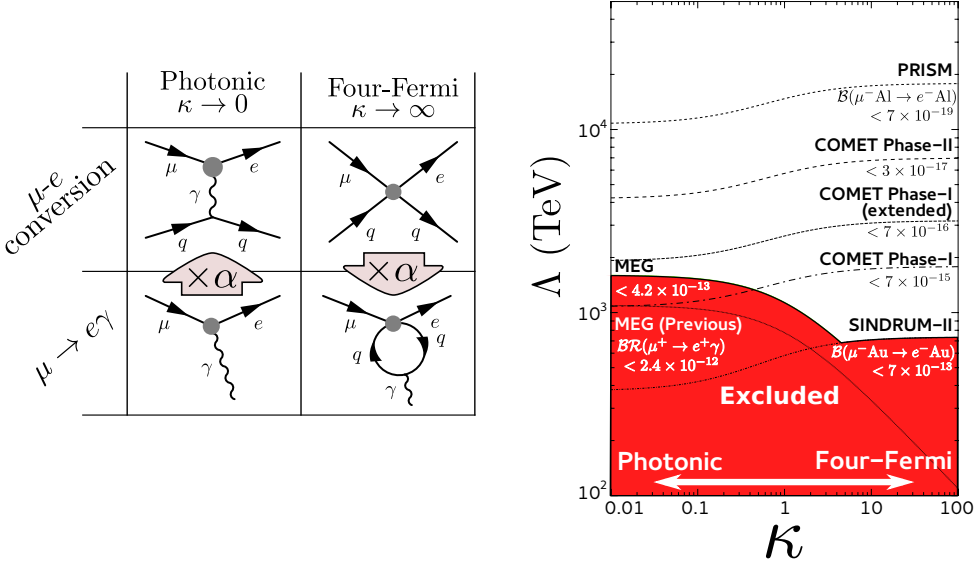


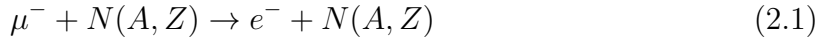
Figure 1.6.: Searches for μ - e conversion and $\mu^+ \rightarrow e^+\gamma$ have relative sensitivities that depend on the underlying physics, making the two channels highly complementary. As shown on the left, New Physics can produce a signal in both channels, but one channel or the other can be comparatively suppressed due to the need to include extra vertices and loops. The plot on the right is adapted from [36], based on [41], and shows the relative sensitivity for the toy lagrangian of equation (1.2) as a function of κ , how non-photonic the New Physics is, and Λ , the mass scale assuming coupling strengths of unity.

searches, but μ - e conversion maintains high sensitivity in nearly all generic extensions to the Standard Model.

Chapter 2.

Muon-to-Electron Conversion and the Muonic Atom

Muon-to-electron conversion is the spontaneous decay of a muon to an electron within the Coulomb potential of an atomic nucleus and without the emission of neutrinos. It proceeds according to the formula:



In general, the nucleus involved can be excited under μ - e conversion, although all experimental searches to date have required that the nucleus be left unchanged. This constraint has two effects: firstly, coherent terms in the μ - e conversion cross section dominate, since the interaction will largely take place with the whole nucleus. Being coherent, the rate of μ - e conversion will, in general, grow more quickly as a function of the atomic mass or number (though exactly which of these determines the rate is itself model dependent). Secondly, the constraint of an unchanged nucleus means that all the free energy of the initial muon has to go into the kinetic energy of the electron and the recoil of the nucleus. Since the initial system is at rest, and as a two body decay, the energy of the outgoing electron is fixed:

$$E_e = M_\mu - E_{\mu, \text{binding}} - E_{\text{recoil}} \quad (2.2)$$

where $M_\mu = 105.66 \text{ MeV}/c^2$ is the muon mass, $E_{\mu, \text{binding}}$ the binding energy of the muon in the ground state of the muonic atom, and E_{recoil} is the kinetic energy of the recoiling nucleus. In the aluminium target used for COMET (see section 3.2.3) the electron energy

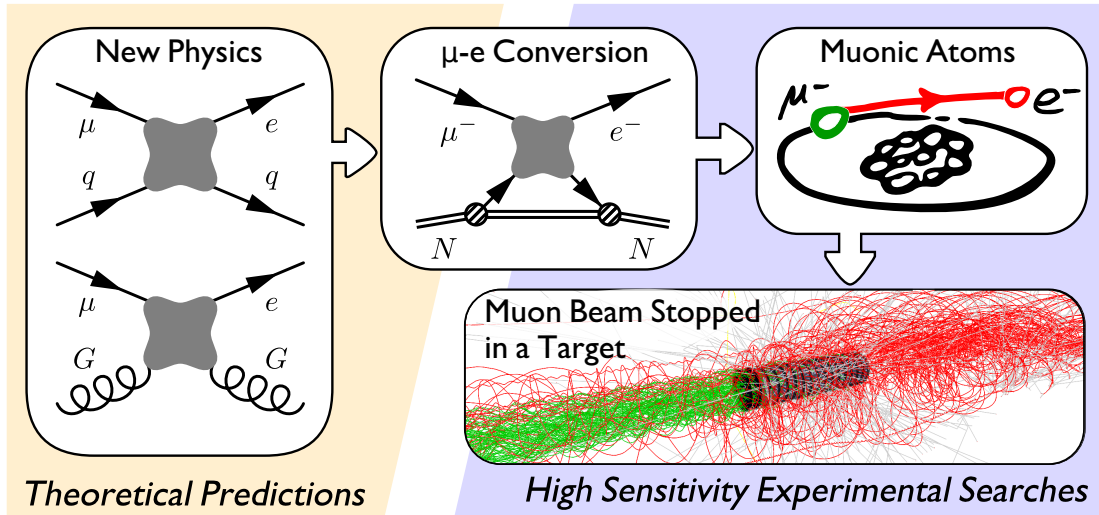


Figure 2.1.: A New Model introducing CLFV generates μ - e conversion when connected to a nucleus. Observing this requires many muonic atoms be formed and so μ - e conversion experiments progress by stopping an intense muon beam in a target and looking for electrons leaving with a specific energy.

is $E_e = 104.97$ MeV. The simplicity and model independence of the signal – a single, monoenergetic electron – makes the process experimentally very attractive.

The various scales involved in a search for μ - e conversion are illustrated in Fig. 2.1. To observe μ - e conversion, a muonic atomic is formed with the muon in the ground state. An interaction between the muon and the nucleus causes Lepton Flavour Violation and producing an electron. In order to form the muonic atoms, a beam of negative muons is brought to stop in a target and the resulting electrons, if μ - e conversion takes place, then detected.

When muons in the beam enter the target they will initially lose energy predominantly through ionisation. Once they reach energies of around a few keV they become atomically bound to the Coulomb potential of the nucleus. From here, on the order of 100 fs, these muons will undergo Auger and radiative transitions to the ground state. The X-rays emitted during this electromagnetic cascade have well defined energies and intensities and can therefore be detected as a means to evaluate the number of muons stopped in the target. Fig. 2.2 shows the most intense transition peak, $2p - 1s$ in the X-ray spectrum for muonic aluminium, and the muonic magnesium lines that occur with similar energies.

From the ground state there are two processes that can occur to the bound muon in the SM: decay in orbit (DIO) and nuclear capture. DIO is the normal decay of a muon with neutrino emission, although the spectrum of the emitted electron is modified

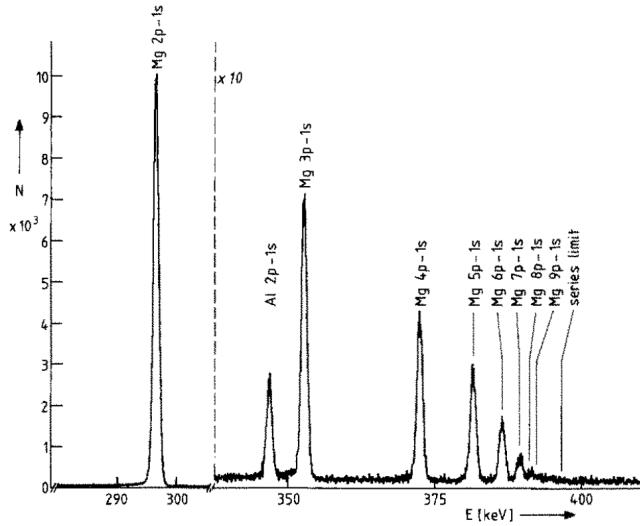


Figure 2.2.: The most intense line of the muonic atom atomic cascade, the $2p - 1s$ transition, surrounded by the peaks of the muonic-magnesium Lyman series. Reproduced from [55].

compared to the free muon decay due to the presence of the nucleus. Nuclear capture of the muon occurs when the muon is absorbed into the nucleus decreasing the atomic number by a single unit, in analogue to nuclear electron capture or inverse beta decay. A single muon-neutrino is emitted as well as various possible gamma-rays and hadrons, since the daughter nucleus is often unstable.

Both of these are important in μ - e conversion searches, since they impose various experimental constraints. Furthermore, these two processes determine the lifetime of the bound muon, which is not the same as the free muon. In the case of decay, being bound to the nucleus reduces the available energy, therefore reducing the available phase-space for the resultant electron and neutrinos. In addition, a time-dilation effect occurs since the bound muon is never truly at rest. As a result, the partial lifetime of muon decay increases in the bound muon system compared to the free muon, and this increase grows with the atomic number as the muon binds more tightly to the nucleus. However, whilst the rate of decay decreases with atomic number the rate of muon capture increases. This occurs, firstly, because there are more protons against which to capture and, secondly, because the overlap between the muon wavefunction and the nucleus increases. For atomic numbers larger than $Z = 30$ this effect begins to saturate since the muon wavefunction becomes contained almost completely within the nucleus. Whilst for light elements, up to around $Z = 12$, the decay process is more frequent, for the rest of the periodic table the capture process dominates. For an aluminium target, the two processes are comparitively

similar, with branching ratios of 61 and 39% for capture and decay respectively, giving the muon a lifetime of 864 ns¹ [70].

Since the muon is 200 times heavier than the electron, the muon wavefunction feels the effect of the nucleus a lot more, creating some theoretical uncertainty on the initial muon wavefunction. Rather than the full branching ratio, typically μ - e conversion experiments discuss the conversion rate, which is given by:

$$\mathcal{C.R.} = \frac{\Gamma(\mu\text{-}e \text{ conversion})}{\Gamma(\text{nuclear capture})} \quad (2.3)$$

which reduces the theoretical uncertainty introduced from the initial wavefunction.

Based on this, one defines the Single-Event Sensitivity (SES) to be:

$$\text{S.E.S}(\mu^- N \rightarrow e^- N) = \frac{1}{N_\mu \mathcal{B}_{\text{capture}} A_{\mu \rightarrow e}} \quad (2.4)$$

where N_μ is the number of muons stopped, $\mathcal{B}_{\text{capture}}$ is the branching ratio for muon nuclear capture, and $A_{\mu \rightarrow e}$ is the total acceptance of electrons coming from μ - e conversion.

2.1. Muon Decay in Orbit

In free muon decay the maximum energy for the outgoing electron occurs when the neutrinos recoil back-to-back with the electron. In this configuration, exactly half the energy released in the decay is available to the electron, so that the maximum energy of an electron coming from the decay of a free and stationary muon is: $\max(E_e^{\text{free}}) = m_\mu/2 = 52.5 \text{ MeV}$.

The end-point configuration is altered significantly once the muon becomes bound to the nucleus of an atom. Once bound, the neutrinos can be arranged back-to-back with one another, and thus carry away a negligible amount of energy. Four-momentum can still be conserved however, since the nucleus of the atom recoils against the electron. Given the enormous mass of any nucleus compared to the electron, conservation of momentum is possible for small kinetic energies of the nucleus and thus the maximum electron energy is hugely increased compared to the free decay. In fact, in the limit where the neutrinos carry away no energy, the kinematic configuration of this decay becomes

¹ This is very important to the COMET experiment and so we revisit this aspect in the next chapter.

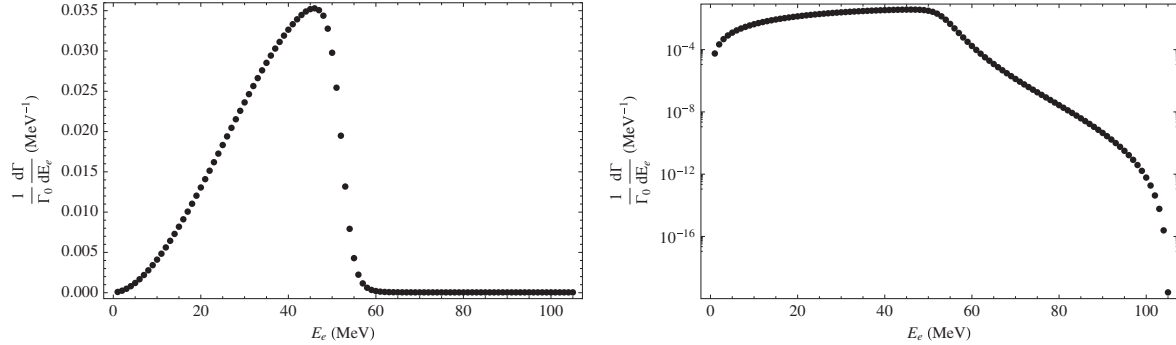


Figure 2.3.: The spectrum of electrons produced by muon decay-in-orbit, according to Czarnecki et al. [38]. The two plots show the same data, but left is on a linear-linear scale whilst the right plot is on a log-lin scale which shows clearly the high-energy tail reaching up to the μ - e conversion signal energy of 104.97 MeV.

identical to that of μ - e conversion, but for the mass of the neutrinos², and accordingly: $\max(E_e^{\text{DIO}}) \simeq E_e^{\text{conversion}}$.

The spectrum of electrons from DIO in aluminium is shown in Fig. 2.3. It can be seen how the peak electron energy is close to the free muon decay end-point, and in reality about 99% of DIO electrons will be emitted below 58 MeV. Whilst the end-point for the spectrum is indeed around 104.97 MeV, it is clear how suppressed this part of the spectrum is – some twenty orders of magnitude less likely than at the peak energy. Achieving the end-point energy requires radiative connections between the nucleus and either the incoming muon, intermediate W -boson, or the outgoing electron; the low value of the neutrino momenta brings about a helicity suppression; and the specific energies of all particles implies a small phase-space volume for the decay products.

Given the enormous suppression at the end-point, μ - e conversion searches historically described themselves as ‘background free’. However, at the projected sensitivities of modern experiments, the DIO rate close to the end-point of the spectrum is now at an appreciable level. Indeed, the next generation of searches (and COMET Phase-I in particular) will be the first to measure the DIO spectrum above 90 MeV, itself an important cross-check for the theoretical prediction of muon DIO³.

² It would be interesting whether precise observations at the DIO end-point would be sensitive to the absolute neutrino masses of the muon and electron neutrinos, $\langle M_{\nu_e} \rangle + \langle M_{\nu_\mu} \rangle$. The current limits of less than 1 eV mean a direct measurement of the end-point is not realistic, but if the shape of the spectrum contained information then this might be exploitable. Certainly, massive sterile neutrinos could be searched for as a kink or shoulder at the DIO end-point with sensitivity to masses down to a few MeV.

³In addition to neutrino mass and sterile neutrino searches, the precision measurement of the end-point of the DIO spectrum feels like it should be extremely interesting for theoretical physicists given its

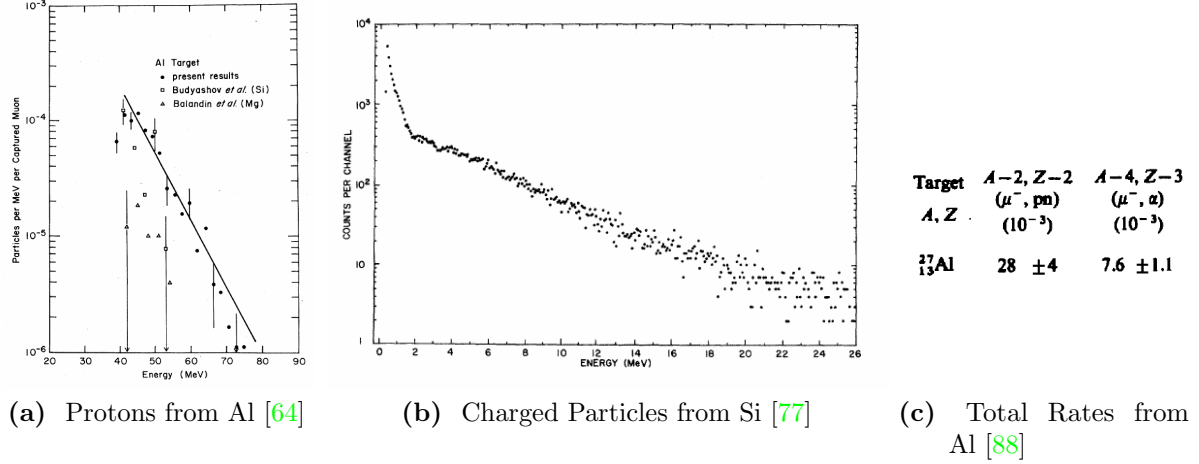


Figure 2.4.: Selected experimental measurements of charged particle emission following muon capture, from the late 1960s to 1970s.

2.2. Muon Nuclear Capture

The nuclear capture of negative muons is governed by the equation:

$$\mu^- + N(A, Z) \rightarrow \nu_\mu + N'(A, Z - 1) \quad (2.5)$$

and as an incoherent process, one would expect direct capture of the muon against a proton to result in a prompt neutron being produced. However, prompt protons can also be produced if the capture takes place between a nucleon cluster and the muon. The typical nuclear excitation from such a process is around 50 MeV, with the remainder of the total incoming energy lost to the outgoing neutrino and nuclear recoil. Even if prompt neutrons and protons are produced, the remnant nucleus is often left in an excited, unstable state, such that during de-excitation other particles can also be emitted. These include gamma-rays, deuterons, triton and alpha particles as well as additional neutrons and protons.

From the perspective of a sensitive μ - e conversion experiment, the emission products following nuclear capture can be dangerous since, in the case of charged particles, they can

connection to things like muon g-2 and the Lamb-shift of muonic hydrogen. The end-point calculation requires radiative corrections, which would likely be sensitive to vacuum corrections in a similar way to these other measurements. If, at COMET Phase-I, we observe any deviation in this region, even if it does not look like μ - e conversion, I would be very excited of the additional evidence this might imply for lepton non-universality. In contrast, if we observe no deviation, might this be translated into limits on New Physics models that explain the other anomalies?

swamp the detector if left unchecked. Similarly, neutrons and gamma rays produced by nuclear capture can damage electronics systems if left unchecked. As such it is important to understand the rates at which these particles are emitted following nuclear capture of the muon.

However, due to the nuclear environment theoretical predictions of the rates and energy distributions of capture products are extremely complex, and experimental measurements are necessary. Unfortunately, in the case of aluminium — the target choice for COMET— the existing experimental data is not extensive. Fig. 2.4 shows a summary of the available literature, where one can see how incomplete the current available data is. Accordingly, it has been necessary to measure this directly.

The AlCap experiment [13] is a joint effort between COMET and Mu2e tasked with measuring the rate and spectra of particles emitted following muon capture in aluminium. Three runs have been held at The Paul Scherrer Institute ([PSI](#)) from 2013 to 2015, and data analysis is on-going, although preliminary neutron and proton spectra and rates have been achieved. The measured proton rate is low enough that COMET does not expect to have to take any precautionary measures to reduce it further. For more information on AlCap, see appendix D and the PhD thesis by Nam Tran [84].

2.3. SINDRUM-II: Present Limits

The current limit on μ - e conversion was set by the SINDRUM-II experiment in 2006 to be $\mathcal{C.R} < 7 \times 10^{-13}$ at 90% confidence level. The experiment, shown in Fig. 2.5, used a gold target sitting in the centre of a cylindrical detector. Both sat coaxially with a solenoidal field allowing for momentum measurements by reconstructing the helical trajectories of the detected electrons.

The dominant backgrounds at SINDRUM-II were cosmic events and pions in the beam. The observed energy distribution (from the main event category) is shown to the right of Fig. 2.5. The single Class 1 event that was observed above the expected μ - e conversion energy in gold was attributed to a pion in the beam.

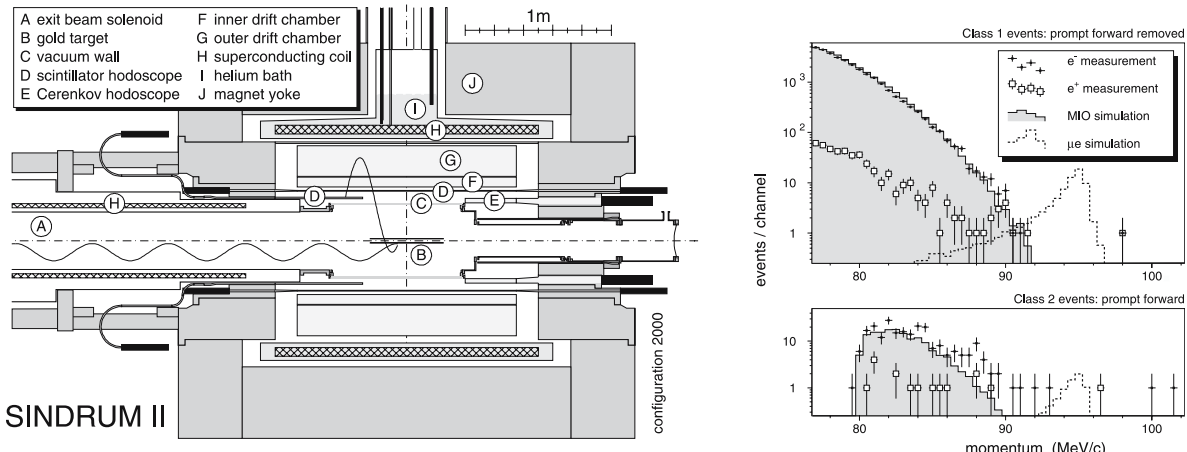


Figure 2.5.: The SINDRUM-II experiment, which holds the current limit on $\mu\text{-}e$ conversion. Left: the detector and target, with the muon beam produced from decay of a pion beam created by protons striking a target. Right: the observed electron and positron energies and expected background and signal spectra. Reproduced from [25].

Chapter 3.

The COMET Experiment

The COMET experiment will search for COherent Muon to Electron Transitions with a single-event-sensitivity of around 3×10^{-17} . This amounts to an improvement of four orders of magnitude compared to the current limit by SINDRUM-II [25], which requires some significant changes to the way the experiment operates compared to its predecessor.

Reaching such a sensitivity requires that COMET stops many muons in aluminium, maintaining a high signal acceptance, whilst suppressing potential background sources to well below a single event during the lifetime of the experiment. This tension between simultaneously high signal sensitivity and background suppression can be translated into the more specific requirements of:

- a very high intensity muon beam,
- a low energy muon beam,
- a thin stopping target and low material budget detector,
- the use of timing information of signal process with respect to backgrounds.

The design of COMET realises these goals by using several novel experimental techniques, and as such it has been decided to operate in two stages, Phase-I and Phase-II. Phase-I aims both to help understand these techniques, the muon beam, and key backgrounds rates, as well as making an intermediate measurement of μ - e conversion at a sensitivity of 3×10^{-15} —two orders of magnitude better than the SINDRUM-II experiment. Phase-II will follow and should achieve the final objective of 3×10^{-17} .

Type	Background	Number of events during run	
		Phase-I [80]	Phase-II [35]
Intrinsic	Muon Decay-in-Orbit	0.01	0.15
	Radiative Muon Capture	0.0019	< 0.001
	μ^- Capture w/ n Emission	< 0.001	< 0.001
	μ^- Capture w/ Charged Part. Emission	< 0.001	< 0.001
Prompt	Radiative Pion Capture	0.00028	0.05
	Beam Electrons		< 0.1*
	Muon Decay in Flight	≤ 0.0038	< 0.0002
	Pion Decay in Flight		< 0.0001
	Neutron Induced	$\sim 10^{-9}$	0.024
Delayed	Delayed Radiative Pion Capture	~ 0	0.002
	Anti-proton Induced	0.0012	0.007
	Other delayed B.G.	~ 0	—
Cosmic	Cosmic Ray Muons	≤ 0.01	0.002
	Electrons from Cosmic Ray Muons		0.002
Total background		< 0.032	< 0.34
Signal (Assuming $B = 1 \times 10^{-16}$)		0.31	3.8

Table 3.1.: Backgrounds for COMET Phase-I [80] and Phase-II [35]. Prompt backgrounds arise by protons that occur in between bunches and are therefore suppressed by the extinction factor. For Phase-I, the recently measured value of 10^{-12} was used for the extinction factor, but for Phase-II the older expectation of 10^{-9} was used. If this is not taken into account, the Phase-I estimates suggest a greater background to signal sensitivity than for Phase-II. *) Result was statistically limited.

3.1. Overview of Signal and Backgrounds

The Single-Event Sensitivity (SES), defined in the previous chapter, is a statement purely of signal efficiency and does not account for background rates. It is clear, however, that for any observation to be confidently labelled as signal or, in the event of a null-observation, in order to set the tightest possible confidence limit, the background rate must be kept comparably low. In order to understand the design of the COMET experiment, a simple appreciation of the key backgrounds is therefore necessary.

Table 3.1 summarizes the results of previous studies for background rates at Phase-I and Phase-II. There are four groups of background source: intrinsic, prompt, delayed and cosmic sources.

Intrinsic processes are those that arise from muons stopping in the target and will always be present regardless of the muon beam properties. Of these, the dominant background is muon decay in orbit (DIO), which was described in the previous chapter. In addition, radiative nuclear capture of a muon is kinematically capable of producing 101.85 MeV photons, which can produce backgrounds if the photon is converted to a high-energy electron and then mis-reconstructed to have additional energy.

Delayed and prompt processes come from impurities in the muon beam, be they pions, antiprotons, or high energy muons and electrons. The key distinction between these two is the timing at which the background is detected with respect to the arrival of the proton beam. For example, pions that reach the stopping target region are dangerous since they can produce high energy gamma rays which can pair produce to create 105 MeV electrons. Since pion capture against a nucleus is extremely fast, the timing of pion-induced backgrounds is determined solely by the arrival time of pions into the target region. In order to reach this region without decaying, the pions must be relatively high momentum of about 60 MeV/c or greater.

As a result, backgrounds from pion capture are typically expected close to the arrival of protons at the production target. Prompt processes such as this are suppressed by using a pulsed proton beam (discussed in more depth later) and ensuring very few protons in between pulses. Other beam related issues include the decay of muons and pions to electrons. An electron of 100 MeV/c can be produced by muons or pions with greater than 70 or 50 MeV/c respectively, and so the flux of higher energy particles in the beam must also be removed.

Delayed processes are those where the timing of the proton beam cannot be used to improve suppression since the characteristic time between detection of the background and a proton on target for these processes is large compared to the beam pulsing. Possible sources of this delay include the mirroring of particles by the magnetic field, or by some heavy particle from the production target producing pions and high-energy electrons. At a given momentum, antiprotons travel considerably more slowly than muons or pions given their considerably larger mass, washing out any timing information from their production.

Finally cosmic backgrounds arise from high energy muons that pass through the building and enter the detector or beamline. Events where a muon decays to an electron which is then detected as 105 MeV are counted as backgrounds. In particular, muons that produce high energy electrons close to the target are dangerous since cuts on the reconstructed direction and position will be less effective.

All these processes will be discussed and evaluated in more depth in the section on background estimates.

3.2. General Experimental Techniques

Suppressing background rates while maintaining a high signal efficiency leads to several novel techniques being used in the COMET experimental set-up.

3.2.1. Proton Beam Energy and Production Target

The muon beam used in COMET is produced from the decay of a secondary pion beam created by protons striking a target. If maximising the muon intensity were the only concern, then both the proton beam power and atomic mass of the target material would similarly be maximised since the pion production cross section grows with these two parameters. However, the need to suppress background rates and maintain the mechanical and operational stability of the target constrains both of these parameters.

In particular, protons striking an individual, stationary (and, in theory, unbound) nucleon with more than about 6 GeV have sufficient energy to produce antiprotons which travel relatively slowly (see 3.2.3) and can produce backgrounds. Since the antiproton yield grows very quickly above this threshold, it has been chosen to use protons with 8 GeV kinetic energy.

As well as the beam energy, the intensity is ideally maximised to increase the number of protons on target per second. For Phase-II running, the main ring will operate at $7 \mu\text{A}$ so that a beam power of 56 kW is achieved. Phase-I on the other hand will use a lower beam intensity of $0.4 \mu\text{A}$ or 3.2 kW.

Whilst a heavy metal target is preferable since it increases the number of nucleons that interact with the proton beam and therefore the pion yield, the target must maintain its mechanical strength. This requires the selection of a high melting point material and

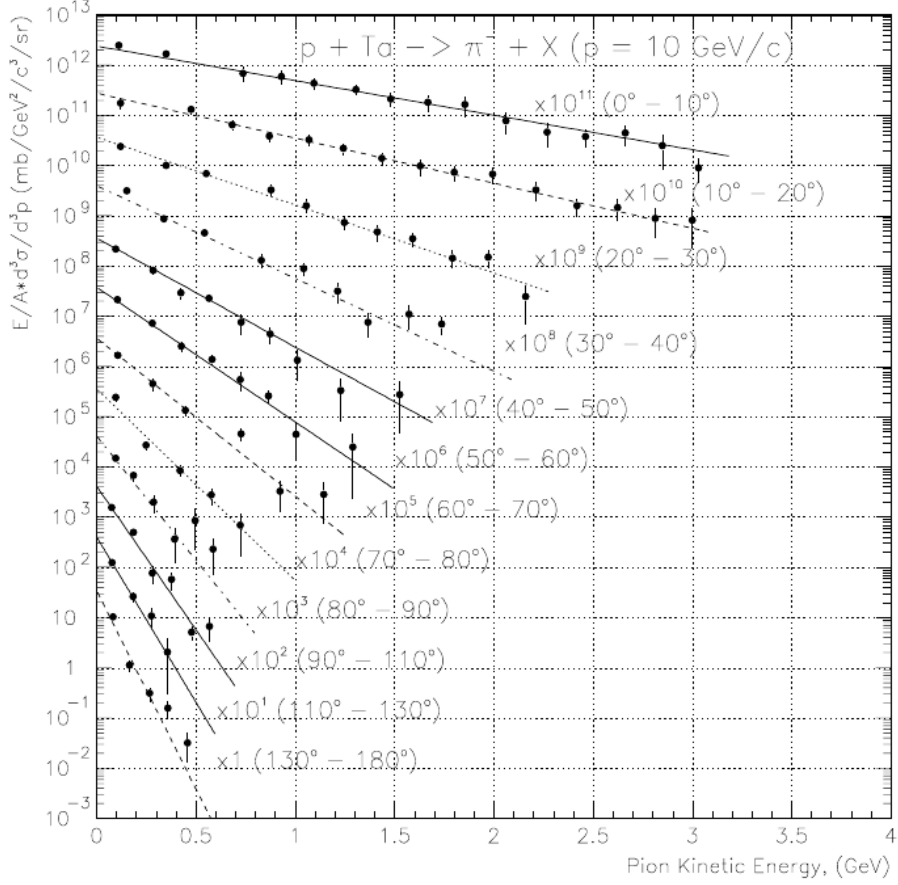


Figure 3.1.: Double differential cross section of pion production on a tantalum target from protons with 10 GeV kinetic energy (reproduced from Meco note 23 [45] which itself used [19]). It is clear that the high-energy component of the spectrum is suppressed as you move to higher production angles which is important for reducing background rates.

possibly the use of active cooling. To simplify the situation in Phase-I, a graphite target will be used which can be passively cooled by thermal radiation. In Phase-II however, tungsten has been selected due to its high melting-point of 3422 C, although water cooling will also likely be employed.

Finally, only those pions and muons emitted in the backwards direction with respect to the proton beam are captured and transported to the muon beamline. This is a strong way to reduce the high-energy components of the muon and pion distributions since the yields for low momentum pions in the forward and backwards directions are similar, whilst the high energy tail is greatly suppressed in the backwards direction. At this time however, there is a dearth of experimental measurements for pion production in the backwards direction with 8 GeV protons on a graphite or tungsten target. Fig. 3.1

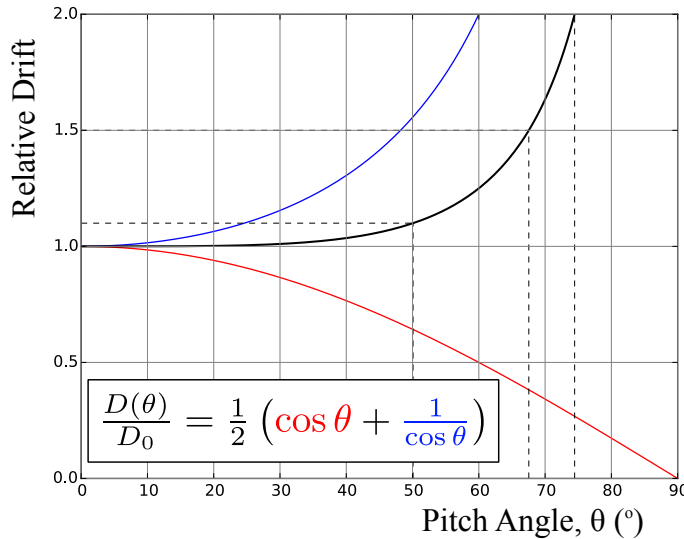


Figure 3.2.: Angular dependence of the magnitude of vertical drift in a bent solenoid field. The total variation (black) remains below 10% for pitch angles below 50° .

shows a measurement of the cross section for pion production with 10 GeV protons on tantalum (which is adjacent to tungsten on the periodic table).

3.2.2. Particle Transport through Bent Solenoids

Both Phase-I and II make use of bent solenoids to help select particles of a particular momentum. In bent solenoids, a transverse dispersion occurs that is proportional to the momentum and charge of the particle passing through it.

Charged particles moving through a straight solenoid follow a helical trajectory, orbiting a point that moves parallel to the solenoidal axis with constant velocity fixed by the longitudinal momentum of the particle. The frequency that the particle rotates about this point (the cyclotron frequency or frequency of gyration) is determined by the transverse momentum.

By comparison, if a charged particle moves through a solenoid channel that has been bent, the particle can still be considered to orbit a point, only now the motion of that point can be shown to drift vertically, out of the plane of bending. This drift arises from the gradient introduced to the field by bending the solenoid but also from the non-rectilinear coordinate system of the field lines. The total drift, D , of a particle with mass and charge m and q respectively through a solenoid bent with a fixed radius of

curvature, R , is given by:

$$D = \frac{1}{qB} \left(\frac{s}{R} \right) \frac{p_L^2 + 0.5p_T^2}{p_L} \quad (3.1)$$

$$= \frac{1}{qB} \left(\frac{s}{R} \right) \frac{p}{2} \left(\cos \theta + \frac{1}{\cos \theta} \right) \quad (3.2)$$

where B is the magnetic field strength¹, s is the distance travelled through the solenoid, p the momentum of the particle, with longitudinal and transverse components with respect to the solenoid axis, p_L and p_T respectively (see appendix A for a full derivation of these equations). The pitch angle, θ , is a property of the helical trajectory taken by the particle and defined as:

$$\theta = \tan^{-1} \left(\frac{p_T}{p_L} \right) \quad (3.3)$$

The angular dependence of equation (3.2) is shown in Fig. 3.2 where it can be seen that for angles below 50 degrees the variation in the drift is less than 10%, such that the drift is determined almost completely by the momentum of particles up to these angles.

Bent solenoids are used in COMET to disperse high-energy muons and pions in the muon beam for both Phase-I and II, and as a spectrometer system for electrons coming from the stopping target in Phase-II, which will both be described in more detail below.

Since the drift is proportional to the momentum of the particle, those with zero momentum would remain on axis, whilst higher momentum particles, including those of interest (105 MeV electrons in the Phase-II electron spectrometer and around 40 MeV/c muons in the muon beam line), drift to the sides. However, an additional vertical component is introduced to the magnetic field. If the solenoid were straight the axis of a particle's helical trajectory would follow the field line. A vertical component would therefore cause the trajectories to move upwards with the field line itself, irrespective of the particle's momentum. The same result is true in a bent solenoid and since the drift this introduces is not proportional to momentum a vertical component can be used to select the momentum of particles which remain on axis.

Two techniques have been considered to introduce this vertical component: tilting the solenoid coils themselves, or adding additional dipole coils around the solenoids. COMET has opted to pursue the latter, using a special, proprietary winding technique

¹Strictly speaking, B is the field strength along the path of the centre of gyration, which is constant for a fixed transverse distance from the focus of the bent solenoid.

developed by Toshiba to introduce a vertical component by placing additional conductor around the other solenoid coils. Since the current through these dipole coils can be altered separately to the solenoid coils, this approach has the advantage that the two components can be tuned against the other so that the optimal dipole field can be found whilst running or the on-axis momentum and charge shifted to study backgrounds or other physics searches. Additional collimator material can also be introduced to remove particles with undesirable momentum.

3.2.3. Stopping Target Material and Beam Pulsing

The combination of using backwards going pions and the long, bent-solenoid transport channel is already effective at removing potential background issues. In addition to these however, there is one further method which helps both to reduce beam-related backgrounds and improve the detector occupancy and reconstruction requirements: the use of a pulsed proton beam with a relatively light stopping target.

Since the signal process is coherent, its cross section grows roughly as the square of the number of nucleons (or protons, depending on the model)² until the muon is contained almost completely within the nucleus at which point the rate levels off. It is therefore desirable to use a high-Z target in order to increase the probability of conversion and indeed SINDRUM-II used both lead and gold targets, with its most stringent limit set on gold target [25].

However, as the nucleus gets larger, the lifetime of the muonic atom falls steeply due to the increase in the nuclear capture rate. This is illustrated in Fig. 3.3 where it can be seen that for elements heavier than iron ($Z > 26$) the muon lifetime is less than 200 ns. The COMET production target and beamline produces a beam flash that lasts for about 200 ns after the arrival of a proton. This means that for targets heavier than iron timing information can not be used to distinguish particles coming from the beam from those of muons stopped in the target.

Whilst these are the two dominant factors in deciding the target material, other factors like the mechanical stability, cost, isotopic purity and the stability of the daughter nuclei following muon capture on the target must also be considered. Accordingly, titanium and aluminium are considered the two most viable target materials. Titanium, in which the

²Although this growth is offset by the normalisation to the capture rate which is typically treated as incoherent so that it grows linearly with the number of nucleons. The overall conversion rate itself is roughly proportional to the atomic number for lighter elements.

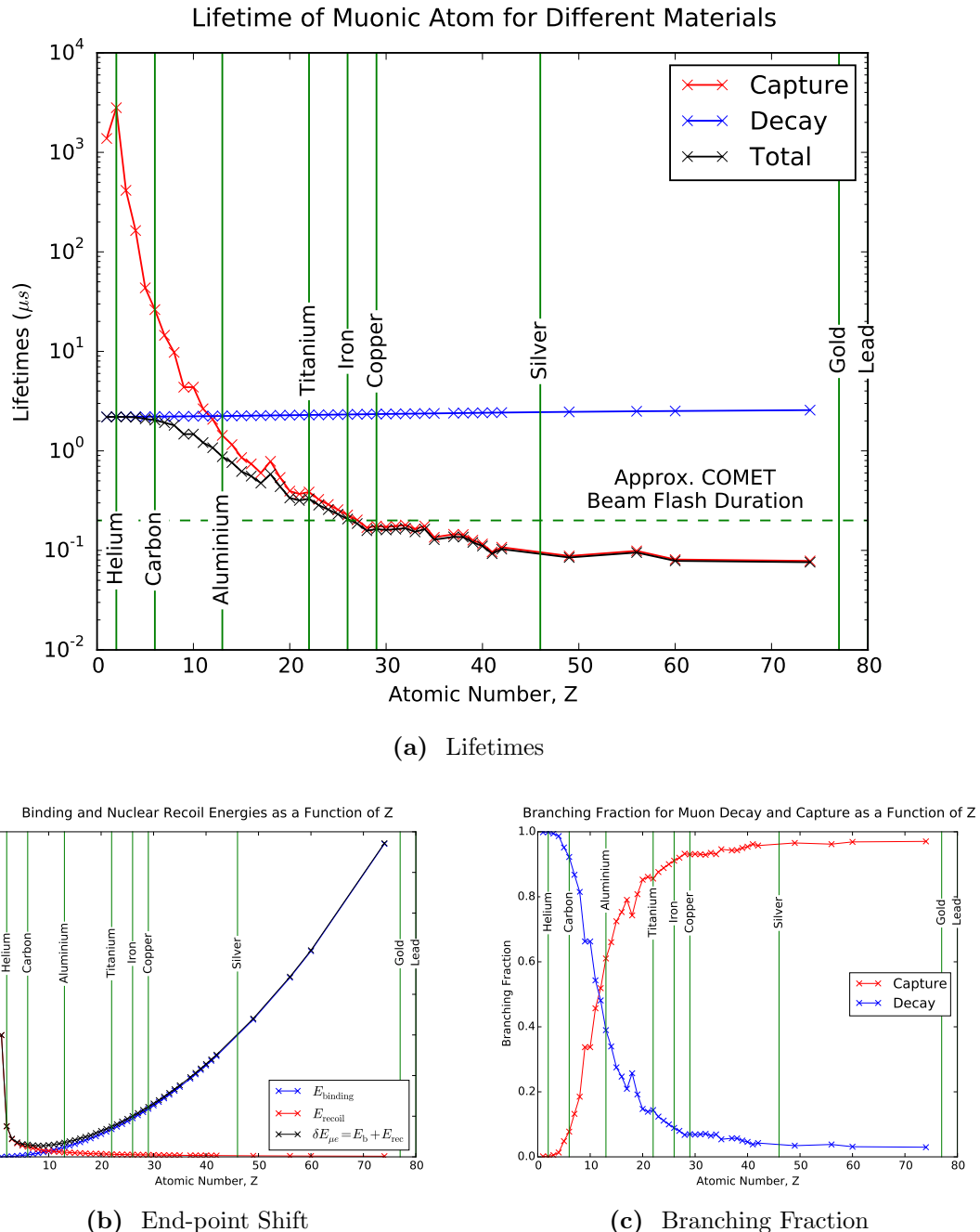


Figure 3.3.: The effect of changing the atomic number on the branching ratio, lifetime and electron energy spectrum end-point. For the branching ratio and lifetime plots, the partial rate for muon nuclear capture and decay-in-orbit are shown separately. The capture and decay rates are taken from the Geant4 [12] parametrisation for stopped negative muons. Only elements for which at least 1 isotope uses a measured value are plotted. The values for the end-point energy level are calculated using the Bohr model for the muon ground-state binding energy.

muon lifetime is about 330 ns, would be considerably harder to measure μ - e conversion so at this stage the COMET experiment is focussed on using aluminium where the muon lifetime is about 864 ns [79].

The J-PARC accelerator has buckets separated by 550 ns, although separations of multiples of this number can in principle be achieved. For COMET running the intention is to fill every other bucket so that a separation of 1.17 μ s is achieved. Fig. 3.4 shows the beam timing schematically. A window from about 700 to 1100 ns after the proton beam arrival is then used to look for signal events, by which time most of the beam flash should have passed whilst signal events remain probable.

Having a well-defined bunch structure is crucial for this scheme to work. Protons arriving in between bunches would produce (a fragment of) beam flash that could include high energy muons or pions which could result in background electrons arriving within the timing window. The extinction factor quantifies the rate of late arriving protons and is given by:

$$R_{\text{Extinction}} = \frac{N(p \text{ between bunches})}{N(p \text{ per bunch})} \quad (3.4)$$

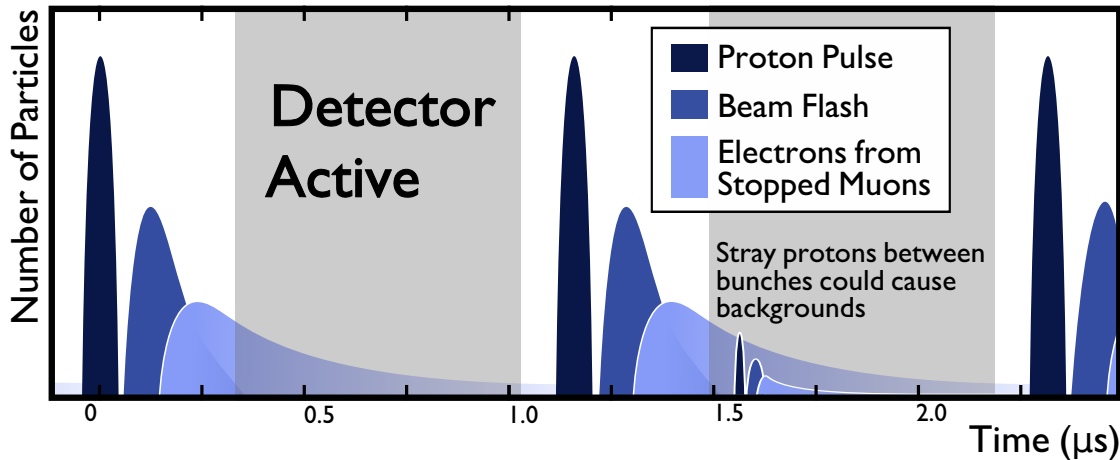


Figure 3.4.: Schematic for the timing structure used in the COMET experiment. Protons arrive at the production target in 100 ns bunches separated by about 1.17 μ s. These pulses create a flash of particles in the detector some 100 ns which lasts for about 300 ns. Muons that stop in that aluminium target last with a life-time of 864 ns, such that signal electrons would reach the detector in this time scale when the detector is able to be triggered. Very few protons should arrive in between bunches, else the corresponding secondaries could be detected as backgrounds.

Original estimates were made assuming $R_{\text{Extinction}}$ was around 10^{-9} [35] (about 1 out-of-time proton for every 7 Phase-I bunches) although recent measurements have been able to demonstrate extinction at a level of 10^{-12} [?] (about 1 out-of-time proton for every 7100 Phase-I bunches).

The bunch structure is initially defined by the linac at J-PARC which accelerates protons up to 600 MeV. The J-PARC Rapid Cycling Synchrotron ([RCS](#)) then takes these protons up to 3 GeV where up to two buckets can be stored at a time, although for COMET only one bunch at a time will be filled. The protons are then injected into the J-PARC Main Ring ([MR](#)) which accelerates them up the final energy of 8 GeV and is capable of storing up to 9 buckets at once. Using the Linac chopper alone would not be sufficient to produce the desired extinction factor since stray protons tend to drift into the unfilled buckets. Achieving the high extinction factor then is possible only by using the injection kicker from the [RCS](#) to the [MR](#) in a ‘double-kick’ mode. The kicker excitation length is set to two buckets (so that the [RCS](#) is completely emptied into the [MR](#)). The kicker is then activated again immediately after the first filled bunch has performed a complete rotation of the [MR](#) such that protons that had diffused into the second bunch of the [RCS](#) are now kicked away. Thus only every second bucket in the [MR](#) is filled and all other buckets are kept empty.

3.3. COMET Phase-I

Phase-I will see the construction of the COMET hall, the production target capture solenoids, the first 90 degrees of the bent muon transport solenoid, and the detector solenoid. The beamline is shown schematically in Fig. 3.5 where the two interchangeable detector systems can also be seen.

There are two key goals to Phase-I:

1. measure μ - e conversion at a Single-Event Sensitivity ([SES](#)) of 3×10^{-15} ,
2. prepare for Phase-II by measuring the beam profile, particle yields and background rates, and prototype the detector technology.

Since the dynamics of bent solenoids are complicated, it is important to study the beam as close to the production target as possible. However, due to the high radiation environment around the production target, the detector and electronics cannot be placed too close and must be well shielded. Phase-I will therefore measure the beam after the

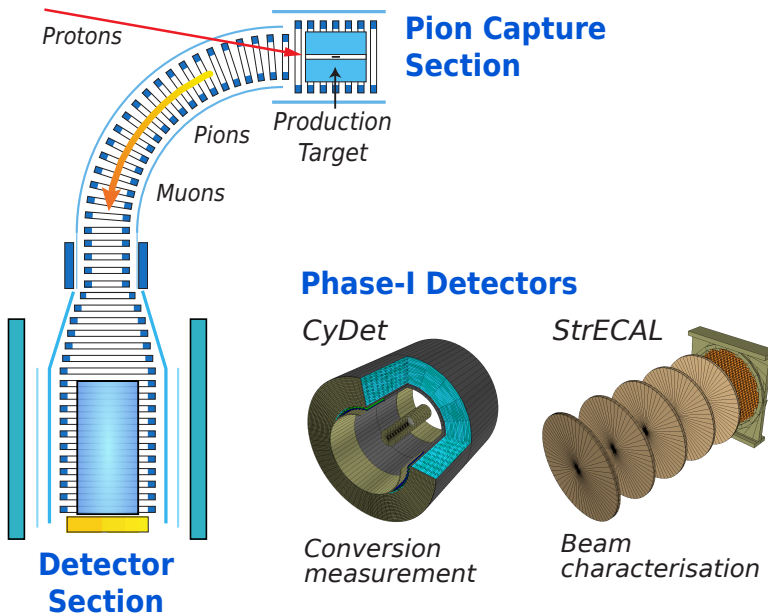


Figure 3.5.: Schematic layout of COMET Phase-I including the two detector systems that will run separately, being swapped in and out of the detector solenoid depending on the study.

first 90 degrees of bent solenoid using the same detector system to be used in Phase-II, namely the Straw tube tracker and Electromagnetic Calorimeter ([StrECAL](#)) detector – a series of Straw Tracker stations followed by an ECAL all sitting in the beam.

However, since the [StrECAL](#) detector will be hit by the full force of the muon beam, it would not be feasible to conduct a μ - e conversion search using this detector. As such, for Phase-I a second detector, known as the Cylindrical Detector ([CyDet](#)) will be used for this purpose. The [CyDet](#) uses a Cylindrical Drift Chamber ([CDC](#)) to reconstruct the trajectories of charged particles and a pair of Cherenkov and Scintillation counters (one upstream and one down) to trigger the read-out of the system. The [CyDet](#) escapes the issue of the beam flash that the [StrECAL](#) would face at Phase-I since only the outer region is instrumented. Since the detector sits in a 1 T solenoid field (and both the detector and solenoid are co-axial), particles follow helical trajectories with the radius of gyration determined by the transverse momentum of the particle. The beam is introduced in the centre and typically remains in an envelope of 15 cm whilst the stopping target sits in the centre of the detector with a radius of 10 cm. As such the detector itself is geometrically blind to charged particles in the beam and electrons coming from muon [DIO](#) in the target with momentum less than 60 MeV/c which make up the majority of

the [DIO](#) spectrum. To reconstruct the longitudinal position of the particle’s trajectory an all-stereo configuration is used in the Cylindrical Drift Chamber, where each layer is rotated in the opposite direction compared to the previous layer by an angle of 4° with respect to the solenoid axis.

Because the Phase-I detector sits much closer to the stopping target than at Phase-II, there is greater exposure to hadrons emitted following nuclear capture of the stopped negative muons, such as protons, deuterons, alpha particles and so on. Despite being emitted with kinetic energies of a few tens of MeV, momenta above 60 MeV are readily achieved given the large mass of these particles. For similar reasons these particles are typically very heavily ionising, so if left unchecked could easily dominate the occupancy of the [CDC](#). The AlCap experiment has shown that for muon capture on Al-27 nuclei, the emission of a proton occurs for about 3% of every muon capture [84]. At this level, it is believed that no specific shielding is required beyond the carbon inner wall of the [CDC](#) needed to contain the gas mixture.

Four layers of scintillation bars will surround the outside of the detector to provide a veto for cosmic ray events. The most dangerous event would be a high energy muon reaching the target and decaying to a 105 MeV electron which is then detected. Dedicated cosmic runs will be performed prior to operation with a beam in order to understand the flux of cosmic muons.

3.4. COMET Phase-II

Since chapter 5 presents an in-depth optimisation of the design of Phase-II, I shall only give a brief introductory overview here, most of which is based on the design as laid out in the 2009 CDR [35].

COMET Phase-II will be the final stage of the experiment. It will extend the muon beamline built in for Phase-I by an extra 90° , and add two extra solenoid sections: one to hold the stopping target, and a second 180° bent solenoid with a large aperture of 60 cm radius. This layout is shown in Fig. 3.6. The bent solenoid after the stopping target acts both as a spectrometer, but also to remove the low energy [DIO](#) electrons which otherwise could significantly increase the hit rate in the detector. The final detector system for Phase-II will use the [StrECAL](#) from Phase-I but probably with thinner diameter straw

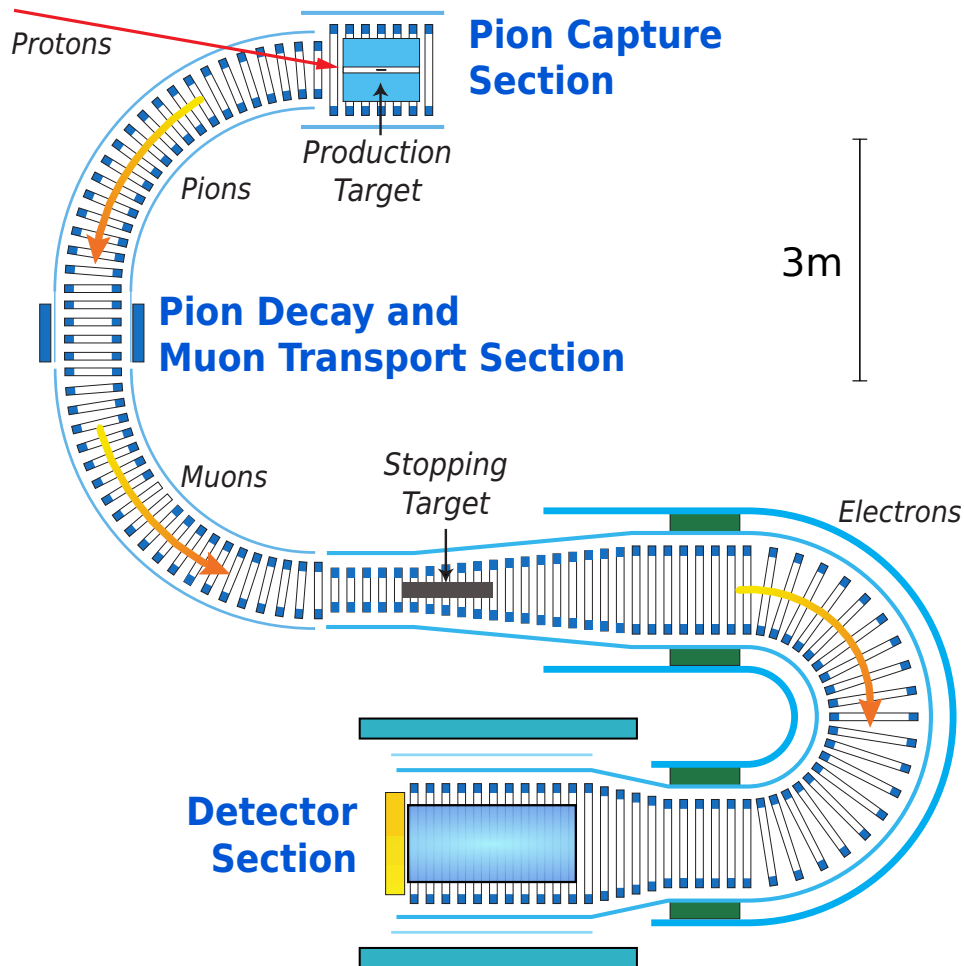


Figure 3.6.: Schematic layout of COMET Phase-II. The 8 GeV proton beam enters from the top-left, producing (amongst other things) pions. Pions and muons travelling backwards with respect to the proton beam are then transported around 180 degrees of bent solenoid, during which time most of the pions decay producing an intense muon beam. About 40% of these muons then stop in the stopping target (centre of image). Any electrons coming from μ - e conversion are then transported through another 180 degrees of bent solenoid into the detector system.

tubes, thinner straw material, and more tracking stations in order to improve the energy resolution.

The stopping target itself has typically been designed as thin disks of aluminium, followed by a beam blocker. Even including the growth of the beam envelope as it passes from the 3 T field in the bent muon transport solenoids to the 1 T of the bent electron spectrometer solenoid the beam blocker removes all line-of-sight between the entrance of

the electron spectrometer and the muon transport solenoids so that most of the beam flash is prevented from reaching the detector. The tapering of the field occurs almost completely across the target itself with the intention that signal electrons heading initially upstream will be magnetically mirrored back towards the detector.

As for Phase-I, an active cosmic ray veto will prevent triggering on events caused by cosmic muons. At least the detector solenoid will be covered, but there is some scope

3.5. Schedule and Status

The overall schedule for the COMET experiment is shown in Fig. 3.7. Phase-I is due to start data taking in Japanese Fiscal Year ([JFY](#)) 2018 so that construction and development is well underway.

At the time of writing, with regards to the facility, the building to house the experiment is now finished attached to the side of the existing Hadron Hall at the Japanese Proton Accelerator Research Complex ([J-PARC](#)). Cooling and power supplies are being installed and the shielding for the concrete hatch area is being produced. In the mean time the development of the new beamline to extract protons from the [MR](#) and deliver them to the COMET area is being installed. In particular, the Lambertson magnet which directs the protons towards COMET rather than the existing Hadron Hall has been built. For the muon beamline, the Phase-I section of the bent muon transport solenoids has

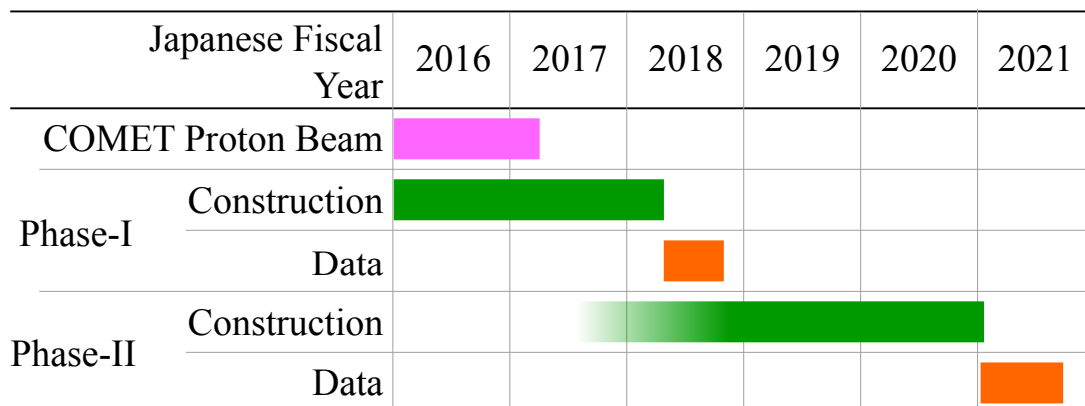


Figure 3.7.: A summarised timeline for the COMET experiment including Phase-I and Phase-II based on the 2016 TDR [\[80\]](#). At the time of writing, construction of the detector solenoid is underway as well as the final stages of the facility.

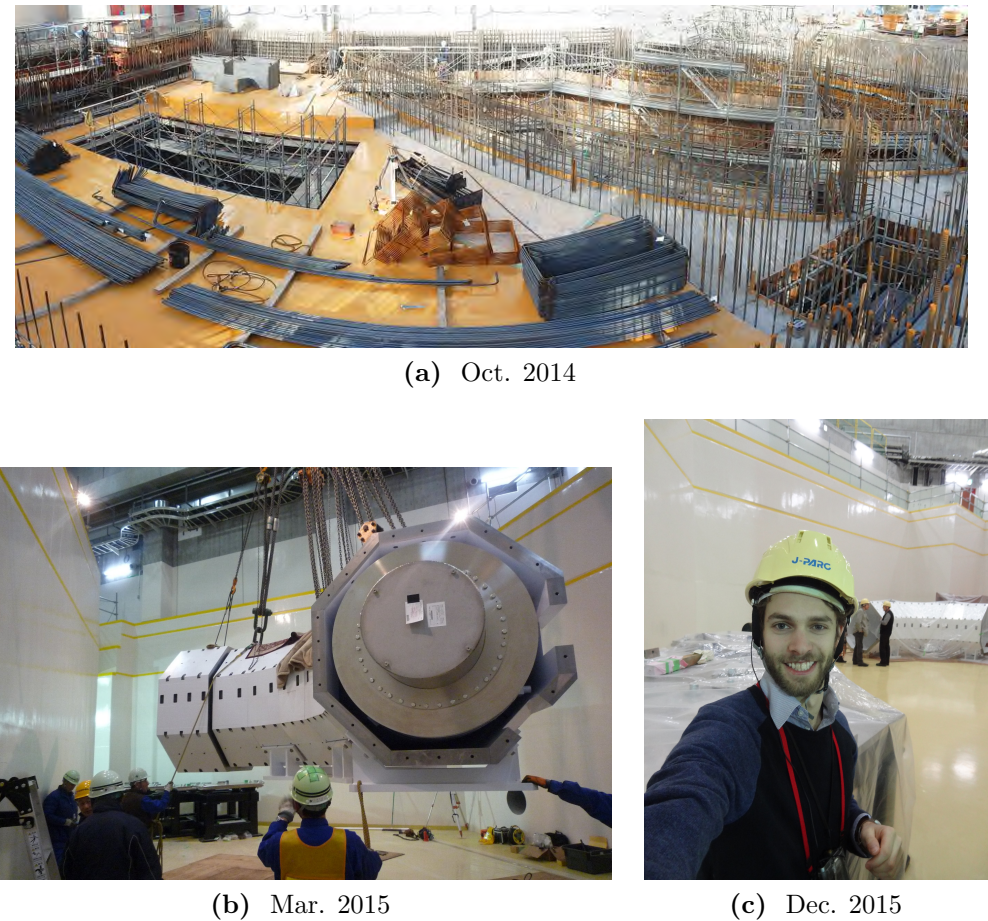


Figure 3.8.: Photographs of the experiment hall being constructed and first sections of beamline being installed.

been built and installed and is now under commissioning studies. Construction of the detector solenoid has also begun with the capture solenoids around the production target soon to begin. A selection of photographs that show the construction of the facility and installation of the bent transport solenoid are shown in Fig. 3.8.

Much of the recent activity for the collaboration has been on the design and construction of the detector systems. Beam tests to understand the performance and resolution of prototype ECAL crystals, straw tubes and the [CDC](#) have taken place. For the [StrECAL](#), production of all 2500 Phase-I straws has been completed and procurement of the Cerium-doped Lutetium Yttrium Oxyorthosilicate ([LYSO](#)) crystals for the ECAL is under way with some 200 or so crystals already purchased. Aging tests of the straw tubes are on-going with straws under pressure and tension being held for an extended duration at KEK. Beam-test data is being analysed to understand the position resolution for a given straw and the energy resolution of the ECAL although for the latter better than

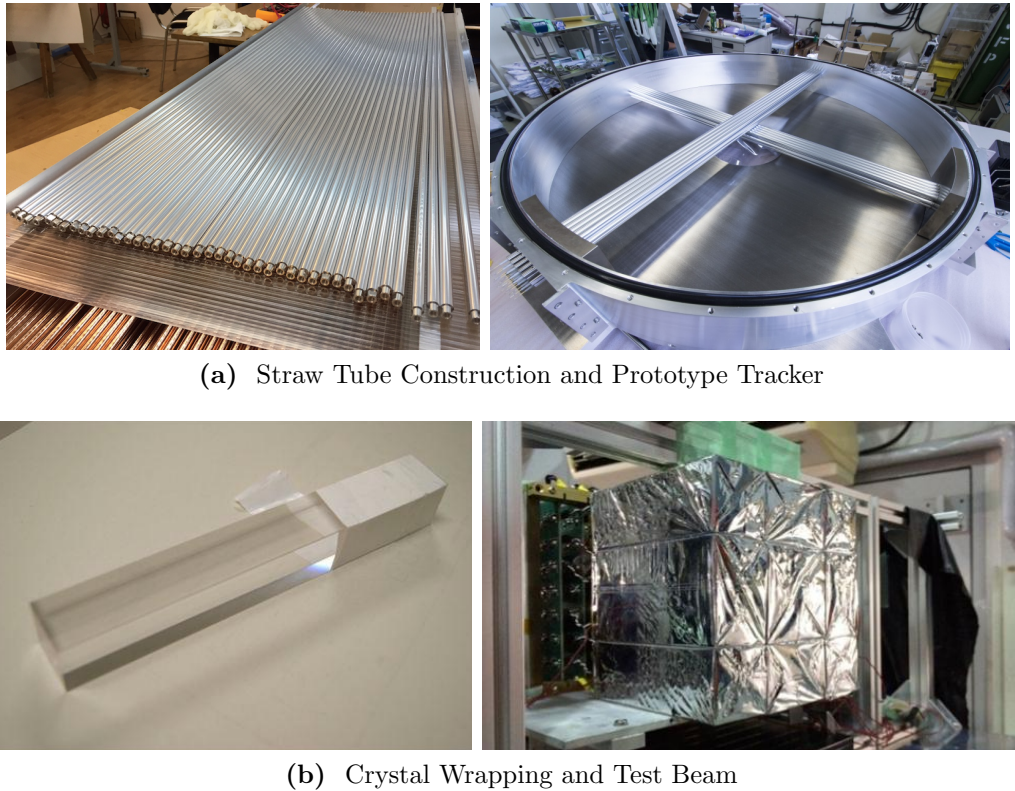


Figure 3.9.: Research and development for the [StrECAL](#) showing both the individual straws or crystal and a prototype set up used at test beams to characterise the sub-detectors.

5% resolution for 105 MeV electrons has already been shown. Fig. 3.9 shows photographs of the prototypes and beam test set-ups of the Straw Tube Tracker and the ECAL.

In the meantime the full [CDC](#) has been strung, with some 20,000 wires less than 10 microns thick ***CHECK: is this the correct wire size*** being inserted. Every wire has had its tension checked using a vibrational resonance method, which showed some ***-- CHECK: How many wires needed to be replaced*** wires were out of design tolerances. These have since been replaced. In June 2016, the inner wall of the [CDC](#) was successfully inserted, completing the [CDC](#) construction, so that leak tests can begin shortly. Fig. 3.10 shows photographs from the stringing of the [CDC](#). In parallel, cosmic ray tests have been used to study the performance of [CDC](#) prototypes and analysis of the data is under way to deduce the X-T curve for the [CDC](#) cells.

In the less-tangible realm that is software and simulation, in April last year the offline software reached its first stable release, and has since been used to perform three large-scale Monte Carlo productions of Phase-I. Reconstruction algorithms, including

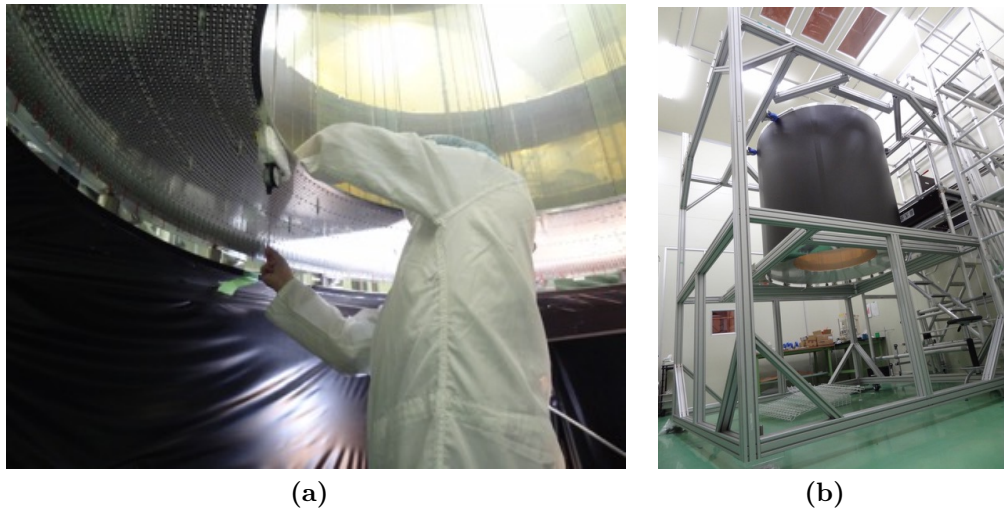


Figure 3.10.: The CDC being assembled and strung.

track finding and fitting in the [CDC](#) are under development and techniques to perform Particle Identification ([PID](#)) using the [StrECAL](#) in the Phase-I beam are also under development. More discussion on the software and simulation can be found in the next chapter.

Chapter 4.

Offline Software and The COMET Simulation

In 2013, when I first worked on the COMET experiment, many disparate and stand-alone simulations were being used without a unified approach in the data structures and analysis. Since then, a single unified software framework has been prepared and is now being used throughout the collaboration. Developing this framework has been a large part of my work over the last four years, so this chapter presents both a summary of the framework and its development, as well as an explanation of the techniques used.

4.1. Developing the COMET Offline Framework

Work to produce a common, standardised software framework for COMET began when funding was awarded for Phase-I. With some four years to go before the switch on, it was clear that the support structure to handle and analyse the data needed to be in place soon. Given the scale of the project and the available resources, the decision was taken to base the COMET offline framework on an existing one, which would reduce the amount of work needed and improve the reliability of the software since it would have been tested elsewhere. A requirements document [81] was drawn up with a list of items that the software should meet and a survey of existing experiments undertaken to build a list of candidate frameworks. The list contained:

art A framework being developed primarily at Fermilab [66] which is also being used by Mu2e amongst other experiments.

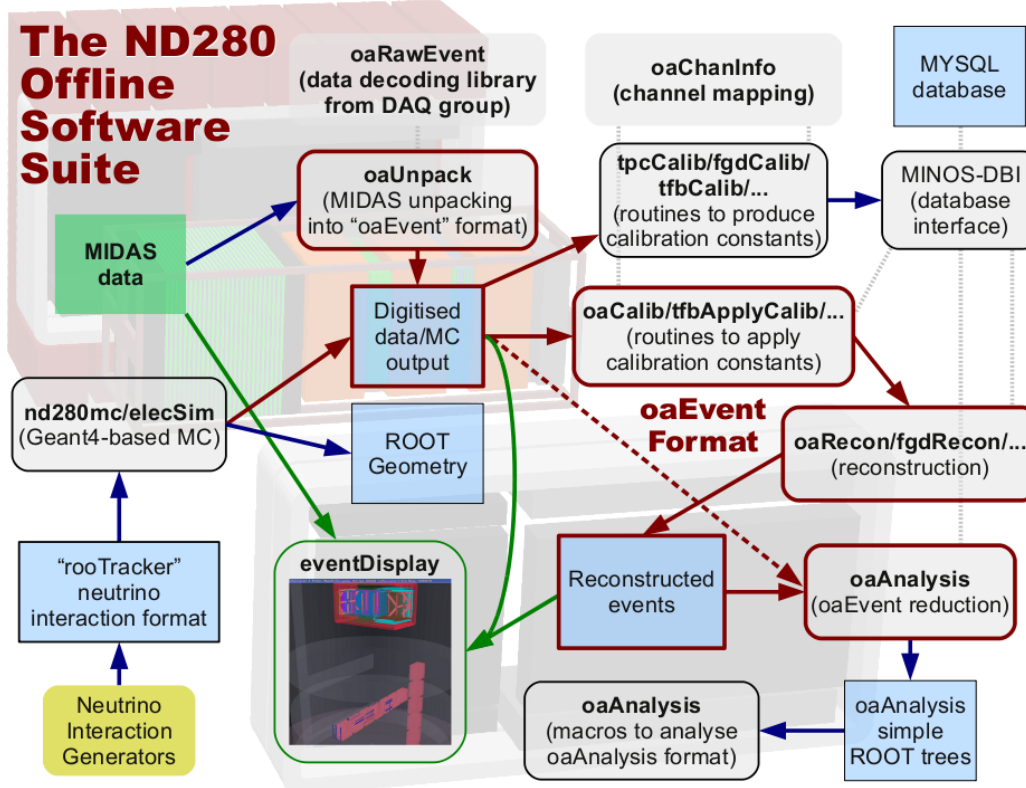


Figure 4.1.: Overview diagram for the ND280 framework.

ND280 The framework [11] used by the near detectors of the T2K experiment, which are also based at J-PARC.

GAUDI which is used by LHCb amongst other experiments [22].

MARLIN The software being developed for the International Linear Collider (ILC) [1].

The final decision was to use the ND280 framework¹ since GAUDI and MARLIN would have required too much effort to adapt to the COMET requirements; since art is used by Mu2e and keeping the software distinct is important for the two experiments to co-exist as cross-checks; and because the ND280 software was already known to a large part of the COMET collaboration and had been tested on real data at J-PARC.

Fig. 4.1 shows an overview of the ND280 framework, including its package structure and the various interactions between packages.

¹The term ‘ND280’ can refer to one of either the ND280 detector itself, the site at J-PARC that houses both the ND280 and INGRID detectors, or the software used to analyse and simulate the T2K near-detectors. For the purposes of this chapter, unless specified explicitly, the term ‘ND280’ should be taken as referring to the software.

With the decision to base the COMET experiment on the ND280 framework – and with the selection of the new name: ‘ICEDUST’ – the process of forking the software was begun. Since the ND280 framework had evolved somewhat organically a review of the conventions and code names was performed. For example, whilst the ND280 software prefixes all classes with a capital ‘T’, the ICEDUST conventions [65] agreed to swap this to a capital ‘I’ to reduce clashes with ROOT which also uses ‘T’. The package renaming scheme [82] was developed so that the purpose of a package and its role with the other packages could be more clearly identified.

Whilst fundamental, low-level packages have been left relatively unchanged, higher-level packages which include more detector specific details had to be developed. Additionally, some aspects of COMET needed considerably more support than had been present in the ND280 software. Some of the key changes that have been introduced between ICEDUST and ND280 are:

Simulation Although the fundamental data types have not been changed, the simulation has been nearly completely rewritten. In particular, support for hadron production codes have been added to model the production target; both the Geant4-based package (renamed to SimG4) and the detector response simulation (renamed as SimDetectorResponse) were given near-total makeovers; a new package (SimHitMerger) for resampling the G4Hits (simulated charge or energy deposits) was added. Custom physics models have been added to SimG4 to improve the modelling of the COMET-specific physics processes.

Magnetic Field handling whilst the ND280 detector has a fairly straight-forward magnetic field, the COMET experiment has anything but this. Accordingly, significant work has been made to replace the way the magnetic field was handled, from essentially a few constants to the ability to use complete fieldmap descriptions made with external field calculation software.

Geometry handling The unusual shape of the COMET experiment, the level of detail needed for background estimations in a high-precision experiment, and the changing nature of a staged experiment meant a more elaborate scheme for handling the geometry was necessary than had existed in ND280.

Reconstruction and Calibration packages As simply renaming of the packages, the interdependence of the calibration and reconstruction packages has been improved. Additionally, support for track fitting using Genfit2 [59] has been added as well as new track finding algorithms developed.

In addition to the above changes to the way the software runs, the distribution of the software has changed from using CMT [2] with CVS version control to being based on git with a GitLab [37] web-based user interface for the official repository. The switch to GitLab also brought a ‘merge-request’, which has allowed development of ICEDUST to progress rapidly with only a small number of developers. Although initially the intention was also to switch the build system from CMT to CMake [3], this decision has since been reversed due to improvements in CMT.

In the 3 years since the initial work forking ND280 to produce ICEDUST in summer 2013 some 3,200 commits have edited about two million lines of code in the official version of the framework. This has been the work of some 25 collaborators whilst about 15 other users have GitLab accounts and use the software. ICEDUST has been used to run three large Monte Carlo productions, most recently simulating about 10^{11} Protons on Target (POT) events – equivalent to 18,000 Phase-I bunches – in some 100 TB of simulated data.

4.2. Overview of ICEDUST

ICEDUST Can Efficiently Do Useful Software Things and stands for the Integrated COMET Experiment Data User Software Toolkit. Fig. 4.2 shows the flow of data through the different packages of the framework and the data formats used.

Inside the framework, nearly all processing is done using a ROOT file-based format known as oaEvent. Files of this type contain header information providing run identification numbers as well as a description of the geometry and magnetic field. The data payload contained in oaEvent files is stored in a ROOT TTree with a single branch containing a single COMET event per entry. Each COMET event has a dynamic structure and can have any object which derives from the IDatum base class added to its list of data on an event-by-event basis.

Data from the detector systems is recorded in MIDAS [7] format, which also contains data from the slow control monitors such as temperature sensors and high-voltage power supplies. The task of converting the MIDAS files into the oaEvent format is handled by the package oaUnpack, which writes out new, converted files, and oaRawEvent, which can convert the MIDAS files to oaEvent format on the fly.

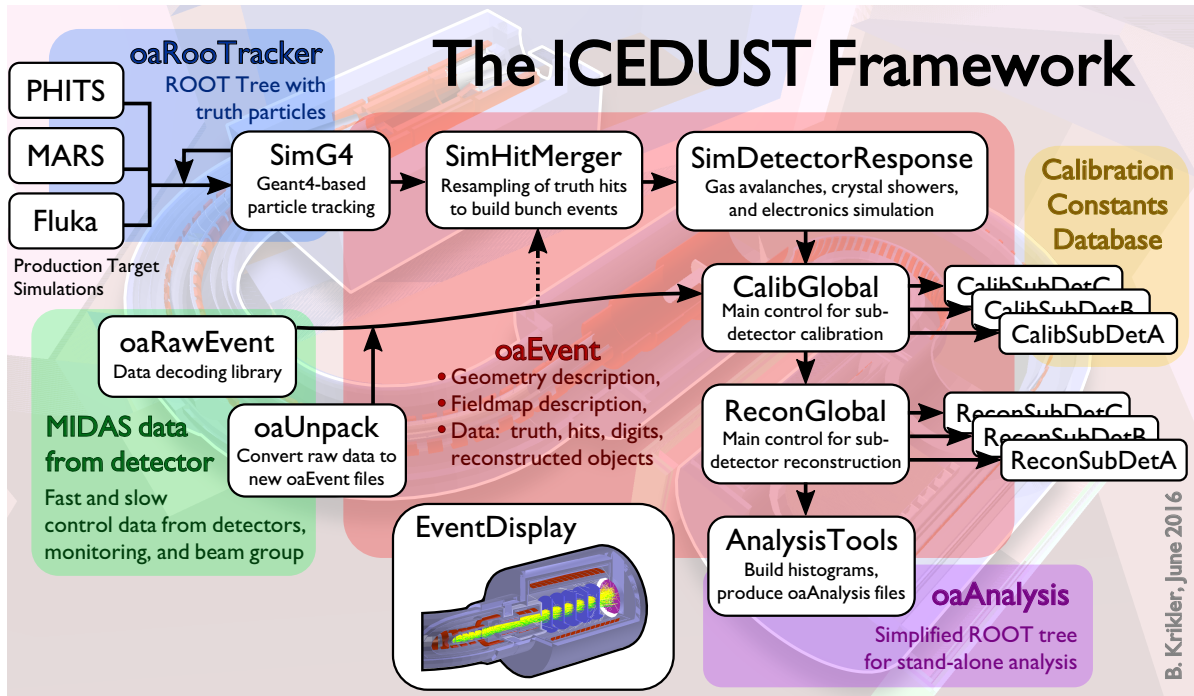


Figure 4.2.: Overview diagram for the ICEDUST framework. Data produced from simulation or taken in the real experiment are treated identically through the calibration and onwards up to analysis.

Simulated data is also produced in the oaEvent format and involves some 4 to 6 packages being called, described in more depth in section 4.3.

Once either simulated data has been produced or real data has been converted, calibration routines can then be applied. Each sub-detector is capable of pulling constants that were previously generated from a MySQL database and applying these to the detected (or simulated) energy deposits. These calibrated hits are then passed into the reconstruction stage. Here again each sub-detector system is first allowed to handle the data until a full reconstructed event is produced. For the tracking detectors this stage typically involves an initial track finding stage, where noise hits are removed and track candidates consisting of a list of hits are collected and, secondly, a track fitting stage where the actual path of the underlying particle is reconstructed and key values like momentum and helical pitch-angle deduced.

Nearly all of the processing of data up to this stage has used the oaEvent format. The final analysis stage, however, moves into a simpler, flatter format, known as oaAnalysis, which produces a data summary tree (as opposed to tape) that can be accessed without a dependence on the full ICEDUST software.

Around all of this there are several utility packages such as the event display, which can visualise any oaEvent file, and IcedustControl, which can run a single set of data through the data chain and is the main steering mechanism used for production running.

4.3. The COMET Simulation

The ability for an experiment to set stringent confidence limits in the event of a null-observation is determined both by the expected signal acceptance (which should be high) and the predicted number of background events (which should be low). For COMET’s target single-event sensitivity – which is only a measure of the signal efficiency – to translate to a comparable confidence limit if no signal is observed, less than one background events should be expected during the entire run. By comparison, some 10^{19} and 10^{21} protons will impinge the production target in Phase-I and Phase-II respectively, so it is clear that the ability to suppress backgrounds must be demonstrably high.

Simulation plays a crucial role in making such a demonstration. Before the experiment is built and operated it allows one to optimise crucial aspects of the geometry and parameters, such as the magnetic field strengths or timing cuts. In addition, using Monte Carlo techniques in an accurate simulation allows an estimation of the background rate by sampling the parameter space corresponding to each stage of the experiment. Clearly, then, the simulation itself must be as faithful a reproduction of the true experiment as possible.

The COMET simulation therefore needs to be both highly accurate and highly efficient. As well as custom physics modelling, and special handling for the magnetic field, several resampling techniques have been introduced to increase the statistical power. The steps needed to build up the COMET simulation are shown in Fig. 4.3.

To reduce the uncertainties associated with the production target and the muon and pion yield multiple hadron codes can be used, including PHITS [60], MARS [72], Fluka [49] and Geant4 [12]. The SimG4 package, which is based on Geant4, then takes over the muon beam simulation and tracking of particles to the detectors. These energy deposits, referred to as G4Hits, can then be converted to realistic electronic detector-readouts by the SimDetectorResponse package. On most occasions, though, the G4Hits are first reshuffled with G4Hits from other Proton-on-target events so that a realistic bunch structure is built up and processed, since it is this structure that the true detector

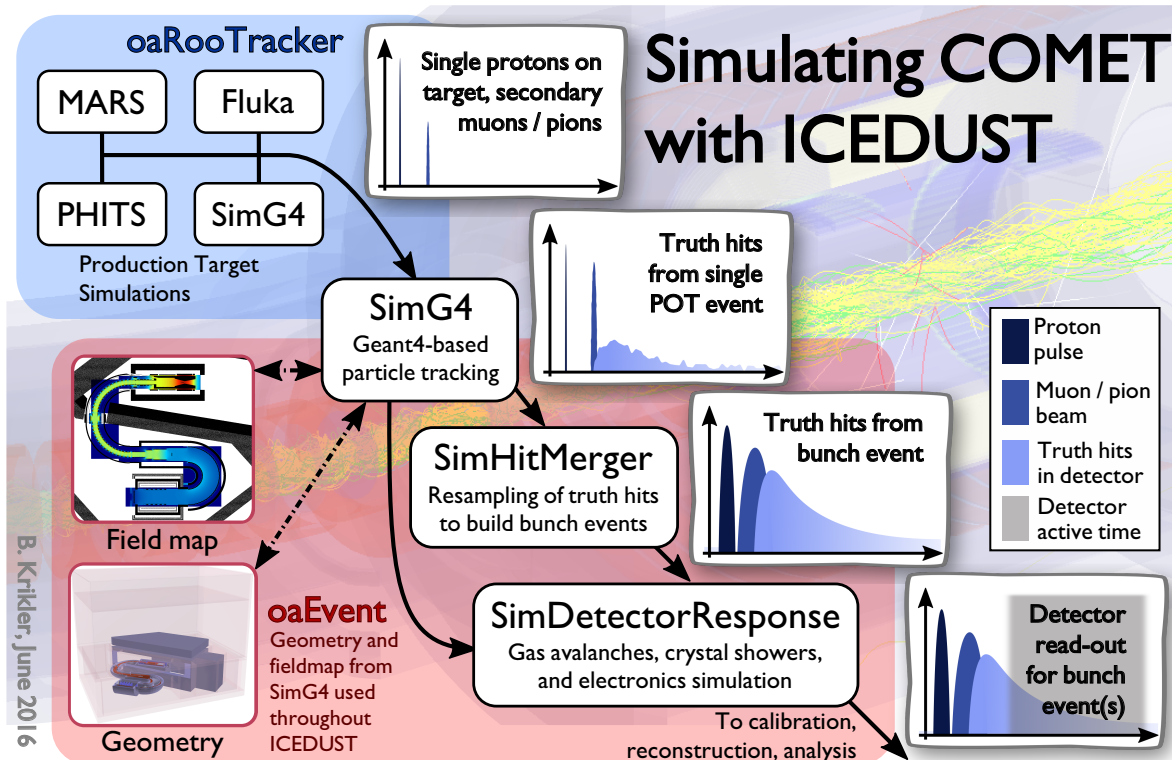


Figure 4.3.: Diagram showing the stages used to simulate COMET. The timing schematics on the right show how a simulated event is built up, firstly by producing many individual proton interactions with the production target, then by transporting the secondary particles to produce energy deposits in the detector, which are then combined with the truth hits from other proton events to produce a realistic bunch structure. Finally, these bunch events are processed through the detector response simulation to produce fake waveforms and other detector read-outs.

will see. SimG4 produces one output event for every primary vertex introduced², whereas SimDetectorResponse needs to produce the same sort of data structure as will be seen in the real experiment, which is one event per proton bunch.

This requires some intermediate step, known as the SimHitMerger, to shuffle the events from SimG4 together and build up realistic bunch events. At this point, a degree of resampling is also introduced, since there are virtually no correlations between proton events. Within a SimG4 output event all timing is given with respect to the original primary vertex. Since protons on target are introduced at $t = 0$, all G4Hits have their timing given with respect to the proton arriving at the production target. In the process of building bunch events, a realistic timing structure for the proton beam is introduced

²This typically means one output event per proton-on-target, but in principle could be something else, such as one output event per signal electron in a dedicated trigger simulation

by shifting the time of all hits for a given proton event by a fixed amount, as if the proton had arrived slightly earlier or later.

A bunch event in Phase-I will consist of about 8×10^6 POT so, without resampling, a simulation of 8×10^8 POT events could only produce 100 bunches. Since the proton events are uncorrelated, by picking different proton events and applying different time shifts to each one it is possible, in principle, to build a much larger number of bunch events.

An additional form of resampling can also be used during the Geant4 simulation, by dividing up the experiment into different stages and restarting the simulation multiple times at a later stage, reusing the output from the earlier section. For example, a simulation of the production target region is used to track particles up to the boundary of the muon beam line. The muon beam simulation is then repeated multiple times using the particles that left the production target section as an input and changing the initial random seed for each restart. This technique was used in the most recent large scale mass production twice – once at the production target section and again at the entrance to the detector solenoid region – restarting the simulation five times for each section, so that for each initial proton on target, 25 times this number of events were tracked through the detector solenoid.

Both of these resampling techniques must be handled with care since this can produce correlations between the events produced from resampled inputs. Reconstruction methods often employ machine learning techniques which are particularly sensitive to correlations within a dataset. To reduce any potential impact due to resampling, the resampled data is handled in distinct sets so that within a set no proton on target event is repeated in more than one output bunch event.

4.3.1. Handling Geometry

During the change from ND280 to ICEDUST, a new geometry handling scheme was introduced to the SimG4 package. This change was motivated by: the fact that COMET has a large number of components with a large variety of complexities, shapes, and sizes; the COMET geometry will change dramatically throughout the lifetime of the experiment; all pieces of material close to the beam could potentially contribute to background rates if, for example, they scatter high energy particles into a high-acceptance region in the phase space.

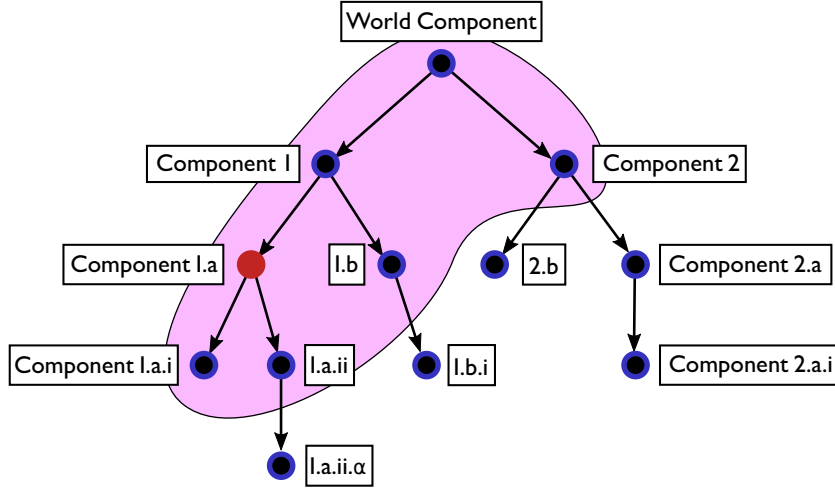


Figure 4.4.: How parameters are shared amongst different components. The Controller of component 1.a in red has access to the parameters managed by Controllers of components contained in the larger violet region.

The aim of the new geometry handling scheme tries to address these issues. The goals in developing the new approach were to:

- define a clear mechanism for how the geometry is implemented and controlled;
- decouple the code for physically isolated parts of the experiment;
- provide the flexibility to add and remove parts of the experiment;
- maximise the maintainability of the code related to geometry;
- allow for easy inspection of both the geometry and the various parameters that control it.

The final scheme uses a nested component structure, which is built up using compiled C++ to define the volume hierarchy in a modular way, with parameters provided at run-time to define the actual shapes and locations of the volumes. The run-time parameters are ‘owned’ by the component they are attributed to and can be assigned values based on that of other parameters and inspected easily by various print commands. Access to the values of other parameters is possible if and only if they are owned by an accessible component. Whether or not another component is accessible depends on its relative position in the component hierarchy: the target component must either be an ancestor, immediate child, or share the same parent component, as demonstrated in Fig. 4.4.

To provide the value of a parameter standard, human-readable, infix notation allows integers, doubles, three-vectors and rotation matrices to be combined and manipulated. In addition, parameters can be easily repeated or indexed, such as for the positions of

```

/comet/Torus2/TS4_First/Dimension InnerR = 23*cm
/comet/Torus2/TS4_First/Dimension OuterR = [InnerR]+22*mm
/comet/Torus2/TS4_First/Dimension Length = 10*cm
/comet/Torus2/TS4_First/Material Material = Copper

/comet/Torus2/TS4_Middle/Dimension InnerR = 23*cm
/comet/Torus2/TS4_Middle/Dimension OuterR = [InnerR]+43*mm
/comet/Torus2/TS4_Middle/Dimension Length = 10*cm
/comet/Torus2/TS4_Middle/Material Material = Copper

/comet/Torus2/TS4_Last/Dimension InnerR = 23*cm
/comet/Torus2/TS4_Last/Dimension OuterR = [InnerR]+43*mm
/comet/Torus2/TS4_Last/Dimension Length = 10*cm
/comet/Torus2/TS4_Last/Material Material = Copper

/comet/Torus2/Count Coils:Count = 16
/comet/Torus2/Angle Coils:PositionPhiStart = 0*degree
/comet/Torus2/Angle Coils:PositionDeltaPhi \
    = ([PhiTotal]-2*[Coils:PositionPhiStart])/([Coils:Count]-1)
/comet/Torus2/Position (i<[Coils:Count]) Coils:Position \
    = ( r=[LargeRadius], theta=90*degree, \
        phi=[Coils:PositionPhiStart]+[i]*[Coils:PositionDeltaPhi])
/comet/Torus2/Rotation (i<[Coils:Count]) Coils:Rotation \
    = (axis=(1,0,0),angle=90*degree) \
    *( axis=(0,1,0), \
        angle=[Coils:PositionPhiStart]+[i]*[Coils:PositionDeltaPhi])

```

Figure 4.5.: An example set of parameter definitions which control the geometry for the Torus2. Parameter specifications use natural arithmetic notation and can reference other parameters and use standard units. They can also be formed as sets where each element has a different value, such as the Coils:Position parameter.

crystals in the ECAL or straws in a straw tracker plane, where the i^{th} position depends on the value of i . A small demonstration of some valid parameter assignments is shown in Fig. 4.5.

Using this scheme, multiple ‘worlds’ have been developed corresponding to different stages and run-configurations of COMET, between which a user can easily change. Each world is able to re-use much of the code for another such as the experiment hall building, which appears in every geometry. In addition, it has been straight forward to build up significant complexity in key areas such as the production target. Fig. 4.6 shows two of the available worlds that have been created using this scheme.

A more thorough description of the geometry scheme in SimG4, as well as a users guide and walk-through, can be found at www.hep.ph.ic.ac.uk/~bek07/comet/SimG4/documentation/index.shtml.

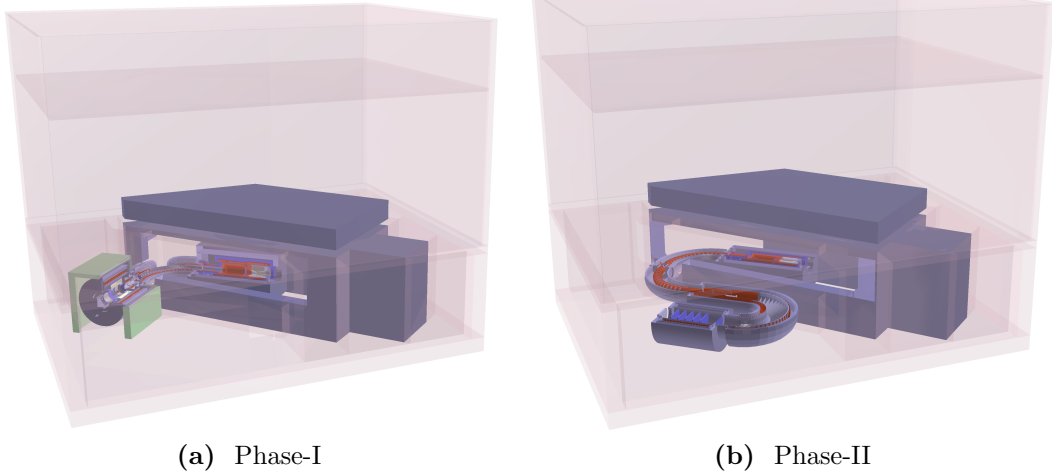


Figure 4.6.: Two of the possible simulation ‘worlds’ that can be selected at run-time: (a) Phase-I with the CyDet detector installed, and (b) Phase-II. Multiple Phase-I worlds exist, one for each potential running configuration.

Once SimG4 has created the geometry, it writes it out to a ROOT-based format alongside the data, using ROOT’s TGeo classes [30]. This is then used by the other packages, such as calibration and analysis. The event display also uses this to show the various hits and tracks overlaid on the geometry.

4.3.2. Field Calculation

An essential aspect of the COMET experiment is the static magnetic field that is used along the beam line to capture, focus and disperse charged particles. Modelling this field accurately is important to ensure any outcomes of the simulation are reliable. In particular, dips in the field have a risk of mirroring particles backwards or even trapping particles for extended periods. This could be especially dangerous for COMET since, in the process, the timing information of the particle is lost, reducing the effectiveness of the timing cut to suppress backgrounds.

Magnetic field calculations can become quite computationally expensive. As a result, approximations and assumptions are often made to simplify the process, such as the assumption of symmetry about an axis or plane to reduce the effective number of dimensions to the problem. As well as modelling the current in the coils, material effects should also be accounted for, particularly in the yoke and surrounding material of the beamline. Often these material effects are linear, but in regions of high magnetic field this

linearity can be lost via processes such as saturation, further increasing the computational complexity.

There are two distinct types of magnetic field used in COMET: a solenoidal field produced by a winding of superconducting cable in a spiral, and that of the dipole fields, which are produced by a novel winding technique that is proprietary to Toshiba. Although there are several areas of ‘bent’ solenoid, these are actually formed by a series of smaller straight solenoid sections and so do not need special treatment in the field calculation. Straight solenoids are used in many other applications such that existing coil calculation methods are reliable. Calculating the dipole field, however, is not so straightforward since the exact configuration is owned by Toshiba.

The COMET collaboration have used several different methods to perform field map calculations. G4Beamline [51] is a simulation toolkit that makes numerous extensions to Geant4 and is able to perform simple solenoid calculations directly. Whilst it cannot model material effects, its speed and simplicity allows quick and simple studies. The methods for solenoid calculations of this open-source project have been incorporated into SimG4, so that the package can directly produce the field for solenoid coils contained in its geometry. The resultant fieldmap is shown in Fig. 4.7b.

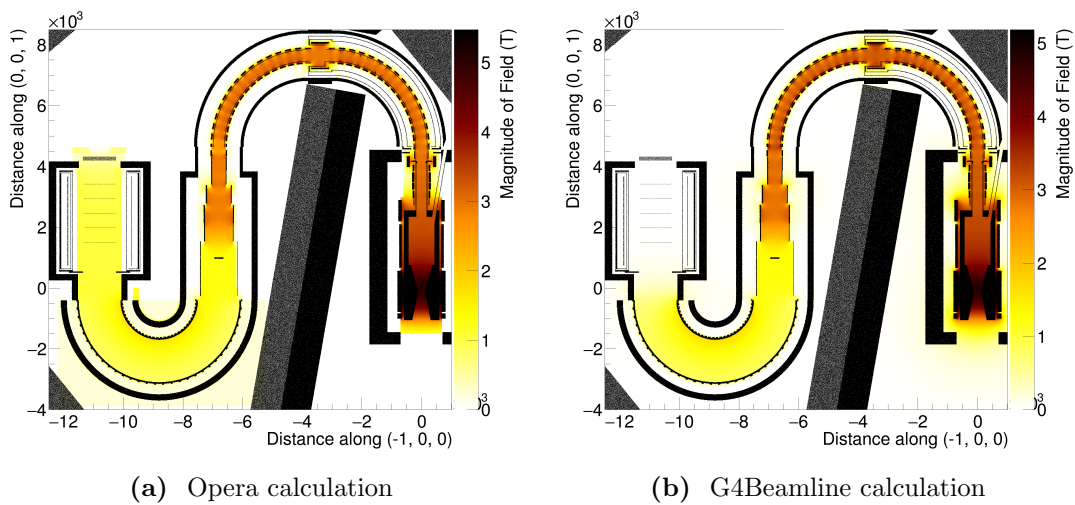


Figure 4.7.: Fieldmap produced by (a) Opera and (b) G4Beamline. Although the fringe field is larger with the G4Beamline calculation, the lack of material effects make this calculation less reliable. Note that the G4Beamline calculation does not include the detector solenoid.

For more elaborate calculations, Opera 3D finite-element-analysis software was used with the TOSCA submodule [76] for static electromagnetic fields. This calculation includes non-linear material effects in the yoke and shielding so that the final fieldmap should be much more accurate. Fig. 4.7a shows the fieldmap calculated by Opera in the plane of the beam line axis. The ratio between the G4Beamline and Opera calculations is given in Fig. 4.8, where it can be seen how the two models disagree most at the exit of the solenoids.

Whilst the above two methods have been used for the solenoid fields, calculating the dipole field structure is a different story, given that the winding is proprietary information belonging to Toshiba. For the dipoles in the muon beamline Toshiba have provided a calculation for one octant of one winding, which is then mirrored and placed multiple

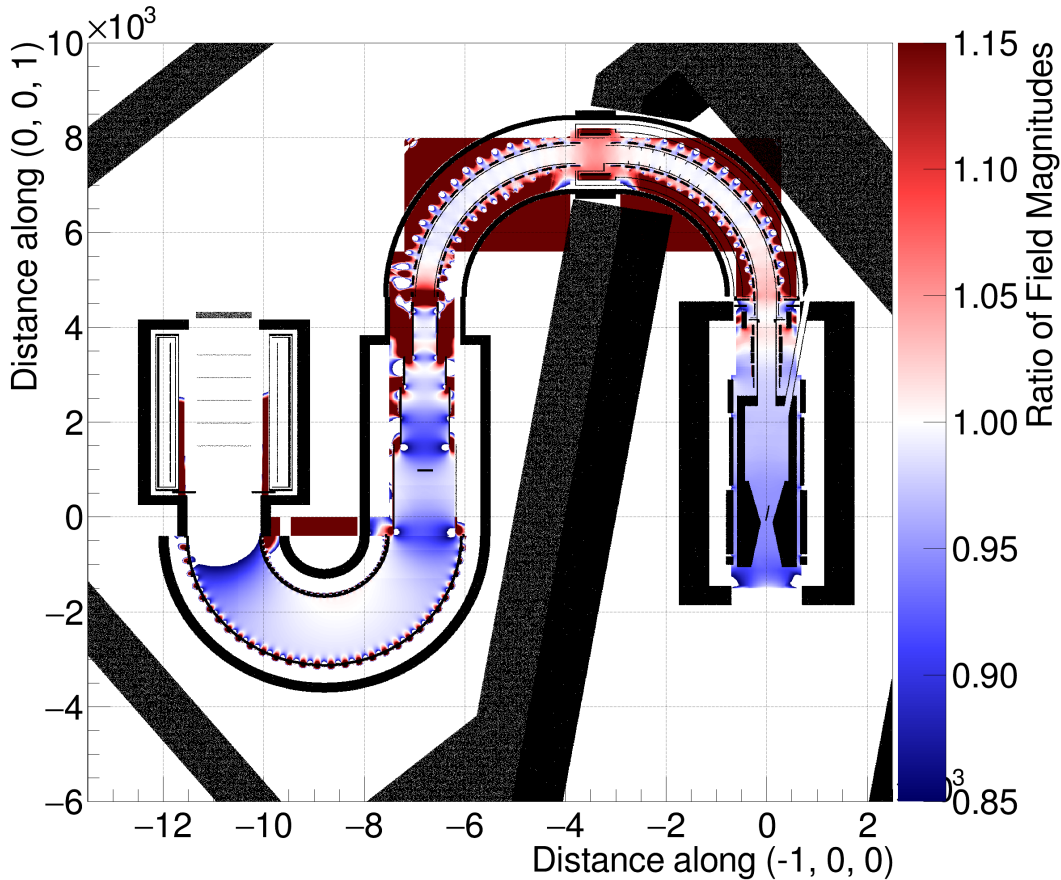


Figure 4.8.: The ratio of the Opera and G4Beamline calculations shown in Fig. 4.7. For most of the field within the beamline the calculations agree within 10%, although around the ends of the solenoids the agreement is poorer.

times along the beamline. For the dipoles along the electron spectrometer of Phase-II there is no accurate calculation at this time.

Whilst only magnetic fields have been used in the simulation up to now, ICEDUST is able to handle electric fields in exactly the same way. For instance future work might see the electric fields for the straw tracker and CDC included to account for the impact that these fields might have on particle scattering in the detector.

Field map files are treated as a single data file which are loaded in and placed with a given rotation and translation as well as an overall field scale factor. It is important that subsequent processing of data files be able to reproduce the same field as used to generate the data. Since many individual field map files are often loaded in to assemble an overall representation of the field to facilitate such book-keeping, a description of each of the used fieldmap files is stored alongside the data, in a similar way to the geometry. This information contains the name and a check-sum for the original fieldmap file as well as the rotation, translation, and scale factor. Given a data file and the location of a directory containing the fieldmap files, all ICEDUST programs are, therefore, able to re-instantiate the field. Other types of field component, such as the solenoid fields produced with the incorporated G4Beamline code, are also persisted and re-instantiated in this manner.

4.3.3. Production Target Simulations

There is currently a lack of experimental data for interactions of protons with 8 GeV kinetic energy with a tungsten target, especially for production of negative pions in the backwards direction. Fig. 3.1 seems to be the best source of experimental data, but even this is problematic in that it represents 10.1 GeV protons striking a tantalum target and that the actual data points are not tabulated anywhere in the literature.

The HARP experiment [32] has also measured pion yields in the context of future neutrino beam facilities and have used an 8 GeV proton beam with a tungsten target. Unfortunately they only observed pion yields at angles of less than around 2 radians for such a combination of target and proton energy.

As a result of this shortage of measured values, it is important to use as many hadron models as possible to pin down the uncertainty on the predicted pion and muon yield. Previous studies have compared the HARP data to predictions from several hadron codes [4, 47] some of which are reproduced in Fig. 4.9. From these it is clear that no one

model can reproduce the experimental data accurately for all angular regions and all materials.

Currently, PHITS [60], MARS [72], Fluka [49], and Geant4 [12] can all be used to run production target simulations and feed results into the rest of the experiment. The level of integration of these packages varies, however. SimG4 (which is based on Geant4) and SimMARS (which interfaces MARS into ICEDUST) are able to read directly the standard ICEDUST geometry and fieldmap formats and they are able to output directly to a format known as oaRooTracker, which the SimG4 package is able to read back in. On the other hand, both Fluka and PHITS (interfaced via SimFluka and SimPHITS, respectively) are written in Fortran and have proved harder to integrate. At this point in time, each must separately produce the geometry and fieldmap and have their outputs post-converted to the oaRooTracker format. Fluka also lacks a primitive Torus volume implementation, so that other studies such as neutron rates are further limited in Fluka at this stage.

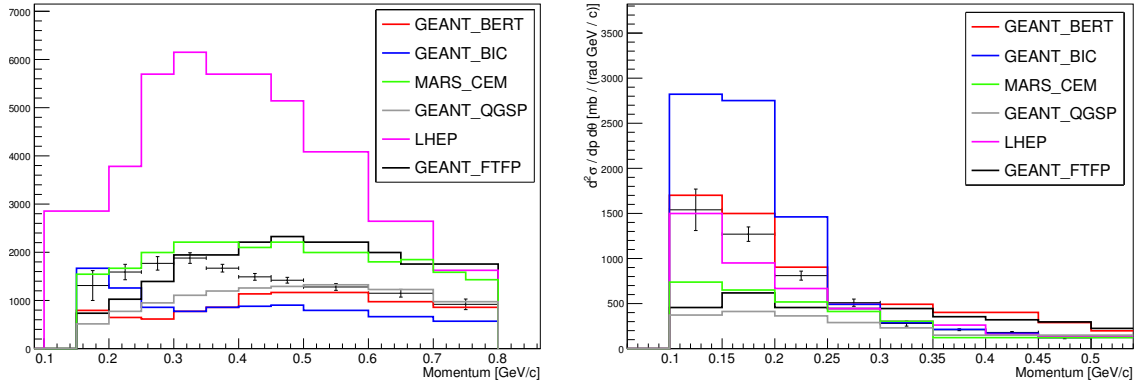


Figure 4.9.: Comparison of various hadron production codes with experimental data from the HARP experiment, taken from the thesis of A. Edmonds [47]. Points with error bars are the experimental data. Left: double differential-production cross-section for pion production from 20 to 32° with respect to the incoming proton direction; right: from 100 to 112°. The hadron production code that best reproduces the data depends strongly on the angular region under consideration.

4.3.4. Extending the Geant4 Physics Modelling

Geant4 physics modelling

Aside from the production target region, most of the tracking of particles and creation of secondaries takes place in the SimG4 package, which is built against the Geant4 library. The trajectory of a particle is built up in steps, each of which terminates either by a physics process (which might change the particle's direction or energy and produce a secondary track) or by the boundary of a volume in the simulated geometry. To decide what actually limits the step taken by a given particle (for example a positron), Geant4 calls the list of possible processes this particle can undergo (for example Bremsstrahlung, annihilation, inverse Compton scattering, etc) and asks each process for a proposed step length. In the case of a geometry limit, the step length is the distance until the boundary of the geometry, including bending in the trajectory due to any electromagnetic field. On the other hand, for a physics process the proposed step length is typically selected randomly using a relevant probability distribution for this process. Often this involves a characteristic length or time of the process, for example the half-life of a particle that will decay. Out of all possible step limits the process proposing the shortest limit (or if the particle is at rest, the soonest limit) is chosen. The current position and momentum of the particle is updated accordingly and any secondary particles produced are prepared for tracking.

Determining which processes are applied to which particles and how each process is modelled is an important part of building a Geant4 simulation; the library provides a list of standard physics lists to help the process. Choosing the right physics list depends on the goal of the simulation, for example which particles are involved; what energy ranges are interesting; and which background effects must be included. To simulate COMET the QGSP_BERT_HP physics list [?] was chosen as a starting point. This model is expected to perform well for low energy dosimetry, shielding, and neutron calculations [5].

On top of this physics list, custom changes have been made to the way negative muons are treated once stopped in material. COMET is unusual in the field of modern particle physics for dealing with muons at very low energy, unlike at the Organisation européenne pour la recherche nucléaire ([CERN](#)) experiments for example, where they are normally treated as minimally-ionising particles (MIPs). As a result, low-energy negative muons are somewhat crudely modelled by the default physics processes of Geant4. In

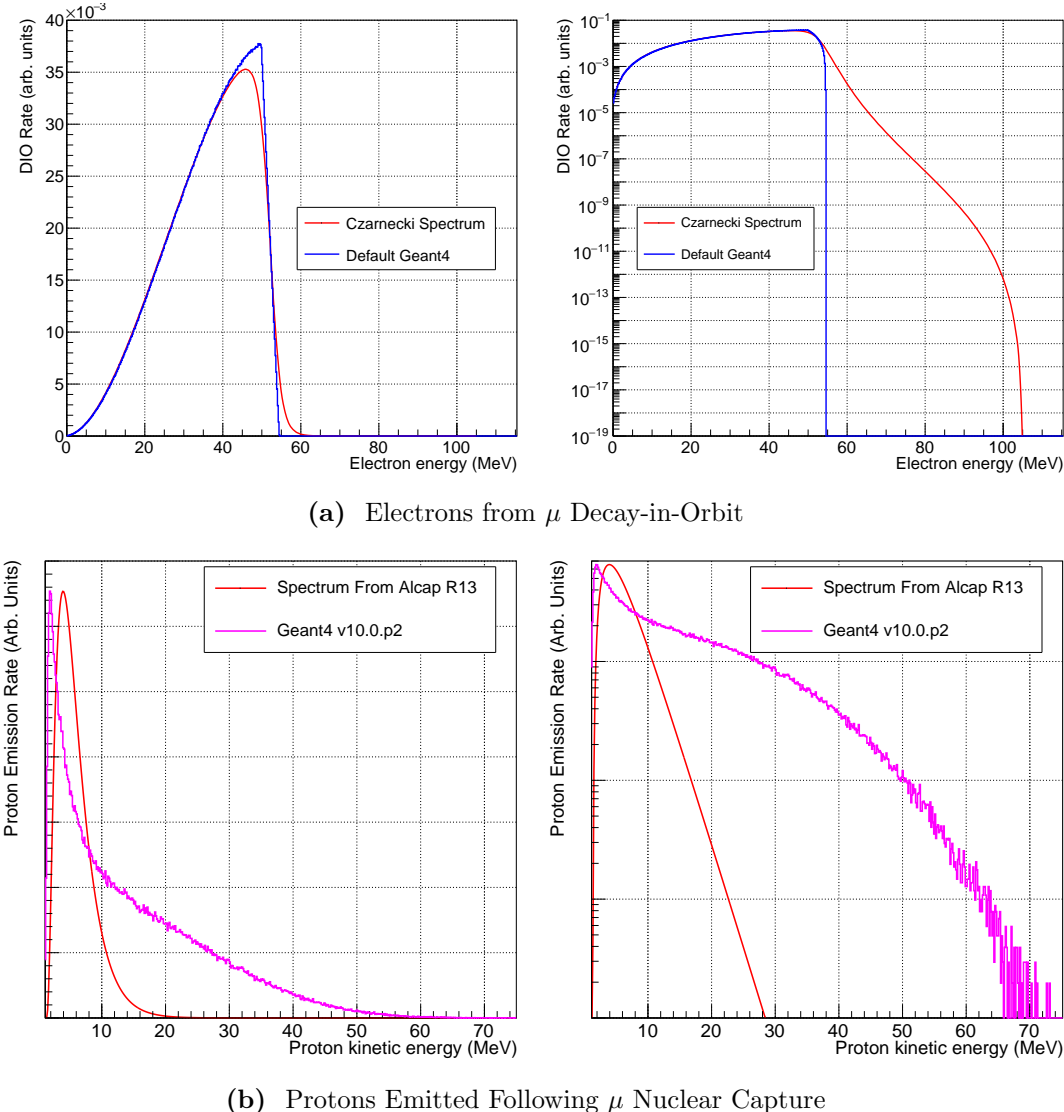


Figure 4.10.: Comparison of the realistic spectra for DIO electrons, (a) (normalised to agree at 35 MeV), and protons coming from muon nuclear capture, (b) (normalised to have the same maximum value), each on a linear scale (left) and a logarithmic scale (right). The DIO spectrum used in default Geant4 has a sharp cut-off slightly above the free muon decay end-point, to be compared with the long but steeply falling tail of the Czarnecki et al. theoretical calculation [38]. The comparison of protons coming from muon capture between the preliminary result from AlCap and default Geant4 shows that the true proton spectrum is much softer than the Geant4 model.

addition to this, for the COMET experiment it is important to add the process of coherent μ - e conversion, which, as a currently unobserved process, is not included in Geant4.

In the SM, a stopped negative muon that has been captured to an atomic orbital can either undergo decay or nuclear capture. As previously discussed, the end-point for electrons coming from muon DIO reaches up to the μ - e conversion limit, or around 105 MeV/c. Vanilla Geant4, however, is unable to produce this tail, and on aluminium is only able to produce electrons up to around 60 MeV/c. This is because the bound muon decay model in Geant4 uses the free muon decay spectrum and applies a boost in a random direction, with the boost factor set by the muon binding energy. A comparison of the electron spectrum from this model and that proposed by Czarnecki et al. [38] is shown in Fig. 4.10a, where it can be seen how the high energy tail falls far more rapidly in the Geant4 spectrum.

Similarly, for the nuclear capture of the muon, there are sizeable disagreements between the available but limited data and the default Geant4 model. For example, the AlCap experiment [13] has improved the knowledge of proton emission following muon nuclear capture in aluminium. This showed that proton emission occurs for around 3 % of all nuclear captured muons; Geant4 produces around 7 to 8 times more than this. The overall shape of the proton spectrum looks wrong as well. Although the AlCap result is still only preliminary, the spectrum that has been observed is much softer than that produced by standard Geant4, as shown in Fig. 4.10b.

Standard Geant4 models nuclear capture of negative muons using a Bertini cascade which was developed using incident hadrons [87]. Muon nuclear capture is thought to occur via a combination of direct capture on a proton, producing a neutron, or via an interaction with a set of clustered nucleons. The latter is typically invoked to explain proton emission. The Bertini cascade model handles negative muon capture by first handling the prompt process of muon capture on the nucleons, then cascading the resultant nucleons through the nucleus. A point within the nucleus is chosen homogeneously and then the muon interacts with either a single proton or a nucleon pair. It is not clear, at this stage, what causes the discrepancy between this model and the experimentally observed result for proton emissions.

Extending the physics processes

To resolve the issues mentioned, custom physics classes have been added to the COMET simulation. The key design goal of these classes was to allow future improvements in the experimental and theoretical inputs to be added, yet decouple the implementation from the normal Geant4 implementation so that future updates to Geant4 could easily be absorbed.

Fig. 4.11 shows the class interaction diagram for the extended physics modelling for stopped negative muons. The standard Geant4 model sets up these processes using the ‘G4MuonMinusCapture’ class, which passes concrete implementations for decay and nuclear capture into its base-class ‘G4HadronStoppingProcess’. This base-class contains three instances of a ‘G4HadronicInteraction’: one to perform the electromagnetic cascade between the atomic orbitals; another to perform bound decay; and a third to perform the nuclear capture. The ‘G4HadronStoppingProcess’ class is also used to simulate stopped negative pions, kaons, and so on, and bound decay is only considered if a valid instance of such a process has been provided. When a stopped particle is processed through this class, the electromagnetic cascade is always run first producing X-rays and Auger electrons. Then one of either bound decay or nuclear capture is chosen by asking the bound decay process whether or not it will kill the particle; if so, bound decay is considered to have taken place and the nuclear capture is not run. Default Geant4 uses nuclear capture rates based on a 1987 paper by Suzuki et al. [79] which fill in experimental blanks with a semi-empirical models, and decay rates based on a largely theoretical 1977 model by Mukhopady [?]. Fig. 3.3 was produced by extracting these parameters.

To extend the default Geant4 modelling and improve the accuracy with the improved theoretical understanding of the DIO process and measurements of muon nuclear capture, three new classes have been written which mirror the way the default Geant4 model is implemented but add more detail. These new classes are shown in Fig. 4.11 in red. Currently they only play a role if the muon stops in aluminium otherwise they invoke directly the default Geant4 model. ‘COMETMuonMinusBoundDecayOrConversion’ takes over the task of bound decay by first deciding whether to capture, decay, or convert based on rates which can be adjusted at run-time by Geant4 commands. The default rates are the normal Geant4 rates of capture and decay and a conversion rate of 10^{-15} (which is multiplied by the capture rate to get the total conversion branching ratio). If the conversion process is chosen an electron with total energy of 104.97 MeV is produced in a random direction. If decay is chosen a DIO spectrum is used to randomly generate

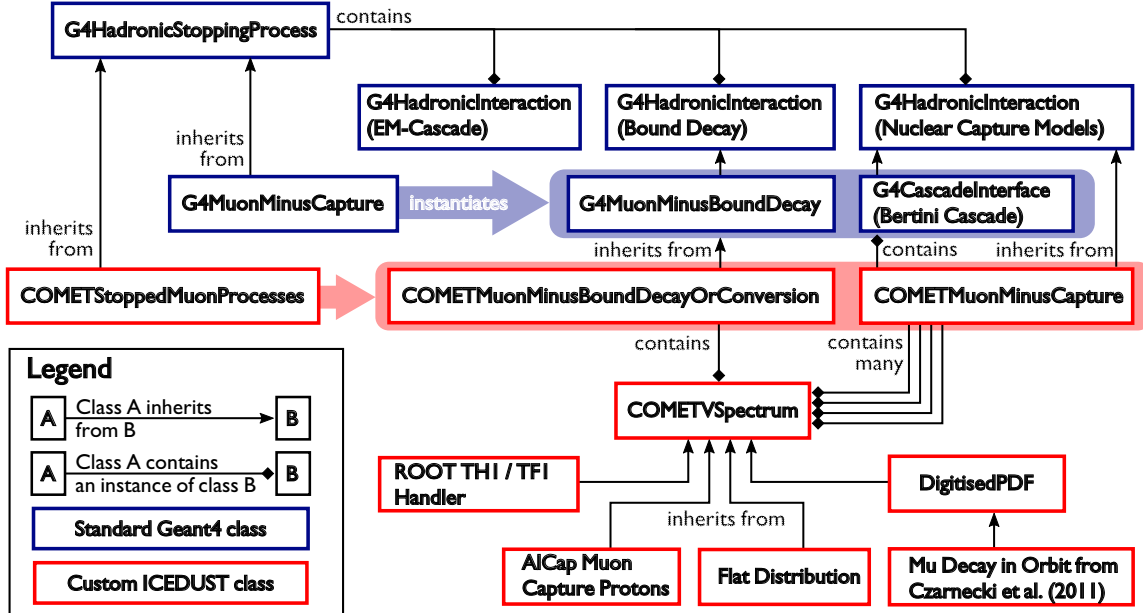


Figure 4.11.: The various classes involved in simulating the various processes of stopped negative muons. The standard Geant4 model is activated by registering ‘G4MuonMinusCapture’, which instantiates ‘G4MuonMinusBoundDecay’ and ‘G4CascadeInterface’ to run the DIO and nuclear capture respectively. To use the custom COMET muon physics, an instance of ‘COMETStoppedMuonProcess’ should be registered, which sets up ‘COMETMuonMinusBoundDecayOrConversion’ to produce the electron (and possibly neutrinos) from DIO or conversion, and ‘COMETMuonMinusCapture’ to do the nuclear capture.

an energy, which at the time of writing defaults to the 2011 Czarnecki spectrum [38], although other spectra can be specified at run-time. If neither of these processes are selected then the ‘COMETMuonMinusBoundDecayOrConversion’ class returns, leaving the muon status as alive such that the capture process takes place. At this point, control would pass to the ‘COMETMuonMinusCapture’ class, which contains an instance of the default Geant4 Bertini Cascade model to use for materials other than aluminium. Run-time controls allow the default model to be re-enabled for aluminium.

The ‘COMETMuonMinusCapture’ class contains a list of types of secondary particle which it is able to produce. For each possible secondary, both a total production rate per capture and spectrum must be supplied. When a muon captures in aluminium, firstly the default model is run. Then, for each of the secondaries produced by this, if a custom rate and spectrum have been provided for a particle of this type the secondary from the Bertini cascade is removed. Then, for each of the particles that do have custom rates and spectra, a particle is produced with the given probability and each of these particles

assigned an energy given randomly according to the selected spectrum. By using the default model first, particles for which experimental rates or spectra do not exist can still be produced in the simulation.

There are, however, some downsides to this approach. Although the remnant nucleus is not actually tracked, in principle energy conservation is not guaranteed since the custom models do not work with the default model to ensure this. In addition, the custom models cannot simulate correlations between different particle types. For example, the probability of emitting a neutron or gamma particle might be dependent on whether or not an alpha particle is emitted. Although such details cannot be included in this modelling, the impact to the outputs of the simulation are expected to be small, if not negligible, since the detector will see particles from hundreds of thousands of stopped muons per bunch, and will not look at the correlations between different particle types.

Finally, to handle the various spectra that might be added to the simulation, a special spectrum and spectrum-factory class design was added. The ‘COMETVSpectrum’ base-class was added to represent the abstract idea of a 1-dimensional spectrum. Custom spectra, such as the Czarnecki [DIO](#) spectrum or the AlCap protons from muon capture spectrum, can be included by writing a concrete instance of a spectrum, derived from ‘COMETVSpectrum’. Custom physics processes can use these spectra as they like, and since the ‘COMETSpectrumFactory’ class is able to produce concrete spectra when given a string with the name of the desired spectrum, the custom physics models can easily have different spectra selected by run-time commands. In addition, a new primary particle generator has been added which allows the momentum or energy of a particle to be set according to a named spectrum, which will be identical to the spectrum used in the tracking process. This makes it easy to run specific acceptance studies and also reduces the effort needed to add a new physics model since one spectrum can be written and immediately used by both the primary event generators and the tracking physics.

Chapter 5.

COMET Phase-II: Optimisation

The last study into the sensitivity of COMET Phase-II was performed in 2009 [35], before the staged approach and Phase-I design had even been considered. That study found that a SES of 2.6×10^{-17} could be achieved in 2×10^7 seconds of running with a total expected background count rate of fewer than 0.34 events over the entire run period. Since then, the collaboration’s focus has shifted to design and R&D for Phase-I and no further studies have been made of the Phase-II design.

The purpose of this chapter is to make use of the updates in the fieldmap calculation, the geometry handling, and physics modelling to revisit the design of Phase-II and demonstrate that it can do at least as well as the previous 2009 design. In addition to updates in the simulation some aspects of the actual design have been refined and fixed alongside Phase-I preparation such as the experiment hall and the coils and cold-mass of the first stages of the muon beamline. The aspects of the experiment that remain open for optimisation are shown in Table 5.1.

As an initial configuration, much of the design from the 2009 study will be used, with updates included for the areas of the experiment that have since been refined by the Phase-I design.

5.1. Optimisation Strategy

Some 32 parameters are listed in Table 5.1 and yet this number alone does not describe the full challenge of optimising the Phase-II design since many of these parameters will be correlated. For example, it would seem natural for correlations to exist between the muon

Region for optimisation	Approx. No. of parameters
Production target dimensions and location	$3 + 3$
Torus1 dipole field strength	1
Torus2 dipole field strength	1
Muon beam collimator shapes, position, and material	$3 + 1 + 1$
Stopping target shape and location	$4 + 3$
Beam blocker position, form, and material	$3 + 3 + 1$
Electron spectrometer dipole field strength	1
DIO blockers in the spectrometer	4
Approx. total number of parameters	32

Table 5.1.: The list of parameters that can be optimised and an estimate for the number of parameters that this represents. In the case of the target, beam blocker and collimator shapes the number of parameters is only approximate; crudely speaking there is at least a width, length and height but in principle one could have a very irregular shape that cannot be parametrised by only three numbers, for example shapes that change as a function of distance along the beamline.

beam collimator(s), the stopping target and the beam blocker, since all involve removing or stopping muons and other particles in the beam. Other less intuitive correlations might also exist and a complete optimisation should be able to include the impact of these as well.

A complete optimisation study then can be considered a scan through a parameter space with at least 32 dimensions. A brute force search of such a space would be nightmarishly slow and require an enormous amount of computing power. Machine learning algorithms or intelligent scanning techniques might be able to tackle such a problem, and perhaps in the future these methods will be used. In the meantime however I am forced to use the technique of 'physicists intuition' to approach the problem, whereby some parameters are assumed uncorrelated whilst others are disregarded on the expectation that their impact be small.

The goal of this chapter therefore is not only to optimise the experiment but also to evaluate the correlations. Ideally this will also identify which parameters are the most strongly correlated, which would help make future optimisation studies more efficient. The outputs of this optimisation should not be considered as final but should instead be treated as a baseline from which more intelligent approaches or physicists can improve.

5.2. Production Target Optimisation

In the Phase-II Conceptual Design Report ([CDR](#)), the production target is given as being 16 cm in length and 4 mm in radius [35]. Since then, there have been changes to the magnetic field in this region, as well as the lengths and locations of solenoids, shielding and beam-pipe, and the proton beam. Previous studies have looked at comparing the tungsten target proposed for Phase-II to other materials [47], and also drawn a comparison between MARS [72], Geant4 [12] and the limited data available.

The goal in this study is to optimise the production target with the up-to-date configurations. This study aims to maximise the total muon and pion yield below 80 MeV at the entrance to the Torus1 bent solenoid, by varying the radius and length of the production target.

5.2.1. Configuration

Table 5.3 gives the key parameters for the beam input and other aspects of this simulation. The location and orientation of the target were held fixed, since the axis of the proton beamline is fixed to intercept the muon beam axis at a given point. Once a more realistic proton beam becomes available, the location and direction of the production target would also benefit from optimisation however. During the scan over length, the back face of the target was kept 8 cm away from the muon beam since the radiation shielding has previously been optimised, and since beyond this the magnetic field will no longer be able to capture the pions and muons produced.

It must be noted that at this point in time there is an appreciable uncertainty in the proton beam profile and position. In particular, whilst the upstream proton beamline has been delivered, the effect of the magnetic field and necessary dipole and quadrupole magnets is still being studied by the proton beamline group. The beam profile is given in the Phase-I Technical Design Report ([TDR](#)) as having a Gaussian position profile and energy distribution [80], although no divergence or location is specified. The effect of the proton beam distribution on the overall sensitivity shall therefore have to be considered in future studies.

Protons in the simulation originated from a plane (distributed as a two dimensional Gaussian across this surface) but since there is some scope to tune the proton beam's position, the input particle plane was moved to remain 1 cm away from the front surface

Proton Beam

Horizontal spread, σ_x	5.8 mm
Vertical spread, σ_y	2.9 mm
Mean energy, μ_E	8.01 GeV
Energy spread, σ_E	0.135 MeV

Target

Material	Tungsten
Orientation	10° between target's principal axis and the muon beam axis.
Location	Back face fixed 8 cm away from muon beam axis.
Length	16 cm in CDR. Varied in steps of 4 cm from 4 to 32 cm.
Radius	4 mm in CDR. Varied from 2 to 10 cm in steps of 2 cm and from 10 to 30 cm in steps of 4 cm.

Software configuration

Packages	heads/1512w51_develop(3a0ee59)_3_UNCOMMITTED_
Externals	heads/Patch_Geant4-G4MultiLevelLocator(11fc8f0)
Fieldmap	160104 CHECK:

Sample Sizes

Length scan	3×10^5 POT (30 runs of 1×10^4)
Radius scan	4.9×10^5 POT (49 runs of 1×10^4)
Final scan	

Table 5.2.: *CHECK: Move this table into an appendix listing the simulation configurations for every section described here.* Key parameters in the configuration of the Production Target optimisation.

of the target. Since the aim is to maximise the muon and pion yield by varying only the length and radius, shifting the proton beam input plane in this way removes any variation of target acceptance due to divergences of the proton beam in the field before the target.

5.2.2. Length Scan

Different length targets were simulated with 3×10^5 POT per length. The target length was varied in steps of 4 cm from 4 to 32 cm, whilst the target radius was held fixed at the CDR value of 4 mm.

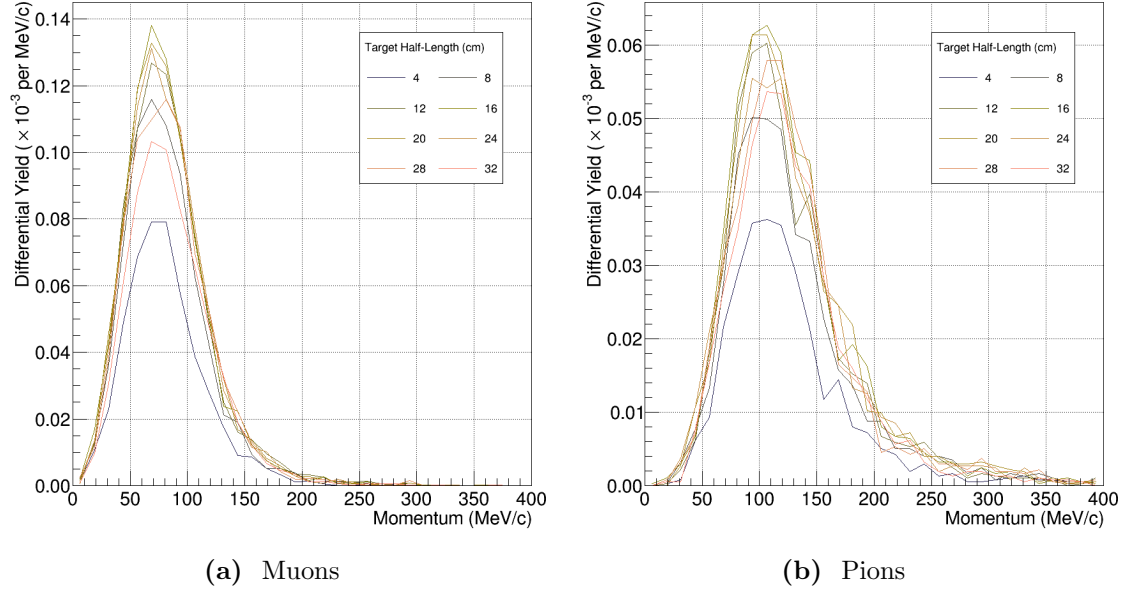


Figure 5.1.: Change to momentum distributions at the entrance to the first 90 degrees of the bent muon beam solenoid for different target lengths. Target length is given as half-length which is the Geant4 convention.

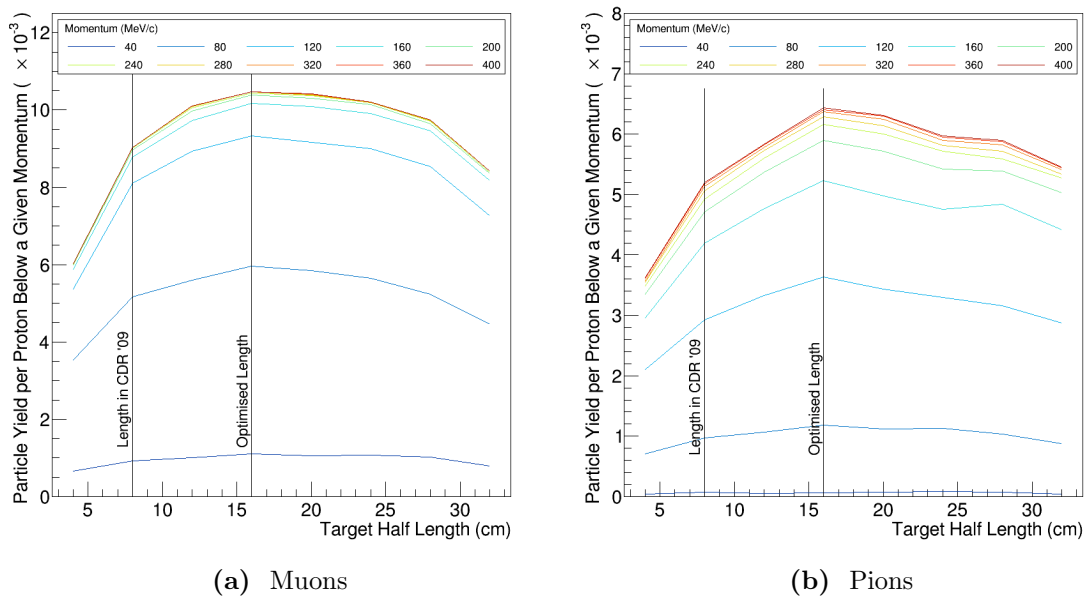


Figure 5.2.: Integrated muon and pion yields up to a certain momentum at the entrance to the first 90 degrees of the bent muon beam solenoid as a function of target length.

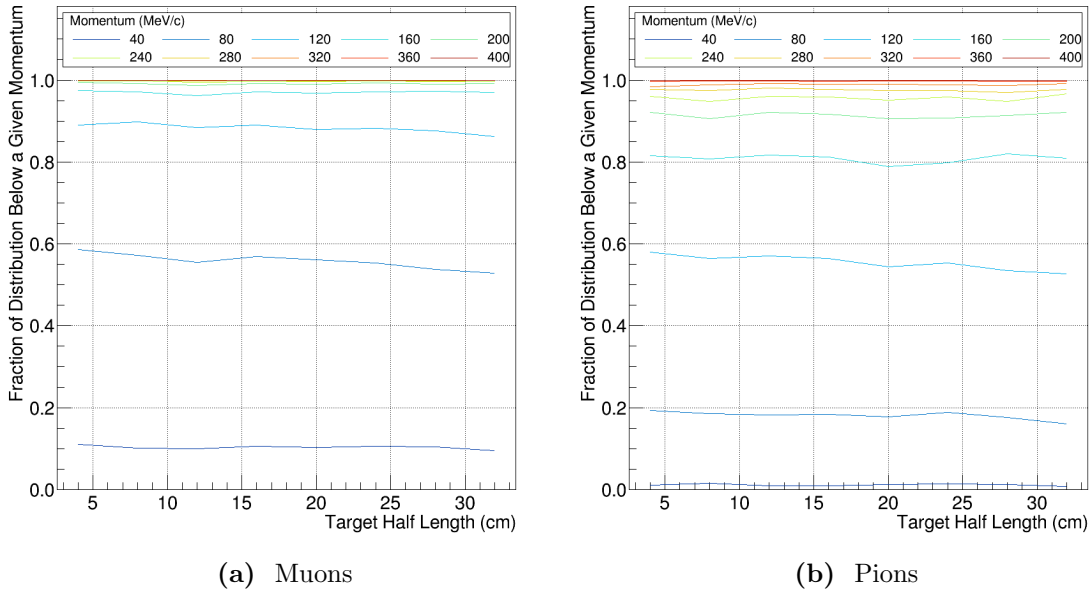


Figure 5.3.: Change in the momentum distribution of muons and pions at the entrance to the first 90 degrees of the bent muon beam solenoid as a function of target length.

Fig. 5.1 shows the momentum distributions of pions and muons for different target lengths, which are given as half-length following the Geant4 convention. Fig. 5.2 then shows these distributions integrated up to different momenta. From these plots it can be seen that for both muons and pions, the optimum target length occurs around a total length of 32 cm.

Additionally it can be seen from Fig. 5.3 that the shape of the momentum distributions changes only weakly as a function of the target length. These plots were produced by normalising the integrated momentum contours of Fig. 5.2 to the total integral below 400 MeV. As a result, it is possible that the actual shape variation is even weaker than apparent here, since in the present sample size, the high momentum tail is not well sampled at small target lengths, such that a skew in the normalisation might occur.

5.2.3. Radius scan

In parallel to the length optimisation scan, different radii targets were also simulated. Targets with radii of 2, 4, 6, 8, 10, 14, 18, 22, 26, and 30 mm were tested. The target length was held at the CDR value of 16 cm in total.

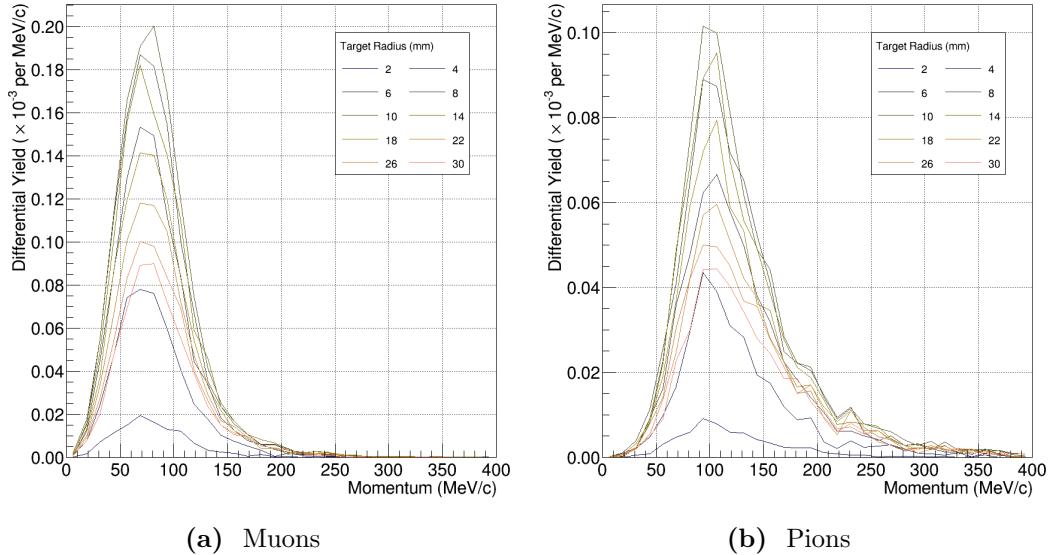


Figure 5.4.: Change to momentum distributions at the entrance to the first 90 degrees of the bent muon beam solenoid for different target radii.

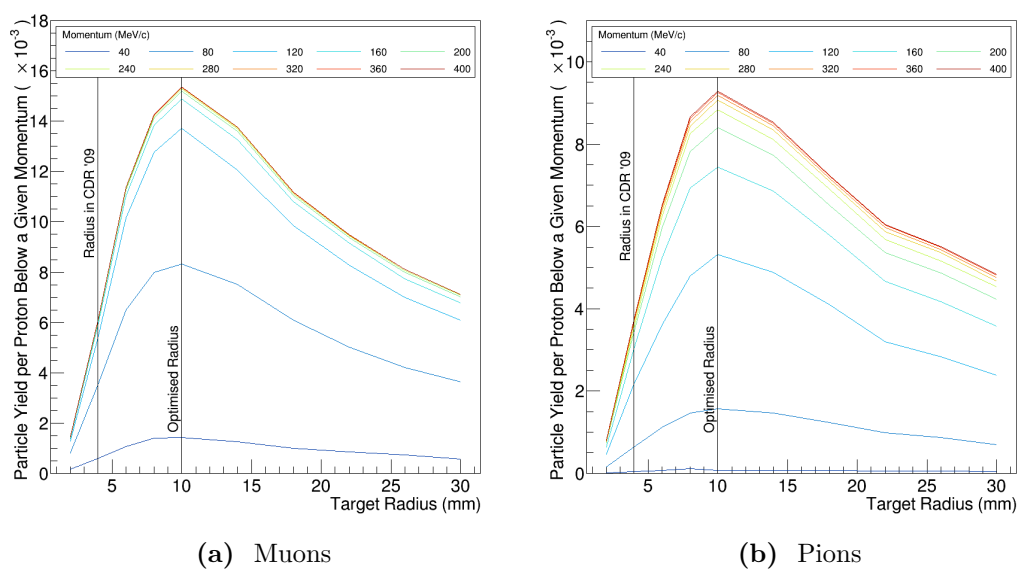


Figure 5.5.: Integrated muon and pion yields up to a certain momentum at the entrance to the first 90 degrees of the bent muon beam solenoid as a function of target radius.

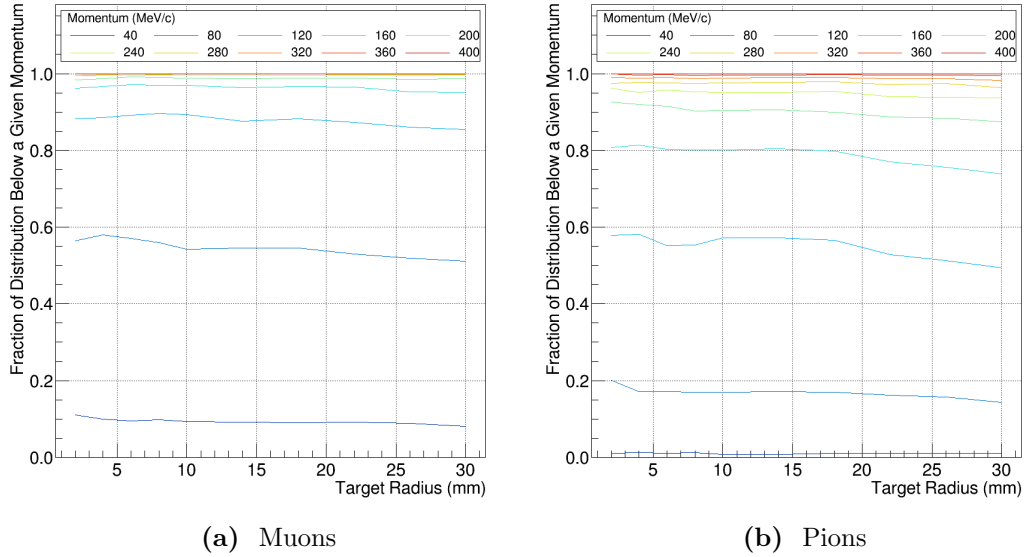


Figure 5.6.: Change in the momentum distribution of muons and pions at the entrance to the first 90 degrees of the bent muon beam solenoid as a function of target radius.

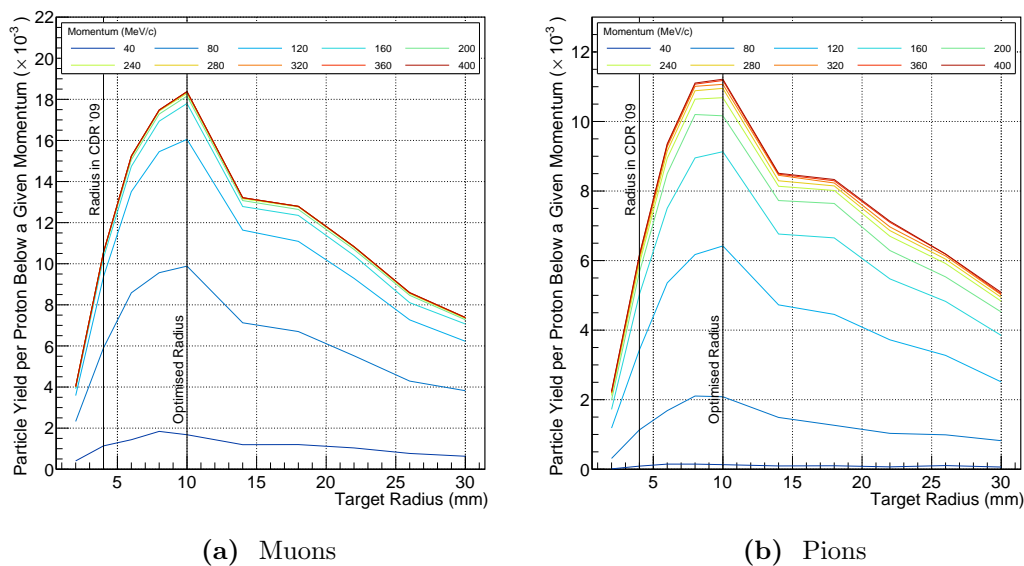


Figure 5.7.: Variation in muon and pion yields as a function of target radius when the total target length is set to the optimised value of 32 cm. Despite the longer target length the optimal radius is still 1 cm.

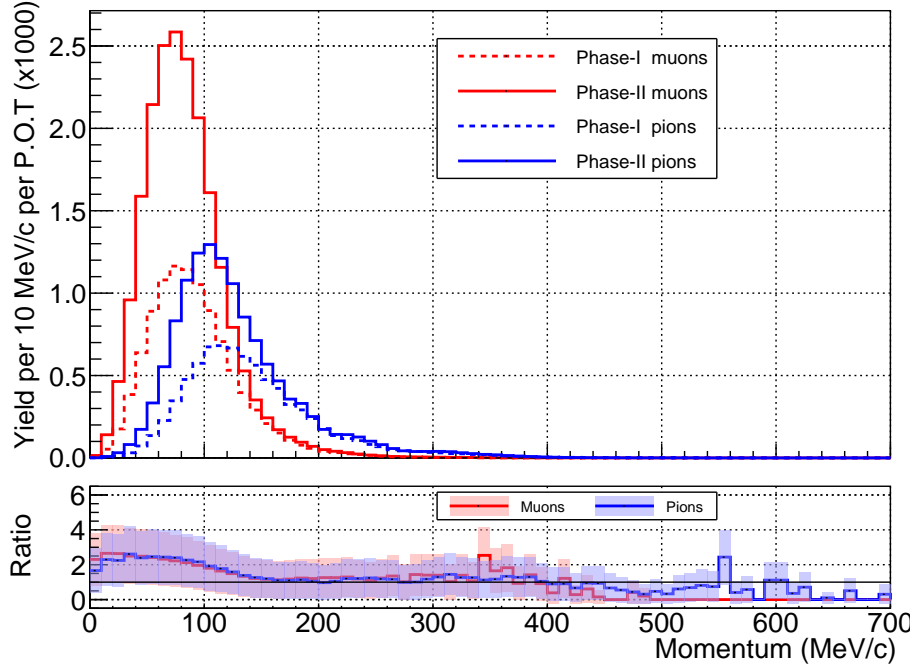


Figure 5.8.: Comparison of the muon and pion yields per POT for Phase-I and Phase-II. The difference arises from the change of target material between the phases.

The results of these scans can be seen in Fig. 5.4 and Fig. 5.5, where it can be seen that a maximum in both the muon and pion yields at the entrance to the Torus1 section is achieved at a radius of about 10 mm. As in the length scan, the variation in the shape of the momentum distributions is rather weak as a function of target radius.

5.2.4. Final Result

Since the length and radius scan were performed in parallel, a final cross check was performed where the optimal radius was confirmed at the optimised target length. The integrated spectrum is shown in Fig. 5.7 where it can be seen that the optimum radius once the target length is increased to 32 cm is still 10 mm.

Fig. 5.8 shows the total muon and pion yields at the entrance to the Torus1 for the final optimised Phase-II target and compares this to the optimised Phase-I target design. The increased yield in the low momentum range is due to the heavier target nucleus which produces more low-momentum pions in the backwards direction. Since only muons below around 50 MeV/c tend to stop in the target, this increase in the low momentum yield amounts to a factor 2 or so gain in the stopping muon rate per POT.

CHECK: Fill this table in properly CHECK: Better yet make this and Table ?? into an appendix / list of simulations and configurations

Pions and muons from Prod. Tgt. simulation

Software configuration

Packages	---
----------	-----

Externals	---
-----------	-----

Fieldmap	160104 CHECK: with additional scale factors applied to Torus dipole field
----------	---

Sample Sizes

Final scan	
------------	--

Table 5.3.: Key parameters in the configuration of the muon beamline dipole field optimisation.

5.3. Dipole Strengths of the Muon Beamline

The full 180° bent solenoid that makes up the bulk of the muon transport beam line is actually broken down into two 90° pieces – Torus1 and Torus2 (also known as TS2 and TS4 by the magnet group). Each of these sections has its own dipole field which need not provide the same dipole field strength. The Torus1 section has been built already and was previously optimised for both Phase-I [80] and Phase-II [35]. The dipole coils that it contains are designed to produce a dipole field of 0.055 T. By running a lower current through these coils one could reduce the Torus1 dipole field without too much effort. However if Phase-II should require a greater dipole field strength for this region that might be trickier since it could require additional windings to be inserted – this would not be impossible but might costly.

5.3.1. Large-sample Production Target Simulation

Before the muon beam section could be optimised, a large set of **POT** events were produced transporting all particles up to the entrance of the muon beam section. In total, 2.3×10^8 POT were simulated through this stage, equivalent to about 1.5 bunches at Phase-II. The production target used the optimised geometry from the previous section. All particles that hit the surface of the Torus1 container volume were read out for later re-use in a way that ensured double-counting of particles could not occur. In addition, particles entering the proton beam dump were also saved if later simulations wished to study their impacts.

5.3.2. The Optimised Dipole Field Strengths

The figure-of-merit for this optimisation is the muon stopping rate, which will be maximised at the optimal field configuration. To identify such a configuration, a 2D-grid scan was done where the Torus1 and Torus2 dipole fields were simultaneously varied. Varying the field strength was done by applying a scale factor to the fieldmaps for each 90° section described in 4.3.2. These scale factors were varied in steps of 0.125 (equivalent to 6.875 mT) and for each point muons and pions from 8×10^6 POT were transported to the stopping target. The stopping rate for each combination of scale factors was then assessed.

The muon stopping rate as a function of the two dipole field strengths are shown in Fig. 5.9. A scale factor of 1 on the x-axis means no change to the current Phase-I design and since there is little improvement by moving to larger values for Torus1 the optimal scale factors are chosen to be 1 and 0.5 for the Torus1 and TTorus2 respectively. This translates to dipole field strengths of 0.055 and 0.0275 T respectively.

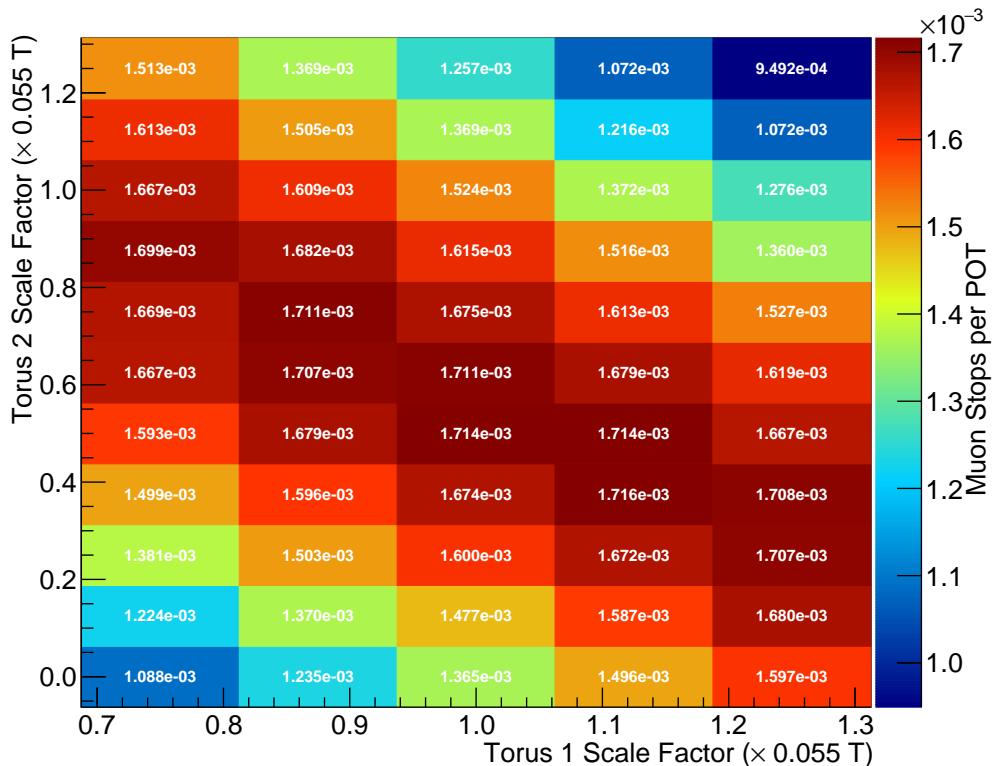


Figure 5.9.: Muon stopping rate as a function of the two dipole field strengths (given relative to the Phase-I design specification). A clear anti-correlation is visible which is discussed in the text.

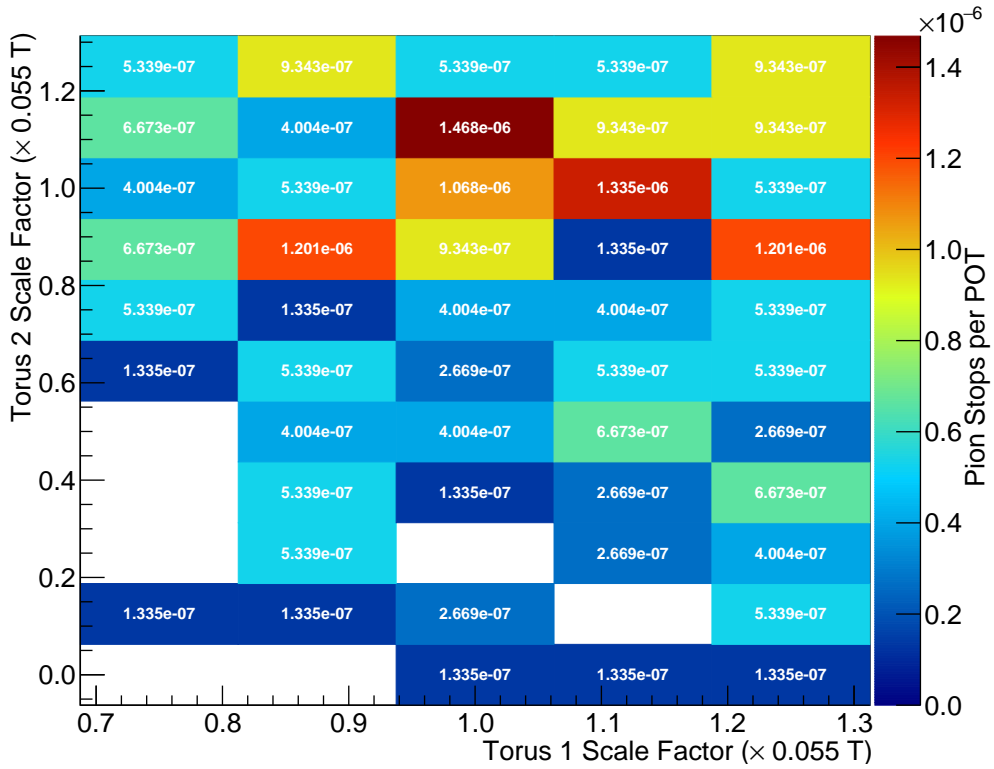


Figure 5.10.: Pion stopping rate as a function of the two dipole field strengths (given relative to the Phase-I design specification). At the level of statistics used to generate each point, no clear trend is obvious. Empty squares are those where no pions stopped in the run.

Also striking from Fig. 5.9 is the anti-correlation between the two dipole field strengths. Roughly speaking the sum of the optimal dipole field values is constant, i.e. $B_1^{\text{optimal}} + B_2^{\text{optimal}} = \text{const}$. Although this was not previously foreseen, such a correlation can be understood accordingly. The stopping target geometry and position is held fixed in this parameter scan, which essentially fixes the upper momentum of muons that can stop in the target. The drift of a particle due to the dipole field is proportional only to the distance travelled in that dipole field and the dipole field strength, and does not depend on the particle's momentum. This means that the total drift due to the Torus1 and Torus2 dipole components is proportional to the weighted sum of the two dipole field strengths, where the weight is the distance travelled through each of the two sections. Since each section is the same length, the time for a particle to pass through Torus1 will be roughly the same as the time in Torus2 so that the weights would be roughly equal. This leads to the total drift being proportional to the sum of the two dipole fields. Since the production target (as the source of muons) and stopping target (as the muons'

destination) are at a fixed height with respect to one another the optimal vertical drift is also fixed so that the sum of the dipole field strengths should also be roughly fixed.

With that said, the Torus1 section has a higher pion flux which causes some assymetry between the two sections. Keeping more pions on-axis in the Torus1 section means that more muons will enter the Torus2 section from those pions that have decayed. But since the pion momentum distribution is slightly higher than the muon distribution keeping pions on axis requires a larger dipole field strength. This could explain the slight assymetry where the muon stopping rate appears slightly larger if Torus1's field is larger than that of Torus2.

It is also interesting to consider the pion stopping rate as a function of the dipole field strengths. However, as can been from Fig. 5.10 the stopping rate is close to the level of POT events used in the simulation so that the plot is dominated by statistical fluctuations.

5.4. Electron Spectrometer's Dipole

The next element in the beamline after the muon transport solenoids will be the stopping target. However, in order to study the impact of changing the stopping target parameters one will need to look at the impact on the signal acceptance into the detector. To study that requires the components of the beamline intermediate to the target and the detector be optimised, namely the electron spectrometer. The key free parameter in this section is the dipole field strength along the spectrometer. The solenoidal field and solenoid aperture could also be optimised in principle, but these are considered beyond the scope of this study at this point and so the CDR values are held fixed here. The point of this section is to establish the optimal dipole field strength given fixed target parameters which will then be studied separately together with the stability of the dipole field tune checked.

5.4.1. Method and Potential Short-comings

To study the effect of the dipole field on signal acceptance, a realistic muon stopping distribution in the target was produced by transporting muons from the production target simulation through to the stopping target. Signal electrons were then injected at

the target with the realistic stopping distribution and propagated through the beamline to the detector with different dipole field strengths.

A non-trivial short-coming of the current study is that the dipole field along the spectrometer is poorly modelled – no realistic coil simulation exists, unlike for the bent muon transport beamlines. As a result, a perfectly uniform dipole field is assumed with a sharp switch on and off at the entrance and exit of the spectrometer. The impact that this has on the final result is not clear: one might expect it to be small given the relative strengths of the dipole and solenoidal fields and overall it is the integrated field that tends to matter. However, the sharp switch-on of the field at the entrance and exit of the spectrometer is clearly not physical. Given that the gradient introduced in the field by bending is present before the actual entrance and exit of the spectrometer (as a fringe field), some drift can be anticipated in this region. A realistic dipole field with a realistic fringe field might overcome some of this drift however, so that the uniform field used here will most likely not capture this effect. Nevertheless, given the absence of a realistic dipole field and scope of this study, the uniform one is the only real option at this point.

5.4.2. Results

Fig. 5.11 shows the projection of electron trajectories to the beam axis coordinate system for three different dipole field values. The potency of this approach is clear from these plots; the tuneable dipole fields allow the momentum of electrons which remain on-axis to be accurately controlled (during run-time), which will benefit systematic and calibration studies that wish to study the DIO spectrum at a lower energy. Fig. 5.12 then collects these plots with other dipole field strengths, plotting the mean height for all simulated electrons against the distance along the beam axis. From this plot it can be seen how a dipole field of about 0.18 T appears optimal to keep the signal electrons on axis.

The probability for electrons to reach a given point in the beamline is shown in Fig. 5.13, and indeed from this it can be seen that to maximize the probability of an electron reaching the detector a dipole of around 0.18 T is desirable. The behaviour of the low dipole field values (0 to 0.08 T) in this plot was not expected, but it is believed this is an artifact of the way this plot is made, coupled with a degree of mirroring at the entrance to the spectrometer which is enhanced as the dipole field strength increases. If correct, a realistic dipole field calculation would be important to quantify and confirm this behaviour.

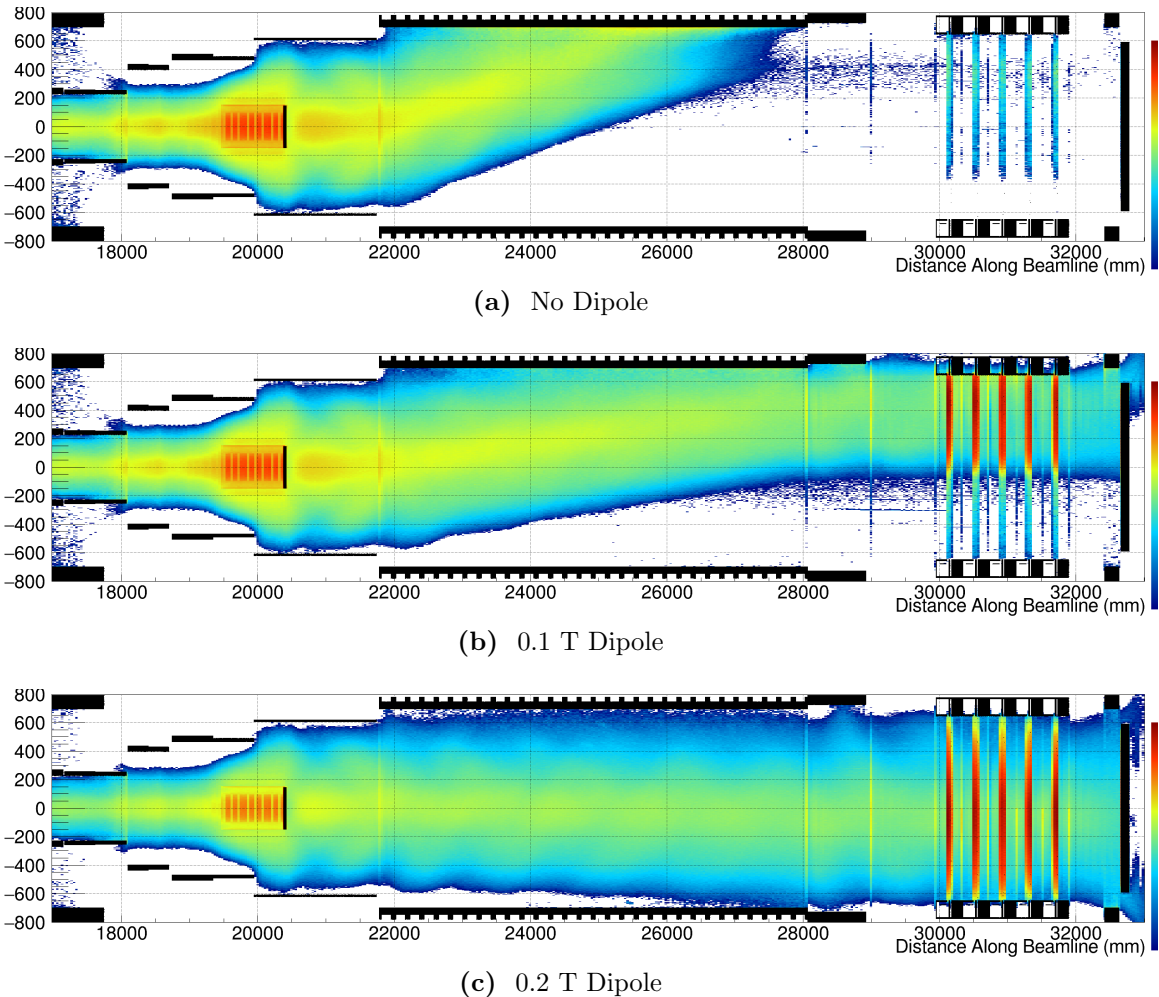


Figure 5.11.: The heights of signal electrons for different dipole field values.

Finally, to confirm the optimal dipole field strength the true geometric acceptance of the detector system is checked as a function of the dipole field strength, which is shown in Fig. 5.14. An electron is considered to have been geometrically accepted by the detector in this simulation if it produces at least one hit in the detector system. In principle this could be in any straw plane, but in practice this is almost always in the first layer of straws. Since this is a different way to analyze the acceptance compared to the survival probability it would not suffer to the artifact seen for low dipole field values in Fig. 5.13. Nonetheless, Fig. 5.14 confirms that the optimal dipole field strength is very close to 0.18 T.

A second important conclusion can be drawn from the fact that the dependence on the dipole field strength is relatively weak around the optimal value of 0.18 T. A change

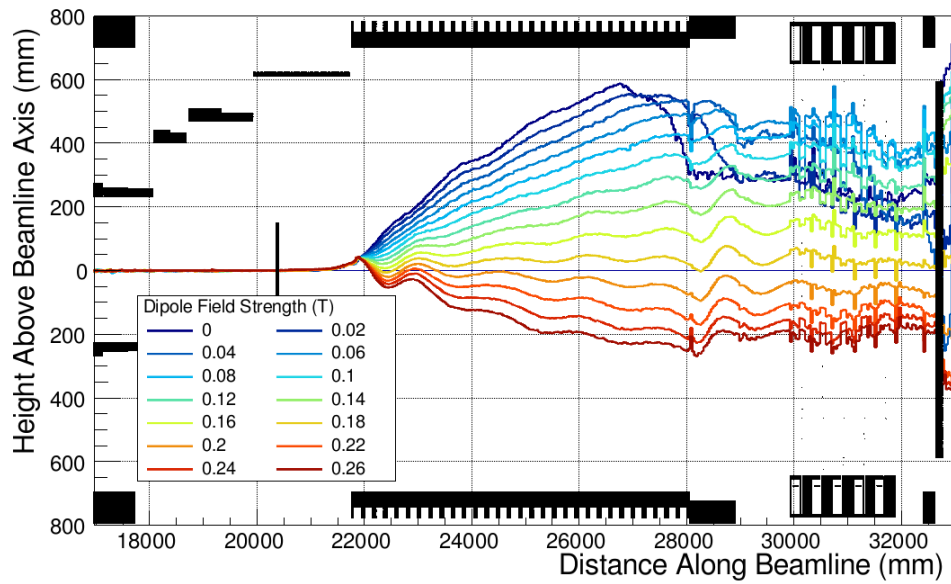


Figure 5.12.: Mean height of signal electrons for different values of the dipole field strength.

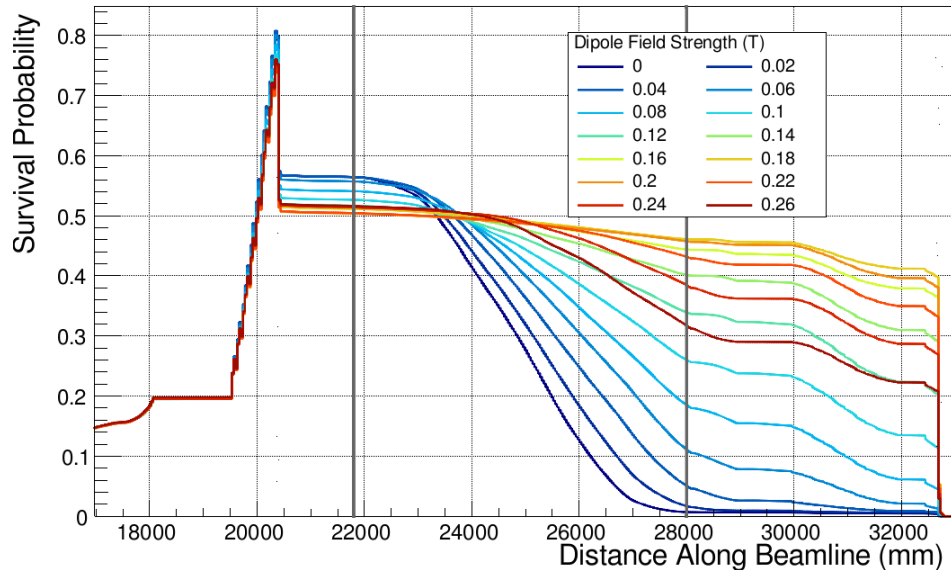


Figure 5.13.: Survival probability for signal electrons as a function of the distance along the beamline for different values of the electron spectrometer's dipole field strengths.

of about 10% in the dipole field strength only reduces the signal acceptance by about 3% whilst a change of about 5% would see a reduction of only about 0.7%.

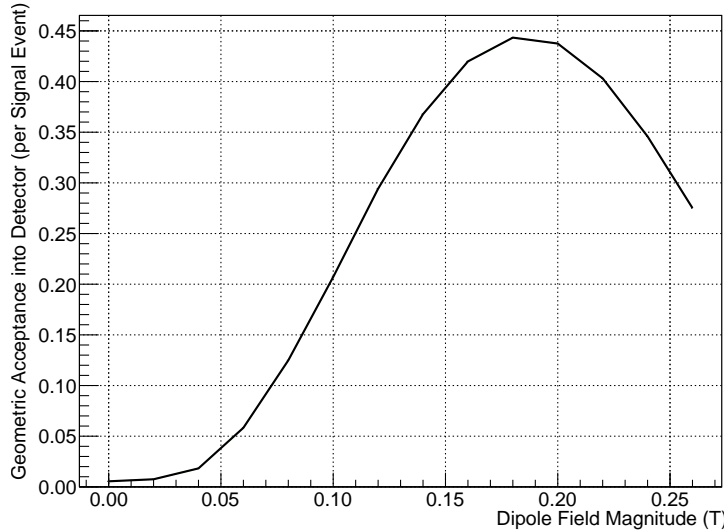


Figure 5.14.: Geometric acceptance into the StrECAL detector as a function of the dipole field strength over the electron spectrometer.

5.5. Stopping Target Position

The final aspect to be studied with regards to maximizing the signal sensitivity is the stopping target. In principle there are many parameters related to the stopping target such as the location, disk shape (profile and thickness), and disk spacing. In addition the beam blocker should be considered in parallel with the stopping target since it sits so close to the target itself and can be expected to have a big impact on the signal acceptance. However, this leaves far too many parameters to be considered all at once.

Since the field around the target tapers sharply various competing factors must be considered. For example, prior to the stopping target region the muon beam is transported through a 3 T solenoidal field. The magnetic field in the target region, however, tapers to about 1 T, which would cause the envelope of the muon beam to grow. Moving the stopping target downstream would mean that the muon beam arrives with a larger aperture, and would therefore prefer a larger stopping target or else fewer muons will actually hit the target. On the other hand, from the perspective of signal acceptance, the tapered field can be used to mirror signal electrons that are initially produced heading upstream therefore increasing the signal acceptance. Moving the target further upstream then will reduce this effect as the difference between the magnetic field strengths at the exit of the bent muon transport solenoid and at the stopping target is reduced.

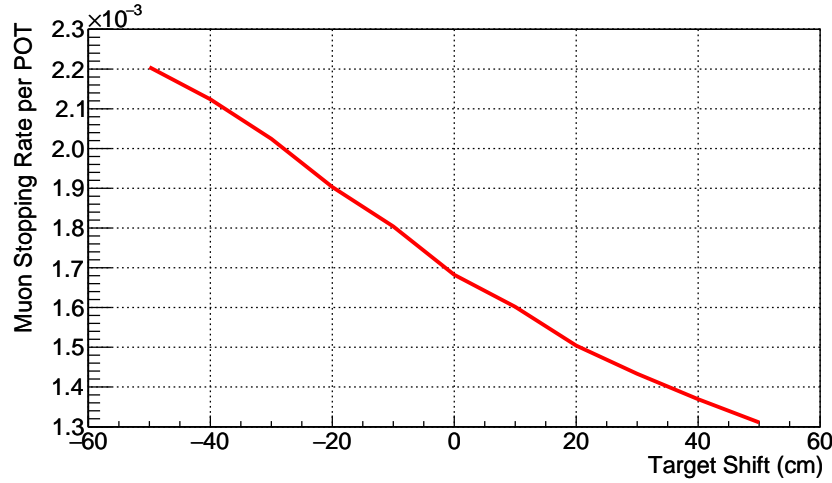


Figure 5.15.: Muon stopping rate per POT for different target positions. The linear behaviour arises from the reduced field strength and fixed target radius such that fewer muons impact the target as it is moved downstream.

Given this and the need to reduce the number of parameters inspected, the target and beam blocker design was held fixed in this study and only the position was changed by moving the target upstream and downstream by ± 50 cm with respect to the nominal target location as given in the CDR [35]. Given that the target disks will occupy in total about 1 m, a shift of 50 cm corresponds to half the target length. In each different position of the stopping target, as for the spectrometer dipole optimisation, a realistic stopping distribution was produced by running muons from the large-scale production target simulation through to the target. This stopping distribution was then re-used to introduce signal electrons accordingly. Additionally, low momentum electrons were also studied in order to study the impact of target position on the height of both signal and low-energy electrons as they pass through the spectrometer. This is important both to check the correlation of the dipole field tune with the stopping target position, but also how the subsequent DIO blocker height optimisation will correlate the target position.

Fig. 5.15 shows how the rate of muon stops per POT is affected by changing the position of the stopping target. The relationship is roughly linear, dropping from around 2.2×10^{-3} muon stops per POT when the target is shifted upstream by 50 cm to about 1.3×10^{-3} muon stops per POT if the target is shifted 50 cm in the other direction. This relationship is as expected given the fixed radius of the target and the growth of the muon beam aperture arising from the reduction in the field strength.

In Fig. 5.16 one can see the way the electron acceptance changes for different target positions. Acceptance here is defined as producing at least one hit in the detector and

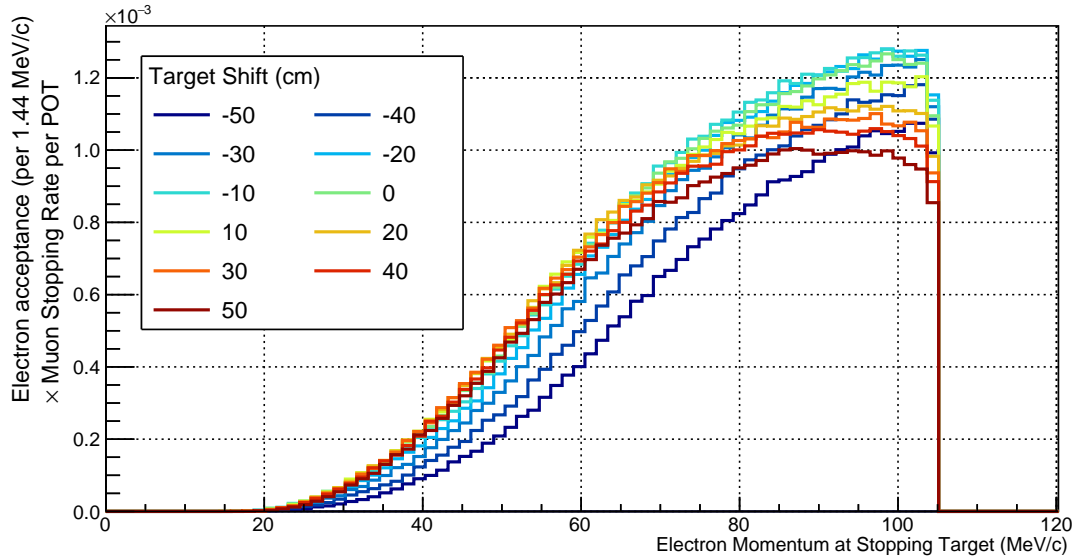


Figure 5.16.: The momentum dependence of the electron acceptance into the detector for different target positions. The spectrum for each target position is normalised to the muon stopping rate for that position, such that each The linear behaviour arises from the reduced field strength and fixed target radius such that fewer muons impact the target as it is moved downstream.

the momentum shown is the momentum at the target, which is not necessarily the same as the momentum at which the electron is observed. Each histogram in Fig. 5.16 is normalised to the number of primary electrons introduced at the target per MeV/c and then scaled to the muon stopping rate. This normalisation makes the value of each curve proportional to the sensitivity of the experiment to different momentum electrons, up to factors such as analysis cuts like timing and reconstruction quality.

Since the parameter we wish to optimise here is the location of the stopping target, Fig. 5.17a represents the same data as in Fig. 5.16 but with each line representing the content of a different $5 \text{ MeV}/\text{c}$ bin as a function of the target position. For signal, it is the $105 \text{ MeV}/\text{c}$ line (dark burgundy) that is most important and it can be seen that this is optimised for shifts upstream of the nominal position from between 10 and 20 cm. It is also interesting to note that the acceptance of lower energy electrons is relatively decreased as the target is moved upstream, as can be seen in Fig. 5.17b. This could be useful as a way to suppress hit rate from DIO electrons later.

Whilst we do not intend to optimise the beam blocker at this point, to check the impact that it has on the optimisation of the target position simulations were performed where the blocker was completely removed. Fig. 5.18 shows the product of the stopping rate and electron acceptance when the blocker is removed. From this the trend is much

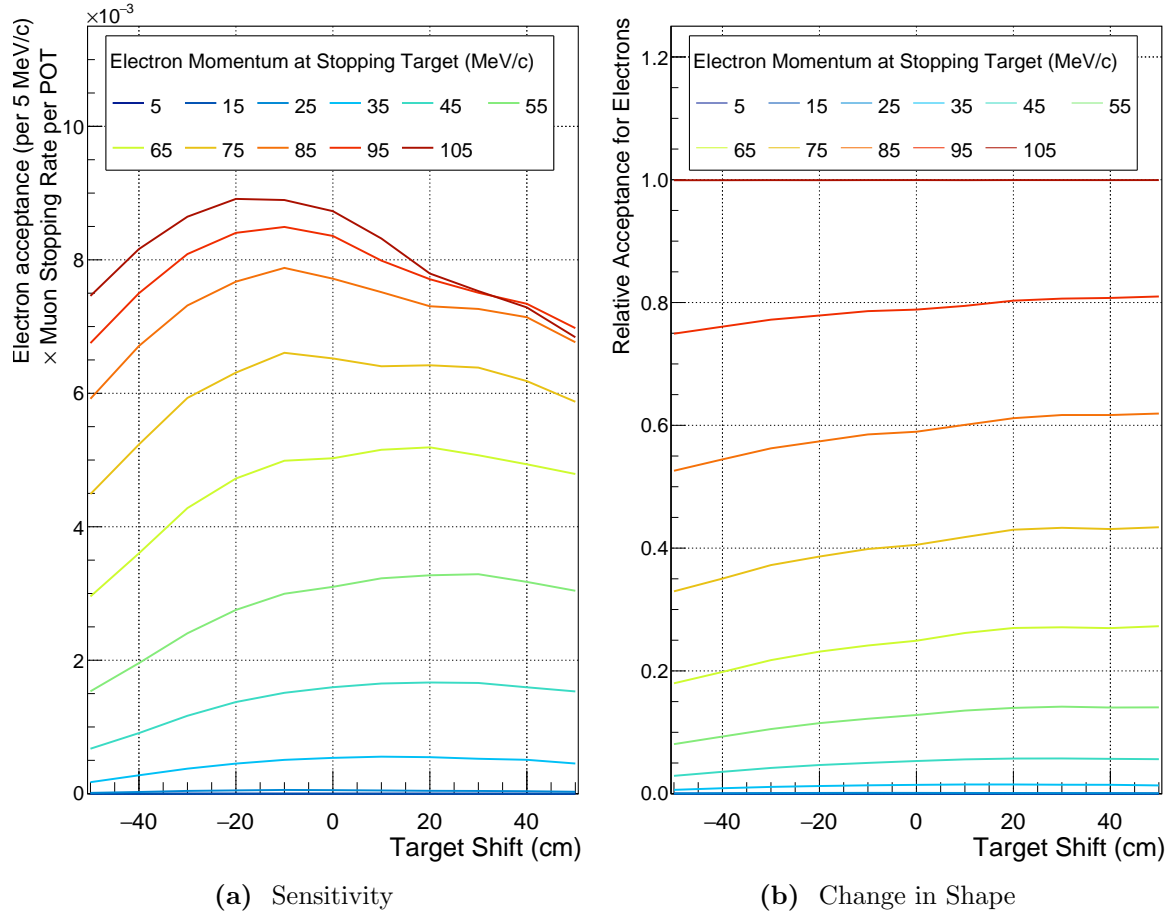


Figure 5.17.: (a) The variation in sensitivity (acceptance \times stopping rate) to electrons with different momenta as a function of the target position with respect to the nominal location. The darkest red line towards the top of the plot represents the sensitivity to signal, and it is that line that should therefore be maximised. (b) The change in the shape of the acceptance vs. momentum spectrum as a function of the stopping target location.

cleaner, electrons below 70 MeV/c are suppressed as you move the target upstream whereas the high energy electron acceptance increased.

Finally the relationship between the stopping target position and the mean height of electrons through the spectrometer is demonstrated in Fig. 5.19. Each plot shows the mean heights for electrons with a given momentum for different stopping target positions and it is clear that there is some correlation between the mean height and the position of the stopping target. For this reason, a more complete optimisation should consider optimising the two parameters simultaneously. Nonetheless the change is not particularly large, only about a few cm difference by the end of the spectrometer for signal electrons.

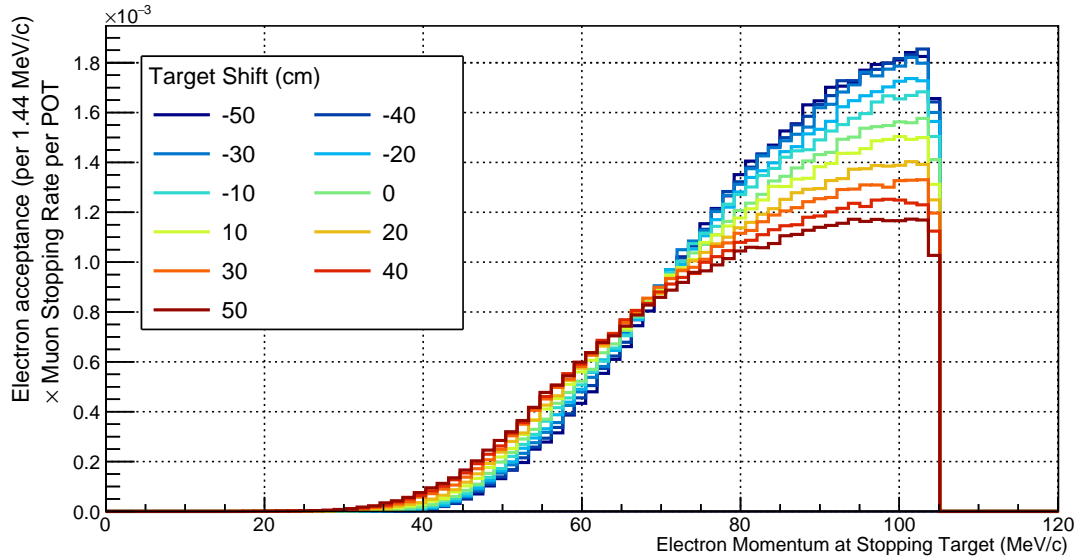


Figure 5.18.: The momentum dependence of the electron acceptance into the detector for different target positions when the beam blocker is removed.

This correlation is also likely related to the way the acceptance changes for different target positions when the beam blocker is removed.

The second striking feature from the plots in Fig. 5.19 is the way the mean height acquires a strong sinusoidal component for large target shifts upstream. This suggests that when the target is shifted upstream the electrons passing the entrance to the spectrometer tend to have a particular value for the pitch and phase angles of the trajectories. Several separate mechanisms could produce this effect. Firstly the acceptance around the target itself could acquire a stronger preference for certain pitch and phase angles when the target is moved upstream. Secondly, since the stopping target disks will see more of the muon beam upstream, the muon stopping distribution could become less homogenous. Whilst electrons are produced isotropically path with less target material along them will tend to accept outgoing electrons more readily such that if more muons stop at one side of the target than the other a dependence on pitch and phase could arise.

Clearly then the stopping target region is a very complicated area; even though this study has focussed on a single parameter – the position of the target itself – it is clear that this correlates to many other variables. This is a region in the experiment most ripe for further optimisation then, and indeed appendix C shows some of the first steps that have made in this direction since the optimisation described here was completed. Unfortunately, at the time this work was carried out an error in the normalisation of these plots lead to the conclusion that the optimal shift was between 0 and 10 cm upstream.

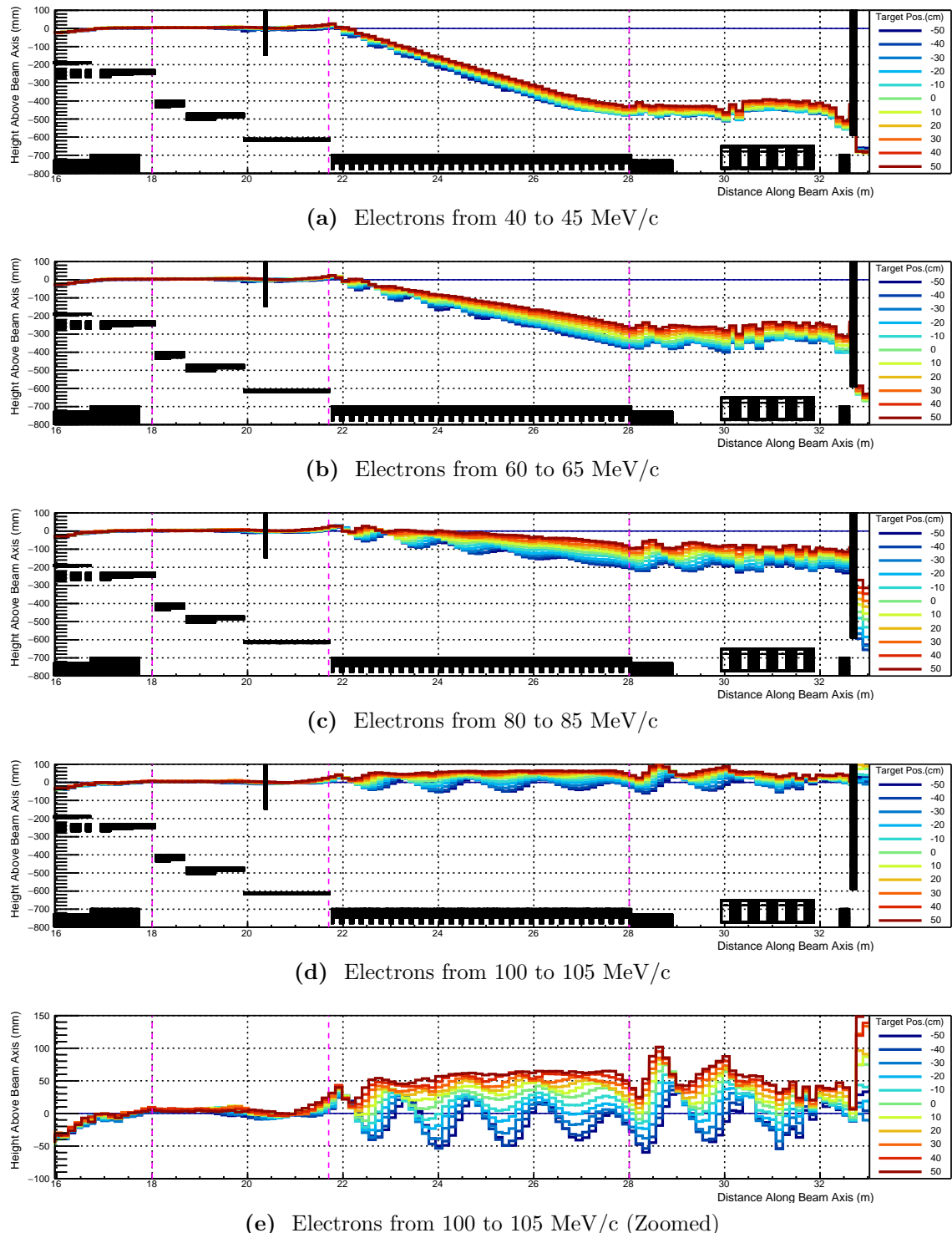


Figure 5.19.: The effect of stopping target position on the height of electrons with a fixed momentum as they pass through the Electron Spectrometer. The size of the variation indicates the stability of the dipole tune; the two parameters are clearly correlated. Also striking – particularly in (e) – is the way the dependence on the helical pitch angles is affected by the stopping target position.

Given the complexity of the optimisation in this region, it was therefore decided to keep the stopping target at the nominal location for the subsequent steps. Having corrected the normalisation of the plots, the conclusion now is that the optimal location is between 10 and 20 cm upstream, so perhaps the target should have been shifted back. However the improvement to the sensitivity would have been small: shifting the target back about 20 cm improves the sensitivity by around 2% compared to the signal acceptance at nominal position.

5.6. Collimators in the Muon Beamline

With the beam line optimised for high signal efficiency, one can look at improving the background by adding collimators into the muon beam line to reduce the flux of high-momentum muons and pions.

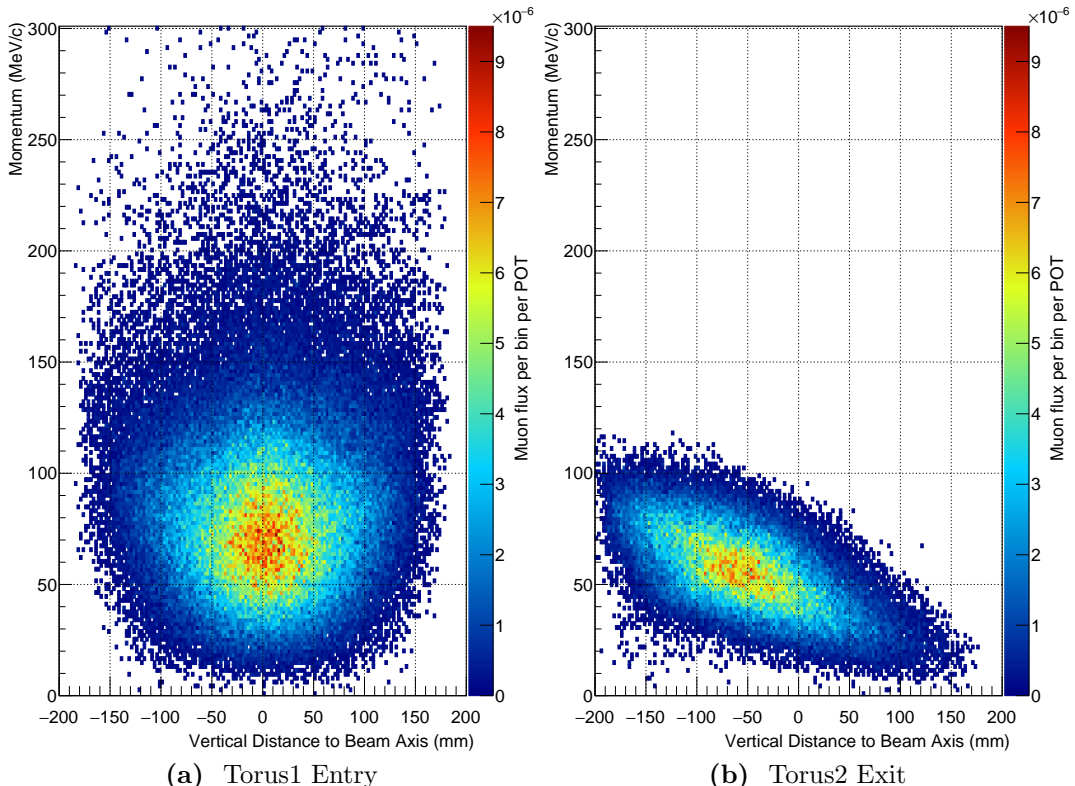


Figure 5.20.: Dispersive effect of the 180° bent transport solenoid and dipole field on muons. No collimating material is yet included, so the high-energy muons being removed is due purely to the beam-pipe itself.

Fig. 5.20 shows the dispersive effect of the bent solenoid and dipole field on muons passing through the beamline. Thanks to this dispersion low momentum muons that can stop in the target and high momentum muons which could produce backgrounds are separated sufficiently so that material in the beam pipe can selectively remove the dangerous, high-momentum muons with only a small impact on the muon stopping rate.

5.6.1. Collimator Placement

The plots in Fig. 5.21 give a sense of where best to locate the collimating material. In Fig. 5.21a the paths of all muons along the beamline is shown. Fig. 5.21b then separates out the muons that stop in the target which should be compared to Fig. 5.21c showing the paths of muons that reach the stopping target region with momentum greater than 70 MeV/c (the threshold for a muon to decay to an electron with $p > 100$ MeV/c).

It is interesting to note the apparent asymmetry in the high-momentum muons at the entrance to the Torus1 that can be seen in Fig. 5.21c. This is not because of some momentum-dependence in the acceptance of the preceding beamline, but due to the fact that muons in that plot are only included if they are ‘dangerous’ in the region around the stopping target. Even without additional collimators, the beam pipe itself removes high momentum muons that enter in the lower half of the beamline. The validity of only tagging high momentum muons around the stopping target region comes from the assumption that the products of high-momentum muons that decay before this region can be reliably removed. It is important then that this assumption be checked, but for this work this is left as a task for the future.

Finally then in Fig. 5.21d the difference between the high-momentum muons and the paths of those that stop is shown. Regions in blue on this plot show where many more high-momentum muons pass than stopping muons; it is in these locations that collimator material will be most effective. This approach could also be improved, since taking the straight difference between the two plots implies equal weighting for stopping muons and high-momentum ones. In reality, whilst a muon tagged as stopping is definitely going to stop, a high-momentum muon should be weighted by the probability to produce a signal-like electron and the probability that this electron survives to be accepted into the detector, passing all analysis cuts. This would make the weighting for the high-momentum muons be a function of the beamline distance itself which again requires a study into how high-momentum electrons are accepted. However for the purposes of obtaining a qualitative sense of where to collimate the unweighted difference should be sufficient.

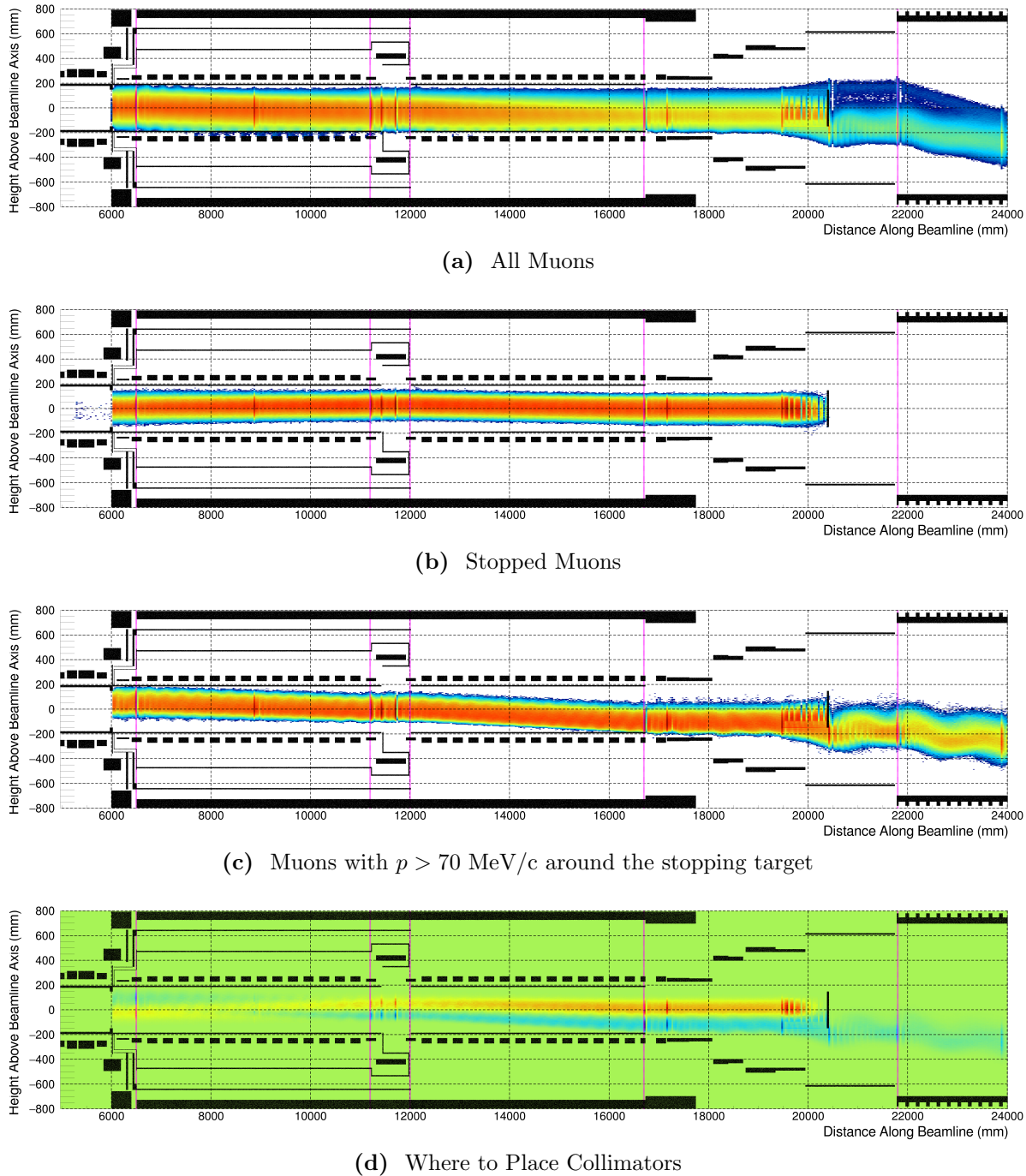


Figure 5.21.: The heights of muons as they pass along the beamline. (a) The path of all muons. (b): The paths of muons that stop in the target. (c): The heights of muons with momentum greater than 70 MeV/c when they enter the region around the stopping target. These could potentially decay in flight to give electrons with 100 MeV/c or greater. (d): The difference between plot (b) and plot (c). Regions in dark blue would give the greatest impact in removing high momentum muons whilst leave the stopping muons untouched. These plots should be compared to those of Fig. 5.26 once collimators have been introduced.

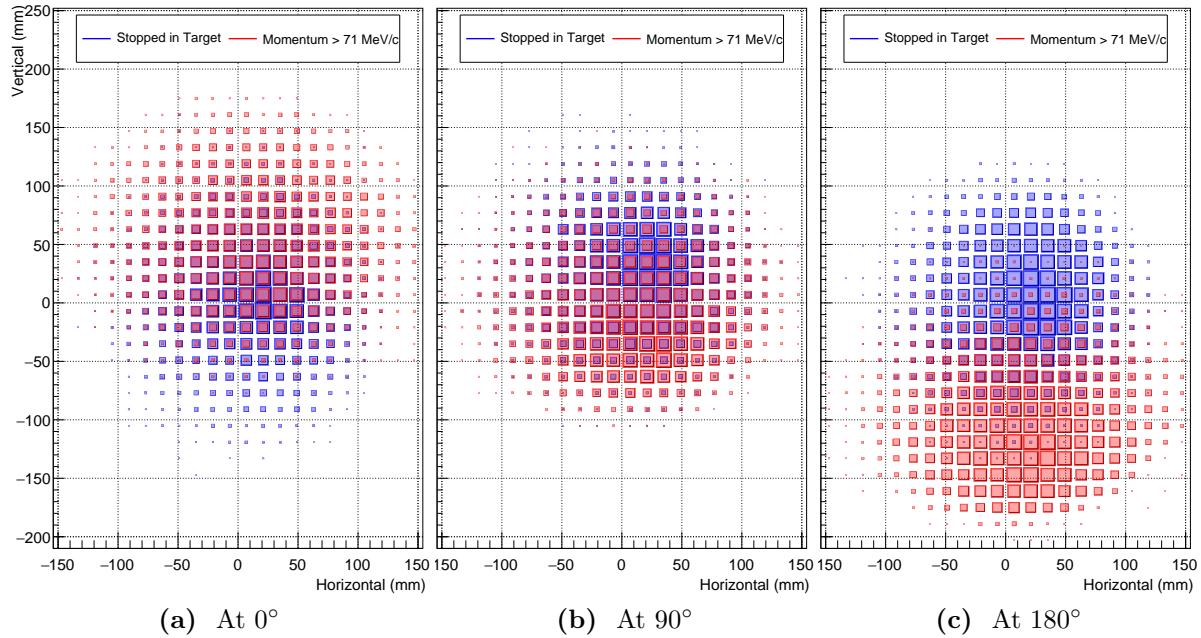


Figure 5.22.: The separation between stopping and dangerous muons. The separation is largest at the exit (180°), reasonable at the entrance (0°), and smallest around the mid-point (90°).

Two regions of interest appear: in the upper half of the entrance to Torus1 and the lower half of the exit of Torus2. Collimating at the Torus1 entrance is justified by the basis that high momentum muons will tend to have larger gyroradii compared to the muons that stop, and that at this point the beam is largely on-axis and has not yet been dispersed. Collimating at the exit of Torus2 is readily understood on the grounds that the high momentum muons will have all drifted downwards by this point, compared to the low momentum stopping muons which are kept on-axis by the dipole fields.

These conclusions are backed by the plots shown in Fig. 5.22 which show transverse slices through the beamline at the entrance to Torus1 (0° of bent solenoid), the midpoint between Torus1 and Torus2 (after 90° of bent solenoid) and at the exit of Torus2 (after 180°). From these plots one can also see how in the middle of the bent solenoids (at 90°) the separation between muons that will stop and those that will have momentum greater than or equal to $70 \text{ MeV}/c$ in the stopping target region is weakest, and hence collimators in this location will not be so effective.

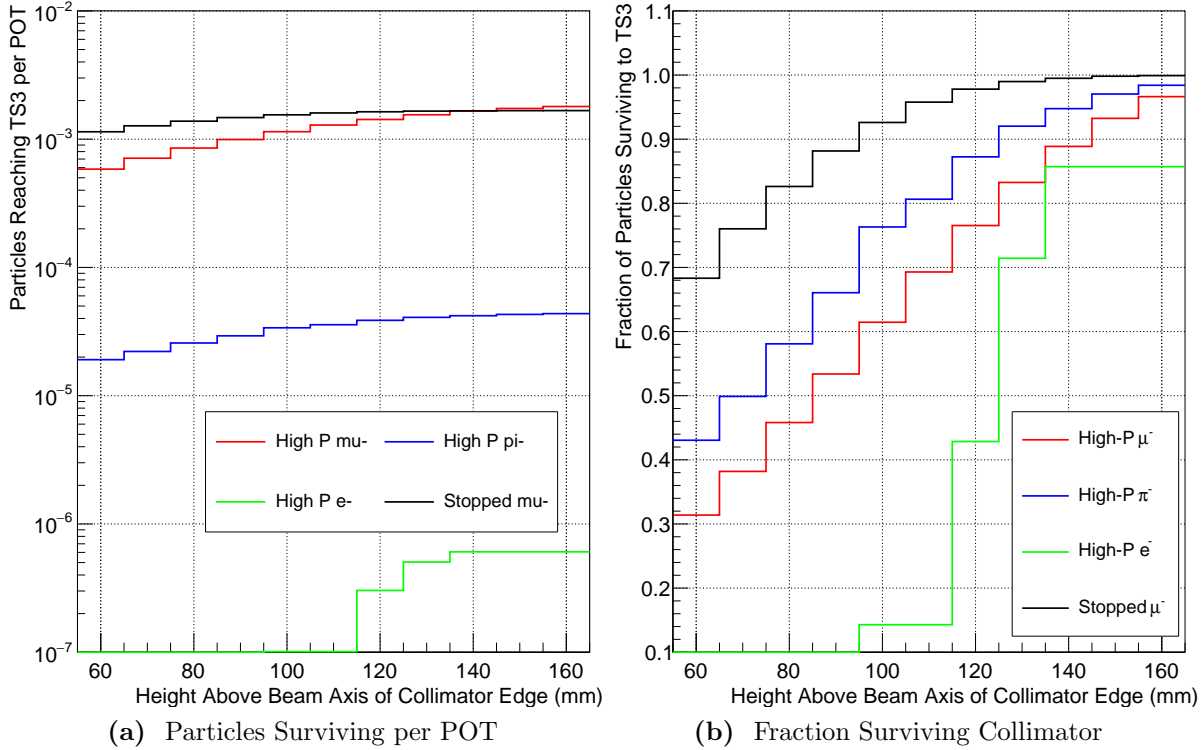


Figure 5.23.: The effect of changing the height of the collimator in Torus1 on the particle distributions.

5.6.2. Collimator Height Optimisation

To identify the optimum height for the collimators in a computationally efficient way, events were generated without any collimators included. The full three dimensional trajectory of all particles as well as the decay tree were persisted. This allows for a ‘virtual’ collimator to be used, where particles that enter a defined region and their secondaries are removed from the downstream plots. Whilst this method allows for many collimator shapes and heights to be tested quickly, it comes with a couple of limitations. Firstly, the accuracy depends on the trajectory sampling density, which should be fine but this results in large data sizes. Secondly, realistic material effects of the collimator cannot be captured, such as the probability a particle is simply scattered rather than stopping completely, or the result of secondary particles produced in the collimator itself.

Fig. 5.23 shows the results of lowering the bottom edge of the collimator material in Torus1. Fig. 5.23a shows the probability per POT that different types of particle (stopped muons and high momentum muons, pions, and electrons) pass the collimator as a function of the collimator height. On the other hand, Fig. 5.23b shows the same plots

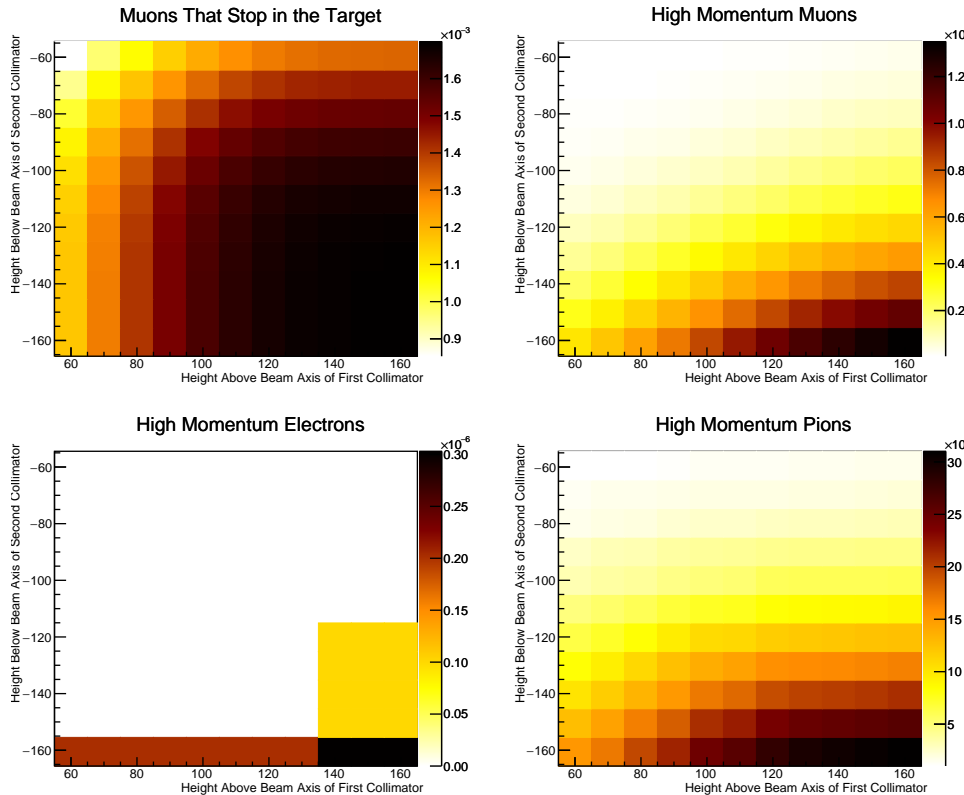


Figure 5.24.: The number of particles reaching the end of the Torus2 solenoid relative to the number that enter the Torus1 solenoid (i.e. the survival probability) for different heights of both collimators in Torus1 and Torus2.

but normalised to the total number of each particle type that reaches the collimator in the first place, therefore showing the survival probability along just the collimator region. Based on these plots, for a collimator that starts at 120 mm above the beamline axis, 14% of high momentum pions are removed, high momentum muons are suppressed by 14% whilst the muon stopping rate is reduced only by 3%.

For the second collimator at the exit to Torus2, the situation is slightly more complicated since in principle the optimum height could be correlated to the height of the upstream Torus1 collimator. To account for this, the virtual collimator technique was applied for both the Torus1 and Torus2 collimator sections simultaneously. As a result, the 1-dimensional plots of Fig. 5.23 become 2D as can be seen in Fig. 5.24, which is normalised to the particle flux just before the collimator similar to Fig. 5.23b.

Fig. 5.25 represents the stopping and high-momentum plots in a way that is easier to compare the two directly. Each line in that plot is a contour showing a change of 2.5 percentage points to the yield. Total acceptance, or 100% is in the bottom right

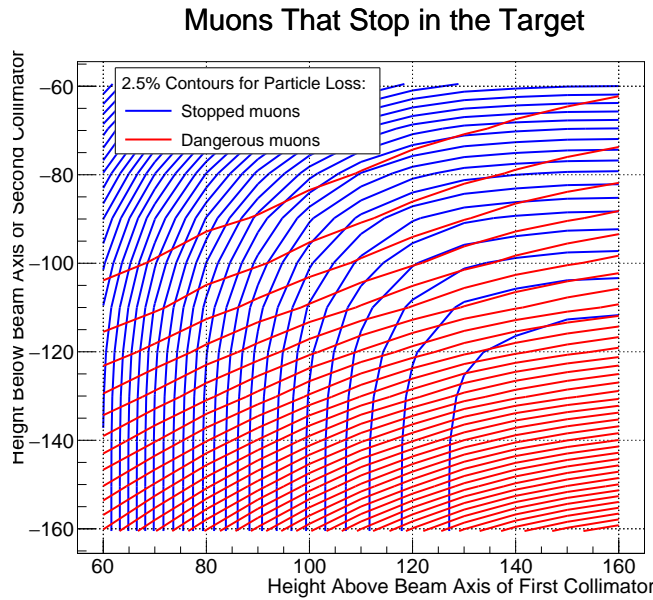


Figure 5.25.: 2.5% contours showing how changing the collimator height affects the stopped and high-momentum muon rates. Each contour represents a reduction of 2.5 percentage points to the particle flux, with 100% acceptance sitting in the bottom right. Blue lines represent the flux of stopping muons, whilst red lines represent the flux of high-momentum muons. For example, for collimator heights within the first blue contour towards the bottom-right corner, less than 2.5% of stopped muons are lost.

corner. From this plot it can be seen that whilst keeping more than 97.5% of the muon stopping rate (the bottom-right most blue contour), the maximum high momentum muon suppression is achieved when the Torus1 collimator sits about 140 mm above the beam axis, and the Torus2 collimator sits about 120 mm below it. To be precise, at these collimator values the muon stopping rate is kept at 99% of the no-collimator rate, whilst high momentum pions, muons and electrons drop to 27.6%, 20.9% and 11% (although this last value is very statistically limited) respectively, compared to their no-collimator rates. At this point the selected values for the collimator heights give conservative background suppressions and tighter values could be chosen. Given that backgrounds from high-momentum muons are suppressed compared to the actual rate of ‘dangerous’ muons by the geometric acceptance of the remaining beamlne and the timing and momentum cuts this seems reasonable at this stage although this will of course be investigated in the next chapter.

Finally, for comparison to the original plots, Fig. 5.26 shows the impact the new collimators have on the muon components of the beam. It is clear how greatly reduced the number of muons passing the stopping target region has now become.

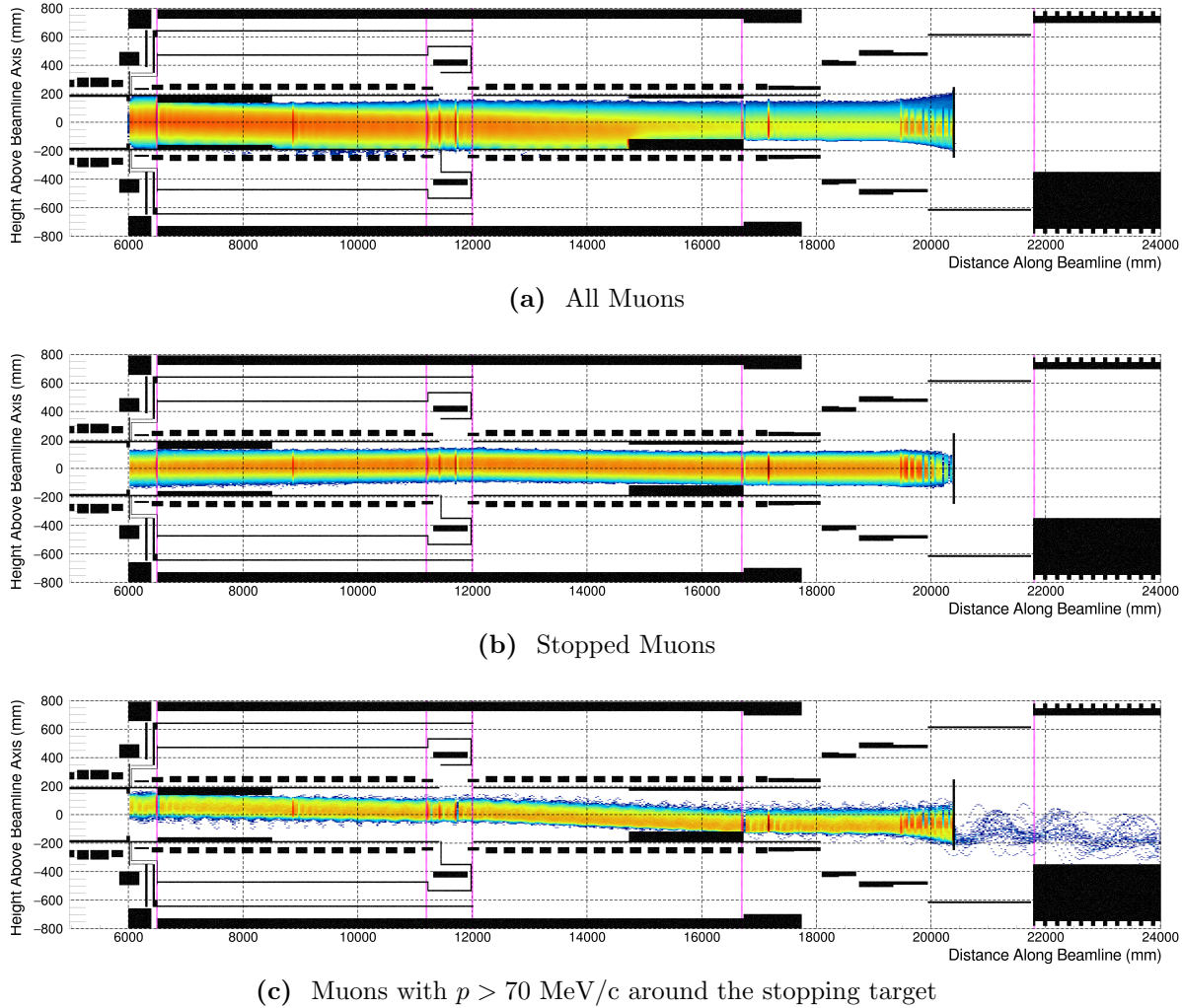


Figure 5.26.: The heights of muons as they pass along the beamline. (a) The path of all muons. (b): The paths of muons that stop in the target. (c): The heights of muons with momentum greater than 70 MeV/c when they enter the region around the stopping target. These could potentially decay in flight to give electrons with 100 MeV/c or greater. These plots should be compared to those of Fig. 5.21 before collimators were introduced, where it is clear how well the dangerous muons are being suppressed.

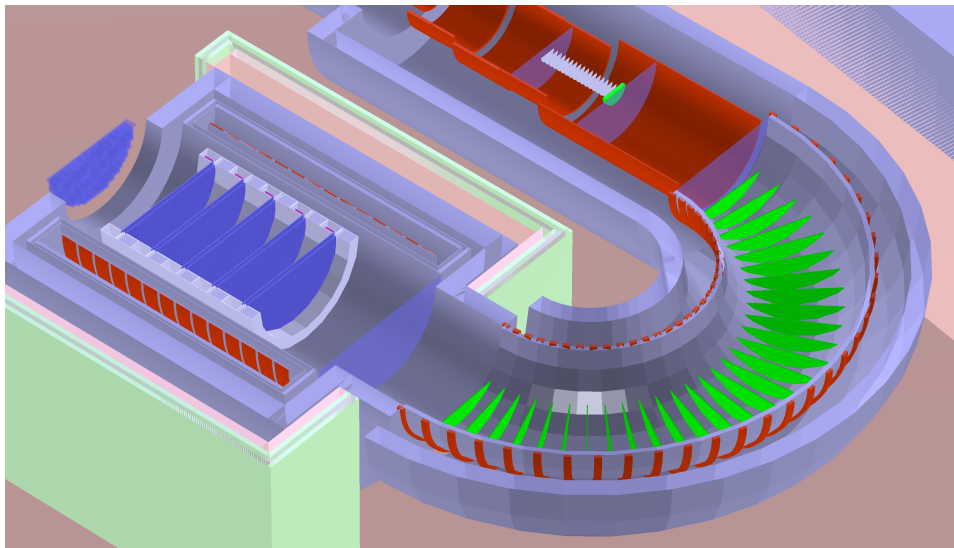


Figure 5.27.: Location of the beam blocker and one possible geometry for the **DIO** blockers, both highlighted in green, shown here before optimisation.

5.7. The Beam and Decay-in-Orbit Blockers

For every muonic atom formed in the stopping target some 39% will undergo decay in orbit (**DIO**). With some 1.4×10^8 **POT** per bunch and a muon stopping efficiency around 1.7×10^{-3} stops per **POT**, one can expect about 9×10^4 DIO events per bunch. If the detector system were exposed to this level of hits it would be impossible to resolve any signal electrons. However, above the end-point energy for electrons coming from free muon decay, the DIO spectrum falls extremely quickly, with around 99% of DIO electrons being produced with less than 59 MeV/c. To this end the electron spectrometer's primary purpose is to disperse away the electrons below 60 MeV/c whilst keep signal electrons on-axis, such that material in the beamline can be tuned to remove the low energy DIO electrons. The beam and DIO blockers are highlighted in green in Fig. 5.27.

Fig. 5.28 demonstrates the dispersion that appears at the end of the spectrometer with the nominal beam blocker design and no DIO blockers in place. The DIO blockers will be inserted along the bottom of the spectrometer and tuned to scrape away a sufficient number of DIO electrons, which will tend to travel towards the bottom of the beam pipe. However whilst the centre of gyration drifts with a well-behaved proportionality in a bent solenoid, the actual separation between signal and **DIO** electrons is in reality less clear as can be seen by the lower plot in Fig. 5.28.

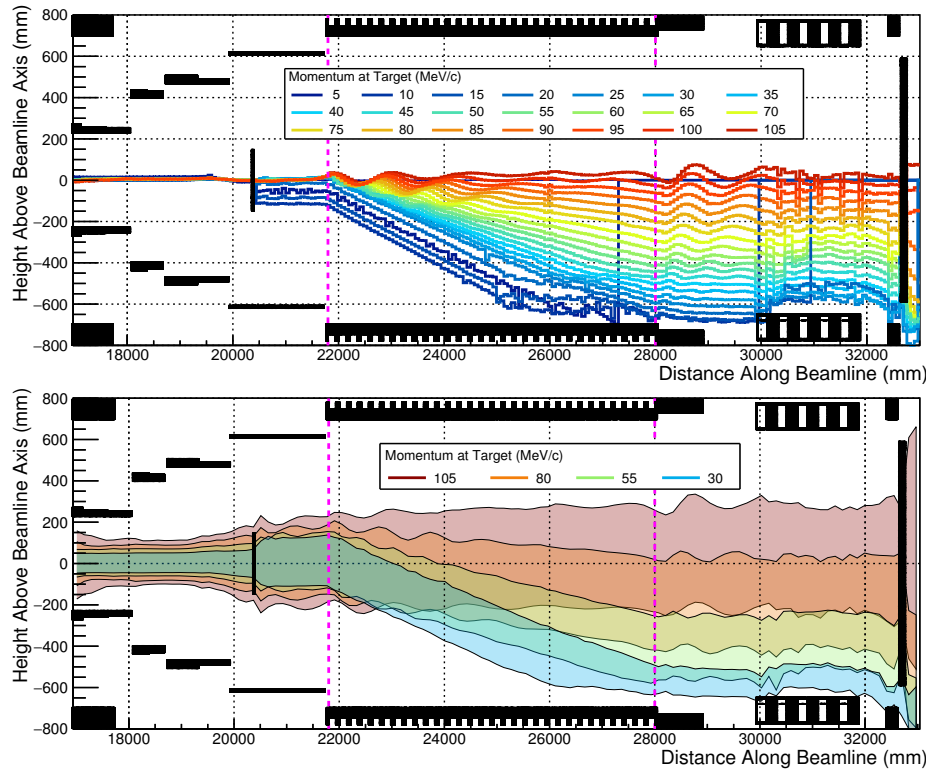


Figure 5.28.: Momentum-dependent dispersion of electrons passing through the spectrometer. Top plot: the mean height of different momenta electrons as a function beamline distance, showing how the drift of the centre of gyration is truly proportional to the momentum. Bottom plot: single standard deviation bands for electrons at different momentum, which shows how the envelope for different momenta overlap considerably, reducing the effectiveness of any collimators.

In addition to the DIO blockers along the spectrometer, the material of the beam blocker immediately after the stopping target also plays a role in suppressing the [DIO](#) rate since low energy electrons remain closer to the beam axis, as can be seen in the lower plot of Fig. 5.28 around the stopping target.

This section therefore describes a simultaneous optimisation of the beam blocker radius and the DIO blocker height. The overall goal is to suppress the DIO rate to less than a single DIO electron per bunch whilst maintain maximal signal acceptance. As for the muon beam collimators, we use the analysis-based collimator approach, where no blocking material is included during simulation. Instead a high-sampling density for particle trajectories is used such that during analysis particles and their secondaries can be ‘killed’ if they enter a region that would contain material of either the DIO or beam blocker.

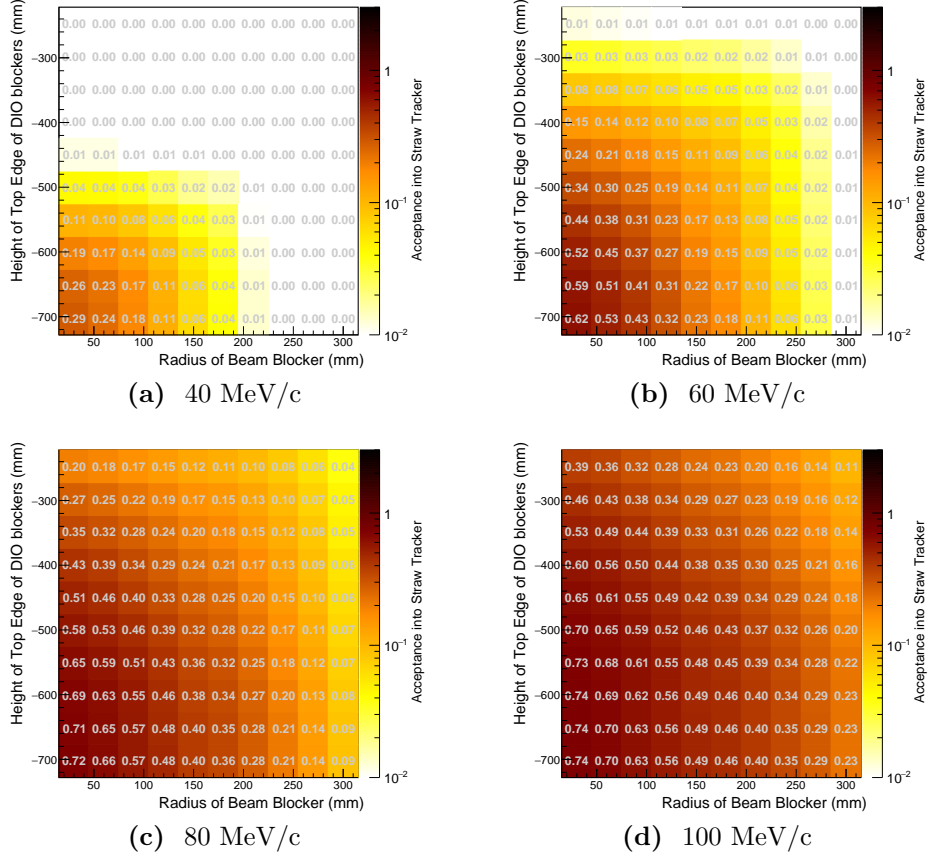


Figure 5.29.: Acceptance into the straw tracker for electrons with different momentum at the stopping target as a function of the beam and DIO blocker dimensions. Note the logarithmic scale for the colour bar.

The results of this study are shown in Fig. 5.29, where the geometric acceptance into the detector is shown for four different electron momenta as a function of the beam blocker radius and DIO blocker height. It is clear that for all values of the blockers' dimensions, electrons above 100 MeV/c have a much better acceptance.

The mean hit rate per DIO event is shown in Fig. 5.30a. It is formed by, for each combination of DIO and beam blocker dimension, the weighted integral of the acceptance of electrons as a function of momentum with the mean DIO rate in each momentum bin. To compare the hit rate to the acceptance of signal, the ratio between the hit rate and the high-momentum electron acceptance is shown in Fig. 5.30b. It is clear from this figure how quickly (note the logarithmic colour scale) the DIO hit rate is suppressed by increasing the DIO and beam blocker dimensions compared to the signal acceptance.

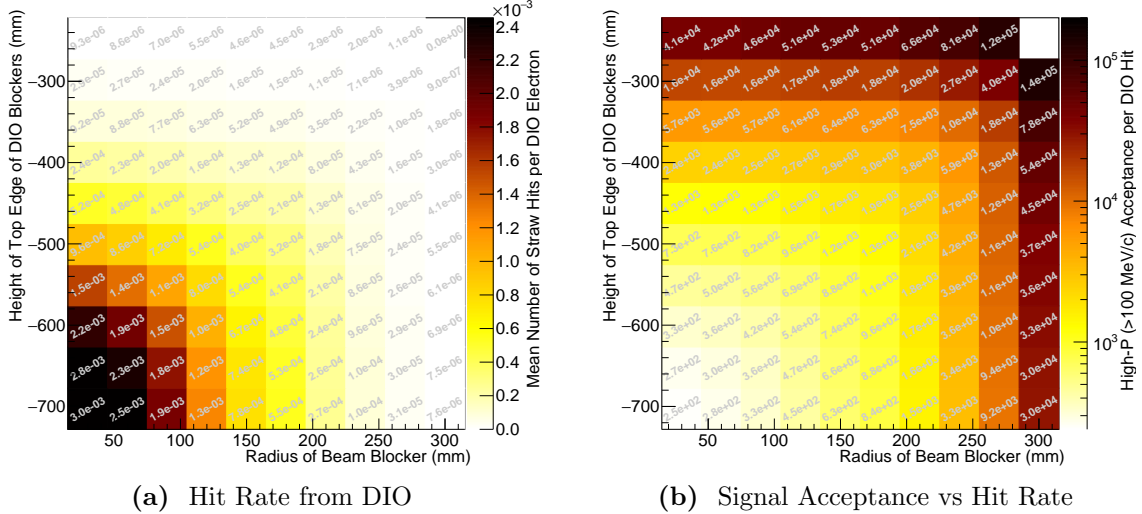


Figure 5.30.: (a) Number of straw tracker hits per DIO electron. (b) Ratio between the high-momentum electron ($p > 100 \text{ MeV}/c$) acceptance to the number of hits per DIO electron. Colour is on a logarithmic scale.

With a beam blocker of 24 cm radius and DIO blockers set to 35 cm below the beam axis, the DIO hit rate is about 2.2×10^{-5} per DIO event, or about 2 DIO hits per bunch. For the same blocker dimensions, the geometric signal acceptance is about 0.22%. Given the steep drop-off in hit rate versus signal acceptance around these values a finer scan in this region is an important check for the future. What hit rate in the straw tracker is tolerable is a number for future studies. In Phase-I, the straw tracker is expected to operate with a hit rate around 1 kHz per straw. Phase-II will likely use finer straws, but with the current Phase-I design, some 133 straws occupy a layer, so that a total hit rate into the Straw Tracker of around 200 kHz should be acceptable.

Given the scope for future improvements in the granularity of the Phase-II straw tracker and the sensitivity to the beam and DIO blocker dimensions, the somewhat non-conservative values described above of 24 cm and 35 cm for beam blocker radius and DIO blocker depth below the beam axis are selected here.

5.8. Summary of optimised parameters

The complete set of optimised parameters is shown in Table 5.4.

Parameter	Value	Comments
Production Target Length	32 cm	Placed asymmetrically about muon beamline axis
Production Target Radius	1 cm	
Torus1 (TS2) Dipole Strength	0.055 T	same as Phase-I
Torus2 (TS4) Dipole Strength	0.0275 T	same as Phase-I
Torus1 Entrance Collimator Height	14 cm above beam axis	From top of beam pipe downwards
Torus2 Exit Collimator Height	12 cm below beam axis	From bottom of beam pipe upwards
Stopping Target Location	0 cm	Unchanged from CDR value
Electron Spectrometer Dipole	-0.18 T	Negative compared to Torus1 and Torus2 dipole fields
Beam Blocker Radius	24 cm	
DIO Blocker Height	35 cm below beam axis	From bottom of spectrometer upwards

Table 5.4.: Optimised values for the parameters studied in this chapter. Many more parameters remain to be optimised that were considered beyond the scope of the present work.

5.9. Future optimisations

The primary goal of this work is to update the previous optimisation from the 2009 CDR and provide a new baseline design. However whilst touching every aspect of the layout of Phase-II, the optimisation developed here is not exhaustive and there is much scope for further work.

The following list is a short summary of some of the areas that could be developed further:

Refine the optimisation criteria In many of these studies only the signal efficiency, or even some proxy, is used to identify the optimal value of the parameter under question. In reality one ought also to study simultaneously the background rates. These two quantities should be combined into the expected confidence limits given a null or background-only measurement. At the same time other quantities such as

cost and run-time will also need considering, although the latter is likely reduced simultaneously with maximising the overall sensitivity.

High energy electron acceptance vs. beamline distance When tuning the muon beam collimators, the key goal is to remove high-energy particles that can produce high energy electrons. A particularly useful study would be to evaluate the acceptance to signal-like electrons which originate along the beamline. This should include those electrons which originate with momentum greater than 105 MeV/c but which arrive at the detector with signal-like energies. With this information, it becomes easier to identify how soon along the beamline one must collimate away the high-energy particles which may lead to improvements in the muon stopping rate or the signal acceptance.

Stopping target shape, thickness, and disk spacing This study has focussed only on the position of the stopping target. Clearly the actual shape should be studied as well. In particular, given the dispersion in the muon beam, and the changing solenoidal field strength around the target, a target design that uses disks of varying profile or even thickness has potential to improve the experimental sensitivity.

Correlation between dipole fields and stopping target shape Since the bent solenoids introduce dispersion into the beam and the dipole fields compensate for this, the height and momentum of the muon beam at the stopping target can be controlled to a degree. Whilst in the optimisation of the muon beam dipoles of this thesis the target shape was held fixed, in principle some of the identified correlations might be different if the target design was allowed to vary simultaneously. Such a study would clearly involve an enormous parameter space, so perhaps this is a study that could be best performed with a smarter machine-learning based approach.

Spectrometer's solenoidal field strength and aperture Since the dispersive effect of a bent solenoid is inversely proportional to the solenoidal field strength, reducing the field in the spectrometer will likely improve the DIO–signal separation, reducing the hit rate. This could however also affect the signal acceptance since the trajectories will acquire larger envelopes. Increasing the spectrometer aperture size could compensate this, but then one faces an increase in the cost of the spectrometer and the detector solenoid which would need to be considered.

Chapter 6.

COMET Phase-II: Signal Sensitivity

As discussed previously, the signal sensitivity of COMET is a measure of both the ability to produce a signal event and the ability to detect it. The signal efficiency per POT is therefore the product of the muon stopping rate, the rate of muon capture from the ground state of a muonic atom (the normalisation in the conversion rate), and the total signal acceptance after all analysis cuts and geometric acceptances are considered.

Since signal efficiency describes only the ability to produce and detect signal, this chapter could in principle ignore all possible backgrounds. However in order to tune analysis cuts, one must consider at some level the potential background rates, which must be minimised and controlled. Furthermore, until the full analysis chain is implemented, we consider only a handful of crude analysis cuts, namely the momentum and timing of electrons. The 2009 CDR additionally included cuts on the reconstruction [35] such as track fitting quality, and the ratio between transverse and longitudinal momentum of particles (related to the pitch angle).

6.1. Muon Stopping Rate

Based on a simulation of some 1.1 billion POT the muon stopping rate of the optimised design was found to be 1.61×10^{-3} per POT. This amounts to some 43% of the muons that reach the target itself, a fraction that is driven mostly by the muon momentum distribution and the total amount of target material, as demonstrated by Fig. 6.1 showing the momentum of muons at different points in the beam. **CHECK: Add the muon momentum plot**

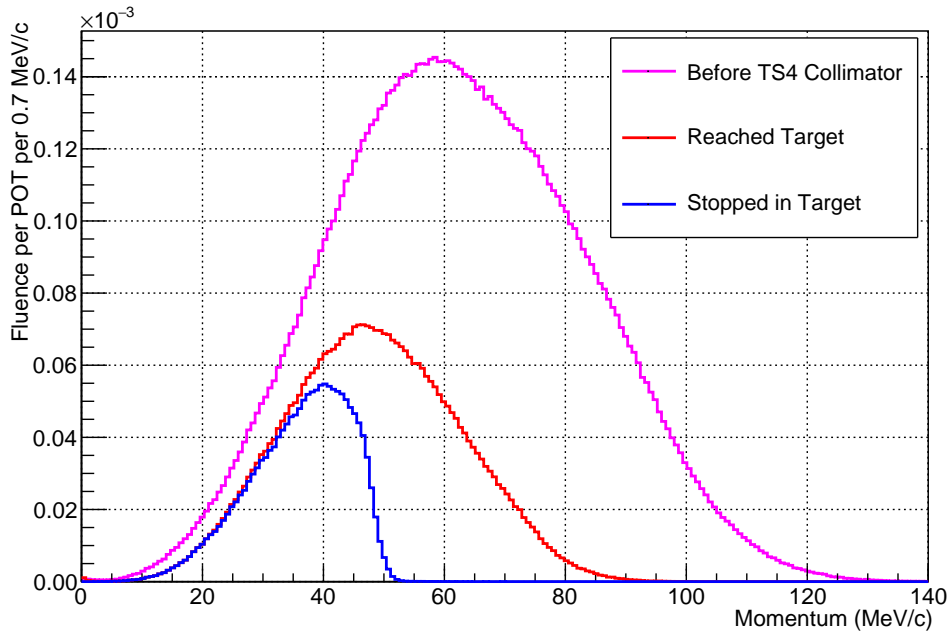


Figure 6.1.: The Momentum and rates of muons reaching the final beam collimator, the stopping target, and actually stopping in the target. It can be seen how the present target geometry is unable to stop muons of greater than around 50 MeV/c.

Fig. 6.2 shows where muons stop in the target based on this simulation from which it is clear that several asymmetries and correlations exist. Firstly the correlation between Z and Y shown in Fig. 6.2a arises due to the disperse muon beam arriving at the target. Since high momentum muons are vertically lower (towards negative Y) in the beam and since these muons have a larger stopping distance, muons lower down in Y tend to travel further through the target (towards lower values of Z). It is interesting however that when the integration is taken over all target disks the distribution in Y demonstrates little asymmetry. This is most likely due to the fact that the Y-position is controlled by the Torus1 and Torus2 dipole fields which were optimised to maximise the stopping rate, which one might expect to be achieved when the stopping distribution is symmetric. **CHECK: Is it worth adding the 1D projections of the stopping distribution?**

Given this correlation, there might be a gain in signal sensitivity if there were less material at the top of the target. Since this material is less important for stopping the low energy muons removing the extra material might have little impact on the stopping efficiency. On the other hand it will likely increase signal acceptance since signal electrons will pass through less material.

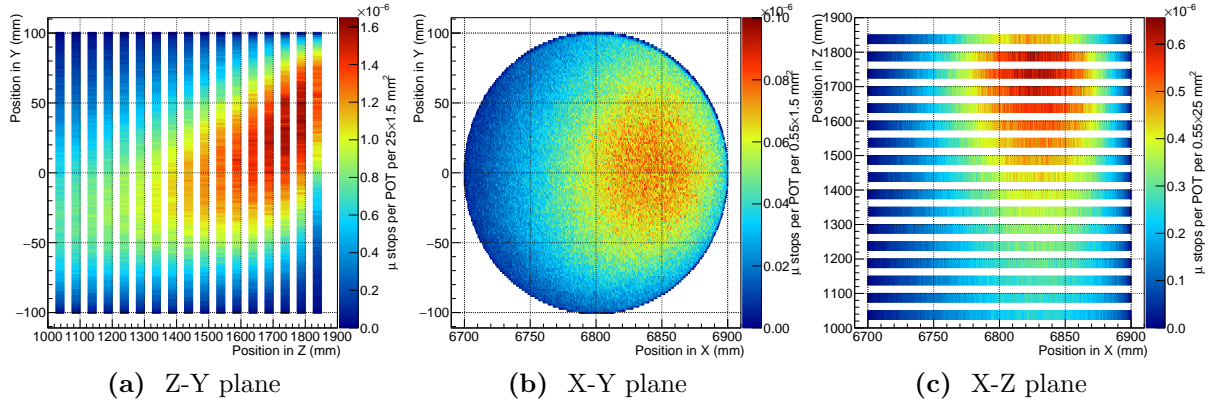


Figure 6.2.: Projections of the final position of stopped muons in the stopping target. Axes are from the SimG4 global coordinate system, so that $+X$ points away from the production target, $+Y$ is vertically upwards, and $+Z$ is the direction of the muon beam at the production target. The muon beam in these plots is therefore travelling in the negative- Z direction since it has travelled 180° around the bent solenoid.

Whilst the vertical stopping distribution is largely symmetric (in the integral), a striking asymmetry exists in the horizontal stopping distribution. The cause of this asymmetry is at this stage unclear. It could arise from the fact that the production target itself is asymmetric in the horizontal transverse direction, such that more muons and pions are produced to one side of the beam axis. On the other hand, it could also arise from the transportation dynamics of the bent solenoid, dipole field and collimator design. Since this asymmetry could suggest low energy muons are missing the target on one side studying the cause of this asymmetry is important as removing it could be another source of sensitivity increases.

6.2. Acceptance of Stopping Target Electrons

Many factors contribute to the signal acceptance, and we consider here the geometric acceptance and efficiency of the timing and momentum cuts. And whilst stopping rate and signal acceptance are often discussed separately, they are in reality coupled through the position and time of the stopped muons. The position impacts on the amount of material the electrons must pass through and therefore their momentum at the detector, and their subsequent transport through the very inhomogeneous magnetic field of the COMET beamline. To study signal acceptance then, a realistic muon stopping distribution was

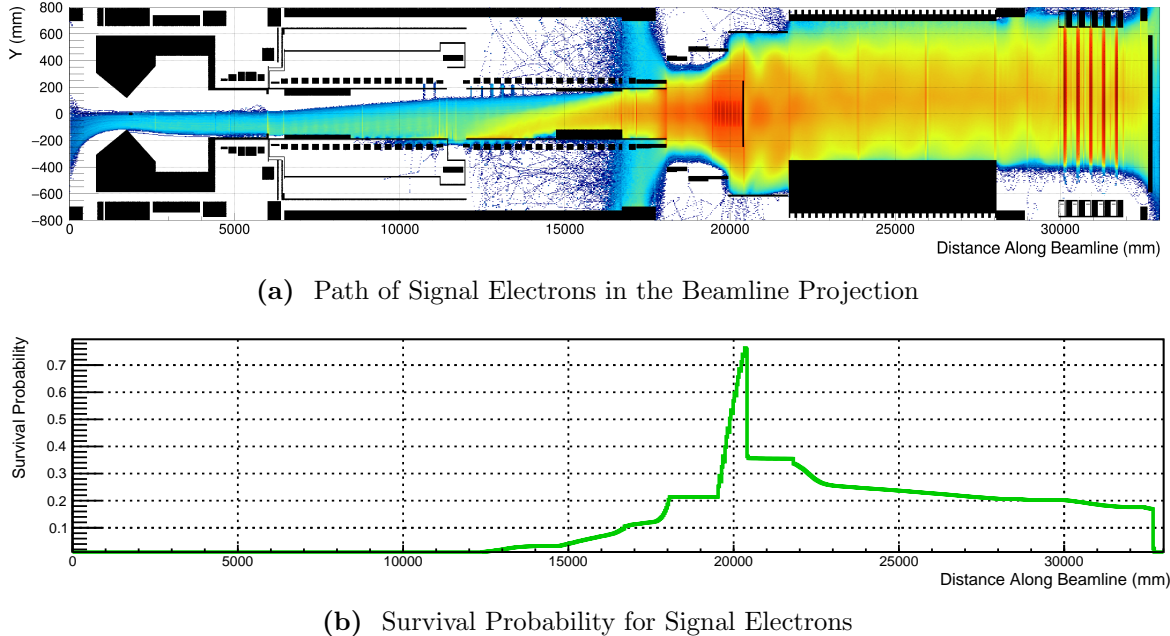


Figure 6.3.: Geometric acceptance of signal events. (a) Projection of the trajectories of signal electrons to the beamline axis-vertical surface. (b) Survival probability of signal electrons as a function of the distance along the beamline axis. From these plots it is clear how the acceptance is diminished by the DIO blocker in the spectrometer, although after the initial few hundred millimetres of blocker the rate of signal loss reduces.

first acquired which was then re-used as the input position and time distribution for signal electrons.

6.2.1. Geometric Acceptance

Fig. 6.3a demonstrates the path of signal electrons injected at the target with a realistic stopping distribution. From this one can see how the initially isotropically directed electrons are mirrored back to head downstream towards the detector. Fig. 6.3b is then a projection of the above plot normalised to the number of primary signal electrons, and as such gives the survival probability for electrons as a function of beamline distance.

Based on this and a second analysis that uses the hits in the Straw Tracker directly, the geometric acceptance of the beamline and Straw Tracker is found to be 22.3%. This should be compared to the value expected with the analytic collimator approach from 5.7 suggesting that such an approach is adequate for this sort of study.

6.2.2. Timing Window Efficiency

A time gated detector window is used as a way to reduce the background rate. Whether this is implemented in the trigger, offline in the analysis, or at different levels in both of these is yet to be determined, be the impact on signal efficiency will likely be the same.

Fig. ?? shows the arrival time of signal electrons **CHECK: Add the muon stopping time, and beam flash timing to this plot?**. A subtlety of the gated time window is that since the signal lifetime is large compared to the pulse separation of $1.17 \mu\text{s}$, a signal electron has a reasonable chance of arriving in detector windows later than the first one. Fig. ?? shows the signal acceptance as a function of the start time of the detector window for three different stop times. Time in that plot is with respect to the proton pulse's arrival; since it takes about 100 ns before any beam flash hits the detector, it is reasonable that the gated-time detector window be open at the very moment when the proton pulse arrives. This would be the case at the very end of the window that ends at 1200 ns given that pulses are separated by about 1170 ns.

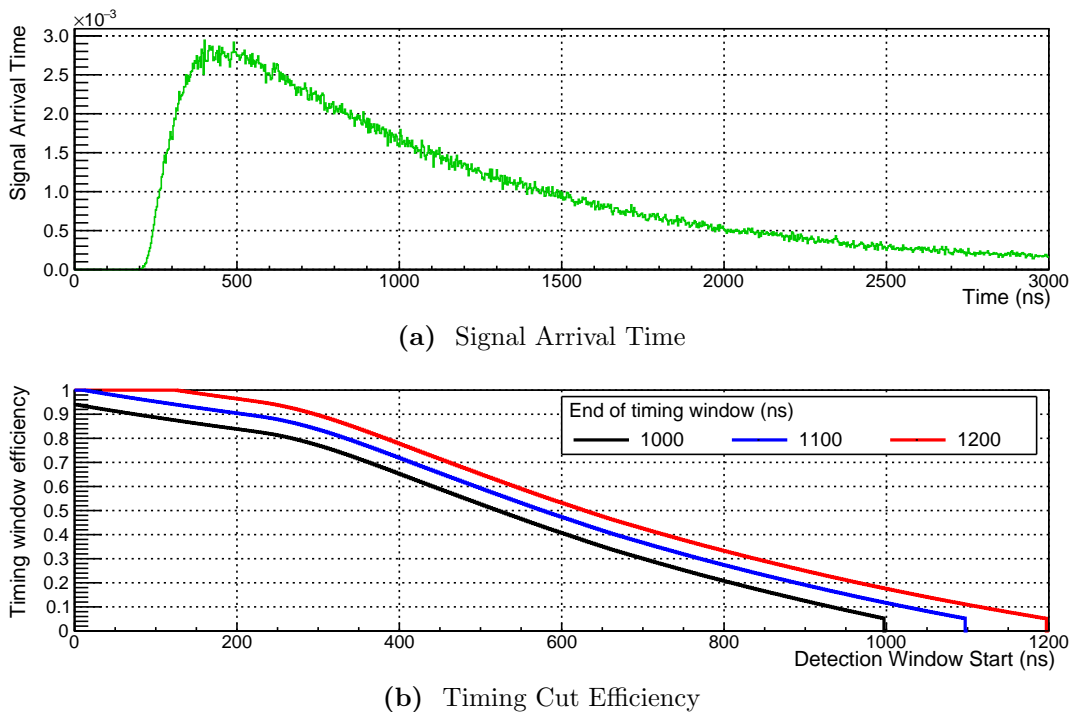


Figure 6.4.: Timing of signal electrons. (a) The arrival time of signal electrons at the detector, including the effect of the proton pulse width, particle transportation, and the muon lifetime. (b) the efficiency of the timing window as a function of the switch-on time. Assumes a pulse separation of $1.17 \mu\text{s}$.

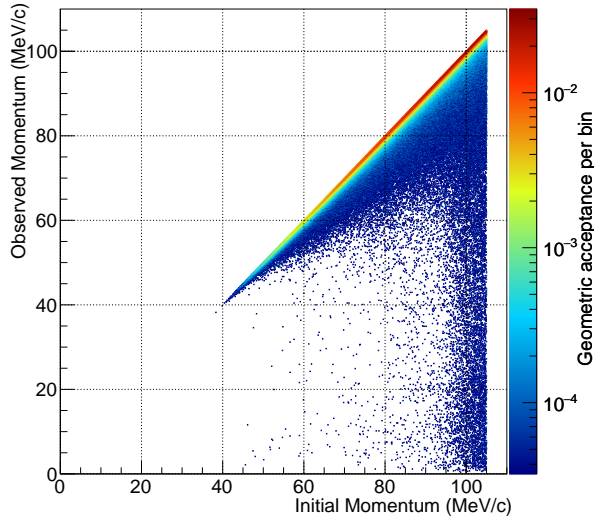


Figure 6.5.: The transfer matrix for electrons originating at the target, including the geometric acceptance and energy loss.

One must also consider the timing of background processes to pick a valid time window. Motivated primarily by the pion radiative capture background (which will be discussed in completion in section 7.3, the time window of 600 to 1200 ns is selected. The signal efficiency of this timing window is 0.53%.

6.2.3. Momentum Cut Efficiency

Between production in the stopping target and detection at the StrECAL, electrons lose energy by scattering, brehmstrahlung and ionisation of material in the electron's path, including the stopping target itself and the detector. Fig. 6.5 shows the momentum transfer function for electrons coming from the target and reaching the detector. Each bin represents the probability that an electron is observed at a particular momentum given an initial momentum.

Crucial for signal sensitivity is how this energy loss effects signal electrons compared to DIO electrons. Fig. 6.6a shows the impact this energy loss has close to the signal energy, where it is clear that a low-energy tail appears to what is intrinsically a monoenergetic signal.

In addition to energy losses in material in the beamline, further smearing of the signal spectrum occurs during particle trajectory reconstruction. No reconstruction algorithm can ever reproduce the true momentum of a particle with perfect accuracy. A

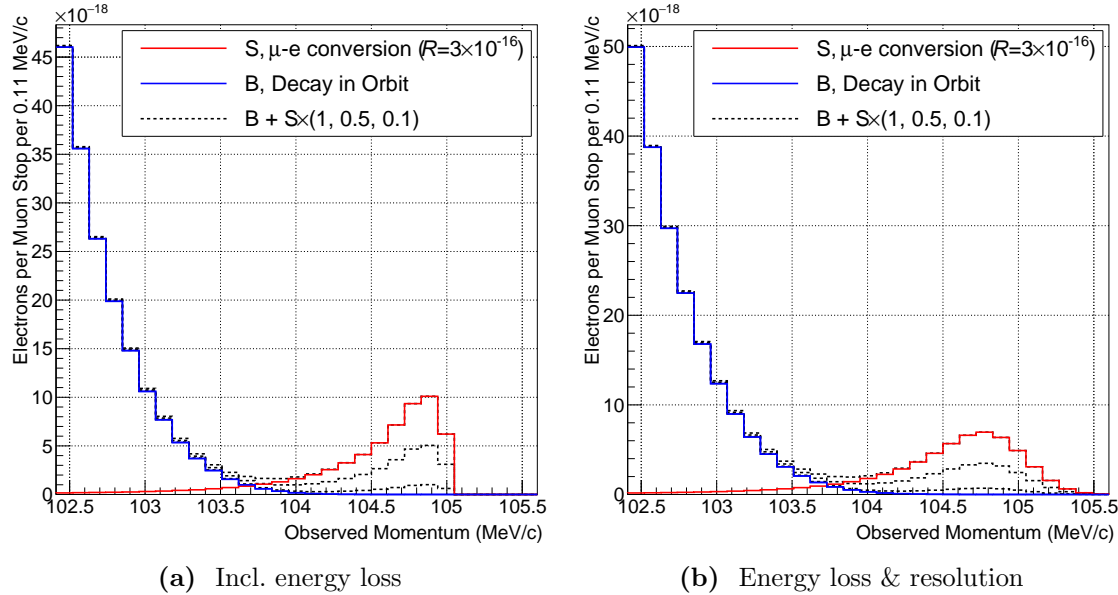


Figure 6.6.: The spectrum of electrons coming from DIO and μ -e conversion assuming a conversion rate of $\mathcal{R} = 3 \times 10^{-16}$. (a) Includes energy losses in the target, beamline, and detector; (b) also includes resolution effects (assumed the resolution function is perfect gaussian with a width of $\sigma = 200$ keV/c).

design requirement of the StrECAL has been that it achieves 200 keV/c resolution for 105 MeV/c electrons and indeed work on Phase-I has demonstrated performance better than this. Since at this time work on the Phase-II reconstruction has not yet begun and even the Phase-I StrECAL reconstruction requires further development, we approximate the residual function – the difference between reconstructed and true momentum – by a single gaussian with a variance of 200 keV/c. The impact that such a residual function would have on the observed DIO and μ - e conversion spectra is shown in Fig. 6.6b.

Elaborate analysis techniques might then count the number of signal events by fitting simultaneously fitting the above signal and background functions to the measured total spectrum. For the purpose of developing a baseline sensitivity estimate however, we envisage instead a simple analysis procedure which puts a single cut on observed electron energy. In that procedure one would tune the cut to maximise the signal to background separation, as demonstrated by Fig. 6.7 where the cut value is increased and the number of electrons passing above that cut are integrated. Also shown is the function of signal divided by the square root of signal plus background, an indicator of the relative signal to background fluctuations one can expect and a function which peaks at around 103.68 MeV/c. Since this value is only optimal for the demonstration signal conversion of $R = 3 \times 10^{-16}$ and to bring the DIO rate down further (see 7.1), a cut of

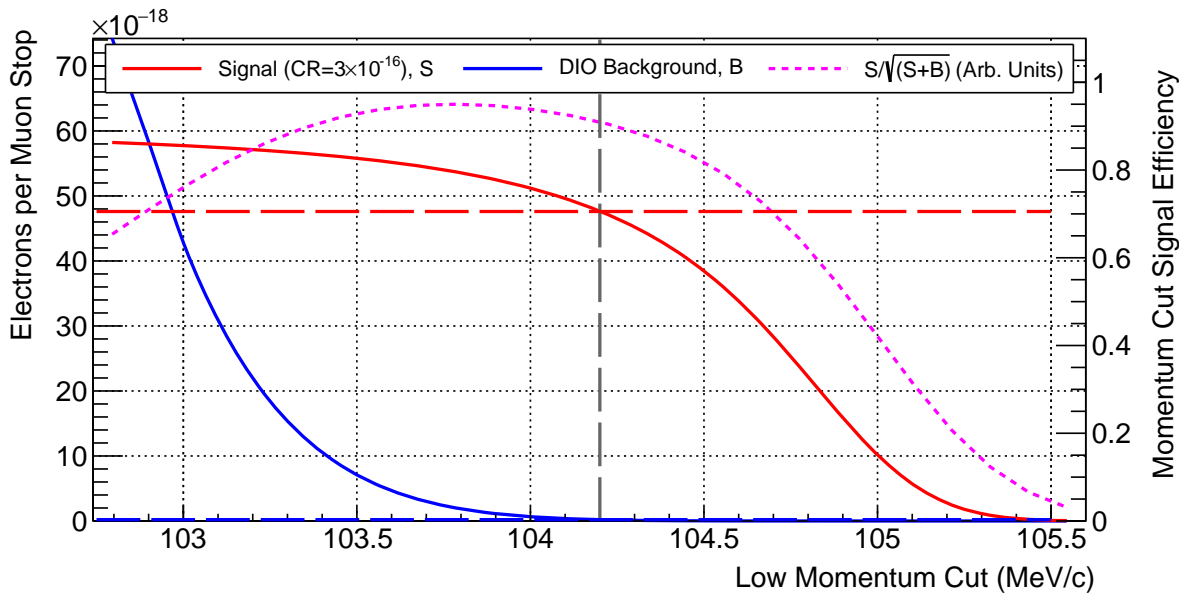


Figure 6.7.: Relative signal versus DIO background as a function of the low momentum cut value assuming a conversion rate of $\mathcal{R} = 3 \times 10^{-16}$. The magenta line is the signal over square root of signal plus background for this conversion rate shown as an indicator of the optimum cut value.

103.9 MeV/c is selected. At this value the signal efficiency of the cut is 77.9%. It should be noted though that whilst changing the cut value leaves the signal efficiency relatively unchanged, the DIO rate varies dramatically: a shift of the threshold up or down by 0.1 MeV/c changes the signal acceptance by about 1.5 percentage points, but changes the DIO rate by a factor of 2.

6.2.4. Total Signal Acceptance

Table 6.1 gives a break down of the signal acceptance as estimated here compared to the values from the previous study for the CDR. For the CDR the geometric acceptance had to be factorised into each section of the beamline to reduce the processing power required. The present study, being able to perform this in a single step, is likely more reliable for the total geometric acceptance yet agrees well with the previous estimate.

For reconstruction and Trigger and DAQ efficiencies, we expect the CDR value to be a reliable lower limit and so we re-use these here as a conservative baseline. This is another aspect of this study that can be improved in the future, and indeed thanks to the Phase-I run will not only be finalised within the next year or so but will be tested

Overall Acceptance	2009 CDR [35]	This Study
Geometric acceptance	0.20	0.22
<i>Solid angle with mirroring</i>	(0.73)	
<i>Beam blocker acceptance</i>	(0.57)	
<i>Spectrometer acceptance</i>	(0.47)	
Timing window efficiency	0.39	0.53
Momentum cut efficiency	0.72	0.70
TDAQ acceptance and efficiency	0.90	N/A
Reconstruction aspects	0.78	N/A
<i>Recon. efficiency</i>	(0.88)	
<i>Track quality cut efficiency</i>	(0.89)	
Additional analysis cuts	0.81	N/A
<i>Transverse momentum cut efficiency</i>	(0.83)	
<i>E/p cut efficiency</i>	(0.99)	
<i>Pitch angle cut efficiency</i>	(0.99)	
Total acceptance at ‘truth level’	0.056	0.091
Total (with CDR recon. and TDAQ efficiencies)	0.039	0.057

Table 6.1.: Numbers that go into estimating the total signal acceptance from this study and compared to the previous study documented in the 2009 CDR. Since this study has not estimated reconstruction issues, we include the previous values in the final estimate on the expectation that with the improvements in reconstruction techniques and with the benefit of Phase-I final reconstruction efficiency will be improved compared to the 2009 CDR values.

and debugged on real data prior to the Phase-II run. Finally, although the CDR include a number of additional analysis cuts which reduce the sensitivity but were necessary to improve background separation. In this study such cuts are not applied, and so the efficiency of these values is not included in the final acceptance calculation.

6.3. Single Signal Event Sensitivity (SES) and Run Time

Finally, it remains to pull all these numbers together into equation (2.4). Since our target SES is fixed we instead tune the amount of running time needed to stop enough muons

I_p	7 μA	Proton beam current
$R_{\mu\text{-stop}}$	1.61×10^{-3}	Muon stopping rate per POT
f_{1s}	90%	Probability of reaching the ground state
$\mathcal{B}_{\text{capture}}$	61%	Branching ratio for muon nuclear capture in Al
$A_{\mu\rightarrow e}$	5.7 %	Total signal acceptance of Phase-II

Table 6.2.: Parameters that determine the run time and single event sensitivity for COMET Phase-II based on this study.

to achieve this goal, hence the by inversion of (2.4) we get the necessary run time as:

$$t_{\text{run}} = \frac{1}{(I_p/e)R_{\mu/p}f_{1s}\mathcal{B}_{\text{capture}}A_{\mu\rightarrow e}\text{S.E.S}}, \quad (6.1)$$

where N_μ has been expanded to the proton beam current divided by the proton charge, I_p/e , times the muon stopping rate per POT, $R_{\mu/p}$. Table 6.2 lists the values of these parameters, from which we can see that a single signal event sensitivity of 3×10^{-17} can be achieved in around 1.57×10^7 seconds or about 180 days. Alternatively, if we ran for some $2. \times 10^7$ seconds, an Single-Event Sensitivity (SES) of 2.27×10^{-17} would be possible. Table 6.3 compares this to the CDR estimate, which expected to achieve a SES of 2.6×10^{-16} in a run time of 2×10^7 s, and Phase-I which is expected to reach its goal of 3×10^{-15} in about 140 days of running. On a year-by-year basis the predicted Phase-II sensitivity is about 3.5 times better than the Mu2e experiment’s expectation [23].

		Single event sensitivity	Total POT ($\times 10^{19}$)	Beam time t_{run} (s)	Sensitivity per year of continuous beam
COMET (this study)	Phase-II	2.27×10^{-17}	87	2.00×10^7	1.44×10^{-17}
COMET (CDR 2009 [35])	Phase-II	2.60×10^{-17}	85	2.00×10^7	1.65×10^{-17}
Mu2e [23]		2.40×10^{-17}	36	6.00×10^7	4.57×10^{-17}
COMET Phase-I [80]		3.00×10^{-15}	3.2	1.26×10^7	1.19×10^{-15}

Table 6.3.: Comparison between the run time and single-event sensitivity from this study and from the 2009 CDR, the Phase-I TDR, and the Mu2e experiment’s TDR. The sensitivity per year of continuous beam is the single-event-sensitivity that can be achieved in 3.15×10^7 seconds of running, assuming no beam shutdown periods.

CHECK: All of this needs updating with the probability of an atomically captured muon reaching the ground state. Yoshi Kuno said it was about 90%, but need to check

Chapter 7.

COMET Phase-II: Backgrounds

Having optimised and evaluated the signal sensitivity, it is now important to check the expected background rates. Interpreting the final result to declaring an observation or produce a confidence limit is only possible if the number of background events has been predicted. The certainty of any observation or the stringency of a final confidence limit is determined by the relative background rate and signal sensitivity; ideally the background rate should be small, well below a single expected event.

The types of background we must consider for COMET were outlined in 3.1, but in this section they are evaluated in the optimised experiment design using the improved simulation.

7.1. Muon Decay in Orbit (DIO)

In order to decide the optimal threshold for the momentum cut, it was necessary, in section 6.2.3, to study the rate of DIO events. At the selected momentum threshold of 104.2 MeV/c, the number of expected DIO events per muon stop is 6.2×10^{-20} . Given the 1.40×10^{18} muon stops that should take place during Phase-II, the total expected number of background events due to DIO is 0.086.

However, it is important to note just how steeply falling the DIO rate is in this region. Fig. 7.1 shows how, given a fixed signal sensitivity, the number of DIO background events is affected. Changing the momentum threshold also affects the signal acceptance, so that for a fixed SES one must increase the running time. Simultaneously, with more muons stopped the DIO rate will increase for a fixed momentum threshold. Fig. 7.1 was produced using the same DIO and signal spectra shown in Fig. 6.6b, which included

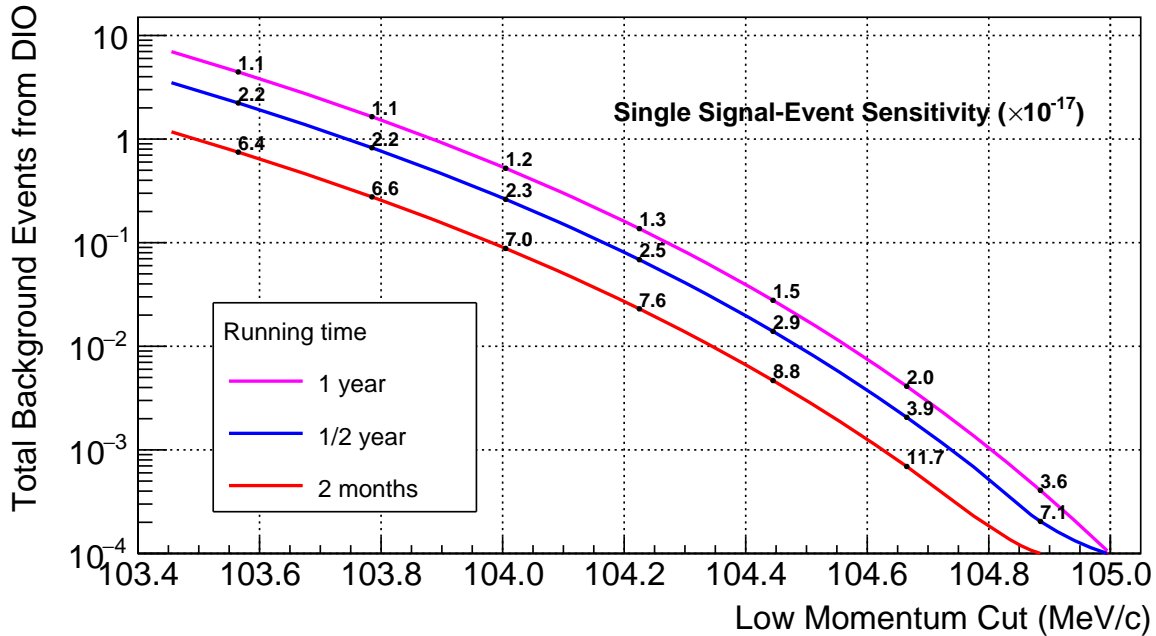


Figure 7.1.: The DIO background rate as a function of momentum threshold for different total running times. Given a fixed the running time, the total number of stopped muons is also fixed, which in turn sets the DIO background rate for a given momentum threshold. All signal acceptance parameters were held fixed, except for the efficiency of the momentum threshold, which when combined with the number of stopped muons determines the SES. The SES is indicated in the number along the lines in units of 1×10^{-17} .

energy losses in the material of the target, beamline, and detector, as well as a 200 keV/c Gaussian resolution function. In addition, all the acceptance parameters of the sensitivity chapter were held fixed, except for the momentum cut efficiency.

The fact that the run-time, signal acceptance, and background rate depend so strongly on the momentum threshold makes the theoretical prediction for the DIO spectrum particularly important. The two most recent calculations of the high energy tail of the DIO spectrum are shown in Fig. 7.2, as well as the cruder function that fits the whole spectrum range, used in SimG4. The more conservative spectrum from the 2011 paper has been used in this study. However, if one were to use the more recent 2015 spectrum, background rates due to DIO would fall to 0.072 events at the same momentum threshold. This would agree with that papers statement that the inclusion of radiative corrections suppresses the DIO background by 15% at the end-point.

In total, based on the 2011 DIO spectrum, 14×10^{-17} electrons would be produced per muon stop with momentum greater than 104 MeV/c. Therefore, the DIO rejection

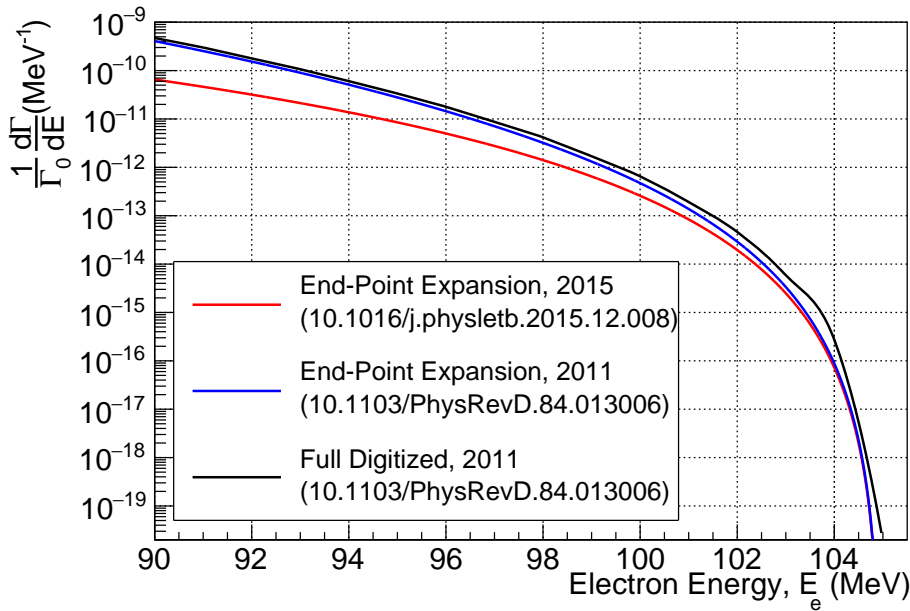


Figure 7.2.: Comparison of the various available end-point expansions. The red and blue lines show the parametrisations reported in the literature, whilst the black shows the digitisation of the spectrum used in SimG4. For this study, the more conservative parametrisation from the 2011 Czarnecki paper [38] has been used.

efficiency, including both geometric effects and the threshold on the detected momentum, suppress the detection of DIO end-point electrons by about 98.4%.

7.2. Radiative Muon Capture (RMC)

During the process of nuclear muon capture, there is a finite probability of a hard photon being radiated from the muon, nucleus, or the exchanged W -boson. This is known as Radiative Muon Capture (RMC) and is distinguished from radioactive gamma-ray production during nuclear de-excitation or decay of the daughter nucleus. The maximum energy this photon can take, $\max(E_e^{\text{RMC}})$, differs from the μ - e conversion signal and DIO end-point by the minimum energy needed to change the nucleus from $N(A, Z)$ to $N(A, Z - 1)$:

$$\max(E_e^{\text{RMC}}) = (M_\mu - B_{\mu, \text{binding}} - E_{\text{rec}}) - (M_{N_2} + \sum_i M_{h_i} - M_{N_1} - \Delta Z \cdot M_e), \quad (7.1)$$

$$= E_e^{\text{Conversion}} - \Delta M, \quad (7.2)$$

Reaction	Atomic Mass of Daughter (u)	ΔM (MeV/c ²)	$\max(E_e^{\text{RMC}})$ (MeV/c ²)
$^{27}\text{Al}(\mu, \gamma\nu)^{27}\text{Mg}$	26.984 341	3.12	101.85
$^{27}\text{Al}(\mu, \gamma\nu 2n)^{26}\text{Mg}$	25.982 593	9.56	95.41
$^{27}\text{Al}(\mu, \gamma\nu 2n)^{25}\text{Mg}$	24.985 837	20.66	84.31
$^{27}\text{Al}(\mu, \gamma\nu p)^{26}\text{Na}$	25.992 633	18.13	87.37
$^{27}\text{Al}(\mu, \gamma\nu np)^{25}\text{Na}$	24.989 954	23.71	81.77
$^{27}\text{Al}(\mu, \gamma\nu d)^{25}\text{Na}$	24.989 954	21.49	84.00
$^{27}\text{Al}(\mu, \gamma\nu \alpha)^{23}\text{Na}$	22.994 467	15.49	91.01

Table 7.1.: Several potential daughter nuclei of nuclear muon capture in ^{27}Al . The mass of ^{27}Al is 26.98153863 u , and one u is taken as 931.494061 MeV/c² [75]. All masses come from [20].

with M_{N_1} and M_{N_2} the mass of the parent and daughter nuclei respectively, and M_{h_i} the mass of the i -th hadron (proton, neutron, alpha, etc.). The mass of the electron, M_e , must also be included since for ever proton removed from the nucleus, given by ΔZ , a free electron must be ejected from the atomic orbitals. ΔM is then the total energy lost to changes in the atomic mass¹ of the nuclei and other emitted hadrons.

When an aluminium-27 nucleus captures a muon various daughter nuclei are possible. If no other particles are emitted, as part of a prompt process or direct nucleon capture, the daughter nucleus will be magnesium-27. In general, this could be left in an excited state, but to reach the end-point of the RMC spectrum it will be left in the ground-state configuration. The atomic mass difference between these two nuclei is shown in Table 7.1, where it can be seen the RMC end-point is separated from the μ - e conversion signal energy by around 3 MeV.

Fig. 7.3 shows the summary table of experimental data on Aluminium, taken from the summary by Gorringe [54]. It is interesting to note that in all experiments to date none of the empirical fits to RMC used have suggested an end-point above 90.1 MeV [18, 24, 46]. This is close to the end-point predicted by the various transitions besides $^{27}\text{Al}(\mu, \gamma\nu)^{27}\text{Mg}$. The most recent of these two experiments both measure the branching ratio for RMC producing photons with $E > 57$ MeV to ordinary muon capture to be 1.43×10^{-5} .

¹ One has to think of the atomic mass difference, rather than the nuclear mass difference. The distinction is important since consideration of the nuclear masses alone would ignore the effect on the atomic electrons. Under nuclear muon capture (radiative or otherwise), the number of protons in the nucleus is reduced by at least one, and accordingly atomic electrons become unbound. The notation here follows that of the COMET TDR [80] and CDR [35], where the electron mass is absorbed into the value of ΔM (although there it is called Δ_{Z-1}).

Target	α	$R_\gamma (\times 10^{-5})$	k_{\max} (MeV)
Bergbusch <i>et al.</i> (1999)			
$^{27}_{13}\text{Al}$	0.077	1.43 ± 0.11	90.1 ± 1.8
$^{28}_{14}\text{Si}$	0.000	2.09 ± 0.20	89.4 ± 1.8
Armstrong <i>et al.</i> (1992)			
$^{27}_{13}\text{Al}$	0.077	1.43 ± 0.13	90.0 ± 2.0
$^{28}_{14}\text{Si}$	0.000	1.93 ± 0.18	92.0 ± 2.0
Döbeli <i>et al.</i> (1986)			
$^{27}_{13}\text{Al}$	0.077	1.83 ± 0.26	88.8 ± 1.8

Figure 7.3.: Summary of experimental values of the rate of RMC producing photons with energy greater than 57 MeV, and the observed end-point, reproduced from [54]. The column labelled ‘ α ’ is the neutron excess for the element, determined by: $\alpha = (A - 2Z)/Z$.

To produce a background event in the detector, the high energy photons produced from RMC must be produced to a high energy electron. Asymmetric pair production from this photon is one such process, although producing the positron at rest is highly suppressed. In addition, around 1 MeV is consumed by the mass of the electron-positron pair. Compton scattering provides another mechanism by which the high-energy photon can convert to a high-energy electron. In the limit where the photon is reflected directly back, the resultant electron is around $M_e/2$ more energy than the incoming photon. As such it is Compton scattering which is more of a concern for COMET.

Finally, given the maximum photon energy is below the momentum threshold of 104.2 MeV/c, the energy needs to be mis-reconstructed by around 2.4 MeV. If the final resolution function were Gaussian with a 200 keV/c width (at signal energies), then mis-reconstruction by such an amount would be an 11σ event, i.e. $P(p_{\text{recon}} - p_{\text{true}} > 2.4 \text{ MeV}/c) = 1.9 \times 10^{-28}$. However, the resolution function is not likely to be a pure Gaussian. On-going studies for reconstruction with the Phase-I StrECAL currently suggest that $P(p_{\text{recon}} - p_{\text{true}} > 2.4 \text{ MeV}/c) = 7.5 \times 10^{-3}$ [6]. Although this is considerably larger than the pure Gaussian, this is based on the most preliminary results of reconstruction algorithms. If need be, cuts on fit quality can be improved over the current Phase-I values; the sensitivity estimate presented here should be robust against this since it includes the CDR estimate for the signal efficiency of such a cut.

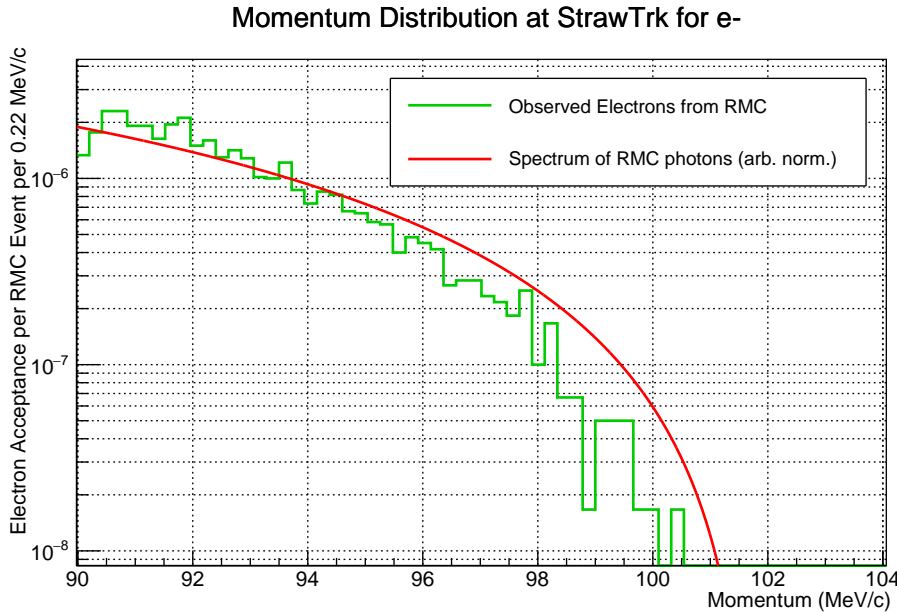


Figure 7.4.: Observed electrons from a simulation of 6×10^7 **RMC** photons. The overlaid spectrum is normalised arbitrarily to fit on the plot.

7.2.1. Calculation and Simulation of RMC

Conversion of the RMC photons can take place in any of the material around the target, such as the beam blocker, solenoids, or cryostat. To estimate the acceptance of the electrons produced from this conversion a simulation was performed where RMC photons were input at the stopping target, using the realistic muon stopping distribution obtained previously. Geant4 implements the process of photo conversion via both of the above methods.

To build a realistic end-point spectrum, the same recipe as used in the Phase-I TDR was applied [80]. The spectrum shape near the end-point is modelled by the equation [33]:

$$\Gamma(\text{RMC}) \propto (1 - 2x + 2x^2)(x)(1 - x)^2, \quad (7.3)$$

where $x = E_\gamma / \max(E_e^{\text{RMC}})$. The largest observed branching ratio for **RMC** – 1.83×10^{-5} compared to ordinary muon capture – is used to set the normalisation. The relative rate of **RMC** resulting in photons with energies above 90 MeV is, based on the spectrum in equation (7.3), 7.7×10^{-3} of the experimentally observed rate.

Given the total number of muon stops during Phase-II, the probability of ordinary muon capture, and the relative rates for **RMC**, one expects some 1.2×10^{11} photons

to be produced in the target with energies above 95 MeV. Since this is an intrinsic background, the lifetime of this process will be the same as for signal events. Assuming, therefore, the same timing window acceptance, and applying the same reconstruction and TDAQ efficiencies as for signal, this number is reduced to 3.3×10^{10} . If the resolution function were truly a 200 keV/c Gaussian, then this would be no issue, regardless of the geometric acceptance or probability of Compton scattering. If, however, the current Phase-I high-energy reconstruction tail were present, we would expect some 2.4×10^8 events to be considered dangerous if they were all accepted.

To check the geometric acceptance of the beamline, some 6×10^7 RMC events were generated in the stopping target, with initial photon energies greater than 90 MeV and distributed according to the spectrum in equation (7.3). Fig. 7.4 shows the momentum and rate at which these were detected. Based on this, the fraction of events reaching the detector with momentum larger than 98 MeV/c was 6.2×10^{-7} , whilst above 100 MeV/c only 3.3×10^{-8} electrons per $\text{RMC}|_{p>90}$ event were detected.

As a result, if the current Phase-I resolution were applied, we would expect around 8 background events during the entire run. However, since the resolution function at this stage is so poorly known, it seems premature to define a value. Instead, the predicted RMC rate provides a constraint on the high-energy tail of the resolution function: to do better than 0.1 background events during Phase-II from RMC, fewer than 1 in 1×10^4 high-energy electrons can be reconstructed with a momentum more than 2.4 MeV/c larger than the true value.

7.2.2. Aluminium-26 and RMC

Based on the above energy calculation, the end-point for RMC against ^{26}Al (to ^{26}Mg with no other particles emitted) would be 108.5 MeV. Clearly such photons would be extremely dangerous to COMET if they are produced.

Aluminium-26 comes in two isomers, one with a half-life of around 6 seconds [50], the other lasting around 700 thousand years [20]. Since Al-26 is unstable its abundance in natural aluminium is low. However, it can be produced by various methods, such as proton and deuteron bombardment of magnesium and sodium, or photoneutron emission of the aluminium-27 isotope [83]. With such production mechanisms, it is likely that aluminium-26 will be produced in the COMET stopping target, via the interaction of daughter nuclei of muon capture (which are typically magnesium and sodium) with

protons, deuterons, gammas, and neutrons coming from either the beam or as products of muon capture. The exact rate of Al-26 production, however, is a complicated value to estimate and one that unfortunately cannot be estimated here.

One can, however, set an acceptable rate of production if the induced background event rate is to be kept at the level of 0.1 events. Based on the previous simulation of Al-27 RMC, the probability of an electron being detected within 5 MeV of the RMC end-point is 5.6×10^{-18} per nuclear muon capture. With 1.40×10^{18} muon stops during Phase-II, and assuming that the branching ratios for both ordinary and radiative muon capture are the same for Al-26 and Al-27 (61%), then the concentration of Al-26 in the stopping target must be less than 1% (by number density) on average during the entire Phase-II run. The branching ratio for radiative muon capture is, in reality, likely to be slightly more than in Al-27, based on the fact that the neutron excess of a given isotope seems a better indicator of the branching ratio than atomic number, and that the two are anti-correlated [54].

Clearly though, there is more work to be done on this, including a better understanding of RMC events coming from Al-26, as well as understanding the rate of Al-26 production from muon beams. Data from the AlCap experiment might be able to help with this, however, since the production rate could depend a lot on the exact beam conditions, measuring this directly should be an important goal of Phase-I.

Finally, if this does produce a sizeable background contribution, one can imagine several techniques to mitigate or reduce the challenge this poses. Provided one can measure the concentration of Al-26 in the stopping target at the end of the run, and ideally at various stages whilst running, then the number of backgrounds can be predicted and possibly subtracted. Additionally, it could be possible to remove the stopping target and replace it with a fresh one such that the Al-26 concentration never rises beyond an unsafe level.

CHECK: *Mention that this could be a useful source of calibration*

7.3. Radiative Pion Capture (**RPC**)

When low-energy negative pions are stopped in material they behave similarly to negative muons and form pionic atoms. The probability that the pion is then captured by the nucleus rather than decays in orbit is, however, considerably larger than for a muon.

Furthermore, given the extra $30 \text{ MeV}/c^2$ of the pion mass and the lack of an outgoing neutrino, the end-point for Radiative Pion Capture ([RPC](#)) by the nucleus is well above the μ - e conversion signal energy. As for photons of [RMC](#), the [RPC](#) photons can then be converted via Compton scattering or pair production to signal-like electrons. Pion capture could, therefore, be a dangerous source of backgrounds and was likely the dominant source of background events at SINDRUM-II.

Since the pion interacts via the strong force, negative pions capture almost immediately in the nucleus, on the order of picoseconds [48]. The timing of backgrounds caused from pion capture are therefore determined predominantly by the time when the pion was produced. If a background arises from pion capture and the pion was produced in the main muon pulse, then the pion or resultant background electron must have been significantly delayed. Delayed [RPC](#) backgrounds are therefore suppressed by the time-gated detector window. If however a background arises because the pion was produced outside of the main proton pulse, due to late-arriving protons (or from antiprotons, but we will treat these separately below), then this background is considered prompt. These prompt [RPC](#) background events are, therefore, suppressed by the extinction factor.

The background rate per [POT](#) for prompt and delayed pions is therefore:

$$R_{\text{prompt}} = R_{\pi/p} \mathcal{B}_{\text{RMC}} f_{e,\text{RMC}} A_{\text{time}}, \quad (7.4)$$

$$R_{\text{prompt}} = R_{\pi/p} \mathcal{B}_{\text{RMC}} f_{e,\text{RMC}} \epsilon_{\text{extinction}}, \quad (7.5)$$

where $R_{\pi/p}$ is the pion stopping rate per [POT](#) and \mathcal{B}_{RMC} is the branching ratio of [RMC](#) for stopped pions. $\epsilon_{\text{extinction}}$ is the extinction factor, whereas A_{time} is the acceptance of the time-gated detector window to RMC electrons. $f_{e,\text{RMC}}$ is the probability that an RMC photon converts to an electron which reaches the detector with signal-like momentum. To a reasonable approximation, this can be factorised as:

$$f_{e,\text{RMC}} = f_{\gamma \rightarrow e^-} A_{\text{geom}} A_{\text{mom}} \quad (7.6)$$

where $f_{\gamma \rightarrow e^-}$ is the conversion rate of RMC photons to an electron, A_{geom} and A_{mom} are, respectively, the geometric acceptance and momentum cut efficiency for such electrons. However, such a factorisation misses out various correlations, such as where in the experiment the conversion takes place and at what momentum the secondary electron is produced, so that only a single value for $f_{e,\text{RMC}}$ will be reported here.

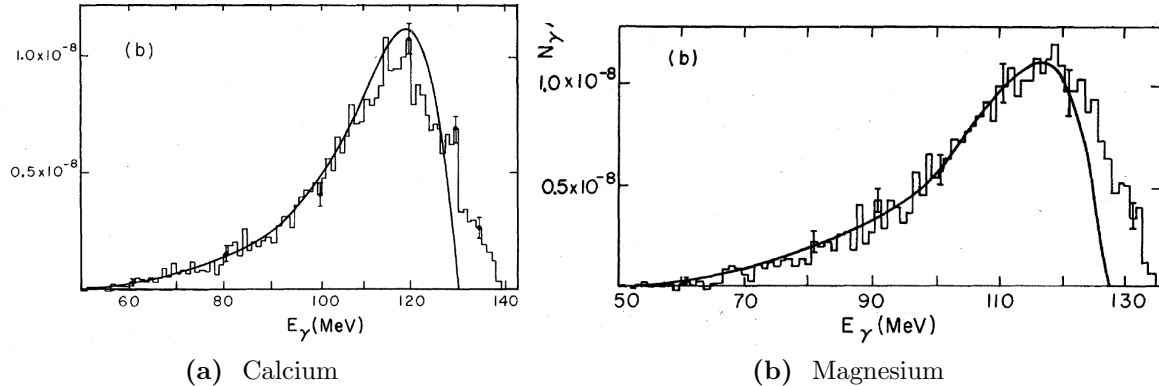


Figure 7.5.: Spectrum of photons coming from Radiative Pion Capture (RPC) [26]. The spectrum of manesium, which is adjacent to aluminium on the periodic table, was used as the basis of these studies.

7.3.1. Photons from Radiative Pion Capture (RPC)

There is a range of experimental and theoretical data on RPC. Fig. ?? shows what is perhaps the most useful data currently available: the observed spectrum of photons coming from RPC for magnesium and calcium. Magnesium being adjacent to aluminium on the periodic table, this spectrum is a reasonable proxy for the spectrum of RPC on aluminium. The relative rate for RPC compared to ordinary pion capture is discussed in Amaro et al. [15]. For experimental and theoretical studies of the three isotopes summarised in that paper — carbon, oxygen, and calcium — the measured and predicted branching ratios are all within 1.19% and 2.27%. To be conservative, we take here the branching ratio for RPC on aluminium to be the largest of these as 2.27%.

7.3.2. Pion Stopping Rate

To simulate the pion stopping rate, the pions from the main production simulation were resample multiple times to build up a large number of pion stops. Fig. 7.6 shows the distribution of pions stopping in the target, in one-dimensional projections to the ICEDUST global coordinate system. In that coordinate system, pions arrive from large values of Z at the target, so the pion beam in Fig. 7.6c is going from right to left. By comparison with the plots in Fig. 6.2, pions tend to stop further downstream in the target. This is readily understood by the fact that pions reaching the stopping target tend to have much higher momentum than muons reaching the target, as shown in Fig. 7.7.

In total, the number of pions stopping in the target per POT is $R_{\pi/p} = 4.33 \times 10^{-7}$.

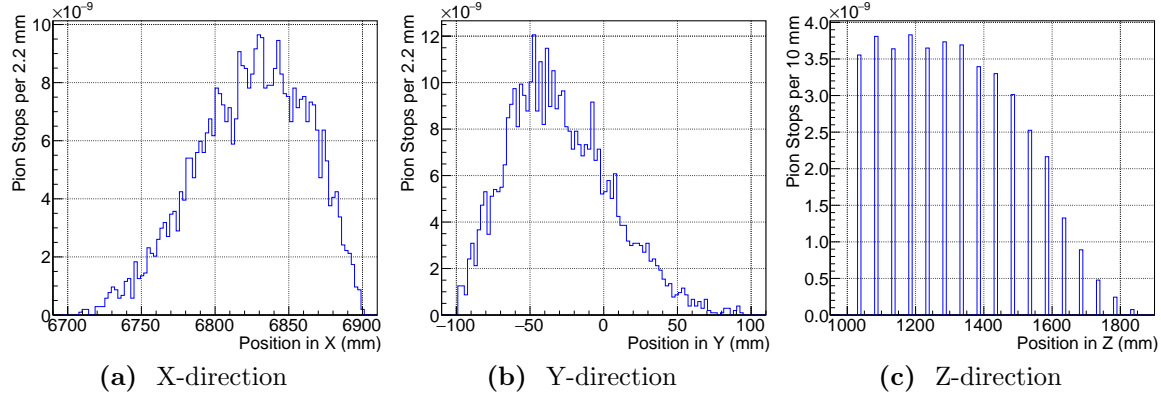


Figure 7.6.: Stopping distributions of pions in the target. These distributions have considerably different forms to the muon stopping distributions shown in Fig. 6.2, mostly due to the different momenta of muons and pions.

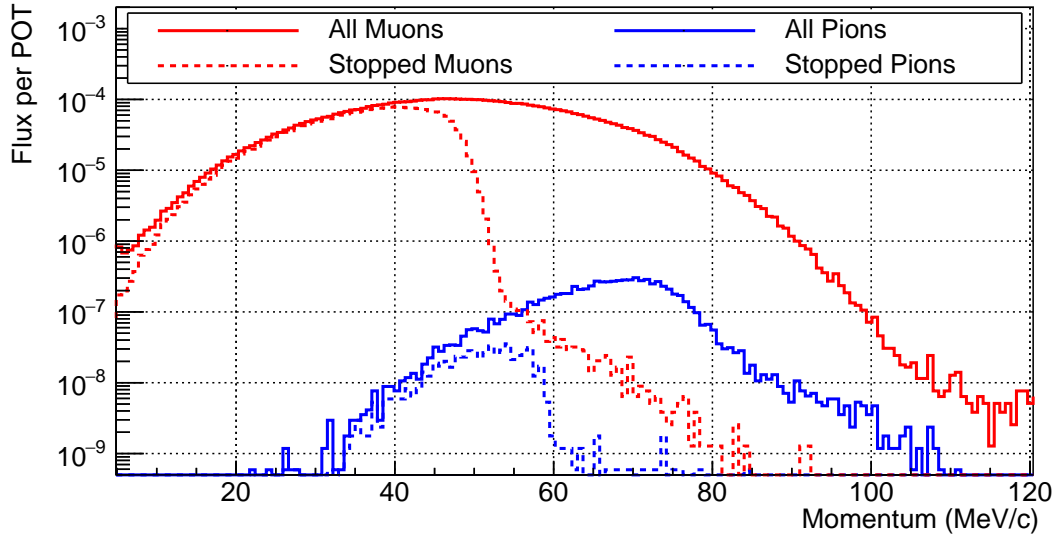


Figure 7.7.: The momentum of muons and pions for those that reach the target area and those that actually stop. It is clear how the pion momenta are in general higher, including those that stop, although the maximum stopping momentum for pions is similar to that of muons.

7.3.3. Simulating RPC

Using the realistic pion stopping distribution shown in Fig. 7.6, RPC photons were generated in the target and Geant4 used to convert and track electrons resulting from this process. To model the distribution of photon energies from RPC, the experimentally obtained spectrum from magnesium of ref. [26] was used. To build the model, the raw spectrum was first digitised and then smoothed, using ‘TGraphSmooth::SuperSmooth()’ from the ROOT library [31]. These steps are shown in Fig. 7.8.

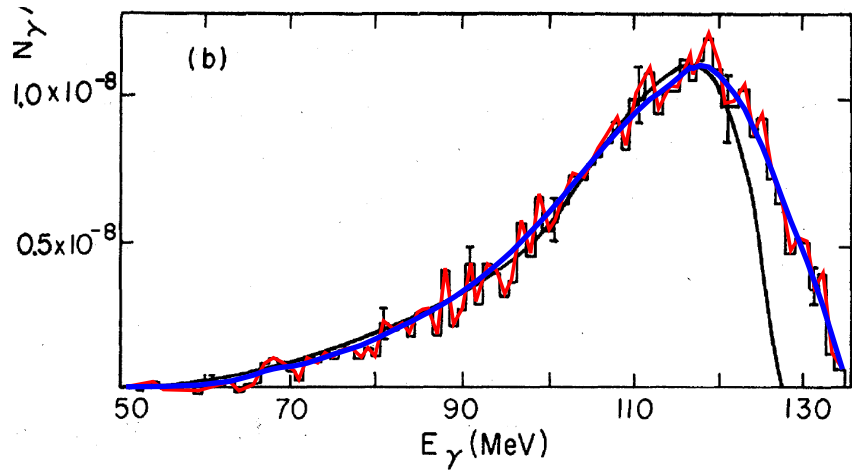


Figure 7.8.: Digitised (red) and smoothed (blue) spectrum of RPC from magnesium (see Fig. 7.5b) used as input to the Monte Carlo simulation.

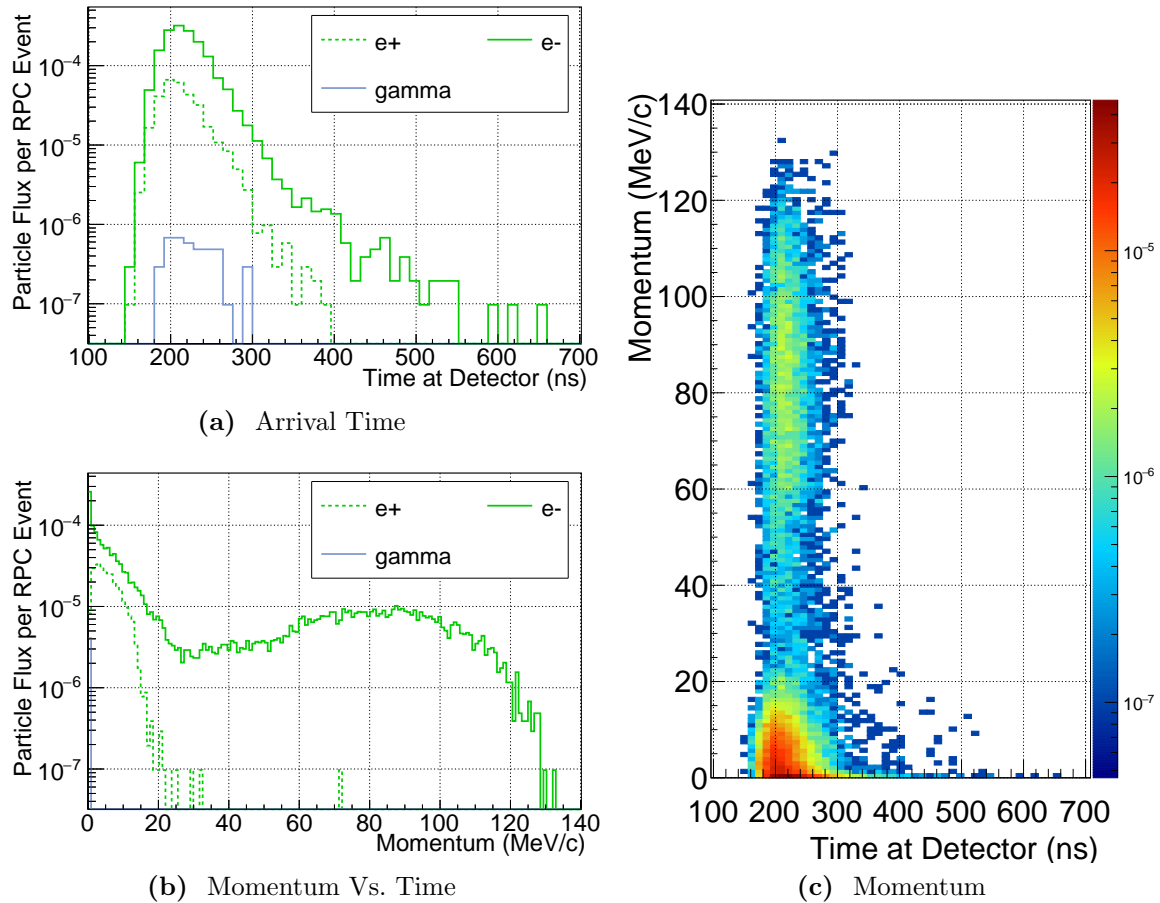


Figure 7.9.: Detection of secondaries from RPC photons in the target. Although many high-momentum electrons are detected, they are all well before the time-gated detected window.

Parameter	Value	Description
$R_{\pi/p}$	4.33×10^{-7}	Pion stopping rate per POT
\mathcal{B}_{RPC}	2.27×10^{-2}	Branching ratio of RPC
$f_{e,\text{RPC}}$	1.05×10^{-5}	Probability of an RPC photon producing signal-like electrons in the detector
A_{time}	9.51×10^{-15}	Acceptance of timing window to secondary electrons from RPC
$\epsilon_{\text{extinction}}$	1.00×10^{-12}	Extinction factor

Table 7.2.: Parameters and their values in the determination of the RPC background rate.

Based on a simulation of 4×10^6 RPC photons, the distribution of electrons and positrons reaching the detector was obtained. The timing and momentum of such electrons is shown in Fig. 7.9, where it is clear that although many signal-like electrons are detected, they all arrive well before the gated-time threshold of 600 ns.

The probability of an RPC photon producing an electron that reaches the detector with momentum between 104.2 MeV/c and 105 MeV/c is: $f_{e,\text{RMC}} = 1.05 \times 10^{-5}$. To estimate the rate of delayed RPC backgrounds, we also need to know the value of A_{time} . As can be seen in Fig. 7.9b, the timing for electrons originating from RPC photons and detected with momentum greater than 30 MeV/c is independent of the momentum. By fitting the tail of this distribution with a single exponential, the lifetime of the high energy electrons is found to be 18.6 ns, such that with the timing window between 600 and 1200 ns we find the acceptance of the timing window to be: $A_{\text{time}} = 9.51 \times 10^{-15}$.

Table 7.2 summarizes these numbers, from which we find that the rate of backgrounds for delayed RPC is 1.82×10^{-25} per POT, whilst the prompt form occurs at 1.73×10^{-27} .

7.4. Antiprotons in the Beam

Antiprotons can be produced when the primary 8 GeV proton beam interacts with the production target, creating a proton–antiproton pair:

$$p + N(A, Z) \rightarrow p + N^*(A, Z) + p + \bar{p} \quad (7.7)$$

Given their relatively large mass, antiprotons travel much more slowly than other products of the same momentum which results in a smearing of the beam’s time structure for antiprotons and their secondaries. The pulsed beam and time-gated detector window are, therefore, less effective at suppressing the induced backgrounds.

The interaction of antiprotons with matter has a strong analogy with muons and negative pions, particularly at low energies, when the antiprotons stop. In matter, antiprotons with energies of a few tens of keV — similar to that of atomic electrons — can become bound in the Coulomb potential of the atom’s nucleus. X-rays emitted in the ensuing electromagnetic cascade are typically not more than a 100 keV [17]. Unlike for muons, the antiproton will only rarely reach the atomic ground state, before the interaction with the nucleus takes over. This interaction can take the form of an immediate annihilation or the formation of a composite nucleus where the antiproton is now bound within the nuclear potential [71, 86]. The binding energy of some of these nuclear levels can reach up to hundreds of MeV, and so in the transition, pions and other hadrons can be readily produced. Eventually though the antiproton will annihilate in the nucleus, producing large multiplicities of pions and other mesons.

As such, although antiprotons themselves are not an immediate source of high energy photons or electrons, they are an additional source of pions, which can produce backgrounds via Radiative Pion Capture ([RPC](#)).

7.4.1. Antiproton Production Rate and Spectrum

The literature on antiproton production with 8 GeV protons on a tungsten target and at large angles is somewhat lacking. Accordingly most hadron models are particularly under-constrained when it comes to antiproton production. The QGSP_BERT_HP model used as the basis for SimG4 is, in fact, completely unable to produce antiprotons.

In the COMET TDR [80], the yield of antiprotons per [POT](#) is given as 4×10^{-5} , based on the results of a MARS simulation performed for the MEKO experiment [44]. Based on this, simulations of antiprotons showed that absorber foils would be needed along the beamline. Since the Phase-II geometry in ICEDUST re-uses most of the implementation for the Production Target Capture and Torus1 sections, the upstream absorbers are also contained in the geometry used to study antiprotons here, although the absorber near 90° has been removed.

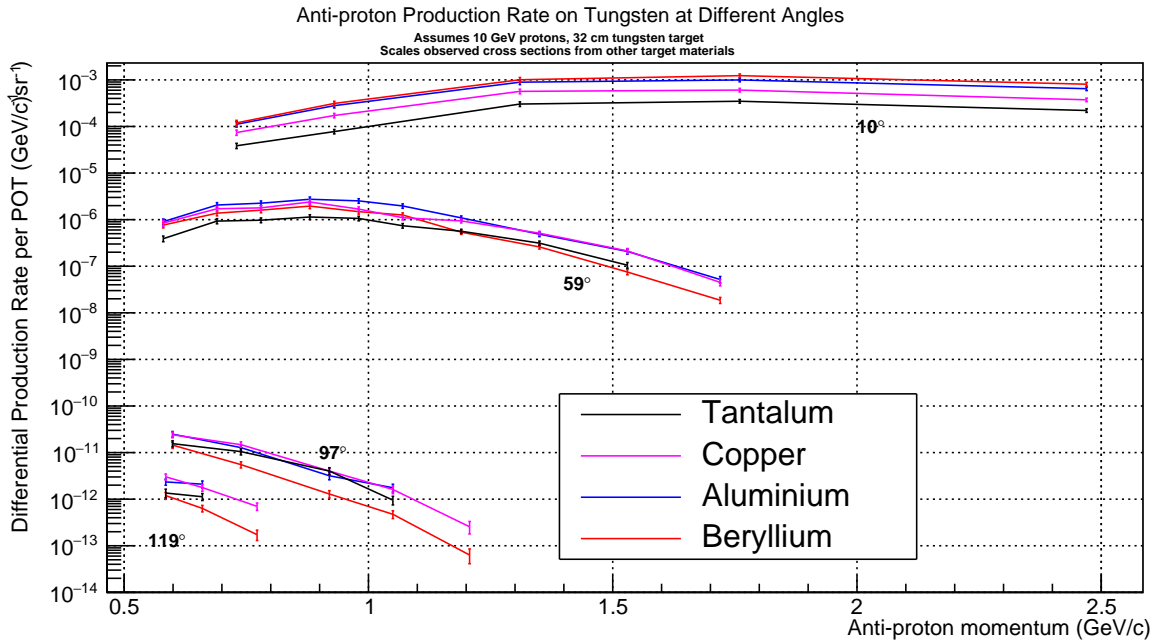


Figure 7.10.: Experimental data for antiproton production rates for 10 GeV protons [28, 63]. Each line represents the cross section obtained for the four different target materials covered in those papers, scaled to match the number of nucleons of tungsten and with the additional factors of (7.9) included.

Whilst tungsten targets have not been studied at the relevant angles and proton energies, a set of papers [28, 63] do exist covering antiproton production up to 2 radians for tantalum (which is adjacent to tungsten on the periodic table), copper, aluminium, and beryllium targets and using 10 GeV protons. Between them, these two papers provide the invariant triple-differential cross section as a function of antiproton momentum for production angles of 10, 59, 97 and 119°, defined as:

$$F(p, \theta, \phi) = E \frac{d^3\sigma}{dp^3} = E \frac{d^3\sigma(p, \theta, \phi)}{p^2 dp d\Omega} \quad (7.8)$$

where E and p are the antiproton energy and momentum. The earlier Boyarinov paper actually reports $f = F/A$, where A is the relative atomic mass of the nucleus. Fig. 7.10 shows the data from these papers converted to the relative rate such a cross section would imply for the Phase-II tungsten target. From the measured cross sections, it is clear that as you move to larger angles, the spectrum becomes considerably softer whilst the overall rate falls quickly, in much the same way as for pion production. To convert the differential invariant cross sections given in the literature (equation (7.8)) into a

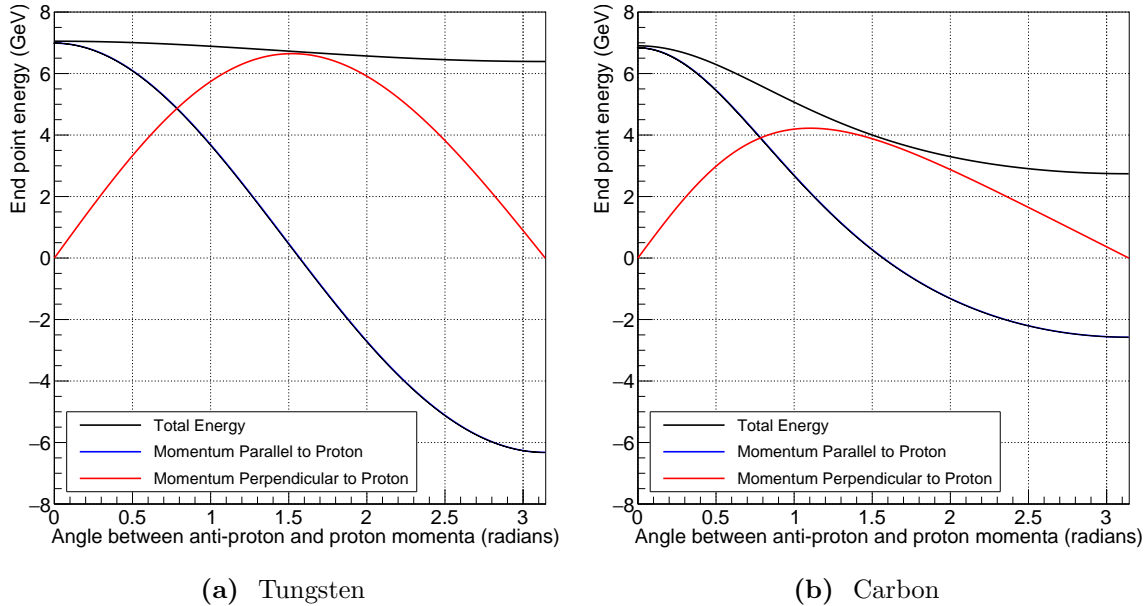


Figure 7.11.: The kinematic end-point for antiproton production as a function of the outgoing antiproton direction with respect to the incoming proton in the frame of the target nucleus (the lab frame). The absolute end-point is only achieved when the nucleus and out-going protons recoil coherently.

differential production rate per POT, $d^3R(\theta)/dpd\Omega$, the following formula is used:

$$\frac{d^3R(p, \theta, \phi)}{dp^3} = \frac{F(p, \theta, \phi)}{E} \frac{\rho N_A l}{m_N} \quad (7.9)$$

where ρ is the mass density of the target, 19.25 g/cm³ for Tungsten, m_N the atomic mass, 183.86 g/mol for tungsten, l the length of the target, and N_A is Avodadro's number.

To build the limited number of data-points from this paper into a complete but conservative spectrum, empirical fits to the data were performed after adding two data points for the minimum and maximum momentum. The minimum momentum only added the constraint that at zero momentum the cross section also be zero. On the other hand, to calculate the maximum momentum the kinematic end-point was found by considering the entire nucleus and the two out-going protons to recoil directly against the antiproton. The value of the end-point kinetic energy and longitudinal and transverse momenta for tungsten and carbon are shown in Fig. 7.11 using the formulae derived in appendix B. This end-point will be a highly conservative estimate, since in reality not all the nucleus will recoil coherently; the de Broglie wavelength for a proton with 8 GeV kinetic energy is

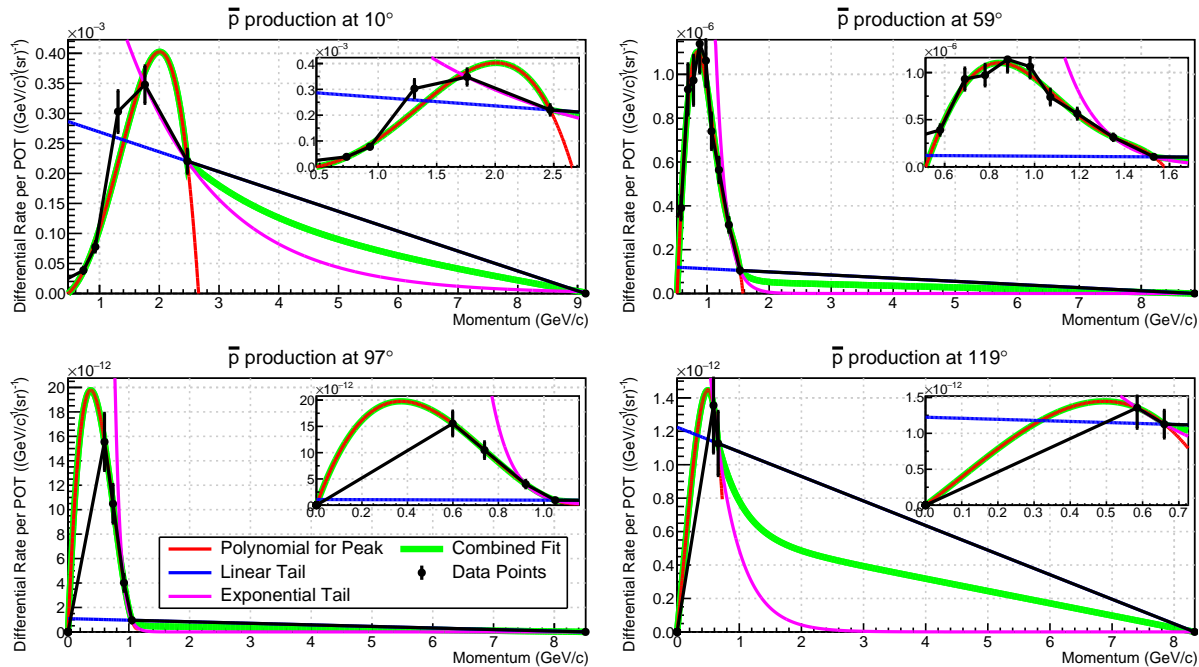


Figure 7.12.: Piecewise fitting to experimental data and kinematic end-points. Inlays show a zoom around the experimental data points.

about 0.15 fm, compared to the 7 fm or so of a tungsten nucleus². Additionally, achieving this end-point configuration would be highly phase-space suppressed.

With the addition of these two end-points, to interpolate and extrapolate the data, a polynomial of order 4 to 6 (depending on the number of available data points) was used to fit from zero up to the last experimental datum. For the high-momentum tails of each spectrum, two fits were tried: a straight line fit between the last experimental datum and the kinematic end-point described above; and an exponential fitted to the kinematic end-point and the last two experimental data points. Fig. 7.12 shows the results of this fitting procedure, where it can be seen that a low momentum peak is visible and a high momentum tail well described. Whilst these spectra are likely a poor representation of the true production spectrum, they serve as useful upper bounds which can be used as inputs for the antiproton background rate estimation.

² Antiproton production from protons in this energy regime was historically referred to as ‘sub-threshold production’, since it is below the threshold for single nucleon interactions, around 5.6 GeV. The fact antiprotons are observed is therefore proof that it is not a single, stationary nucleon that interacts with the proton and the nuclear environment as a whole must be considered. The older literature on this topic in fact refers to a parameter called the ‘cumulative number’ which was related to the number of nucleons that must be involved to produce secondary hadrons (e.g. antiprotons or pions) with such out-going energies, given the incoming proton energy. These sub-threshold secondary particles were themselves sometimes called cumulative particles.

7.4.2. Simulating Antiprotons

To study the resultant backgrounds, antiprotons were generated uniformly in the production target. Four separate simulations were run, corresponding to the four angular regions provided by the data, as shown in Table 7.3. For each simulation, antiprotons were generated isotropically within a cone parallel to the incoming proton beam, with minimum and maximum values of theta defined by the angular region being studied. The momentum distribution for each simulation used the fit to the data for the angle at the lower edge of the region, θ_{\min} (and for the region from $0 - 59^\circ$, the fit to the 10° data was used).

To account for the strong angular dependence visible from the measurements, each input antiproton event was reweighted during analysis based on the angle between the initial antiproton direction and the proton beam. The combined procedure of generating isotropically with a momentum distribution based on the fit to the data, then reweighting based on the angle, amounts to the following factorisation of the measured differential cross section:

$$F(p, \theta, \phi) = \left(\frac{E}{p^2} \frac{d\rho(p)}{dp} \right) \left(\frac{1}{2\pi} \frac{d\Theta(\theta)}{d\theta} \right), \quad (7.10)$$

$$= P(p, \theta_{\min}) \Phi(\theta), \quad (7.11)$$

where $P(p, \theta_{\min})$ is the fitted momentum spectrum for the differential rate at the lower angle of the current region, θ_{\min} . $P(p, \theta_{\min})$, therefore, is the probability density function used to generate the momentum for each antiproton in the simulation, and as such the normalisation of $P(p, \theta_{\min})$ is fixed to unity.

Region		Data source	Total \bar{p} per POT
$0 \leq$	$\theta < 59^\circ$	10° [63]	5.26×10^{-5}
$59 \leq$	$\theta < 97^\circ$	59° [63]	4.17×10^{-9}
$97 \leq$	$\theta < 119^\circ$	97° [28]	1.74×10^{-12}
$119 \leq$	$\theta < 180^\circ$	119° [28]	5.71×10^{-13}

Table 7.3.: Regions and fits used to simulate antiproton production. The values in the final column are result of converting to rates per POT and integrating the differential cross-sections measured in [28, 63].

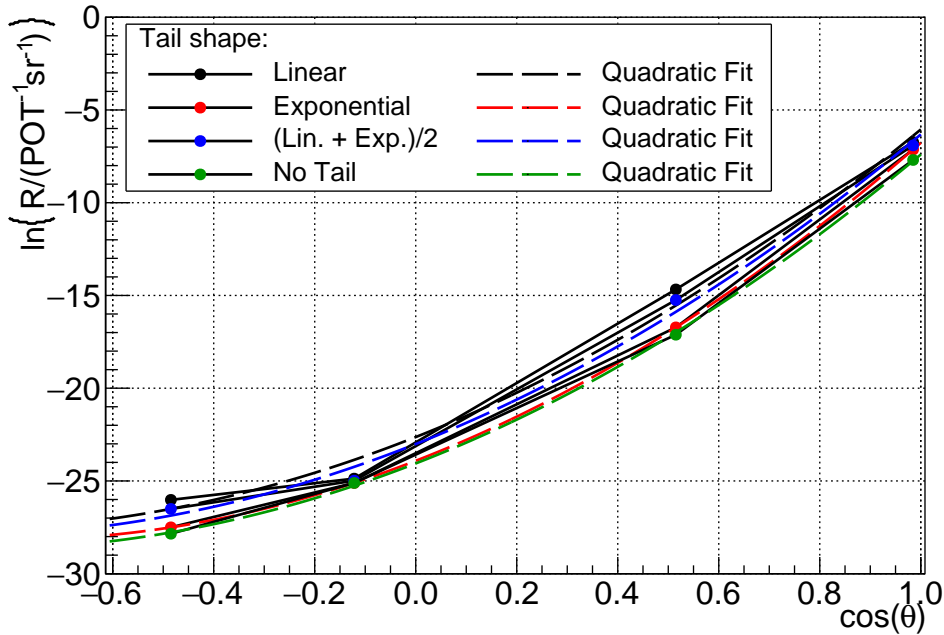


Figure 7.13.: The angular dependence of the rate of antiproton emission, integrated over all momenta. The different lines represent the different fits to the high momentum part of the spectrum. The relationship given in [28] would suggest the data here should fit a straight line. The dashed lines represent instead a quadratic fit to these points, which looks like a better fit. For reweighting events the interpolated (straight solid) lines were used to be conservative.

Instead, $\Phi(\theta)$ is used to provide the event weight. It encapsulates the total probability of an antiproton being produced at the given angle with respect to the incident proton, and is found by integrating the fits shown in Fig. 7.12.

The results of these integrations is shown in Fig. 7.13. Boyarinov et al. state [28] that the angular dependence of antiproton production should take the form:

$$\Phi(\theta) = \alpha e^{\beta \cos \theta} \quad (7.12)$$

where α and β are constants. It is for this reason that the axes of Fig. 7.13 are $\cos \theta$ and $\ln(R)$: if such a function were valid, the points would form a straight line. In fact it seems like a quadratic function might be more appropriate, although the fitted quadratic functions all reach a minimum above $\cos \theta = -1$. To keep things conservative then, instead of a linear or quadratic function fitted to all data points, we use the linear interpolation between each adjacent datum to provide the function, $\Phi(\theta)$. Of the three possible fits to the high momentum tail, the angular dependence obtained by the linear tail is used for the reweighting, again to ensure this simulation be conservative.

Finally, it should be noted that the factorisation in equation (7.10) injects the assumption that the momentum distribution at a given angle is independent of the angle. Whilst this should not be the case for a realistic spectrum, to produce limits on the background rate it is a valid assumption — the spectrum becomes softer with increasing production angle so the spectrum at the smaller angle should be an overestimate. In addition, the ϕ dependence of $\Phi(\theta, \phi)$ is assumed constant, since the target and proton beam in COMET are not polarised.

7.4.3. Results of simulation

Using the procedures described above, a separate simulation was performed for each of the four angular regions listed in Table 7.3, with 8×10^7 antiprotons fed in to each simulation. Within each region, events were generated isotropically and according to the momentum distribution for that region. The beamline's acceptance to antiprotons and the secondary

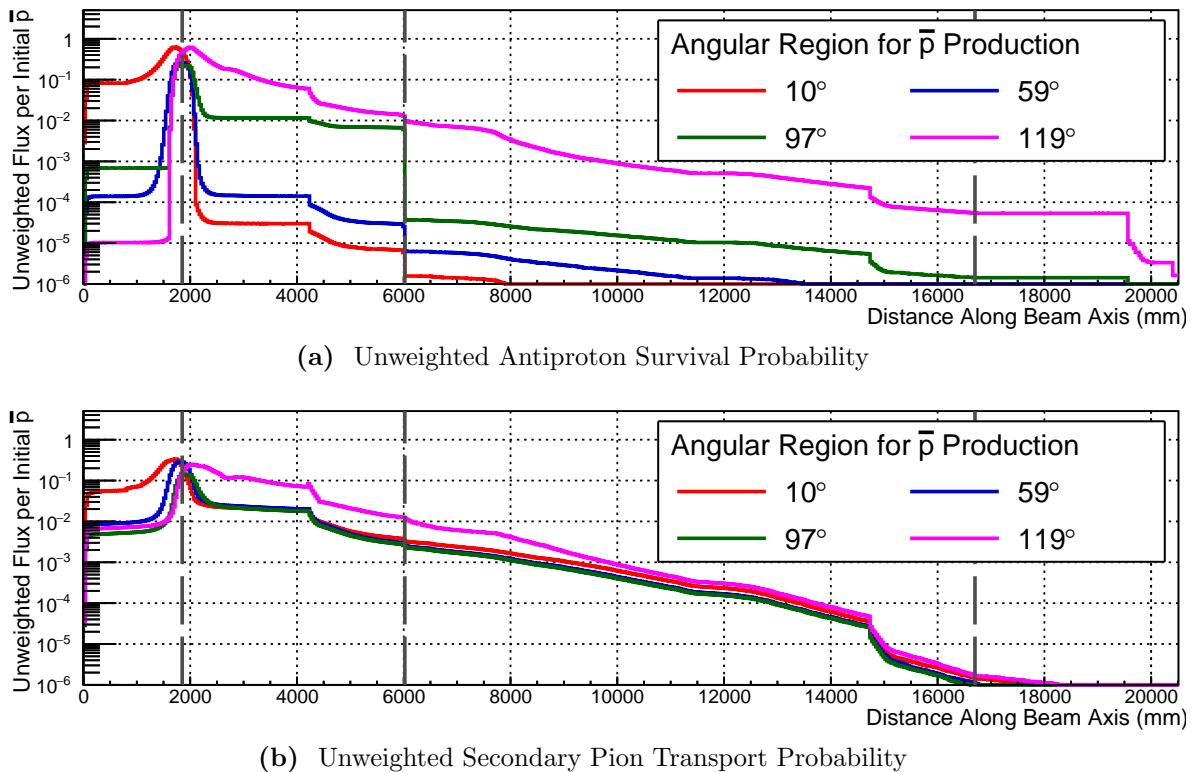


Figure 7.14.: The survival probability of antiprotons and secondaries pions per antiproton produced in the target as a function of distance along the beamline. These plots are not weighted by the probability that an antiproton is produced at a particular angle. From left to right the vertical gray lines indicate the production target, Torus1 entrance, and the Torus2 exit.

pions that they produce is shown in Fig. 7.14. The events in this plot are unweighted by the antiproton angle. From these plots, it is clear that the material at the entrance to the Torus1 solenoid removes a large fraction of the antiprotons—about 99% of the antiprotons produced between 97 and 119°. It can also be seen that the acceptance in the bent solenoids for antiprotons is about two orders of magnitude greater for antiprotons produced at angles greater than 119°, compared to those produced between 97 and 119°. For pion production and acceptance, however, the unweighted rate for the four angular regions is very similar, particularly towards the end of Torus2. It is also clear, given that the transmission probability has a negative gradient for each angular region along the whole beamline, that the main source for pions is the interaction of antiprotons with the primary target. Pions produced by antiprotons hitting collimators or the beampipe will be quickly removed themselves since they will tend to stay close to this material. If pions were produced at the foil at the entrance to the Torus1 then they would be in the centre of the beampipe and have a greater chance of being transported. However, since the pion rate at that point does not seem to increase, based on this work, it does not appear that this is a significant source of pions.

Fig. 7.15 shows the trajectories of antiprotons along the beamline, where each trajectory has been weighted according to the antiproton’s production direction with respect to the proton beam axis. Similarly, Fig. 7.16 shows the same information but for pions instead. The colour scale and range in each of these four plots is the same between all plots. One can see then, that although the acceptance per antiproton is considerably lower for small angle production (0–59°), the production rate is large enough to offset this. As such, it is the antiprotons produced in the forwards direction, followed by a hard scatter within the production target, that will dominate the background rate.

Table 7.4 and Table 7.5 show the number of antiprotons and pions that enter the Torus1 ('Torus1 Entrance'), reached the final collimator ('Before Torus2 Coll.'), and arrived at the target ('Before Target'). Also shown is the sum over all events with each event weighted by the initial antiproton direction, and normalised to the number of antiprotons introduced into the simulation. Since no antiprotons are seen stopping in the target for the angular region from 0 to 59°, to estimate the stopping rate for antiprotons produced in this direction, the probability that antiprotons would reach the stopping target is made by finding the median acceptance of the collimator (which occurs for the region from 59° to 97°) and multiplying the observed weighted sum for antiprotons just before the collimator. The timing distributions for antiprotons and pions is shown in Fig. ??, from

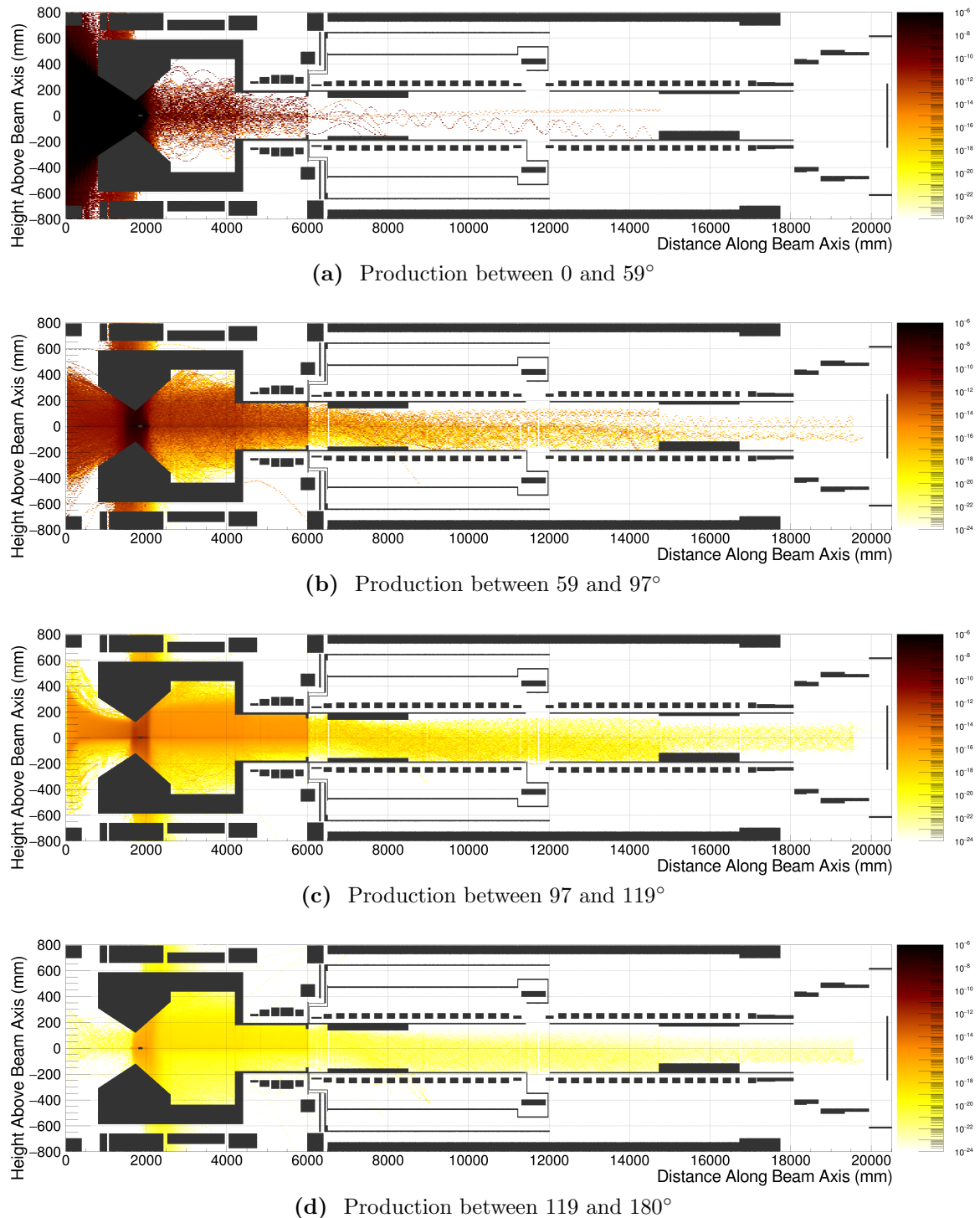


Figure 7.15.: The heights of antiprotons passing along the beamline for the four different angular regions of productions. Each antiproton trajectory is weighted by the probability of producing an antiproton at this angle. The colour scale on all these plots is the same.

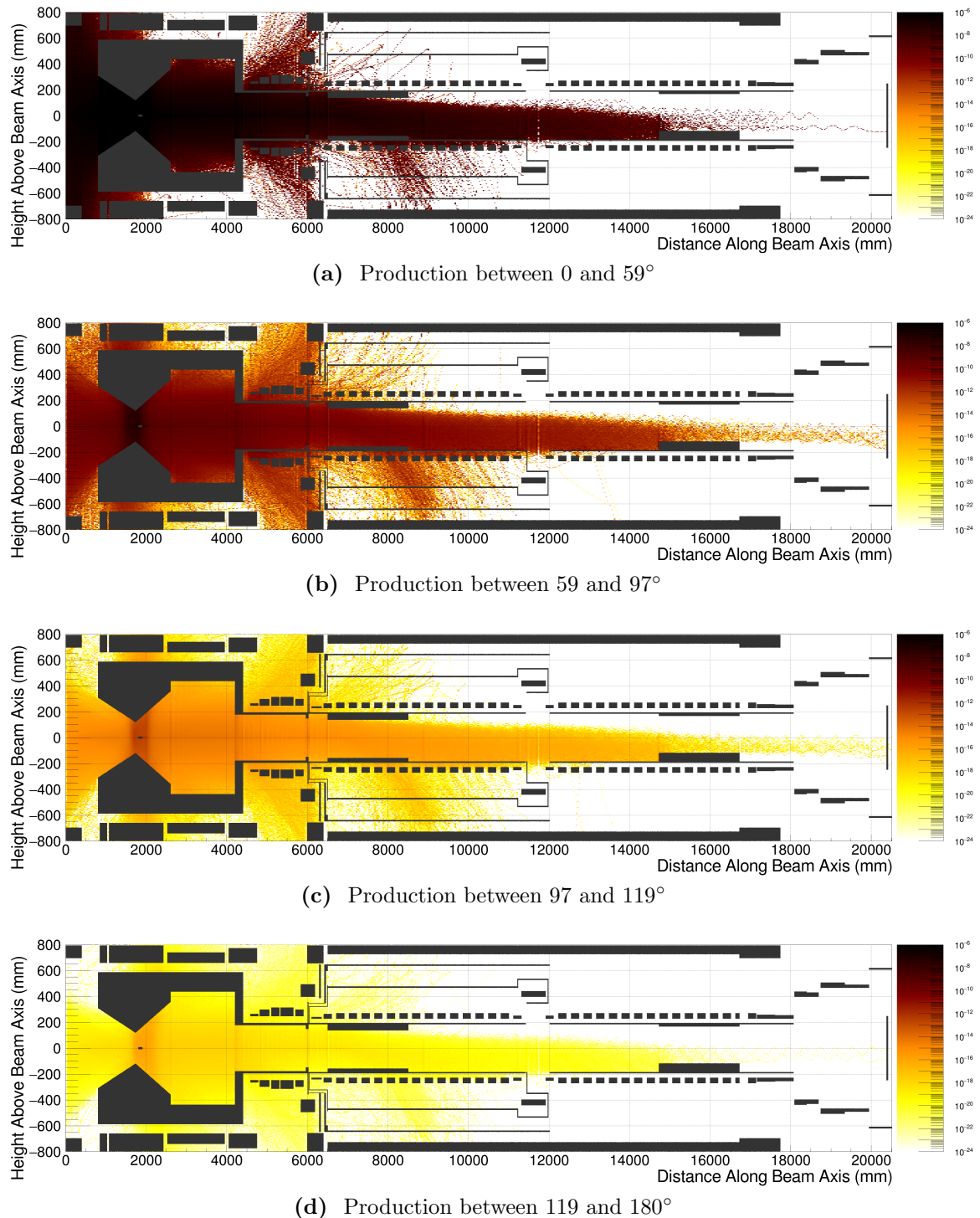


Figure 7.16.: The heights of secondary pions passing along the beamline produced from antiprotons in each of the four different angular regions of productions. Each antiproton trajectory is weighted by the probability of producing the parent antiproton in its initial direction at the target.

Rates for \bar{p} Transport		Angular Region for Antiproton Production			
		$0 \leq \theta < 59^\circ$	$59 \leq \theta < 97^\circ$	$97 \leq \theta < 119^\circ$	$119 \leq \theta < 180^\circ$
Raw Counts	Torus1	7	270	2907	278105
	Torus2	1	39	431	9024
	Target	0	8	114	2237
Weighted Sum	Torus1	1.40×10^{-9}	1.70×10^{-12}	1.10×10^{-16}	2.27×10^{-19}
	Torus2	1.62×10^{-14}	5.15×10^{-14}	1.54×10^{-17}	2.63×10^{-20}
	Target	$*3.65 \times 10^{-15}$	1.16×10^{-14}	5.17×10^{-19}	7.74×10^{-21}
$P(\text{Target} \text{Torus2})$		*0.225	0.225	0.034	0.295

Table 7.4.: Antiproton stopping rates and fluxes at key points. Since no antiprotons were seen stopping for the angular region from 0 to 59° , the value for the final two entries in that column — indicated with an asterisk (*) — are obtained by multiplying the antiproton rate expected at the Torus2 collimator with the median collimator acceptance from the other three angular regions. For each of the angular regions, 80 million antiprotons were simulated.

Rates for Secondary π^-		Secondary π^- from Angular Region for Antiproton Production			
		$0 \leq \theta < 59^\circ$	$59 \leq \theta < 97^\circ$	$97 \leq \theta < 119^\circ$	$119 \leq \theta < 180^\circ$
Raw Counts	Torus1	16943	87230	157385	222486
	Torus2	208	1106	1995	1847
	Target	1	18	25	30
Weighted Sum	Torus1	5.77×10^{-6}	4.64×10^{-9}	4.10×10^{-14}	1.25×10^{-17}
	Torus2	8.59×10^{-8}	5.93×10^{-11}	5.79×10^{-16}	1.23×10^{-19}
	Target	9.98×10^{-11}	2.99×10^{-13}	5.02×10^{-18}	1.91×10^{-21}
$P(\text{Target} \text{Torus2})$		0.039	0.040	0.022	0.017

Table 7.5.: The simulated number of secondary pions from antiprotons observed at key points along the beamline. The raw counts are the total observed events from the simulation of 80M antiprotons for each of the four angular regions. The weighted sum then shows the weighted sum over every particle passing the point, where the weight is determined as described by equation (7.10). The final row, $P(\text{Target}|\text{Torus2 Coll.})$, gives the survival probability for a pion to reach the target, given that it passed the Torus1 Entrance, i.e. it is the ratio between the Target and Torus1 Entrance rates.

		Stopping Rates		Background Rate per POT	
		Unweighted	Weighted	No Timing	With Timing
\bar{p}	$0 \leq \theta < 59$	$< 6.58 \times 10^{-13}$	$< 3.65 \times 10^{-15}$	1.69×10^{-21}	8.66×10^{-22}
	$59 \leq \theta < 97$	4.17×10^{-16}	1.16×10^{-14}	5.36×10^{-21}	2.75×10^{-21}
	$97 \leq \theta < 119$	2.48×10^{-18}	5.17×10^{-19}	2.39×10^{-25}	1.23×10^{-25}
	$119 \leq \theta < 180$	1.60×10^{-17}	7.74×10^{-21}	3.58×10^{-27}	1.84×10^{-27}
π^-	$0 \leq \theta < 59$	6.58×10^{-13}	9.98×10^{-11}	2.95×10^{-17}	1.62×10^{-29}
	$59 \leq \theta < 97$	9.38×10^{-16}	2.99×10^{-13}	8.86×10^{-20}	4.86×10^{-32}
	$97 \leq \theta < 119$	5.44×10^{-19}	5.02×10^{-18}	1.49×10^{-24}	8.15×10^{-37}
	$119 \leq \theta < 180$	2.14×10^{-19}	1.91×10^{-21}	5.65×10^{-28}	3.10×10^{-40}
Sum (per POT)				2.96×10^{-17}	3.62×10^{-21}

Table 7.6.: Final estimated background rates. See text for column definitions.

where it is clear that timing information from the pulsed proton beam is not meaningful for antiprotons. However, since the majority of secondary pions that are successfully transported to the target originate in the production target, the pulsed beam timing is a strong way to suppress the backgrounds these can produce via RPC. In fact, given that these pions originate in the production target, the background rate due to RPC of pions directly produced by the proton beam can be reused, including the timing cut. For antiprotons, the rate of RPC backgrounds per pion stop is also used, however the mean number of negative pions produced per antiproton stop is included, as well as the overall efficiency of the timing window, assuming a flat timing distribution. For both pions and antiprotons, the efficiency of the TDAQ and reconstruction are also included, with the same values as for signal. Based on these factors, the numbers in Table 7.4 and Table 7.5 can be converted to background estimates, which are shown in Table 7.6.

The total predicted antiproton rate per POT is therefore 3.62×10^{-21} , which is completely dominated by antiprotons produced in the forward direction but scatter within the production target and are successfully transported to the stopping target. This number is considerably larger than would be desirable for the COMET experiment. It is important, therefore, to remember that this is an especially conservative estimate:

- The kinematic end-point is a large overestimate for the true end-point of the spectrum since the incoming proton will never interact with the entire nucleus.

- The straight-line-fit to the tail, that was used to generate antiprotons in the simulation will produce higher momentum antiprotons than are likely to occur, which changes the penetration depth in material. In addition, the straight-line-fit increases the integrated yield of antiprotons significantly, which impacts on the event-by-event weight. For example, for the region from 59–97°, there are up to two orders of magnitude difference on the predicted antiproton yield depending on the high-energy description. ♣
- Antiproton events were generated with a uniform distribution in the production target. Given that the proton beam profile will be close to a double Gaussian, with most of the probability concentrated in the centre of the target, there will typically be more material for the antiprotons to pass through as they leave the target. This will increase the rate of absorption and thus reduce the antiproton rate further.
- The data this model is based on uses 10 GeV initial protons. The antiproton yield is expected to grow rapidly at these sorts of energies. According to the model in [44], the cross section at 8 GeV is at least an order of magnitude lower than for incident protons with 10 GeV.
- The final value assumes that all the negative pions produced from stopping antiprotons are captured by nuclei in the target. In reality, many of these will escape from the target and decay in flight or be stopped and captured elsewhere. The pion multiplicity factor used here is likely an overestimate, therefore.

At the same time, the fact that these results are somewhat statistically limited, given the small number of antiproton stops seen from the forward going antiprotons, one can expect a sizeable uncertainty on this value. In addition, some of the other factors that have been included, such as from the RPC background estimation, also increase the uncertainty since there might be other correlations that such factorisation cannot include.

On the other hand, the fact that it is scattering from forward produced antiprotons has some advantage, since there is experimental data in the forward region—admittedly with materials other than tungsten or with proton energies other than 8 GeV—that could be used to develop further understanding of this background.

CHECK
*Add to
the first
table the
integrals
with the
other
tail
descrip-
tions.*

7.4.4. Reducing Antiproton Backgrounds Further

Given that the antiproton with the current beamline design appears larger than desirable, it will be necessary to take steps to reduce it. There are several options that can be pursued, but each must be checked for its impact on the muon beam intensity. Firstly, one can simply increase the thickness of the foil at the entrance to the Torus1. In a similar way, one can introduce additional foils along the beamline, such as at the TS3 solenoid in between the Torus1 and Torus2. The downside of both of these methods is that they will be in the path of the muon beam, and since the dE/dx curve for negative muons below 100 MeV has a negative slope, this material will likely increase the mean muon momentum (but of course decrease the overall intensity).

If material is added, then it would be beneficial if this material were low-Z. This would maximize the ratio of the rate of antiproton loss to the muon loss rate. In fact, a bug in the geometry during initial simulations of antiprotons left air at the exit to the production section. The impact on the muon and pion was found to be trivial, but the antiproton acceptance into the Torus1 was zero at the limit of the sample size of the simulations.

Finally, if a volume in the beamline close to the production target were identified, where the separation between antiprotons that stop and muons that stop, then this should also be exploited. However, in the studies performed here, such a region does not seem apparent. Additionally, material close to the production target would need to be considered from an activation and safety perspective, in addition to the impact on the muon and pion beam.

7.5. Direct Beam-Related Backgrounds

Although neither a muon or pion in their rest frame can decay to electrons greater than 55 MeV, if these particles are boosted sufficiently the resulting electron can be produced with signal-like momentum. For muons at 78 MeV/c Michel electrons can occur at 105 MeV/c if produced in the direction of the muon's momentum. For pions, the threshold for signal-like electrons to be produced during decay is 58 MeV/c, although the branching fraction for this process is helicity suppressed to around 1×10^{-4} .

The bent solenoids and the pulsed beam help to suppress these sorts of backgrounds, whilst the beam blocker, downstream of the target disks, reduces the geometric acceptance.

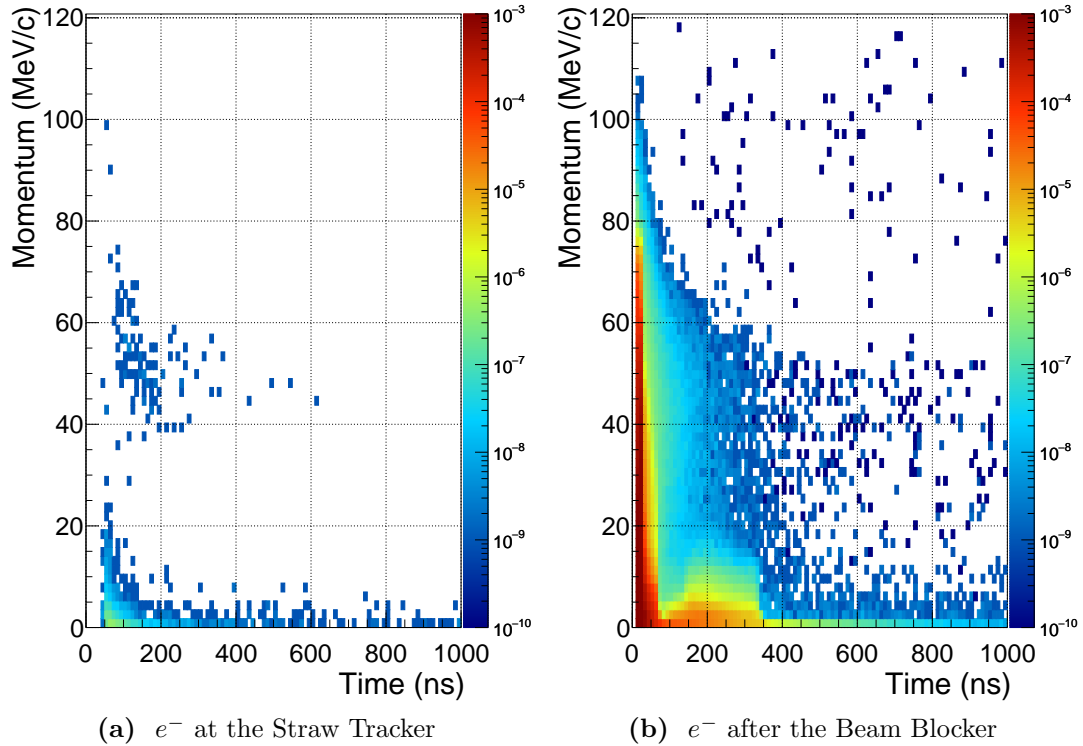


Figure 7.17.: The timing and momentum of electrons detected at the straw tracker and passing a plane immediately after the beam blocker.

The inner radius of the collimator at the exit of Torus2 is set to 12 cm, whilst the beam blocker has a radius of 25 cm. As the beam passes along the stopping target region, the beam envelope grows due to the reduction in the solenoidal field strength. The radius of the beam blocker, however, is large enough that even with this growth there should be no direct line of sight between the muon beam and the spectrometer. As such, the only way for beam particles to reach the detector are by a hard scatter off the target or beam blocker, or to be produced via decay of another particle close to the target itself.

To check the probability that signal-like electrons are produced in the beam and arrive at the detector in the time window, the output of the large production target simulation was resampled five times, so that around 1.4×10^9 POT events were studied, equivalent to 7.5 Phase-II bunches **CHECK: Is this the right number of simulated events?**. Fig. 7.17a shows the momentum and timing of electrons at the straw tracker, from which it is clear that no background events were observed within the gated-time detector window. One electron is observed at 98 MeV/c, but this occurs around 100 ns after the proton bunch. This immediately sets a limit on the background rate—less than 1 in 1.4×10^9 per POT.

Clearly then it is necessary to apply some extrapolation to understand this background better. Indeed, it will never be feasible to directly simulate the 10^{21} or so POT that would be necessary to infer the background rate without some extrapolation. To make this extrapolation, we look at the same distribution immediately after the beam blocker. At this point there are far more electrons so it is easier to fit and model the distributions. Fig. 7.17b shows the momentum vs. time plot for electrons immediately after the beam blocker.

The rate of observing signal-like electrons due to high-energy beam particles is modelled by factorisation of the acceptances:

$$R_{\text{beam}} = A_{\text{geom}} A_{\text{mom}} A_{\text{time}}, \quad (7.13)$$

$$= \left(\frac{N_{\text{obs}}}{N_{\text{POT}}} \right) \left(\frac{\int_{104.2}^{105.5} f(p) dp}{\int_{p_{\text{low}}}^{105.5} f(p) dp} \right) \left(\frac{\int_{600}^{1200} g(t) dt}{\int_{30}^{1200} g(t) dt} \right), \quad (7.14)$$

where A_{geom} , A_{mom} , and A_{time} are geometric acceptance and efficiencies of the momentum and timing thresholds, respectively. N_{obs} is the number of events actually seen at the straw tracker, whilst N_{POT} is the number of simulated POT events.

The functions $f(p)$ and $g(t)$ represent the momentum and time projections of electrons after the beam blocker. Their factorisation in this manner is valid due to the lack of strong correlation visible in Fig. 7.17b. It is reasonable to assume that, close to the signal region, the momentum distribution observed immediately after the beam blocker will have the same shape as the momentum distribution at the straw target. Since the acceptance function is essentially flat at the high energy limit (see ?? and 6.2.3), only the normalisation of the spectrum should change, and this we have encapsulated already in the geometric acceptance.

Finally, the timing distribution, $g(t)$, is also taken by fitting the observed electron distribution after the beam blocker. Here, however, one needs to be careful about extrapolating the distribution from after the beam blocker to the straw tracker. The extrapolation can be imagined as two effects: an overall translation of the distribution to later times, and a broadening of the distribution (an increase in the fitted lifetime). Both effects are determined by the time needed for particles at the beam blocker to propagate through the spectrometer. With a radius of 2 m, the typical distance travelled along the beamline will be at least about 6 m, and since the electrons are relativistic and travelling

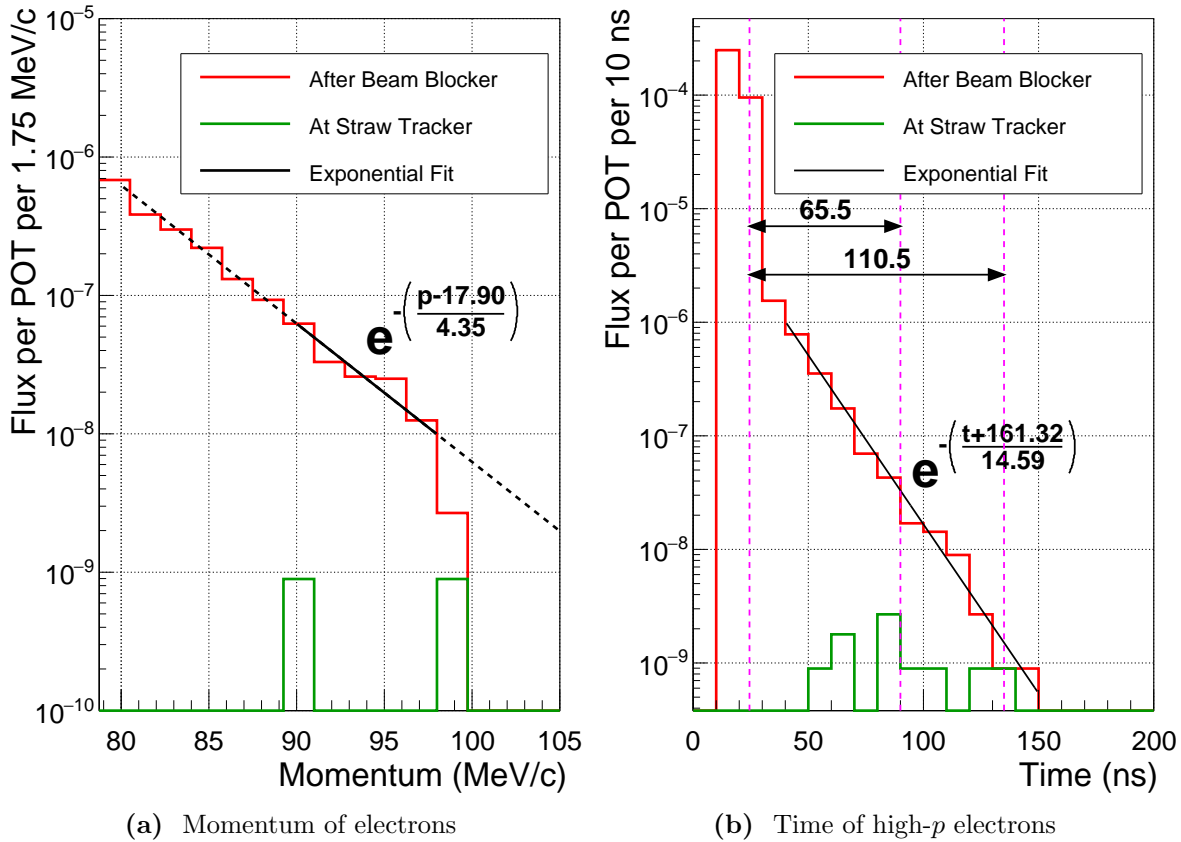


Figure 7.18.: Projections of the momentum and arrival time of electrons. (a) shows the momentum for electrons that arrive at any time, whereas (b) only shows the arrival time for electrons with momentum above 65 MeV/c. Magenta lines in (b) indicate the mean arrival time after the beam blocker and the mean and maximum arrival time at the straw tracker. The black line is an exponential fit to the momentum and time of electrons after the beam blocker, with the equation and constants shown next to the fit.

at close to the speed of light, transport through the spectrometer can be expected to add about 20 ns. This assumes particles follow the beam axis perfectly, so that their pitch angle is equal to zero. With a large pitch angle the distance travelled, and therefore transportation time, will be longer, although since larger pitch angles drift more in the bent solenoids, these particles will tend to be removed more effectively. The effect of broadening on the distribution arises from lower energy electrons moving more slowly, however for the relativistic signal-energy electrons this effect will be negligible.

Fig. 7.18 show the momentum and time functions based on the distribution of electrons after the stopping target. The equations for the lines of best fit are also shown, and the region used to fit indicated by the solid black fitted line. The low momentum threshold

for this study, p_{low} , is set to 65 MeV/c, since this removes electrons from DIO of muons along the beamline, which have relatively long life-times but cannot be produced at signal energies. Above this threshold, there are 65 events at the straw tracker, giving a geometric acceptance of 8.93×10^{-9} . For the efficiency of the momentum cut, using the fit to the projection shown in Fig. 7.18a, the ratio of events expected between 104.2 and 105.5 MeV/c compared to the integrated rate from 65 to 105.5 MeV/c is 3.13×10^{-5} . For the timing efficiency, the fit given in Fig. 7.18b is first shifted so that the mean of timing distribution at the beam blocker sits at the time of the latest arriving electron above 65 MeV/c, as indicated by the vertical magenta lines. This amounts to a shift of 110.5 ns, which is about twice as large as if one were to use the mean of the straw tracker electrons. Having applied this shift (which we implement as a shift in the start and stop time for the integration), we find the suppression of electrons due to the time-gated window gives a factor 5.25×10^{-12} .

Finally, then, we can pull all these factors together using (7.14), from which we find that the predicted beam-related background rate per POT is 1.47×10^{-24} , such that we can expect about 1.28×10^{-3} background events during Phase-II due to these processes.

Given the extrapolation that has been necessary, this result comes with a degree of statistical uncertainty. However, in principle this includes all sources of electrons in the beam: high energy muons, pions, and electrons coming directly from the production target with high energy. This also includes electrons produced from neutron capture, provided the neutron itself originated downstream of the production target section, which were not included here in order to accelerate the simulation speed. In addition these neutrons should be studied carefully using multiple hadron production models. ♣

7.6. Cosmic Ray Background

Cosmic rays at sea level consist primarily of positive and negative muons, produced from high-energy particles originating in the sun or beyond the solar system strike the upper atmosphere and produce a particle shower. About one muon per square cm per minute is expected at sea level, with the average muon energy around 4 GeV [75]. At these energies, not only can they readily produce high-momentum electrons, but they are weakly ionising and therefore penetrate material relatively easily.

CHECK
Add at least a comment or subsection on these neutrons and reference it here.

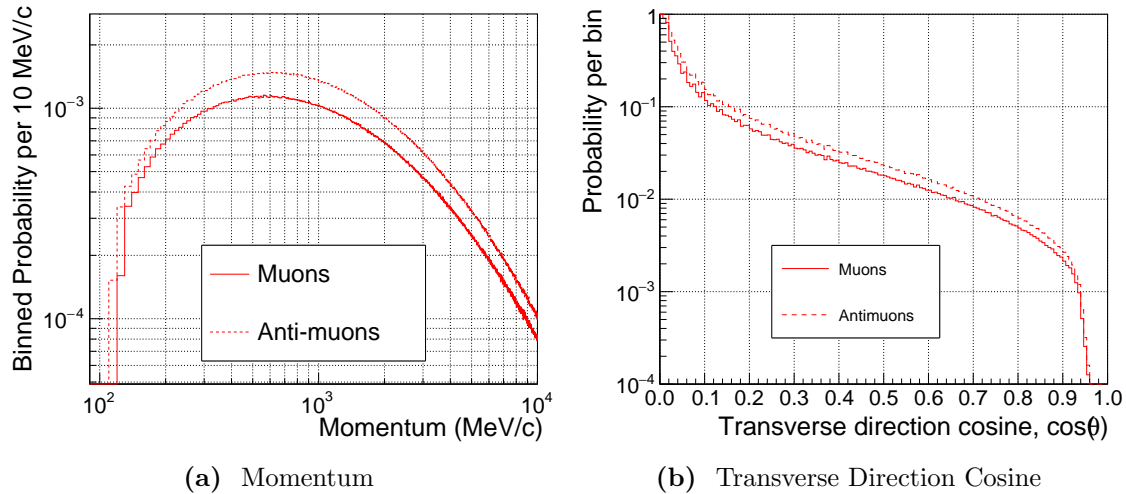


Figure 7.19.: Distributions of momenta and the transverse direction for the muons and antimuons provided by the ND280 collaboration.

This makes cosmic muons a potential source of backgrounds, as the high energy muons can pass through the experiment hall to the beamline where upon, if they decay, may produce signal-like electrons. In addition, this background would lack any timing structure. As a result, a Cosmic Ray Veto ([CRV](#)) is included in both Phase-I and Phase-II made with four layers of scintillator bars as the active material. When a cosmic ray passes this, events in the detector can either be tagged, or any trigger on this event vetoed and not read out, such that signal-like electrons produced from cosmic rays should not be included in the analysis.

At the time of writing, the **CRV** has been optimised and studied for Phase-I [?, ?, 80]. These studies suggest that a miss-rate of less than 1 in 10^4 events is achievable. For Phase-II however, given the different experiment geometry, the situation is a little different. If the muon penetrates into the detector and decays from there, or if a high energy electron produced outside of the detector but close to it, is Principally, the stopping target in Phase-I is surrounded by the **CDC**, such that cosmic muons must escape detection in both the **CRV** and **CDC**, and then decay close to the target. In Phase-II, the stopping target is located well away from the detector, which means cosmic muons must only penetrate the **CRV**. Furthermore, the **CRV** geometry in Phase-II should cover at least the target and intermediate beamline in addition to the detector solenoid itself.

Phase-II is expected to run about $2. \times 10^7$ s as suggested in section ???. During COMET operation, a single accelerator cycle is expected to last 2.48 s, with about 0.7 s for extraction, giving a duty factor of 0.28. In addition, with a time-gated window lasting

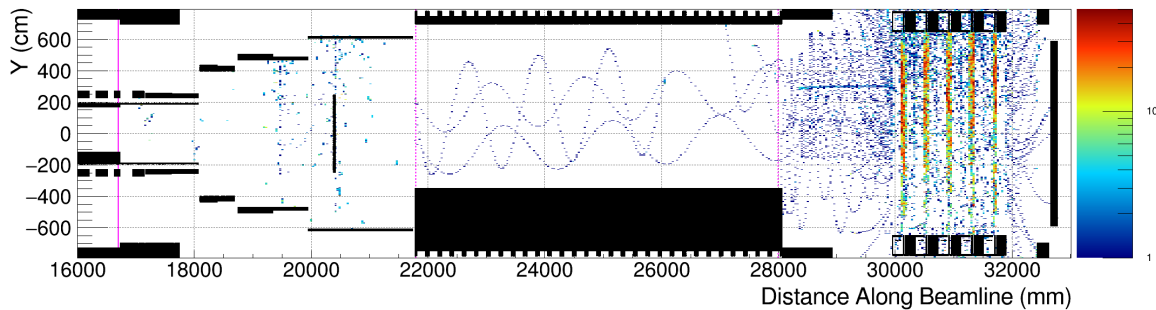


Figure 7.20.: Projection onto beamline coordinate system of electrons from cosmic rays with momenta greater than 100 MeV/c, from a simulation of about 170 million cosmic muons. Three tracks can be seen to enter the electron spectrometer and pass along, although their momenta are all above 105 MeV/c as visible from the upwards drift of the trajectories.

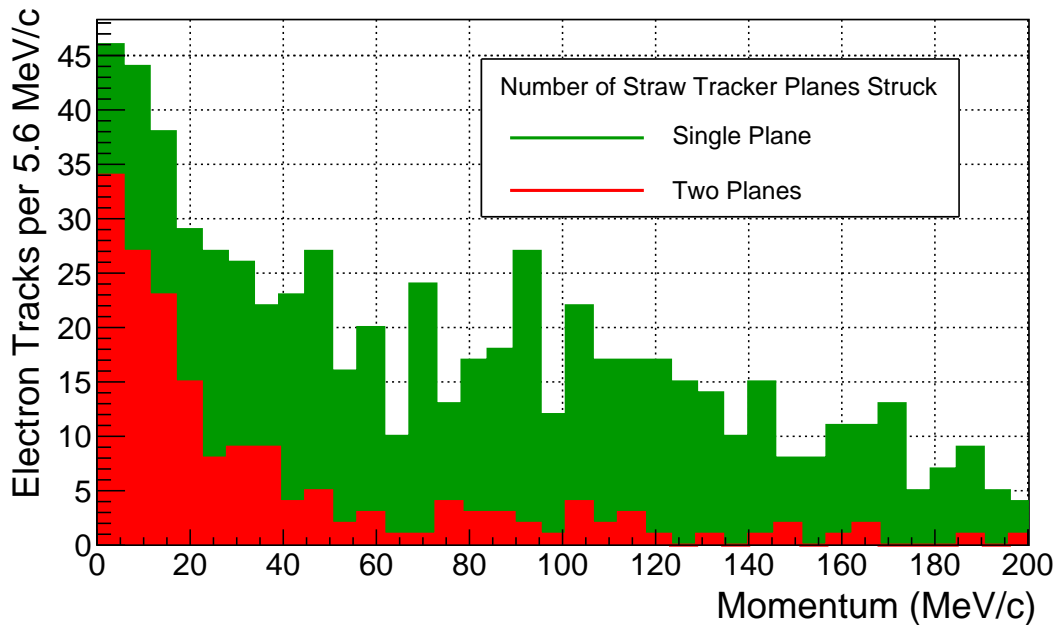


Figure 7.21.: Momentum of electrons that hit one and two layers (planes) of the straw tracker. The vertical axis shows the raw number of observed events based on the simulation of 170 million cosmic muons described in the text.

600 ns and bunches separated by 1.170 μ s, the overall duty factor drops to about 0.14. As such, during Phase-II running there are really only about 2.9×10^6 s when a cosmic muon can produce backgrounds. During this time then, 4.8×10^4 cosmic muons should pass through each horizontal square centimetre of the COMET hall. If we assume the miss-rate for the Phase-II will be no worse than for Phase-I, i.e. 1×10^{-4} , then for each for each square centimetre of the experiment, more than 48 muons should be studied.

To simulate the cosmic ray background, input muon events were provided by the ND280 experiment [52]. These contained positive and negative muons that had been produced in an air shower simulation using the CORSIKA simulation package [56], for the atmosphere above J-PARC. Fig. ?? shows the distributions of momentum and directions that these files contained.

Muons were generated in a horizontal plane directly above the experiment hall (and centred on the origin of the ICEDUST coordinate system, the production target). A $50 \times 50 \text{ m}^2$ square within in this plane was used to generate the events. This immediately adds a limitation to this simulation that very horizontally-moving muons cannot be studied, but it is needed to increase the simulation efficiency. Given the angular distribution shown in Fig. 7.19 and the offset of the detector solenoid with respect to the production target, between XX and XX of all cosmic events can be simulated this way. About 1.76×10^8 cosmic events were generated in this way; for the 2500 m^2 region above the experiment where the simulation was started, more than 1.2×10^8 events should be studied, according to the above calculations.

Material above the beamline can degrade and stop cosmic muons so it is important this is modelled well. The concrete and iron shielding for the entire experimental hall is implemented, as well as the shielding necessary for the CRV. However, at this stage the geometry in the simulation only has the CRV design intended for Phase-I around the detector solenoid (in its Phase-II position). Since the CRV will need to be extended to include all the way up to the stoping target in Phase-II, there will likely be more shielding material inserted above the beamline.

Fig. ?? shows the momentum distribution of observed electrons. There are large fluctuations across the momentum distribution, but this is most likely due to statistical fluctuations rather than truly physical. From 80 to 120 MeV/c, 140 electrons hit at least one layer in the straw tracker, although only 19 of these hit a second plane. The number of background events due to cosmic rays can therefore be estimated as:

$$R_{\text{cosmics}} = R_\mu \frac{n_e^{\text{obs}}}{N_{\text{sim}}} \Delta p (1 - \epsilon_{\text{CRV}}) A_{\text{duty}} A_{\text{timing}} A_{\text{TDAQ,Recon}} \quad (7.15)$$

where R_μ is the rate of cosmic muons expected through the experiment hall per second, n_e^{obs} is the observed number of events per MeV/c, N_{sim} is the number of simulated cosmic ray muons, and ΔM is the width of momentum thresholds, from 104.2 MeV/c to 105.5 MeV/c. ϵ_{CRV} is the CRV efficiency, such that $(1 - \epsilon_{\text{CRV}})$ is the expected miss-rate. The factors $A_{\text{duty}}, A_{\text{timing}}$, and $A_{\text{TDAQ,Recon}}$ represent the accelerator duty factor, fraction

Parameter	Value	Description
R_μ	4.17×10^5	Cosmic ray flux through entire hall per second
n_e^{obs}	0.46	Observed electrons per MeV/c
N_{sim}	1.76×10^8	Number of simulated events
$(1 - \epsilon_{\text{CRV}})$	1×10^{-4}	Miss rate of the CRV
A_{duty}	0.36	Accelerator duty factor
A_{timing}	0.51	Fraction of time within gated-time detection window
$A_{\text{TDAQ,Recon}}$	0.70	Combined acceptance of TDAQ and Reconstruction

Table 7.7.: Parameters and their values for the determination of the cosmic ray background rate.

of time spent during the time-gated detection window, and the combined TDAQ and reconstruction efficiency, respectively. The values for each of these parameters are given in Table 7.7. From this we can estimate that there will be 1.89×10^{-8} backgrounds per second due to cosmic rays.

To reduce the cosmic ray background further, the most important parameter is the CRV efficiency, the complement of which multiplies the entire background rate. Since this background is completely uncorrelated with the beam, the shorter the running time, the lower this background rate will be. If this cannot be reduced further, then it might be necessary to add more material above the beamline or above the experiment hall. Fortunately, rather than depend on simulation for this, Phase-II has the benefit of Phase-I, which will have measured and characterised the cosmic ray flux on the experiment hall floor.

7.7. Summary of Background Rates

Table 7.8 gives an overview of the predicted rates. The final prediction is below 1 but very close to it, and it is therefore important that these studies be continued and developed further. The dominant backgrounds come from antiprotons and cosmic rays, with radiative muon capture similarly high.

Type	Source	Background Rate			Total Events	
		per Stopping μ^-	per POT	per s	This Study	CDR [35]
Intrinsic	DIO	6.2×10^{-20}	0	0	0.086	
	RMC	0	0	0	0	
Delayed	RPC	–	1.82×10^{-25}			
	Beam e^-	–				
	Stopped \bar{p}	–				
Prompt	RPC	–	1.73×10^{-27}			
	Beam e^-	–				
	π^- from \bar{p}	–				
Cosmics		–	–	1.89×10^{-8}		
Total						

Table 7.8.: Final predicted background rates and events. Assumes....

7.7.1. Backgrounds Not Considered

Although some of the methods above are different, compared to the Phase-I TDR and Phase-II CDR, there is only one source of backgrounds that has not been included: the production of high-energy electrons from the capture of neutrons that originate in the production target. These neutrons were killed in order to reach a large number of muons and pions in the simulation, although neutrons produced along the muon beam (from the collimators, stopping target, etc.) have been included with the beam background. Whilst there is a large amount of concrete and iron material in between the production target and the detector, the production target is likely a major source of neutrons in the experiment, and this needs to be studied rigorously using multiple hadron production and neutron transport codes.

Such studies have advanced for Phase-I, with the background rate from neutrons estimated to be about 3.1×10^{-29} per POT. With a different experiment layout, production target material and higher proton beam power, separate studies should be performed for Phase-II. A naive scaling of this to the Phase-II number of protons on target would suggest that 2.7×10^{-8} events can be expected in Phase-II. Since the detector sits further away from the production target and since there is additional beamline then it is likely that the neutron rate is lower still. The increased proton power would already be included in the naive scaling applied above to first order. The different target material will change

the neutron production cross section, but since the target is also made longer to maximize the muon stopping rate the increase in neutron yield might also be compensated for.

7.7.2. Principal Uncertainties

Whilst it is not possible to make a quantitative estimate of the uncertainty at this time, it is clear that for some backgrounds the uncertainty is large.

StrECAL Reconstruction and Resolution In the case of [DIO](#) and [RMC](#), the two intrinsic sources of background, the main source of uncertainty is in the resolution function. The exact distribution for the residuals after reconstruction is not well known, especially for Phase-II. In particular, for [RMC](#), the high energy tail needs to be studied better. It has been assumed that fewer than 1 in 1×10^4 events will be reconstructed with momentum larger by 2.4 MeV/c or more than the true value. This assumption must be confirmed, and if possible improved. RMC on Al-26 was also discussed as a potential concern, however Al-26 has a tiny abundance in natural aluminium, whilst the rate of production in the COMET muon beam is difficult to predict.

RPC Spectrum In the case of Radiative Pion Capture ([RPC](#)), the dominant uncertainty comes from the spectrum of photons produced during RPC. The study here and in the Phase-I TDR depend entirely on a single set of experiments, which do not cover RPC from aluminium, only on magnesium and calcium. This will be difficult to improve further without additional observations, and it would be useful to study this at Phase-I if possible, perhaps by changing the Torus1's dipole field to improve pion acceptance.

Antiproton Production Given the lack of experimental evidence for antiproton production in the ‘sub-threshold’ regime and in the backwards direction, there is large uncertainty over the expected rate. Whilst the model developed here was kept conservative, as one of the dominant backgrounds it is important to study this further. A dedicated study comparing multiple different hadron production codes to all the possible experimental datasets (including forward and backward produced antiprotons from the different targets with different proton momentum) could reduce our uncertainty if new experimental data is forthcoming. Such a study would then be able to extrapolate better for the target material, proton energy and production direction used in COMET.

In addition to the production rates, there is reasonable uncertainty on the mechanisms by which antiprotons can produce background electrons. Here it has been assumed that the primary mechanism is via pion production, but the rates for such production in aluminium is also not well known. Such an assumption must also be confirmed.

Cosmic Ray Veto Geometry and Shielding Without a complete CRV design, it is tough to be confident that the energy loss of cosmic muons is well captured in the Phase-II simulation. In addition, the miss-rate of 1×10^{-4} should be experimentally confirmed and ideally improved.

7.8. Further Studies and Improvements

This chapter has presented an almost comprehensive set of estimates for background sources in Phase-II. It should not, however, be treated as the final set of predictions, but rather as an initial set of studies that should be developed further. The following list, therefore, is a summary of methods that can be pursued to improve and expand the preceding set of estimates.

1. Neutron background with different hadron codes and AlCap neutron spectrum from mu capture
2. Improved cosmic ray veto geometry
3. High-energy electron acceptance
4. Pion stops elsewhere in the beamline
5. StrECAL resolution function
6. Improved proton beam timing structure
7. RMC from Al-26 that is produced from Al27 via neutrons. Photons can be made up to 108 MeV
8. Assumption that the PID abilities of the StrECAL are 100%, is this true? At what level would muons be reconstructed at electrons?
9. RPC from pions stopping elsewhere in the beam - ζ Map of acceptance to RPC electrons vs. position of pion stop in the beamline

Chapter 8.

Summary

10. Chapter 1

10.1. The muon has played a historic role in developing the Standard Model of particle physics

10.2. Outstanding questions around the Standard Model, both experimental and theoretical, motivate searches for Charged Lepton Flavour

10.3. CLFV is a very sensitive probe for New Physics that can solve these issues

11. Chapter 2

11.1. Searches for CLFV using intense muon beams are particularly sensitive due to the high intensity beams available nowadays

11.2. There is a strong complementarity and interplay between the various searches from both theoretical and experimental perspectives

11.3. Mu-e conversion is sensitive to all models, but particularly to those that require massive exchange particles, or direct involvement of quarks or gluons

11.4. The Coherent nature of current μ -e conversion searches makes it very experimentally attractive since the signal requires only a single monoenergetic electron

12. Chapter 3

12.1. The current limit on μ -e conversion was set in 2006 by SINDRUM-II to be 7×10^{-13}

12.2. The COMET experiment is designed to produce around four orders of magnitude improvement on this limit, at 3×10^{-17}

12.3. It will reach this with a staged approach, achieving two orders of magnitude better during Phase-I, at 3×10^{-15}

12.4. The principal means by which COMET makes these improvements are the use of:

12.4.1. a high power 8 GeV primary proton beam to maximise the pion yield and suppress antiproton production;

12.4.2. a 5 T superconducting solenoidal field designed to maximise the capture of backwards produced pion from the production target;

12.4.3. a long solenoidal muon beam transport section that is bent and has a dipole field and collimators included, which produce a high purity muon beam;

12.4.4. a pulsed muon beam with a medium-Z target material, giving a longer muon lifetime than previous experiments, allowing for timing information to suppress most beam-related backgrounds

12.4.5. a large geometric acceptance detector, improved by magnetic mirroring at the stopping target in Phase-II, which has a low material budget and high granularity to ensure better than 200 keV/c resolution

12.5. Performing Phase-I first allows these element to be tested with lower intensity beams and before committing to the full Phase-II design

13. Chapter 4

13.1. If any observation is to be confirmed as signal, or to achieve the most stringent limits in the event of a null-observation, the background rate must be kept as low as possible.

13.2. Being able to predict and evaluate this requires a very accurate, very efficient simulation.

13.3. In addition, the reconstruction software must be able to achieve the necessary resolution and keep the high-energy tails to an absolute minimum.

13.4. The integration of all the offline software, including simulation, reconstruction, calibration and analysis, is well underway.

13.5. The ICEDUST framework is the COMET experiment's offline toolset, which was based on the software of the near-detector for the T2K experiment, ND280.

13.6. Three major Monte-Carlo productions have been run using this software, which itself is now used collaboration-wide for various studies.

13.7. All studies presented in this thesis were performed using ICEDUST, including the optimisation studies for Phase-II.

14. Chapter 5

14.1. Given the effort and focus on Phase-I, Phase-II has received less attention, with the last update on performance given in the 2009 CDR.

14.2. Using the now mature ICEDUST software, revisiting the Phase-II design was prudent in order to validate and improve the past estimates and help inform decisions for Phase-I.

14.3. A comprehensive set of optimisations was performed, covering the production target, muon beam transport, stopping target region, and electron spectrometer and detector.

14.4. These optimisations were all summarised in Table ??.

15. Chapter 6

15.1. Based on these optimisations, the predicted single signal-event sensitivity per 2×10^7 seconds of beam time is estimated to be 2.27×10^{-17} .

15.2. This is a factor XXX improvement over the CDR prediction as summarised in Table ??.

16. Chapter 7

16.1. It is important also as well to understand the backgrounds that would occur with the updated design and improved simulation.

16.2. Although at this stage many of these results are statistically limited and thus the errors should be taken as large ***CHECK: Can I be more quantitative? Assume error of 100% or more?***, the total background rate is predicted to be XXX.

16.3. This includes intrinsic backgrounds from DIO, and RMC, prompt and delayed beam related processes like high-energy particles in the beam, RPC and antiproton production, and cosmic events

16.4. Not included is the rate of background events caused by neutrons produced at the production target, and issues related to pile-up and particle miss-identification.

17. Future work

17.1. This thesis, therefore, presents a baseline design and a set of Sensitivity and Background Estimates for Phase-II of the COMET Experiment.

17.2. There are many aspects that could be studied further, or improvements that could be made to the work presented in this thesis, which have been listed at the end of the relevant chapters.

17.3. Work to revisit the stopping target region, for example, has already shown that the sensitivity could be further improved by a factor of about 2.5 and is summarised in appendix [C](#).

Appendix A.

Drifts in a Bent Solenoid

The Lorentz force:

$$\frac{d\vec{p}}{dt} = \frac{q}{m} \vec{p} \times \vec{B} \quad (\text{A.1})$$

A.1. Uniform Solenoidal Field

B field is uniform and parallel to axis of solenoid. Define the Larmor frequency, ω , and radius, a , as:

$$a = \frac{\gamma m \vec{v} \times \vec{B}}{qB^2} = \frac{p_T}{qB} \quad (\text{A.2})$$

$$\omega = \frac{qB}{m} \quad (\text{A.3})$$

A.2. Field in a Bent Solenoid

Producing a cylindrical solenoid channel can be imagined as directly bending that of a normal uniform and linear one. By symmetry it can be seen that any gradient introduced to the magnetic field can only be radially, in the plane of the bending. Further, by considering Ampere's law with a current loop in the plane of bending formed by two radial straight lines (with length $|r - R| < L$, where R and L are the bending and aperture radii of the solenoid channel) and an arc, it can be seen that the variation in

the field is given by:

$$\frac{\nabla \vec{B}}{B} = \frac{1}{r} \hat{r} \quad (\text{A.4})$$

CHECK: Sketch or figure?

A.3. Drift Calculation

There are two sources of drift in a bent solenoid: the gradient in the field, and the centrifugal force arising from the circular coordinate system needed to describe the field lines. The two can be treated separately in the sense that the motion of a particle moving through a field with straight field lines but with a transverse gradient given by $\nabla B/B \propto 1/r$ would be described by an equation of motion equivalent to that from the first source of drift in the bent solenoid system. Similarly, a system with a uniform field but field lines that follow circular paths would exhibit drift equivalent to the second component mentioned above.

A.3.1. Gradient Drift

“Grad-B” drift is well described in text books, but in the interest of completeness a short derivation shall be given here. The drift arising due to the gradient in the field can be treated as a perturbation of the motion of the particle in a uniform solenoidal field. The total velocity \vec{V} , is given by:

$$\vec{V} = \vec{v} + \vec{v}_g, \quad (\text{A.5})$$

where \vec{v} is the unperturbed velocity of the particle in the transverse plane, and \vec{v}_g is the velocity arising due to the gradient in the field.

Treating the field as a Taylor expansion:

$$\vec{B}(\vec{r}) = \vec{B}_0 + (\vec{r} \cdot \nabla)|_{\vec{r}=0} \vec{B} + \dots \quad (\text{A.6})$$

and substituting equations (A.5) and (A.6) into the Lorentz force, gives:

$$m \frac{d(\vec{v} + \vec{v}_g)}{dt} = q(\vec{v} + \vec{v}_g) \times \left(\vec{B}_0 + (\vec{r} \cdot \nabla)|_{\vec{r}=0} \vec{B} \right) \quad (\text{A.7})$$

$$(\text{A.8})$$

so that to first order, the perturbing velocity is given by:

$$\frac{d\vec{v}_g}{dt} = \frac{q}{m} \left(\vec{v} \times (\vec{r} \cdot \nabla)|_{\vec{r}=0} \vec{B} + \vec{v}_g \times \vec{B}_0 \right) \quad (\text{A.9})$$

Since we are only interested in steady-state solutions where \dot{v}_g is close to zero, the above equation gives:

$$\vec{v}_g = \frac{q}{m} \frac{\vec{B}_0 \times \left(\vec{v} \times (\vec{r} \cdot \nabla)|_{\vec{r}=0} \vec{B} \right)}{B_0^2} \quad (\text{A.10})$$

which by considering the form after time averaging becomes:

$$\langle \vec{v}_g \rangle_t = \frac{\vec{B}_0 \times \left(\vec{v} \times (\vec{r} \cdot \nabla)|_{\vec{r}=0} \vec{B} \right)}{B_0^2} \quad (\text{A.11})$$

Appendix B.

Kinematic End-point for Antiproton Production

In section 7.4 the background rate due to antiproton production from the proton beam was estimated. To build a complete picture from the available experimental data, the maximum energy for antiprotons produced at a given angle was included in the fit to the data. This appendix provides the derivation for this end-point, which although is a straightforward calculation of relativistic mechanics, is included to help any future studies of antiproton backgrounds.

The end-point is achieved when the incoming proton, and the out-going nucleus and created proton recoil as a single object against the produced antiproton. In this case, maximum kinetic energy is transferred to the antiproton. This is treated as an increase in the final nucleus' mass equivalent to two proton masses.

In the following derivation, masses, energy and 3-momenta will be denominated by M , E and \mathbf{p} , while ρ will be used for 4-momenta. The subscripts N , p , N' , and \bar{p} will denote respectively the incoming nucleus, incoming proton, outgoing nucleus (with the additional two protons), and outgoing antiproton. Superscripts of L and C indicate whether or not the variable refers to the Lab frame or the centre-of-mass (COM) frame, respectively. Finally, θ is the angle between the momenta of the incoming proton and outgoing antiproton.

B.1. Derivation

In the lab frame, the proton and nucleus 4-momenta are given by:

$$\rho_p^L = (E_p^L, \mathbf{p}_p^L) \quad (\text{B.1})$$

$$\rho_N^L = (E_N^L, \mathbf{p}_N^L) = (M_N, \mathbf{0}) \quad (\text{B.2})$$

To boost to the **COM** frame, we need only consider the one dimensional Lorentz transform, so the total 4-momentum in the lab frame is related to the **COM** frame:

$$\begin{pmatrix} E_p^C + E_N^C \\ 0 \end{pmatrix} = \gamma \begin{pmatrix} (E_p^L + M_N) - \beta |\mathbf{p}_p^L| \\ -\beta(E_p + M_N) + |\mathbf{p}_p^L| \end{pmatrix}, \quad (\text{B.3})$$

where γ and β are the boost factor and velocity of the **COM** frame with respect to the lab frame, related by the equation:

$$\gamma = \frac{1}{\sqrt{1 - \beta^2}} \quad (\text{B.4})$$

From just the result for 3-momentum, one finds that:

$$\beta = \frac{|\mathbf{p}_p^L|}{E_p^L + M_N}, \quad (\text{B.5})$$

which allows the proton's energy in the COM frame to be calculated (and similarly for the nucleus, although this is not needed):

$$E_p^C = \gamma(E_p^L - \beta |\mathbf{p}_p^L|). \quad (\text{B.6})$$

Conservation of 4-momentum requires that:

$$\rho_N + \rho_p = \rho_{N'} + \rho_{\bar{p}}, \quad (\text{B.7})$$

so that taking the square of both sides results in:

$$M_N^2 + M_p^2 + 2(E_p E_N - \mathbf{p}_p \cdot \mathbf{p}_N) = M_{N'}^2 + M_p^2 + 2(E_{\bar{p}} E_{N'} - \mathbf{p}_{\bar{p}} \cdot \mathbf{p}_{N'}). \quad (\text{B.8})$$

In the **COM** frame the momenta are related by: $\mathbf{p}_p = -\mathbf{p}_N$, and $\mathbf{p}_{\bar{p}} = -\mathbf{p}_{N'}$ (but \mathbf{p}_p is not necessarily parallel to $\mathbf{p}_{\bar{p}}$). In addition, the energy of a particle is related to its momentum and mass by the equation: $E^2 = \mathbf{p}^2 + M^2$. By use of these relations, the above equation reduces to:

$$M_N^2 + 2(E_N^C E_p^C + |\mathbf{p}_p^C|^2) = M_{N'}^2 + 2(E_{N'}^C E_{\bar{p}}^C + |\mathbf{p}_{\bar{p}}^C|^2) \quad (\text{B.9})$$

$$M_N^2 + 2(E_N^C E_p^C + (E_p^C)^2 - M_p^2) = M_{N'}^2 + 2(E_{N'}^C E_{\bar{p}}^C + (E_{\bar{p}}^C)^2 - M_p^2) \quad (\text{B.10})$$

$$M_N^2 + 2E_p^C (E_N^C + E_p^C) = M_{N'}^2 + 2E_{\bar{p}}^C (E_{N'}^C + E_{\bar{p}}^C) \quad (\text{B.11})$$

Now conservation of energy tells us that $E_N + E_p = E_{N'} + E_{\bar{p}}$, and in fact, since we are in the lab frame, this is equal to \sqrt{s} , one of the Lorentz invariant Mandelstram variables. Using this, and the fact that $M_{N'} = M_N + \Delta M = M_N + 2M_p$, reduces the last equation to:

$$E_{\bar{p}}^C = E_p^C - \frac{M_{N'}^2 - M_N^2}{2\sqrt{s}} \quad (\text{B.12})$$

$$= E_p^C - \frac{2M_N \Delta M + \Delta M^2}{2\sqrt{s}} \quad (\text{B.13})$$

$$= E_p^C - \frac{2M_p(M_N + M_p)}{\sqrt{s}} \quad (\text{B.14})$$

Identifying the final term as ΔE , means the 3-momentum of the outgoing antiproton in the **COM** frame can be written as:

$$(\mathbf{p}_{\bar{p}}^C)^2 = (E_{\bar{p}}^C)^2 - M_p^2 \quad (\text{B.15})$$

$$= (E_p^C)^2 - 2E_p^C \Delta E + \Delta E^2 \quad (\text{B.16})$$

Finally, having found the out-going 4-momentum in the **COM** frame, it only remains to boost back to the lab frame. The one subtlety here is that while boosting into the **COM** frame we did not have to think of the transverse momentum since the **COM** and all proton and nucleus motions are all parallel, the emitted antiproton can be produced at any angle, with respect to the incoming proton in the **COM** frame. We must, therefore, use the two-dimensional transform, and so find that the maximum lab frame energy and

momentum of the antiproton is given by:

$$\begin{pmatrix} E_{\bar{p}}^L \\ p_{\bar{p},x}^L \\ p_{\bar{p},z}^L \end{pmatrix} = \gamma \begin{pmatrix} E_{\bar{p}}^C + \beta p_{\bar{p},z}^L \\ p_{\bar{p},x}^L / \gamma \\ p_{\bar{p},z}^L + \beta E_{\bar{p}}^C \end{pmatrix} \quad (\text{B.17})$$

where β has the same value as before, although we have flipped the signs in the boost, and $p_{\bar{p},x}^L$ and $p_{\bar{p},z}^L$ are given by $|\mathbf{p}_{\bar{p}}^L| \sin(\theta_C)$ and $|\mathbf{p}_{\bar{p}}^L| \cos(\theta_C)$, respectively.

Thus we have found the out-going 4-momentum of the antiproton in the lab frame as a parameteric set of equations dependent on the angle between the incoming proton and outgoing antiproton in the **COM** frame. The relation:

$$\tan(\theta_L) = \frac{p_{\bar{p},x}^L}{p_{\bar{p},z}^L}, \quad (\text{B.18})$$

can be used to produce an additional parametric equation for the antiproton's angle of emission in the lab frame as function of its value in the COM frame.

The full set of relevant variables and factors is summarized below, since the fully expanded result is extremely long and harder to implement into any computer code.

$$\begin{aligned} \gamma &= \frac{1}{\sqrt{1 - \beta^2}}, & \beta &= \frac{|\mathbf{p}_p^L|}{E_p^L + M_N}, & E_p^C &= \gamma(E_p^L - \beta p_p^L), \\ \Delta E &= \frac{2M_p(M_p + M_N)}{\sqrt{s}}, & s &= M_p^2 + M_N^2 + 2M_N E_p^L, \\ E_{\bar{p}}^C &= E_p^C - \Delta E, & |\mathbf{p}_{\bar{p}}^C|^2 &= |\mathbf{p}_p^C|^2 - 2E_p^C \Delta E + (\Delta E)^2, \\ \begin{pmatrix} E_{\bar{p}}^L \\ p_{\bar{p},x}^L \\ p_{\bar{p},z}^L \end{pmatrix} &= \gamma \begin{pmatrix} E_{\bar{p}}^C + \beta |\mathbf{p}_{\bar{p}}^C| \cos(\theta_C) \\ (1/\gamma) |\mathbf{p}_{\bar{p}}^C| \sin(\theta_C) \\ |\mathbf{p}_{\bar{p}}^C| \cos(\theta_C) + \beta E_{\bar{p}}^C \end{pmatrix}, & \tan(\theta_L) &= \frac{p_{\bar{p},x}^C}{p_{\bar{p},z}^C}, \end{aligned}$$

Appendix C.

Revisiting the Stopping Target Region

Of the various optimisations presented in chapter 5, the stopping target was only optimised for its position, keeping the shape, thickness and size as in the CDR. It was also observed in that chapter that the beam blocker had a large impact on the signal acceptance. To investigate ways in which the sensitivity of Phase-II can be further improved we develop here the idea of beam blocker-free stopping target as well as investigate the impact of changing the target shape.

The overall result of this study suggests an improvement in the signal sensitivity of Phase-II, equivalent to a factor of 2.5.

C.1. Understanding the Stopping Target Region

One of the challenges when optimising the stopping target is the complexity of the region, and correlations between the various parameters.

The magnetic field around the stopping target, for example, is not a simple solenoidal field. Fig. ?? shows the magnitude of the field along the beamline axis in the stopping target region. At the exit of the bent solenoids and for the first straight section immediately downstream, the field is kept close to 3 T. By the entrance of the electron spectrometer, the field on axis is closer to 1 T, although a transverse gradient is introduced from the bent solenoids. The transition from 3 to 1 T happens over 1.5 m across three solenoid sections.

The stated purpose of the reduction in field strength is to mirror those signal electrons that are produced in the target heading upstream. This, then, is expected to increase the geometric acceptance of the detector. Magnetic mirroring can be understood in various ways, such as via the adiabatic constants. However, qualitatively and intuitively, since magnetic field lines never end ('there are no magnetic monopoles'), when the field strength is reduced, the field lines spread out. This can be seen as a normal solenoidal field, with a radial component superimposed. Normal gyration around the solenoidal field, therefore, generates a Lorentz force that points back along the direction of the solenoidal field, and reduces the longitudinal velocity of the particle. Thus a particle initially with only transverse momentum in the region of tapering field strength will acquire momentum in the longitudinal direction towards the lower field strength. Similarly a particle initially heading from a low field to a high field can be mirrored back if the difference in the field is sufficient. The limit for this to occur is given by the condition [?]:

$$\tan^{-1}(\theta) = \left| \frac{v_L}{v_T} \right| < \left(\frac{B_{\max}}{B} - 1 \right)^{1/2}, \quad (\text{C.1})$$

where B_{\max} and B are the maximum field strength and current field strength. v_L and v_T are the longitudinal and transverse velocity of the particle at this point, the ratio of which is the arctangent of the pitch angle, θ , between the particle's velocity and the solenoidal axis.

Given that the maximum field strength occurs at the exit of the Torus2, with a magnitude of $B_{\max} = 2.88$ T, one can calculate the minimum pitch angle an upstream-heading particle must have in order for it to be mirrored back downstream. This is shown in Fig. ?? where the minimum pitch angle varies from around 85° to about 43° at the end of Stopping Target Section. Since signal electrons are produced isotropically, this limit can be turned into the fraction of phase space for signal electrons produced at a point along the beamline that will be mirrored back, and this is shown in Fig. ???. This clearly motivates putting the stopping target further downstream in order to maximize the mirroring effect.

On the other hand, if the target is located downstream, the muon beam is required to traverse the tapered field. In that case there is another effect, namely the adiabatic growth of the beam envelope, which must be considered. Since particles in the beam follow the field lines, as the field is reduced, the beam profile must grow. This growth is

governed by the expression:

$$Ba^2 = \text{const} \quad (\text{C.2})$$

where B is the field strength at a given point, and a the radius of gyration. ♣ Thus if the field strength reduced by a factor of 4, for example, the beam envelope can be expected to grow by a factor of 2. The radius of gyration is shown in Fig. ??, relative to the radius at the exit of the Torus2, as a function of the distance along the beamline.

The position optimisation of the stopping target shown in chapter 5 kept the target disks at a fixed radius and moved the whole set of target disks (and beam blocker) upstream and downstream. With a fixed radius set of disks, as the target was moved downstream, the fraction of the muon beam expected to hit the target was reduced. This favoured putting the stopping target more upstream in order to increase muon stopping rate.

Thus there were two competing effects: move the target downstream and the mirroring of signal events increases, but move the target upstream and the muon stopping rate is increased. These factors can be combined to give a proxy for the expected signal sensitivity for a target disk of fixed radius placed at one point along the beamline. The muon stopping rate will be proportional to the fraction of the beam profile that overlaps with the target. Meanwhile, the fraction of upstream-pointing phase space that would be mirrored downstream, plus the fraction of phase space pointing downstream in the first place (half of it), should be proportional to the signal acceptance. This combination is shown in Fig. ??.

Indeed, the maxima of this function, at 19700 mm in beamline coordinates, is very close to the optimal location found during the position scan. This neglects many factors, such as the fact that disks upstream will remove muons from the disks downstream, and that not all electrons that head downstream will be accepted into the detector. Nevertheless, it seems to capture the underlying phenomena that determine the optimal target location.

CHECK
*Is it
 really a²
 in this
 equa-
 tion?*

C.2. Improving the Target Design

In order to improve the signal acceptance, and taking into account the previous discussion, we make three key changes to the target design. Firstly we allow the target radius to

Disk Index	Beamline Position (mm)	Relative Gyroradius	Disk Radius in Simulation	Disk Index	Beamline Position (mm)	Relative Gyroradius	Disk Radius in Simulation
0	19 542.0	1.098 32	144.758	18	20 443.8	1.463 30	256.950
1	19 592.1	1.114 05	148.932	19	20 493.9	1.471 51	259.842
2	19 642.2	1.130 64	153.400	20	20 544.0	1.478 23	262.219
3	19 692.3	1.148 36	158.248	21	20 594.1	1.483 47	264.080
4	19 742.4	1.167 53	163.576	22	20 644.2	1.487 45	265.500
5	19 792.5	1.188 47	169.495	23	20 694.3	1.490 56	266.612
6	19 842.6	1.211 30	176.068	24	20 744.4	1.492 96	267.471
7	19 892.7	1.236 01	183.326	25	20 794.5	1.494 78	268.125
8	19 942.8	1.262 27	191.198	26	20 844.6	1.496 12	268.604
9	19 992.9	1.289 43	199.516	27	20 894.7	1.497 03	268.933
10	20 043.0	1.316 68	208.037	28	20 944.8	1.497 30	269.030
11	20 093.1	1.343 04	216.451	29	20 994.9	1.497 30	269.030
12	20 143.2	1.367 71	224.474	30	21 045.0	1.497 14	268.972
13	20 193.3	1.390 05	231.867	31	21 095.1	1.496 92	268.891
14	20 243.4	1.409 84	238.518	32	21 145.2	1.496 71	268.817
15	20 293.5	1.426 88	244.317	33	21 195.3	1.496 67	268.804
16	20 343.6	1.441 27	249.272	34	21 245.4	1.496 73	268.823
17	20 393.7	1.453 30	253.450				

Table C.1.: Parameters of the target disks used in the proof of principle simulation. Since the beamline axis is parallel to the $-z$ direction in the stopping target region, the Z-coordinate can be obtained from the beamline position via: $z = 2164 - (s - 19542)$.

vary as a function of the beamline distance, thus keeping a constant overlap with the muon beam profile. Secondly we remove the beam blocker, which will hugely increase the acceptance of signal events. Finally, to compensate for the missing beam blocker, and to increase the number of stopped muons, we add more target disks into the target. From Fig. 6.2 in section 6.1 it can be seen that the muon stopping rate per disk has not reached zero by the last disk, which implies more muons could be stopped. In addition, the increasing target radius can be used to remove the line of sight between the Torus2 exit and the electron spectrometer that the beam blocker previously provided to remove beam particles.

Although each of these changes should each be studied carefully, as a proof of principle the design shown in the event display in Fig. ?? was tested in a simulation. The disk radii and positions are given in Table C.1.

To check the sensitivity and stopping rates with this configuration, 75 million POT events were fed in to a simulation that had muon **dio!** (**dio!**) and nuclear capture disabled, to be able to study the sensitivity in a single simulation.

C.2.1. Muon Stopping Rate

From this simulation, the muon stopping rate was found to be 2.8×10^{-3} per POT, and increase of 1.75 times compared to the stopping rate described in chapter 6. The stopping distributions in the target are shown in Fig. ???. It can be seen from the projection to the Z-axis that we catch much more of the tail of the distribution. It can also be seen from the YZ projection how there are very few muons stopping in the upper half of the target. This suggests one would really be able to remove this material which would give an additional increase to the signal acceptance.

The extra disks and the enlarged radius also mean that the higher energy muons sitting lower down in the beam are more effectively stopped. Being at the bottom of the beam these muons were more likely to miss the old target design, but also penetrated further, requiring more target material to be stopped. This can be seen by comparison of the muon momentum distribution shown in Fig. ?? and comparing this with the momenta shown in Fig. 6.1. Whereas before we only stopped muons up to around 50 MeV/c, now muons up to 60 MeV/c are consistently stopped. As a result of all of these changes, the stopping efficiency for muons that reach the target has increased from 43% to about 77%.

Unfortunately, it can also be seen from Fig. ?? that some of the high momentum muons that do not stop in the target reach through to the detector. This means the background rate with the design shown here from beam backgrounds would be significantly larger. However, further optimisations of the target based on this concept might be able to remove these high momentum muons using additional disks or adjusting the upstream collimators.

C.2.2. Signal Acceptance

Fig. ?? shows the detected momentum distribution of electrons. Of the signal events that occur, 48% are detected at the detector, which is the geometric acceptance with this design, and a factor of 2.2 times better than the result in chapter 6. The momentum cut however is less efficient now, accepting only 50% of events, compared to the previous 70%. Overall though, the signal acceptance with this target design is a factor 1.55 times better than the old design.

C.2.3. Summary and Future Improvements

By removing the beam blocker, adding more disks and increasing the disk radius along the beam axis, the muon stopping rate and geometric acceptance increase, although the momentum cut efficiency is decreased. The overall sensitivity can be expected to increase by a factor of 2.5.

Backgrounds from such a design need to be studied, in particular, high energy electrons and muons in the beam which are no longer removed by the beam blocker, but should be lost in the target. In addition the DIO background, which given the poorer momentum resolution and greater signal acceptance, might produce more background events with this design, and create a significantly higher hit rate. Other backgrounds like those from antiprotons in the beam, cosmic rays and neutrons will not be changed by the different stopping target. Radiative pion capture will be increased slightly since the pion stopping rate will also likely increase.

In addition to background studies with this design there is further optimisation that can be performed. The most obvious area for improvement is to remove the material at the top part of the target disks, since in this region no muons stop here. In addition one can add more target disks to the lower part to try and catch even more of the high-momentum tail.

The target disk thickness is another parameter that could be studied. In fact, somewhere between these two options is the possibility to use wedge-shaped target disks, that put less material higher up in the beam. If one can control this so that the low momentum muons stop as far downstream as possible, rather than in the first target disk, as currently occurs, then one can improve both the signal acceptance *and* the momentum resolution.

Appendix D.

Summary of the AlCap Experiment

The following was originally submitted for the proceedings of NuFact ‘15 and has been published online from the meeting’s home page. Although peer reviewed, it has not appeared in print, and so I reproduce it here in its entirety.

List of Simulation Configurations

List of Acronyms

BSM Beyond the Standard Model

CDC Cylindrical Drift Chamber

CDR Conceptual Design Report

CERN Organisation européenne pour la recherche nucléaire

CLFV Charged Lepton Flavour Violation

COM centre-of-mass

CRV Cosmic Ray Veto

CyDet Cylindrical Detector

DIO decay in orbit

JFY Japanese Fiscal Year

J-PARC the Japanese Proton Accelerator Research Complex

LFV Lepton Flavour Violation

LYSO Cerium-doped Lutetium Yttrium Oxyorthosilicate

MR J-PARC Main Ring

PID Particle Identification

POT Protons on Target

PMNS Pontecorvo-Maki-Nakagawa-Sakata

PSI The Paul Scherrer Institute

RCS J-PARC Rapid Cycling Synchrotron

RMC Radiative Muon Capture

RPC Radiative Pion Capture

SES Single-Event Sensitivity

SM Standard Model

StrECAL Straw tube tracker and Electromagnetic Calorimeter

TDR Technical Design Report

QCD Quantum Chromodynamics

Bibliography

- [1] see: <http://ilcsoft.desy.de/marlin>.
- [2] see: <http://www.cmtsite.org>. No longer maintained.
- [3] see: <http://www.cmake.org>.
- [4] Private Communication with Ye Yang, KEK.
- [5]
- [6] Private Communication with Yuki Fujii, KEK.
- [7] MIDAS (Maximum Integration Data Acquisition System). <http://midas.psi.ch>. Accessed: 22-May-2015.
- [8] Roel Aaij et al. Test of lepton universality using $B^+ \rightarrow K^+ \ell^+ \ell^-$ decays. *Phys. Rev. Lett.*, 113:151601, 2014.
- [9] Roel Aaij et al. Measurement of the ratio of branching fractions $\mathcal{B}(\bar{B}^0 \rightarrow D^{*+} \tau^- \bar{\nu}_\tau) / \mathcal{B}(\bar{B}^0 \rightarrow D^{*+} \mu^- \bar{\nu}_\mu)$. *Phys. Rev. Lett.*, 115(11):111803, 2015. [Addendum: *Phys. Rev. Lett.* 115,no.15,159901(2015)].
- [10] A. Abdesselam et al. Measurement of the branching ratio of $\bar{B}^0 \rightarrow D^{*+} \tau^- \bar{\nu}_\tau$ relative to $\bar{B}^0 \rightarrow D^{*+} \ell^- \bar{\nu}_\ell$ decays with a semileptonic tagging method. 2016.
- [11] K. Abe, N. Abgrall, H. Aihara, Y. Ajima, J.B. Albert, and D. Allan. The t2k experiment. *Nuclear Instruments and Methods in Physics Research Section A: Accelerators, Spectrometers, Detectors and Associated Equipment*, 659(1):106 – 135, 2011.
- [12] S. Agostinelli, J. Allison, K. Amako, J. Apostolakis, H. Araujo, P. Arce, M. Asai, D. Axen, S. Banerjee, G. Barrand, F. Behner, L. Bellagamba, J. Boudreau, L. Broglia, A. Brunengo, H. Burkhardt, S. Chauvie, J. Chuma, R. Chytracek, G. Cooperman, G. Cosmo, P. Degtyarenko, A. Dell'Acqua, G. Depaola, D. Dietrich, R. Enami, A. Feliciello, C. Ferguson, H. Fesefeldt, G. Folger, F. Foppiano, A. Forti, S. Garelli, S. Giani, R. Giannitrapani, D. Gibin, J.J. Gmez Cadenas, I. Gonzlez, G. Gracia Abril, G. Greeniaus, W. Greiner, V. Grichine, A. Grossheim, S. Guatelli, P. Gumplinger, R. Hamatsu, K. Hashimoto, H. Hasui, A. Heikkinen, A. Howard, V. Ivanchenko, A. Johnson, F.W. Jones, J. Kallenbach, N. Kanaya, M. Kawabata, Y. Kawabata, M. Kawaguti, S. Kelner, P. Kent, A. Kimura, T. Kodama, R. Kokoulin, M. Kossov, H. Kurashige, E. Lamanna, T. Lampn, V. Lara, V. Lefebure, F. Lei, M. Liendl,

- W. Lockman, F. Longo, S. Magni, M. Maire, E. Medernach, K. Minamimoto, P. Mora de Freitas, Y. Morita, K. Murakami, M. Nagamatu, R. Nartallo, P. Nieminen, T. Nishimura, K. Ohtsubo, M. Okamura, S. O'Neale, Y. Oohata, K. Paech, J. Perl, A. Pfeiffer, M.G. Pia, F. Ranjard, A. Rybin, S. Sadilov, E. Di Salvo, G. Santin, T. Sasaki, N. Savvas, Y. Sawada, S. Scherer, S. Sei, V. Sirotenko, D. Smith, N. Starkov, H. Stoecker, J. Sulkimo, M. Takahata, S. Tanaka, E. Tcherniaev, E. Safai Tehrani, M. Tropeano, P. Truscott, H. Uno, L. Urban, P. Urban, M. Verderi, A. Walkden, W. Wander, H. Weber, J.P. Wellisch, T. Wenaus, D.C. Williams, D. Wright, T. Yamada, H. Yoshida, and D. Zschiesche. Geant4 - a simulation toolkit. *NIM in PRS A*, 506(3):250 – 303, 2003.
- [13] AlCap Collaboration. Study of muon capture for muon to electron conversion experiments. http://muon.npl.washington.edu/exp/AlCap/R-13-03.1_BV44.pdf. Accessed: 28-October-2015.
- [14] Wolfgang Altmannshofer, Andrzej J. Buras, Stefania Gori, Paride Paradisi, and David M. Straub. Anatomy and phenomenology of fcnc and cpv effects in susy theories. *Nuclear Physics B*, 830(12):17 – 94, 2010.
- [15] Jose Enrique Amaro, A. M. Lallena, and J. Nieves. Radiative pion capture in nuclei: A Continuum shell model approach. *Nucl. Phys.*, A623:529–547, 1997.
- [16] Aldo Antognini et al. Proton Structure from the Measurement of $2S - 2P$ Transition Frequencies of Muonic Hydrogen. *Science*, 339:417–420, 2013.
- [17] T. Aramaki, S.K. Chan, W.W. Craig, L. Fabris, F. Gahbauer, C.J. Hailey, J.E. Koglin, N. Madden, K. Mori, H.T. Yu, and K.P. Ziock. A measurement of atomic x-ray yields in exotic atoms and implications for an antideuteron-based dark matter search. *Astroparticle Physics*, 49:52 – 62, 2013.
- [18] D. S. Armstrong, A. Serna-Angel, S. Ahmad, G. Azuelos, W. Bertl, M. Blecher, C. Q. Chen, P. Depommier, T. von Egidy, T. P. Gorringe, M. D. Hasinoff, R. S. Henderson, A. J. Larabee, J. A. Macdonald, S. C. McDonald, J-M. Poutissou, R. Poutissou, B. C. Robertson, D. G. Sample, G. N. Taylor, D. H. Wright, and N. S. Zhang. Radiative muon capture on al, si, ca, mo, sn, and pb. *Phys. Rev. C*, 46:1094–1107, Sep 1992.
- [19] D. Armuliiiski, Ts. Baatar, Ts. Batsaikhan, T. Kanarek, E.N. Kladnitskaya, M.U. Sultanov, R. Togoo, G.P. Toneeva, and D. Tuvdendorzh. Hadron spectra in hadron - nucleus collisions. 1991.
- [20] G. Audi, O. Bersillon, J. Blachot, and A.H. Wapstra. The 2003 nubase and atomic mass evaluations the nubase evaluation of nuclear and decay properties. *Nuclear Physics A*, 729(1):3 – 128, 2003.
- [21] D. S. Ayres et al. The NOvA Technical Design Report. 2007.
- [22] G. Barrand, I. Belyaev, P. Binko, M. Cattaneo, R. Chytracek, et al. GAUDI - A Software Architecture and Framework for Building HEP Data Processing Applications.

- Comput.Phys.Commun.*, 140:45–55, 2001.
- [23] L. Bartoszek et al. Mu2e Technical Design Report. 2014.
- [24] P. C. Bergbusch, D. S. Armstrong, M. Blecher, C. Q. Chen, B. C. Doyle, T. P. Gorringe, P. Gumpelinger, M. D. Hasinoff, G. Jonkmans, J. A. Macdonald, J-M. Poutissou, R. Poutissou, C. N. Sigler, and D. H. Wright. Radiative muon capture on o, al, si, ti, zr, and ag. *Phys. Rev. C*, 59:2853–2864, May 1999.
- [25] Wilhelm H. Bertl et al. A Search for muon to electron conversion in muonic gold. *Eur.Phys.J.*, C47:337–346, 2006.
- [26] J. A. Bistirlich, K. M. Crowe, A. S. L. Parsons, P. Skarek, and Peter Truoel. Photon spectra from radiative absorption of pions in nuclei. *Phys. Rev.*, C5:1867–1883, 1972.
- [27] Thomas Blum, Achim Denig, Ivan Logashenko, Eduardo de Rafael, B. Lee Roberts, Thomas Teubner, and Graziano Venanzoni. The Muon (g-2) Theory Value: Present and Future. 2013.
- [28] S. V. Boyarinov, I. I. Evseev, Yu. T. Kiselev, G. A. Leksin, A. N. Martemyanov, K. R. Mikhailov, S. A. Pozdnyakov, Yu. V. Terekhov, V. I. Ushakov, and V. A. Sheinkman. Yields of p, anti-p, pi+-, and K+- emitted at an angle of 97-degrees in the laboratory system from nuclei irradiated by 10.14-GeV protons. *Phys. Atom. Nucl.*, 57:1379–1388, 1994. [Yad. Fiz.57,1452(1994)].
- [29] H. N. Brown et al. Precise measurement of the positive muon anomalous magnetic moment. *Phys. Rev. Lett.*, 86:2227–2231, 2001.
- [30] R. Brun, A. Gheata, and M. Gheata. The ROOT geometry package. *Nucl. Instrum. Meth.*, A502:676–680, 2003.
- [31] Rene Brun and Fons Rademakers. ROOT - an object oriented data analysis framework, proceedings aihenp’96 workshop, lausanne, sep. 1996,. *Nuclear Instruments and Methods in Physics Research Section A*, page 81.
- [32] M. G. Catanesi et al. The HARP detector at the CERN PS. *Nucl. Instrum. Meth.*, A571:527–561, 2007.
- [33] P. Christillin, M. Rosa-Clot, and S. Servadio. Radiative muon capture in medium-heavy nuclei. *Nuclear Physics A*, 345(2):331 – 366, 1980.
- [34] CMS Collaboration. Search for Lepton Flavour Violating Decays of the Higgs Boson in the mu-tau final state at 13 TeV. 2016.
- [35] COMET Collaboration. Conceptual design report for experimental search for lepton violating $\mu^- e^-$ conversion at sensitivity of 10^{-16} with a slow-extracted bunched proton beam (COMET), J-PARC P21.
- [36] COMET Collaboration. Experimental proposal for phase-1 of the COMET experiment at J-PARC.

- [37] Comet group on Gitlab. <https://gitlab.in2p3.fr/comet>.
- [38] Andrzej Czarnecki, Xavier Garcia i Tormo, and William J. Marciano. Muon decay in orbit: Spectrum of high-energy electrons. *Phys. Rev.*, D84(1):013006, 2011.
- [39] G. Danby, J-M. Gaillard, K. Goulian, L. M. Lederman, N. Mistry, M. Schwartz, and J. Steinberger. Observation of high-energy neutrino reactions and the existence of two kinds of neutrinos. *Phys. Rev. Lett.*, 9:36–44, Jul 1962.
- [40] Raymond Davis, Jr., Don S. Harmer, and Kenneth C. Hoffman. Search for neutrinos from the sun. *Phys. Rev. Lett.*, 20:1205–1209, 1968.
- [41] A. de Gouvea. (charged) lepton flavor violation. *Nuclear Physics B - Proceedings Supplements*, 188:303 – 308, 2009.
- [42] Deppisch, Frank F. and Harz, Julia and Hirsch, Martin and Huang, Wei-Chih and Päs, Heinrich. Falsifying High-Scale Baryogenesis with Neutrinoless Double Beta Decay and Lepton Flavor Violation. *Phys. Rev.*, D92(3):036005, 2015.
- [43] D. N. Dinh, A. Ibarra, E. Molinaro, and S. T. Petcov. The $\mu - e$ Conversion in Nuclei, $\mu \rightarrow e\gamma$, $\mu \rightarrow 3e$ Decays and TeV Scale See-Saw Scenarios of Neutrino Mass Generation. *JHEP*, 08:125, 2012. [Erratum: JHEP09,023(2013)].
- [44] Rashid M. Djilkibaev. Antiproton yields simulation. Technical report, Department of Physics and Astronomy, University of California.
- [45] Rashid M. Djilkibaev. Meco muon yield simulation using experimental data. Technical report, Department of Physics and Astronomy, University of California.
- [46] M. Döbeli, M. Doser, L. van Elmbt, M. W. Schaad, P. Truöl, A. Bay, J. P. Perroud, J. Imazato, and T. Ishikawa. Radiative muon capture in nuclei. *Phys. Rev. C*, 37:1633–1646, Apr 1988.
- [47] Andrew Williams John Edmonds. *An Estimate of the Hadron Production Uncertainty and a Measurement of the Rate of Proton Emission after Nuclear Muon Capture for the COMET Experiment*. PhD thesis, U. Coll. London, 2015.
- [48] H. D. Engelhardt, C. W. Lewis, and H. Ullrich. The Absorption of pi- at Rest on Complex Nuclei. *Nucl. Phys.*, A258:480–512, 1976.
- [49] Alfredo Ferrari, Paola R. Sala, Alberto Fasso, and Johannes Ranft. FLUKA: A multi-particle transport code (Program version 2005). 2005.
- [50] P. Finlay, S. Ettenauer, G. C. Ball, J. R. Leslie, C. E. Svensson, C. Andreoiu, R. A. E. Austin, D. Bandyopadhyay, D. S. Cross, G. Demand, M. Djongolov, P. E. Garrett, K. L. Green, G. F. Grinyer, G. Hackman, K. G. Leach, C. J. Pearson, A. A. Phillips, C. S. Sumithrarachchi, S. Triambak, and S. J. Williams. High-precision half-life measurement for the superallowed β^+ emitter $^{26}\text{Al}^m$. *Phys. Rev. Lett.*, 106:032501, Jan 2011.

- [51] G4Beamline. G4beamline homepage. 2009. <http://www.muonsinternal.com/muons3/G4beamline>.
- [52] Melissa Anne George. *Calibrating the Electromagnetic Calorimeter of T2K*. PhD thesis, Queen Mary, U. of London (main), 2010.
- [53] Sheldon L. Glashow, Diego Guadagnoli, and Kenneth Lane. Lepton Flavor Violation in B Decays? *Phys. Rev. Lett.*, 114:091801, 2015.
- [54] Tim Gorringe and Harold W. Fearing. Induced pseudoscalar coupling of the proton weak interaction. *Rev. Mod. Phys.*, 76:31–91, Dec 2003.
- [55] F. J. Hartmann, R. Bergmann, H. Daniel, H. J. Pfeiffer, T. Von Egidy, and W. Wilhelm. MEASUREMENT OF THE MUONIC X-RAY CASCADE IN MG, AL, IN, HO, AND AU. *Z. Phys.*, A305:189–204, 1982.
- [56] D. Heck, J. Knapp, J.N. Capdevielle, G. Schatz, and T. Thouw. Report FZKA 6019. . <http://wwwik.fzk.de/corsika/physicsdescription/corsikaphys.html>, 1998.
- [57] Julian Heeck. Lepton flavor violation with light vector bosons. *Phys. Lett.*, B758:101–105, 2016.
- [58] E. P. Hincks and B. Pontecorvo. Search for gamma-radiation in the 2.2-microsecond meson decay process. *Phys. Rev.*, 73:257–258, Feb 1948.
- [59] C. Hoppner, S. Neubert, B. Ketzer, and S. Paul. A Novel Generic Framework for Track Fitting in Complex Detector Systems. *Nucl. Instrum. Meth.*, A620:518–525, 2010.
- [60] H. Iwase, K. Niita, and T. Nakamura. Development of general-purpose particle and heavy ion transport monte carlo code. *Journal of Nuclear Science and Technology*, 39(11):1142–1151, 2002.
- [61] Savel G. Karshenboim, David McKeen, and Maxim Pospelov. Constraints on muon-specific dark forces. *Phys. Rev.*, D90(7):073004, 2014. [Addendum: *Phys. Rev.*D90,no.7,079905(2014)].
- [62] Vardan Khachatryan et al. Search for Lepton-Flavour-Violating Decays of the Higgs Boson. *Phys. Lett.*, B749:337–362, 2015.
- [63] Yu. T. Kiselev, V. A. Sheinkman, A. V. Akindinov, M. M. Chumakov, A. N. Martemyanov, V. A. Smirnitsky, Yu. V. Terekhov, and E. Ya. Paryev. Probing of compact baryonic configurations in nuclei in $A(p, \bar{p})X$ reactions and antiproton formation length in nuclear matter. *Phys. Rev.*, C85:054904, 2012.
- [64] K. S. Krane, T. C. Sharma, L. W. Swenson, D. K. McDaniels, P. Varghese, B. E. Wood, R. R. Silbar, H. D. Wohlfahrt, and C. A. Goulding. ENERGETIC CHARGED PARTICLE SPECTRUM FOLLOWING MU- CAPTURE BY NUCLEI. *Phys. Rev.*, C20:1873–1877, 1979.

- [65] Ben Krikler, Ajit Kurup, Yoshi Uchida, Andrew Edmonds, Phill Litchfield, and the COMET Collaboration Software Group. Icedust conventions. *Internal Document*.
- [66] Robert K Kutschke. art: A framework for new, small experiments at fermilab. *Journal of Physics: Conference Series*, 331(3):032019, 2011.
- [67] G. Lafferty. Pentaquarks and possible anomalies at LHCb. *Int. J. Mod. Phys.*, A31(20n21):1630032, 2016.
- [68] J. P. Lees et al. Evidence for an excess of $\bar{B} \rightarrow D^{(*)}\tau^-\bar{\nu}_\tau$ decays. *Phys. Rev. Lett.*, 109:101802, 2012.
- [69] John Craig Martens and John P. Ralston. The Muon Experimental Anomalies Are Explained by a New Interaction Proportional to Charge. 2016.
- [70] David F. Measday and Trevor J. Stocki. Comparison of muon capture in light and in heavy nuclei. *AIP Conference Proceedings*, 947(1), 2007.
- [71] I. N. Mishustin, L. M. Satarov, T. J. Burvenich, Horst Stoecker, and W. Greiner. Antibaryons bound in nuclei. *Phys. Rev.*, C71:035201, 2005.
- [72] Nikolai V. Mokhov. The MARS code system user's guide version 13(95). 1995.
- [73] S. H. Neddermeyer and C. D. Anderson. Note on the Nature of Cosmic Ray Particles. *Phys. Rev.*, 51:884–886, 1937.
- [74] Y. Nishina, M. Takeuchi, and T. Ichimiya. On the nature of cosmic-ray particles. *Phys. Rev.*, 52:1198–1199, Dec 1937.
- [75] K.A. Olive and Particle Data Group. Review of particle physics. *Chinese Physics C*, 38(9):090001, 2014.
- [76] Cobham Technical Services. see: <http://operafea.com>.
- [77] S.E. Sobottka and E.L. Wills.
- [78] J. C. Street and E. C. Stevenson. New evidence for the existence of a particle of mass intermediate between the proton and electron. *Phys. Rev.*, 52:1003–1004, Nov 1937.
- [79] T. Suzuki, D. F. Measday, and J. P. Roalsvig. Total nuclear capture rates for negative muons. *Phys. Rev. C*, 35:2212–2224, Jun 1987.
- [80] The COMET Collaboration. COMET Phase-I: Technical Design Report. Technical report, KEK, April 2016.
- [81] The COMET Collaboration Software Group. Comet software framework requirements. *Internal Document*.
- [82] The COMET Collaboration Software Group. Forking from nd280. *Internal Document*, see https://gitlab.in2p3.fr/comet/ICEDUST_documentation/tree/master/Forking_from_nd280.

- [83] M.N. Thompson, J.M. Taylor, B.M. Spicer, and J.E.E. Baglin. The al27(, n)al26m cross section. *Nuclear Physics*, 64(3):486 – 496, 1965.
- [84] Nam Hoai Tran. A Study of Proton Emission Following Nuclear Muon Capture for the COMET Experiment. *Thesis*, 2014.
- [85] E.J. Williams and G.E. Roberts. Evidence for transformation of mesotrons into electrons [1]. *Nature*, 145(3664):102–103, 1940. cited By 13.
- [86] C. Y. Wong, A. K. Kerman, G. R. Satchler, and A. D. Mackellar. AMBIGUITY IN ANTI-PROTON NUCLEUS POTENTIALS FROM ANTI-PROTONIC ATOM DATA. *Phys. Rev.*, C29:574–580, 1984.
- [87] D. H. Wright and M. H. Kelsey. The Geant4 Bertini Cascade. *Nucl. Instrum. Meth.*, A804:175–188, 2015.
- [88] A. Wyttenbach, P. Baertschi, S. Bajo, J. Hadermann, K. Junker, S. Katcoff, E. A. Hermes, and H. S. Pruys. Probabilities of Muon Induced Nuclear Reactions Involving Charged Particle Emission. *Nucl. Phys.*, A294:278–292, 1978.
- [89] Hideki Yukawa. On the Interaction of Elementary Particles I. *Proc. Phys. Math. Soc. Jap.*, 17:48–57, 1935. [Prog. Theor. Phys. Suppl.1,1(1935)].